Storfjorden Trough Mouth Fan (Western Barents Sea): Slope failures in polar continental margins; significance of stress changes and fluid migration induced by glacial cycles

Doctoral Thesis

November 2016

by

Jaume Llopart

Storfjorden Trough Mouth Fan (Western Barents Sea): slope failures in polar continental margins; significance of stress changes and fluid migration induced by glacial cycles

Author: J. Llopart
Advisors: R. Urgeles, A. Camerlenghi
Tutor: J.M. Vilaplana
Programa doctorat: Ciències de la Terra: Riscos geològics i geomorfología

Agraïments - Acknowledgements

Agrair al director d'aquesta tesis, Roger Urgeles, per la paciència, suport i dedicació al llarg d'aquest 5+1 anys que portem treballant junts. També agraeixo a l'Angelo C. com a codirector, i a en Joan Manuel Vilaplana com a tutor que sempre han estat disposats a ajudar i aconsellar.

The whole dataset used in this thesis is under the umbrella of the international project IPY-NICE STREAMS 367. So I want to acknowledge the opportunity to work with these dataset to the PIs of the projects: SVAIS, EGLACOM and CORIBAR. As well as knowledge the former PI A. Camerlenghi and the actual J.L. Casamor of the DEGLABAR project for their work and help throughout this Thesis.

Funding

This study was funded by the “Ministerio de Economia y Competitividad” through the IPY project DEGLABAR (CTM2010-17386). The author of this Thesis benefits from a four-year FPI fellowship (BES-2011-0436149) from “Ministerio de Economia y Competitividad”. The author was also granted within the framework of the FPI with a short stay of almost 3 month at the Norwegian Geotechnical Institute (NGI) in Oslo (EEBB-I-13-06687).

Table of contents

ABSTRACT

Storfjorden Trough Mouth Fan (Western Barents Sea): slope failures in polar continental margins; significance of stress changes and fluid migration induced by glacial cycles

by Jaume Llopart Serra

Late Quaternary climate variations controlled glacial advances and retreats to the shelf edge and therefore the evolution of high latitude continental margins. The variations in ice extension modulated sediment supply to the continental slope resulting in a particular shape and stratigraphy but also exerted a major control on stresses imposed on marine sediments and likely had a major control on fluid flow pattern. This thesis investigates the sedimentary, stratigraphic and hydrogeologic evolution of two Arctic Trough Mouth Fans (TMFs), the Storfjorden and Kveithola TMFs in the NW Barents Sea, from ~2.7 Ma to Present, and identifies how such evolution affected slope instability of the TMFs. The research is carried out by means of sub-bottom and seismic reflection profiles, multibeam bathymetry data and sediment cores on which sedimentological and

geotechnical analysis have been performed. Numerical finite elements models allow inferring the detailed stratigraphic architecture and hydrogeological evolution of the TMFs. We found that the Storfjorden and Kveithola TMFs mainly consist of an alternation of rapidly deposited glacigenic debris flows during glacial maxima and a sequence of well-layered plumites and hemipelagic sediments, which were mainly deposited during the deglaciation phase of the adjacent glacial trough. We have identified eight units above regional reflector R1, which indicate that the ice sheet reached the shelf edge within the Storfjorden Trough on at least three occasions during the last ~200 ka. A shallow subsurface unit of glacigenic debris flows suggests that the ice sheet had a short re-advance over the northern and central part of Storfjorden after the Last Glacial Maximum. From stratigraphy, core and literature data, we estimate that ice sheets reached the shelf edge between 19.5 to 22.5 ka, 61 to 65 ka and 135 to 167 ka.

Geotechnical tests performed in core sediment samples show that plumites have high void ratios and permeabilities with respect to glacigenic debris flows and tills at initial deposition conditions. A number of oedometer tests also indicate that the compressibility of plumite sediments is higher than that of glacigenic debris flows and tills. Compressibility and permeability results obtained in a Rowe & Barden consolidation test are used together with margin stratigraphic architecture derived from seismic data, as input

for hydrogeological numerical finite element models. Two software packages have been used to understand the impact of sedimentary and glacial loads on fluid flow patterns and overpressure development at different spatial and temporal scales. The BASIN (Bitzer, 1999, 1996) software has been used to model the evolution of the Storfjorden TMF from 2.7 to 0.2 Ma. The model results show that onset of glacial sedimentation (deposition of tills), ~1.5 Ma ago, had a significant role in developing permeability barriers (aquitards) on the shelf. These barriers decreased vertical fluid flow towards the sea floor due to consolidation and diverted fluids towards the slope. The BASIN model shows that, prior to 220 ka, overpressure values reached up to 0.6 (i.e., that 60% of the lithostatic pressure was supported by the pore fluids). These higher overpressure occurred 400 m below the shelf edge and in the middle slope (most distal part of the model), in between 1000 and 2300 m deep. The Plaxis (PLAXIS bv, 2015) software provides a more detailed high resolution hydrogeological model for the shelf and upper slope during the latest four glacial/inter-glacial cycles, i.e., during the last 220 kyrs, while allowing for ice loading of the shelf sediments. These models show that ice loading during Glacial Maxima caused initiated consolidation of the shelf sediments inducing high fluid expulsion rates towards the shallower and more permeable plumite sediments on the slope. The high mean sedimentation rates of low permeability glacigenic debris flows during glacial maxima of

up to 18 kg m^{-2} yr^{-1} combined with deposition of tills that acted as aquitards along the shelf and flow focusing caused overpressure within plumite sequences of the upper slope reaching values around to 0.6. The models record the highest overpressures (0.75) during the Last Glacial Maximum at the shelf, but high overpressures remained a few thousand years well into the deglaciation period.

The geophysical data used in this thesis shows that most landslides identified in this part of the NW Barents Sea are located in the inter-TMF area between Storfjorden and Kveithola. Stratigraphic analysis using seismic data supported with core information show that the landslides occurred mainly during the last deglacial where plumites form the thickest deposits and likely highest overpressure values according to the models. A finite element stress-deformation-based slope stability analysis throughout the Last Glacial Maximum, last deglaciation and Holocene has been carried out showing that stability of the margin decreased by ~50% due to the overpressures developed during the Last Glacial Maximum in plumite sediments. The minimum values of the Factor of Safety (SF ~ 1.2) were reached at the end of the last glaciation and were preserved a few thousand years after beginning of the last deglaciation. The timing of these low SF matches with the dating of most landslides identified in the study area. However, the SF values above 1 highlight that additional mechanisms need to be invoked to explain instability of the margin. These additional

mechanisms likely involved earthquakes induced by glacio-eustatic rebound.

The detailed seismo-stratigraphic analysis and hydrogeological modeling performed in this thesis allows refining the sedimentary model of Arctic TMFs. This new model involves four major stages, namely: a) Interglacial stage with hemipelagic sedimentation and dense shelf water flows due to sea ice formation and brine release during winter. b) Glaciation and Glacial Maxima when the material transported by ice streams is dumped over the shelf edge as debris flows. C) Deglaciation when turbid meltwater plumes leave a bed of plumites/turbidite sediments over the area. And, d) A submarine landslides stage induced by ice sheet retreat and earthquakes triggered by isostatic rebound. The main differences to previous models involve gully formation during not only the deglaciation phase, but also during interglacials by dense shelf water cascading, and a specific timing for the occurrence of slope failures (i.e., shortly after the deglaciation phase).

List of Figures

List of Tables

Scope and organization of this Thesis

Scope and organization of this Thesis

Motivation and general objectives

Trough Mouth Fans (TMFs) constitute the preeminent areas of terrigenous sediment accumulation in high-latitude continental margins. TMFs are equivalent in size, volume, and sediment mass allocation to deep-sea fans located on mid to low-latitude continental margins (Dowdeswell et al., 1996; Elverhøi et al., 1998). While sediment transport and deposition of deep-sea fans are well known, such comprehensive sedimentary models still lack for TMFs. The conceptual model of TMF as a uniform sedimentary system dominated by glacial–interglacial rhythmic sedimentation (i.e. Alley et al., 1989; Vorren et al., 2011) needs to be revised because recent evidences suggest complex subglacial and pro-glacial environment processes (i.e. Dowdeswell et al., 2008; Laberg et al., 2005; Ó Cofaigh et al., 2003).

Climatically modulated sedimentation in polar continental margins creates large heterogeneities in sediment type and provides large spatial variability in physical properties of marine sediments. TMF sedimentation patterns and TMF architecture are not only important to reconstruct past ice sheet dynamics and extent within the climatic history of Earth, but also for understanding high-latitude petroleum systems, fluid migration pathways and the geohazard from major submarine slope failures. How the evolution of a glacial influenced

continental margin and its stratigraphy affects the hydrogeology and fluid flow patterns is not well known yet. The development of excess pore pressure from non-equilibrium consolidation, as well as from methane hydrates dissociation and dissolution, represent a geohazard because they are one of the major controls on submarine slope failure initiation (Bryn et al., 2005; Dugan and Flemings, 2000; Grozic, 2010; Mienert et al., 2005; Sultan et al., 2004b; Vorren et al., 1998). Under these constraints, sediment interstitial fluids must have played a significant role in continental margin development, resulting in sediment instability when combined with depositional over steeping (Dimakis et al., 2000). Fluid flow patterns and pore pressure development related to Late Quaternary slope instabilities in continental margins have been previously modeled for both scientific and industrial purposes (i.e. Bunz et al., 2005; Kvalstad et al., 2005b; Stigall and Dugan, 2010; Urgeles et al., 2010). In this regard, numerical models have been used to explain the triggering sources of major landslides in the Norwegian and western Barents Sea continental margins (i.e. Storegga and Bear Island slides), although the ice loading effect on the shelf during glacial maxima has not been considered (i.e. Bryn et al., 2005; Kvalstad et al., 2005a).

During the last decades large submarine landslides have been widely discovered in Polar Regions (Bugge et al., 1987; Haflidason et al., 2005; Laberg et al., 2000; Laberg and Vorren, 2000, 1995, 1993). The Norwegian margin has been subject of a comprehensive study motivated by the occurrence of gas and oil fields

associated to nearby landslides (i.e. Leynaud et al., 2004; Nadim et al., 2005). Large and medium-size landslides between 0.9 to 3200 km^3 in volume are well documented in the Norwegian and Barents Sea margins (i.e. Storegga Slide (Bugge et al., 1987; Haflidason et al., 2005), Bjørnøyrenna Slide (Laberg and Vorren, 1995, 1993), Trænadjupet Slide (Laberg and Vorren, 2000), Andøya Slide (Laberg et al., 2000)). The thick deposits accumulated during glacial and interglacial cycles have been subject to ice sheets dynamics, loading and unloading by the grounded ice sheet, glacio-eustatic sea-level variations, glacio-isostatic rebound and associated seismicity, etc (i.e. Baeten et al., 2014; Bungum et al., 2005; Mulder and Moran, 1995; Urlaub et al., 2013).

High accumulation rates have been pointed as a pre-conditioning factor for slope failures and excess pore pressure development in passive continental margins (i.e. Hjelstuen et al., 2007; Stigall and Dugan, 2010). The highest sedimentation rate values are related to TMFs in high latitudes and large rivers fans in mid and low latitudes (e.g. 36 m/kyr Storegga slide area, 12 m/kyr Mississippi, 4 m/kyr Amazon; Urlaub et al., 2013)). Even though, in high latitude settings the large amount of sediments deposited during glacial periods coupled with the stress developed by ice advances, and also the variability in sediment thickness and sedimentation rates during glacial and interglacial periods could develop a particular fluid flow patterns also overpressure in the slope sediments that may affect the slope stability. A complete explanation of the linking between

stratigraphy, glacial/interglacial cycles, ice loading, continental margin fluid flow patterns, and landslide occurrence is still unraveled.

The aims of this study are therefore to:

i) Determine the nature, timing and relation of processes that shaped a formerly glaciated continental margin.

ii) Understand how alternating climatically-controlled sedimentation together with glacial advances and retreats in a high-latitude trough mouth fan influenced pore pressure development.

iii) Assess how these sedimentary and glacially-controlled processes influenced slope instability of the trough mouth fan through time.

Specific aims of this Thesis

In order to achieve the general goals described above, the following specific objectives have been defined:

- In relationship to the sedimentology and stratigraphy of Arctic Trough Mouth Fans:

    1. Characterize the detailed, recent (last ~200 ka) sedimentary architecture of Artcic TMFs using the Storfjorden and Kveithola TMFs as an example.

2. Characterize the different sedimentary deposits in the Storfjorden and Kveithola TMFs and the related morphological features.

3. Provide new insights into the sedimentary processes that take place in TMFs

4. Identify the cycle of sedimentary processes that shapes the morphology of TMFs.

5. Understand the relationship between alternating glacigenic to marine sedimentation and the occurrence of submarine landslides.

- In relationship to the hydrogeology of formerly glaciated continental margins

6. Characterize the compression and permeability characteristics of glacial, deglacial and interglacial marine sediments in a polar continental margin.

7. Model the Plio-Quaternary evolution of pore pressure across the Storfjorden TMF.

8. Understand fluid flow patterns along polar continental margin from the initial phase of TMF development to Present

9. Evaluate the influence of ice loading along the shelf during Glacial Maxima on the development of pore pressure and its relationship to the observed slope instabilities.

10. Understand how earthquakes related to isostatic rebound contribute to the instability of the TMFs.

Chapter 1
Introduction

Chapter 1. Introduction

1.1. Glacially-influenced continental margins

High-latitude continental margins have been influenced by glacial activity during the last ~34 Ma in Antarctica and ~2.6 Ma in the Arctic (DeConto and Pollard, 2003; Faleide et al., 1996). The interplay between proxies as ocean-surface temperature, sea level, bottom currents, ice sheet volume, ice flow velocity, and sediment have molded the present-day morphology and sedimentary architecture of high-latitude continental margins. In particular, the northern hemisphere orbitally driven alternation of glacial-interglacial periods is reflected in the marine sedimentary record (Sejrup et al., 2005), especially, the onset of the 100 kyr cycles (eccentricity dominated) in the last ~ 1 Ma glaciations (Hao et al., 2012). During glacial periods, ice streams provide a strong terrigenous input for the buildup of sedimentary fans located at the mouth of cross-shelf glacial troughs. These glacial troughs are the result of sediment erosion and till deposition transported subglacially by the ice sheets towards the shelf edge (Fiedler and Faleide, 1996). Ice stream bulldozing and sediment oversteepening at the shelf edge during glacial maxima, induces intense glacially-derived mass wasting over Trough Mouth Fans (TMFs) (Ó Cofaigh et al., 2013; Taylor et al., 2002; Vorren and Laberg, 1997) (Fig. 1.1). Through deposition of basal tills and Glacigenic Debris Flows (GDFs) during glacial periods, ice streams induce shelf edge

progradation that may attain a few kilometers (Rebesco et al., 2011). The dimensions of these fans are proportional to their troughs, drainage area and sediment availability (Vorren et al., 1998). However not all glacially carved cross-shelf troughs develop a TMF at their mouth. Factors such as distance to the ice sheet interior, size of the drainage basin, number of ice advances and duration of glaciations play a significant role in the development of such sedimentary bodies (Batchelor et al., 2013). Ó Cofaigh et al. (2003) suggest an "ideal" criteria for the formation of a well-developed TMF: 1) a favorable depositional setting along a passive continental margin, in front of a cross-shelf trough containing a large, fast-flowing ice stream; 2) an abundant and readily erodible sediments on a wide continental shelf; and 3) a low-gradient (<1º) continental slope, on which mass-movement is dominated by debris flows.

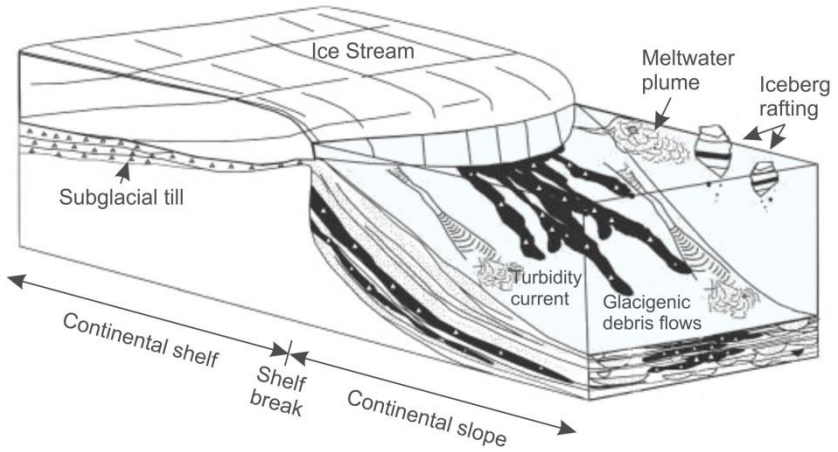

Fig. 1.1 Conceptual model of sedimentation on high-latitude trough mouth fans. Modified from Ó Cofaigh et al. (2013).

TMFs are characterized by alternating sedimentation rates (high during glacial maxima, low during the glacials before the maxima and interglacials) (Laberg et al., 2010) and contrasting sedimentary deposits, both in terms of facies (Lucchi et al., 2013) and physical properties (Llopart et al., 2014). Glacigenic debris flows are interbedded with low-density meltwater plume sediments (plumites) deposited during deglaciation periods (Hesse et al., 1997; Landvik et al., 1998; Lucchi et al., 2012). During interglacial periods, a hemipelagic sediment drape, and sedimentation by contour currents and shelf-derived turbidity currents re-shape the inherited margin morphology (Ó Cofaigh et al., 2002). Therefore, TMFs contain a rather continuous record of the interplay between past glacial dynamics and glacimarine to marine sedimentary processes, even if sediment deposition if focused in extreme episodes during glacial maxima (glacigenic debris flows) and deglaciations (plumites) (Lucchi et al., 2013)

Trough Mouth Fans are particularly well-developed on the western margin of the Barents Sea (Andersen et al., 1996; Laberg and Vorren, 1996a; Sættem et al., 1994). The continental shelf edge on its western boundary extends from about 70ºN to 80ºN and roughly strikes in the N-S direction. It is incised by several glacial troughs, which trend broadly ENE-WSW (Fig. 1.2). From South to North the main TMFs of the western Barents Sea are Bjørnøya, Kveithola, Storfjorden, Bellsund, Isfjorden, and Kongsfjorden (Fig. 1.2). The largest fan in this area is the Bear Island (Bjørnøya) Trough Mouth Fan with around $4 \cdot 10^5$ km^3 of sediments (Elverhøi et al., 1998). While in the fan area fast-flowing ice streams

supply a high debris flux which result in fan progradation, in the inter-fan areas ice flows up to two orders of magnitude slower, resulting in greatly reduced sediment delivery (Dowdeswell et al., 1998).

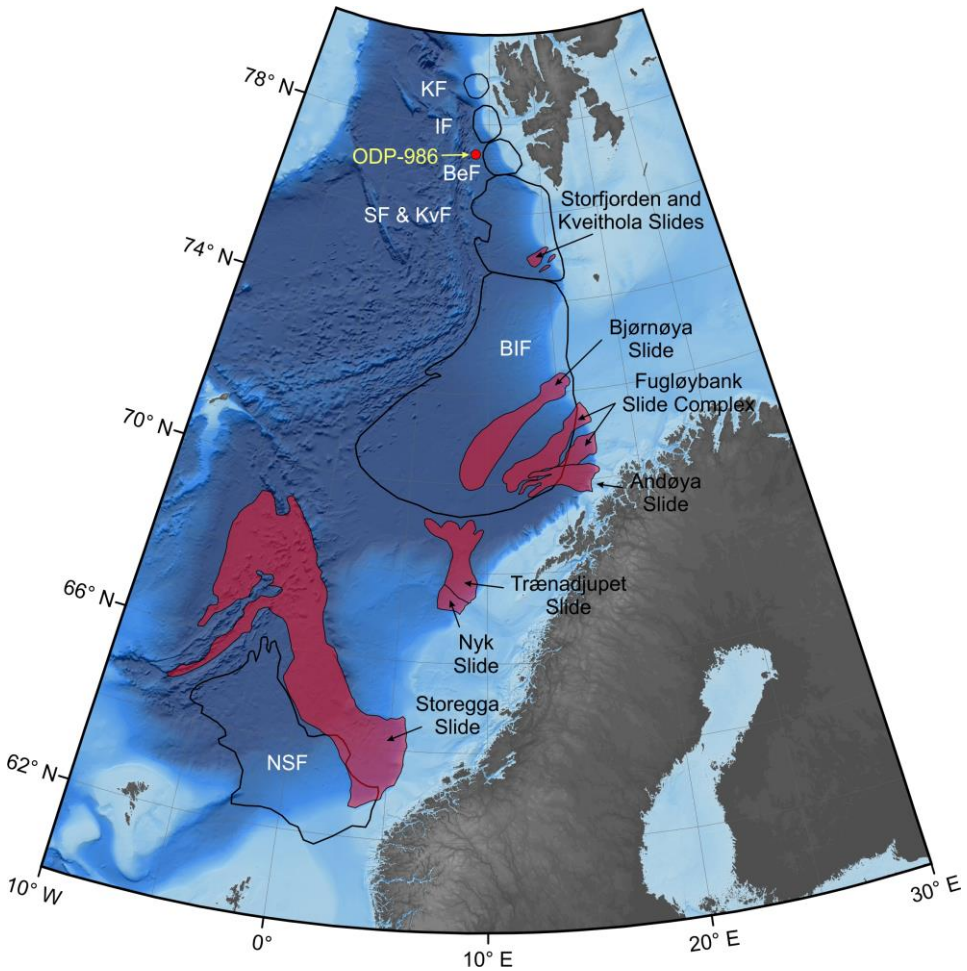

Fig. 1.2 Norwegian and Barents Sea area showing major Trough Mouth Fans (black lines) and major submarine landslides (red shapes). Location of ODP Site 986 is depicted. Compilation from Haflidason et al. (2005); Laberg et al. (2000); Laberg and Vorren, (2000, 1993); Lindberg et al. (2004); Sejrup et al. (2005) and references therein. KF: Kongsfjorden Fan; IF: Isfjorden Fan; BeF: Bellsund Fan; SF: Storfjorden Fan; KvF: Kveithola Fan; BIF: Bear Island Fan; NSF: Nort Sea Fan.

The slower rate of sediment delivery to the upper continental slope at inter-fan areas allows sediments to build up, rather than failing regularly to form the series of debris flow lobes which make up the bulk of glacier-influenced fan sedimentation (Dowdeswell et al., 1996). Therefore, failures in these inter-fan areas as landslides are more intermittent but involve substantially more sediment in each event. The locations of these large failures could be related to the less rapid nature of glacier-influenced sedimentation in inter-fan locations or higher accumulation of deglacial sediments (plumites) (Dowdeswell et al., 1996; Rebesco et al., 2012). Along the Norwegian and western Barents Sea continental margin, a number of landslides have been identified. Most of these landslides are located in a flank of its related trough mouth fan. The larger landslides in this area are Storegga Slide (Bugge et al., 1987; Haflidason et al., 2005), Bjørnøyrenna Slide (Laberg and Vorren, 1995, 1993), Trænadjupet Slide (Laberg and Vorren, 2000), Andøya Slide (Laberg et al., 2000) (Fig. 1.2). In addition to these Quaternary landslides, older landslides of Pleistocene age have been identified in the area such as the Sklinnadjupet and Helland Hansen Slides, Byørnøya Slide Complex, and PLS-1 and PLS-2 in Kveithola (Evans et al., 2005; Hjelstuen et al., 2007; Rebesco et al., 2012). In high-latitude continental margins rapid loading by high sedimentation rate depositional events and the ice advance over the shelf contribute to overpressures development (L'Heureux et al., 2013; Lerche et al., 1997). Specifically, in the Storegga Slide and the Bjørnøya Slide Complexes overpressures have been established as a pre-

conditioning factor, while a trigger event, such and earthquake loading, is needed to generate sediment mass transport (Atakan and Ojeda, 2005; Bondevik et al., 2012; Kvalstad et al., 2005a; Laberg and Vorren, 2000).

1.2. Hydrogeology of continental margins

Many offshore regions of the world exhibit excess pore pressures (pore pressures above the hydrostatic) (Fig. 1.3) caused by rapid sedimentation rates, sediment properties or subsidence (e.g., Storegga, Gulf of Mexico, Caspian Sea, and offshore West Africa) (Dugan and Sheahan, 2012). Because interstitial fluid flow migration is mainly controlled by the sediment load and the hydraulic properties of the different materials, the development of excess pore pressures or overpressures can play an important role in focusing fluid flow (Micallef et al., 2009), which is important for understanding migration pathways of fluids (water, hydrocarbons, etc.). Traditionally, pore pressure evolution modeling studies have been carried out in the frame of oil/gas fields (e.g. Barents Sea (Rodrigues Duran et al., 2013), Caspian Basin (Lee et al., 1999; Liu et al., 2016), Gulf of Mexico (Behrmann et al., 2006), Indonesia (Maubeuge and Lerche, 1994), North Sea (Stricker et al., 2016), or Sichuan Basin (Liu et al., 2016)), but also for scientific purposes (i.e. Dugan and Flemings, 2000; Dugan and Sheahan, 2012; Gutierrez and Wangen, 2005; Leynaud et al., 2007, 2004; Marín-Moreno et al., 2013; Yardley and Swarbrick, 2000). Computational and technological advancements

in the last few years have increased our ability to measure, validate and develop hydrogeological models, which has led to a better understanding of these

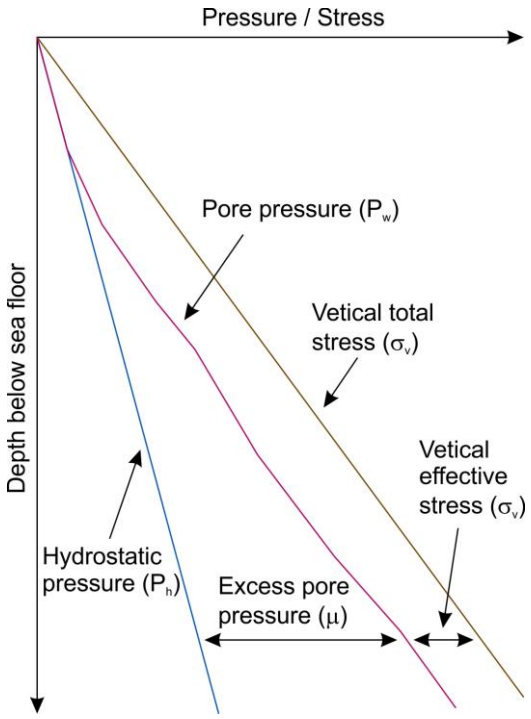

Fig. 1.3 Illustration showing excess pore pressure related to total stress, effectives stress, pore pressure and hydrostatic pressure.

systems, their dynamics, and the coupling of fluids and solids related to deformation and fluid flow (i.e. Flemings et al., 2008; Stigall and Dugan, 2010). 1D, 2D or 3D hydrogeological models need to simulate the principal causes of overpressure development in order to provide accurate results: rapid sedimentation, fluid migration and focusing, thermal fluid expansion or diagenetic water release (Dugan and Sheahan, 2012; Osborne and Swarbrick, 1997). These factors are the main causes of effective stress reduction and sediment destabilization, which can lead to slope instability and generation of

submarine landslides. (Dugan and Flemings, 2000; Dugan, 2014; Masson et al., 2014; Stigall and Dugan, 2010).

1.3. Continental margin related geohazards

Submarine landslides on open continental margins constitute a major geohazard for submarine infrastructures and, in turn, the potentially generated tsunamis for coastal populated areas. The occurrence of submarine landslides is worldwide spread in any kind of continental margin (Fig. 1.4) and they can occur in water depth ranges from 0-4000 m and slope angles <1º (Hühnerbach and Masson, 2004).

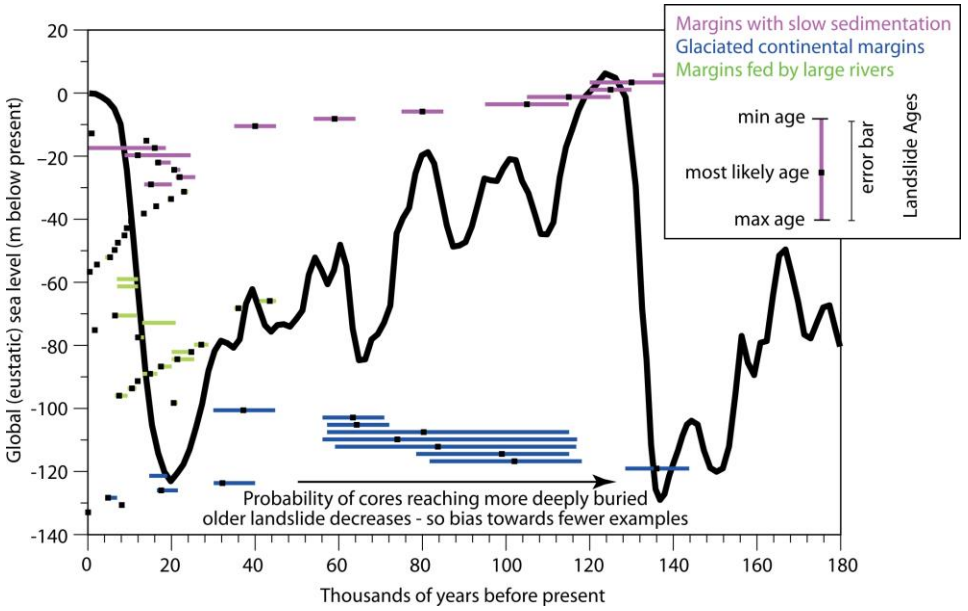

Fig. 1.4 Ages of large (> 1 km3) submarine landslides plotted against global (eustatic) sea level over the last 180000 years. Maximum and minimum landslide ages are shown, together with the most likely actual ages. Landslides are colored according to the types of settings in which they occur (from Talling et al., 2014).

The stability of submarine slopes depends on several factors, among which the hydrological regime is extremely important (Flemings et al., 2008). The most common pre-conditioning factor is the excess pore pressure caused by rapid sedimentation and fluid flow focusing, even though excess pore pressures can develop in slow sedimentation settings if the sediment permeability is very low (Talling et al., 2014). Other factors of sediment destabilization are cyclic wave loading, gas hydrates dissociation, weak layers and earthquakes (Grozic, 2010; Hühnerbach and Masson, 2004; Locat et al., 2014; Locat and Lee, 2000; Urlaub et al., 2013). Although some authors pointed that the frequency of landslides is linked to sea level and in turn, to gas hydrates dissociation (Brothers et al., 2013; Owen et al., 2007), recent compilation of submarine landslides depicts that there is no strong correlation between landslide frequency and sea level (Urlaub et al., 2013).

In high latitude continental margins the most common proposed final trigger for landslides is an earthquake generated by fault reactivation due to isostatic rebound during the onset of glaciations and deglaciations (Bungum et al., 2005; Canals et al., 2004; Hampel et al., 2009; Lee, 2009; Turpeinen et al., 2008). In this regard, Hampel et al. (2009) suggest that earthquakes up to $M_w \approx 8$ could occur in the western Barents Sea during the last deglaciation.

Not all the identified submarine landslides triggered a tsunami. The tsunami generation depends on the combination of factors such as the water depth of

failure, landslide volume, failure mechanism and its cohesive/non-cohesive behavior (Tappin, 2010) (Fig. 1.5). This non-straightforward relation is exemplified by landslides in the Norwegian margin. While Storegga slide triggered a tsunami which affected the Norway, Scotland and even Iceland coasts, no evidences have been found for the Trænadjupet slide (Bondevik et al., 2005; Tappin, 2010).

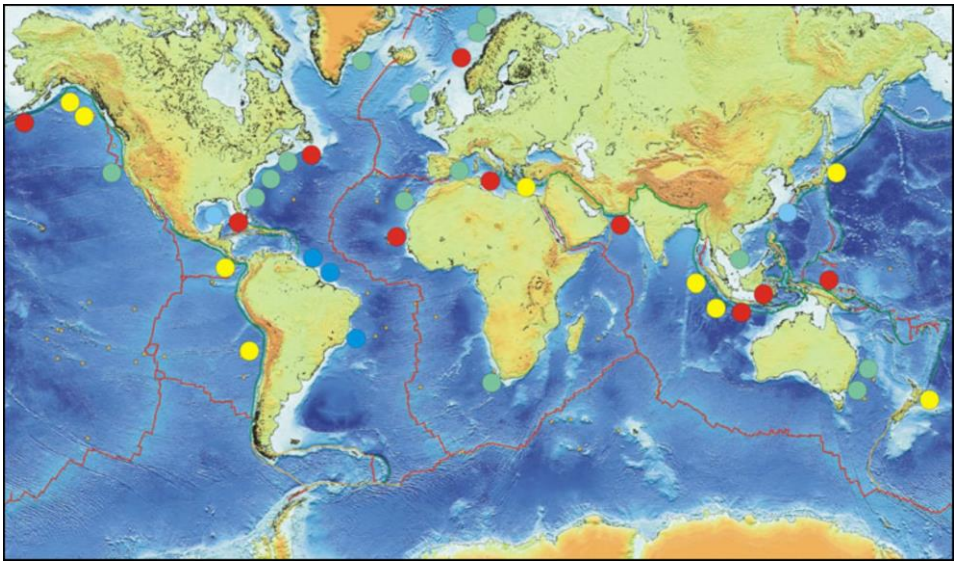

Fig. 1.5 Global distribution of mapped landslides. Green dots, landslides on continental shelves and fan systems, no identified tsunami. Yellow dots, landslides located along convergent margins, no identified tsunami. Red dots, locations of landslides-sourced tsunamis, or where there may be an landslides contribution. Grey-blue dots, active river systems, no tsunami identifie (from Tappin, 2010)

Understanding the past evolution of formerly glaciated margins and the coupling between sediment characteristics, hydrogeology, landslides occurrence is the key for assessing Present day geohazard in these of high latitude areas.

Chapter 2
Geological setting

Chapter 2. Geological setting

2.1 Pre-Pliocene geodynamic history

The Barents Sea is an epicontinental sea bounded by two passive continental margins to the North and West. The gradual northward opening of the Norwegian-Greenland Sea began at the Paleocene-Eocene transition. The western basin province consists of three main areas: (1) a southern sheared margin; (2) a central rifted complex associated with volcanism and (3) a northern initially sheared and later rifted margin along the Hornsund Fault Zone (HFZ; Fig. 2.1) (Eldholm et al., 1984; Faleide et al., 1993; Talwani and Eldholm, 1977). Each segment is characterized by distinct crustal properties, structural and magmatic styles, and history of vertical motion, mainly as a result of three controlling parameters (Faleide et al., 1991): (1) the pre-breakup structure; (2) the geometry of the plate boundary at opening; and (3) the direction of relative plate motion (Faleide et al., 2008).

The Senja Fracture Zone (SFZ) marks the southern segment of the predominantly sheared margin along the western Barents Sea (Fig. 2.1). The crustal thickness changes abruptly from more than 30 km thick on the continental crust of the Svalbard Platform, including the Svalbard archipelago, to 2–6 km thick oceanic crust in the Greenland Sea (Faleide et al., 2008).

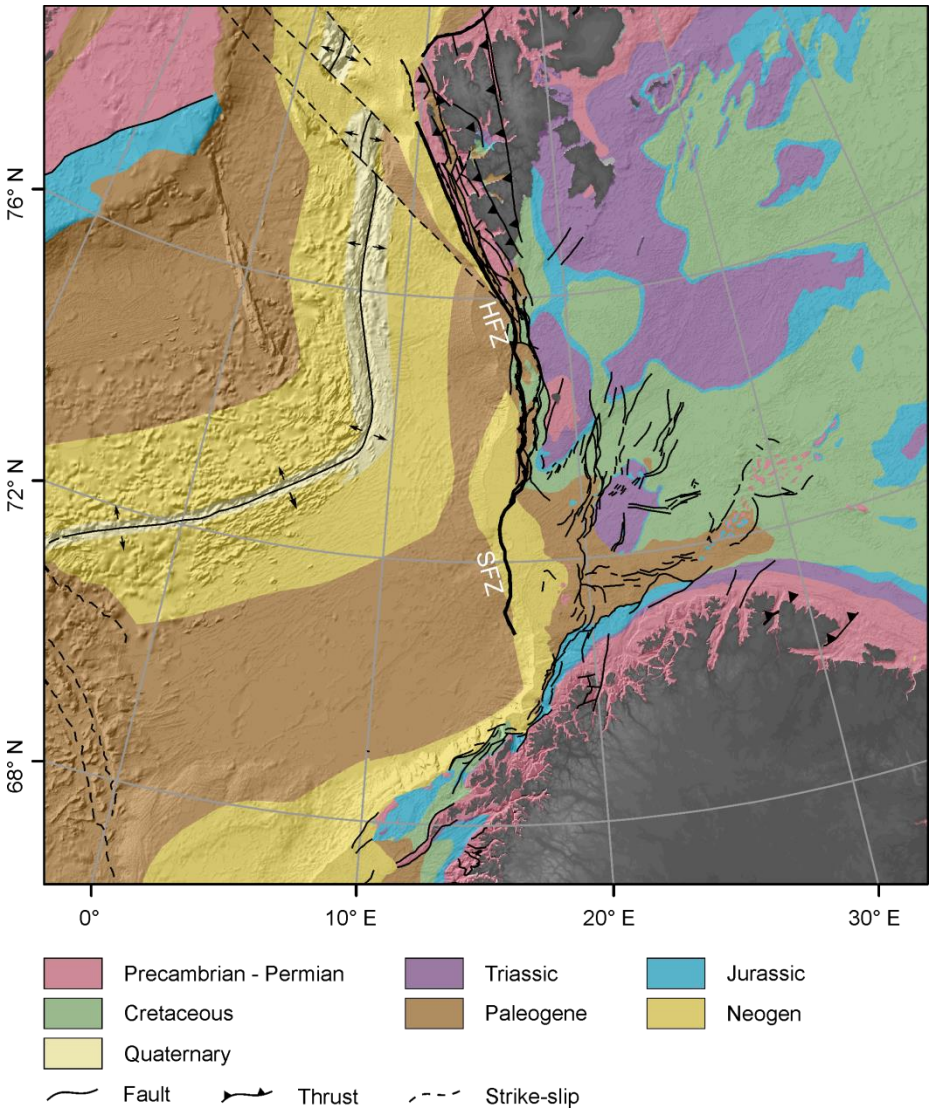

Fig. 2.1 Regional structural map showing the age of the basement rocks and major structures. HSF: Hornsund Fracture Zone; SFZ: Senja Fracture Zone. Modified from Behnia et al. (2013). The traces of the Hornsund and Senja Fracrure Zones are from Faleide et al. (2008).

Upper Paleozoic and Mezosoic rocks constitute the Svalbard Platform and the basin province between the Svalbard Platform and the Norwegian coast (Faleide et al., 1993). The post-rift sedimentary sequence of Paleogene to Late Pliocene

age is overlaid by a 3.5-4 km thick Plio-Quaternary glacial sequence deposited in three phases: (1) an initial growth phase between 3.6 and 2.4 Ma; (2) a transitional growth phase (~2.4-1.0 Ma) and (3) a large scale glacial intensification phase (1.0 Ma to present) (Knies et al., 2009).

Major tectonic structures in the western Barents Sea margin are parallel to the continental margin, starting in the northern-most part of the Svalbard archipelago, crossing the Spitsbergen Island, the Storfjorden trough, and Bjørnøya trough. The most important structure that crosses the Storfjorden trough is the Hornsund Fault Zone (HFZ), which together with other tectonic structures south of Spitsbergen, affects the continental crust and the Plio-Pleistocene sedimentary cover (Faleide et al., 2008, 1993). These structures were likely active during the loading and unloading by ice streams growth and retreat, and are still active nowadays (Pirli et al., 2013). In this area, the historical earthquake record of the last 55 years shows that earthquakes of $M_w \approx 4.7$ magnitude associated to the HFZ south of Storfjorden trough occurred (Fig. 2.2). According to this historical record, the recurrence of earthquake higher than $M_w \approx 4$ is around 10%. However, earthquakes with a magnitude higher than $M_w \approx 5.5$ are restricted to the mid-Atlantic ridge area.

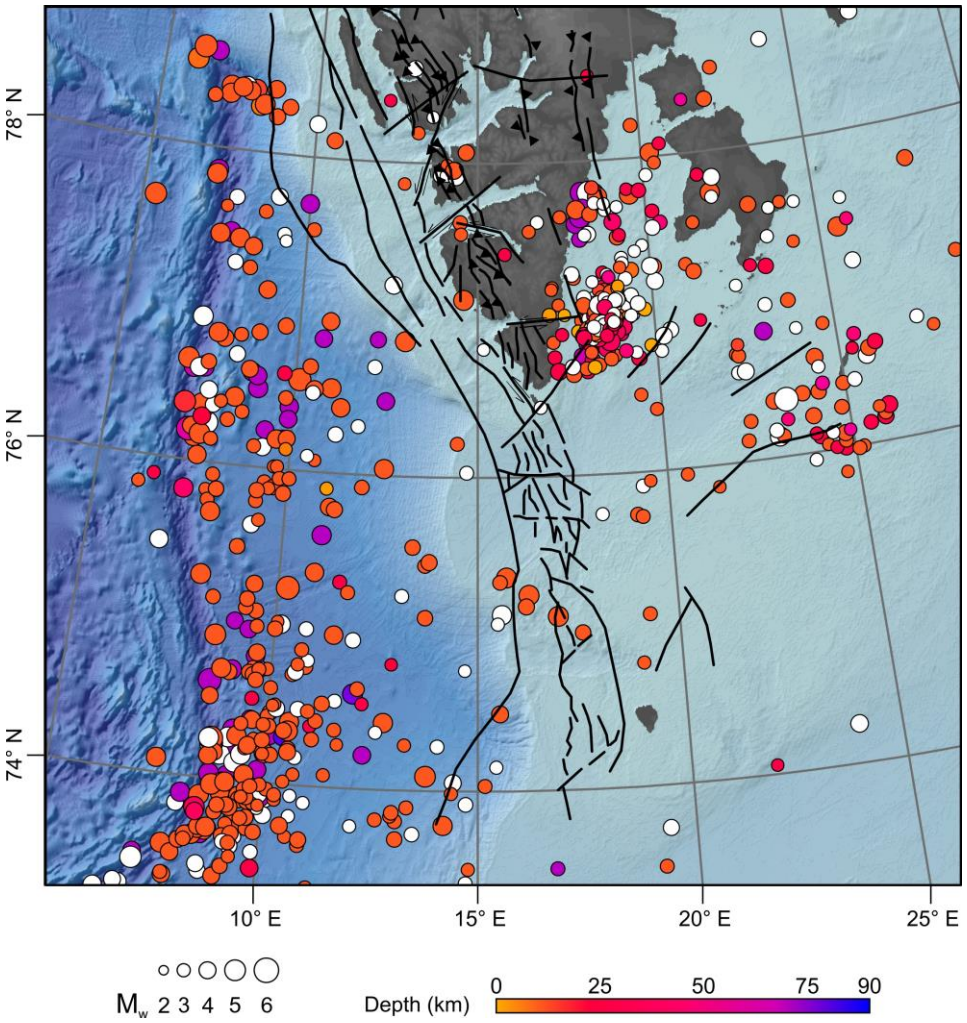

Fig. 2.2 Historical earthquake record from 1960 to 2015 (source IRIS catalogue). White dots depict no depth location. Faults extracted from Bergh and Grogan (2003).

2.2 Plio-Quaternary Western Barents Sea Evolution

The Barents Sea was occupied by a temperate ice sheet with channelized meltwater flow developed during the Late Pliocene to Early Pleistocene. The first evidence of ice streaming and associated channelized meltwater flow is during the Middle Pleistocene, while the onset of major glaciations and the

presence of large ice streams occurred in the middle and late Pleistocene (Laberg et al., 2010).

The oceanic basement is overlain by prominent Plio-Quaternary prograding wedges, which resulted from a significant increase in the sediment input from the margins of the Barents Sea since 2.7 Ma. Along the western Barents Sea three main sequences (GI–GIII) and eight regional seismic reflectors (R7-R1 and R4A have been identified (Faleide et al., 1996; Knies et al., 2009) (Fig. 2.3). R7 marks the onset of extensive glaciation 2.6-2.4 Ma ago, while R4A, dated at ~1.3 Ma, is associated to the full development of shelf glacial troughs and TMFs (Rebesco et al., 2014).

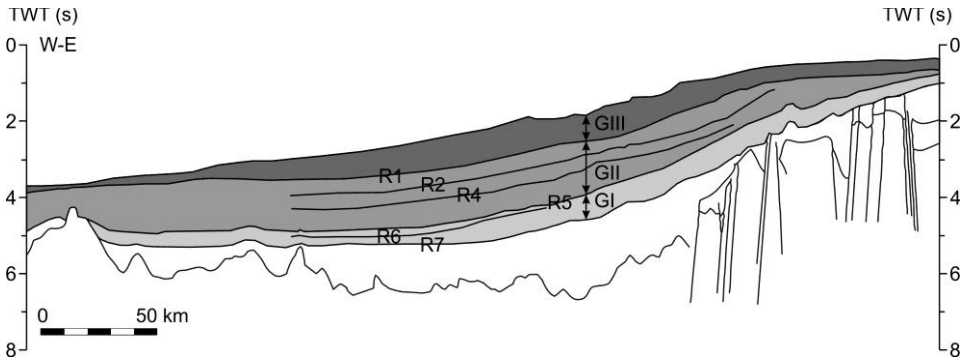

Fig. 2.3 Example of a seismic profile including regional seimic reflectors R7-R1 and the three main sequences GI-GIII (Modified from Dahlgren et al., 2005).

Reflectors R5 (1.0 Ma) (Svalbard) and R3 (0.78 Ma) (Storfjorden) mark the transition from net erosion to net accumulation in the outer shelf areas (Faleide et al., 1996; Hjelstuen et al., 1996; Solheim et al., 1996). During the Pleistocene, the development of Trough Mouth Fans, the onset of glacigenic sedimentation and major progradation are not synchronous in the Western Barents Sea

(Dahlgren et al., 2005). While R7 marks the onset of glacially-dominated deposition along the margin when glaciers reached the shelf break off Svalbard and the Storfjorden Trough, the expansion to the shelf break in the southwestern Barents Sea was delayed and occurred not earlier than R5 time (1.0 Ma). Between R7 to R5 time (2.7-2.0 Ma) a seaward migration of the shelf break of up to 150 km occurred in places (Dahlgren et al., 2005). Using numerical modeling techniques, Butt et al. (2002) inferred that the continental margin of the western Barents Sea had subaerial conditions in the earliest Late Pliocene. Although the onset of the main Northern Hemisphere Glaciations in the Barents/Svalbard margin is considered to have occurred at about 2.6-2.7 Ma (Butt et al., 2000; Knies et al., 2009), terrigenous sediments were initially of fluvial and glacio-fluvial source (Forsberg et al., 1999). From the Middle Pleistocene onwards, they were originated from subglacial sediment discharge from ice streams grounded at the shelf edge to form TMFs.

The shallower GIII sequence above R1 has been described as a succession of glacial/interglacial periods (Laberg and Vorren, 1996b) (Fig. 2.3). Based on paleomagnetic polarity of the upper GIII sequence Sættem et al. (1992) suggested an age <730 ka for reflector R1, while the same author using aminoacids analysis suggested a <440 ka age. Elverhøi et al. (1995) used the sedimentation rates in cores from the Isfjorden TMF to extrapolate an age of 200 ka for the "Upper Glacial Unit", whose base could match reflector R1. Faleide et al. (1996) and Hjelstuen et al. (1996) suggest an age of 440 ka while Butt et al.

(2000), Knies et al. (2009) and Rebesco et al. (2014) favor the younger 200 ka age.

2.3 Late Quaternary Evolution of the Storfjorden and Kveithola Trough Mouth Fans

During the Late Saalian and Weichselian the Barents and Kara Seas were affected by several glaciations (Mangerud et al., 1998). As a consequence of the higher preservation potential, mainly in the fan and inter-fan areas, of the Late Quaternary glacial deposits and their more easy access due to their shallower position, there is inevitably a better knowledge concerning glaciations during this time interval. Although there is a general agreement about the occurrence of four major glaciations during the last ~200 kyrs, the time and extension of ice in the Barents and Kara Seas is still under discussion (Lambeck et al., 2006; Spielhagen et al., 2004). Most of the studies regarding the time span of glacial and interglacial cycles from Late Saalian onwards are based on geological data from the Kara Sea and the Southern and Northern Barents Sea, as well as onshore data from Northern Russia, Scandinavia and Svalbard (Kleiber et al., 2000; Knies et al., 2001; Svendsen et al., 2004b; Vorren et al., 2011). Only a few works have used data from the Western Barents Sea continental margin (Rasmussen et al., 2007; Ślubowska-Woldengen et al., 2008).

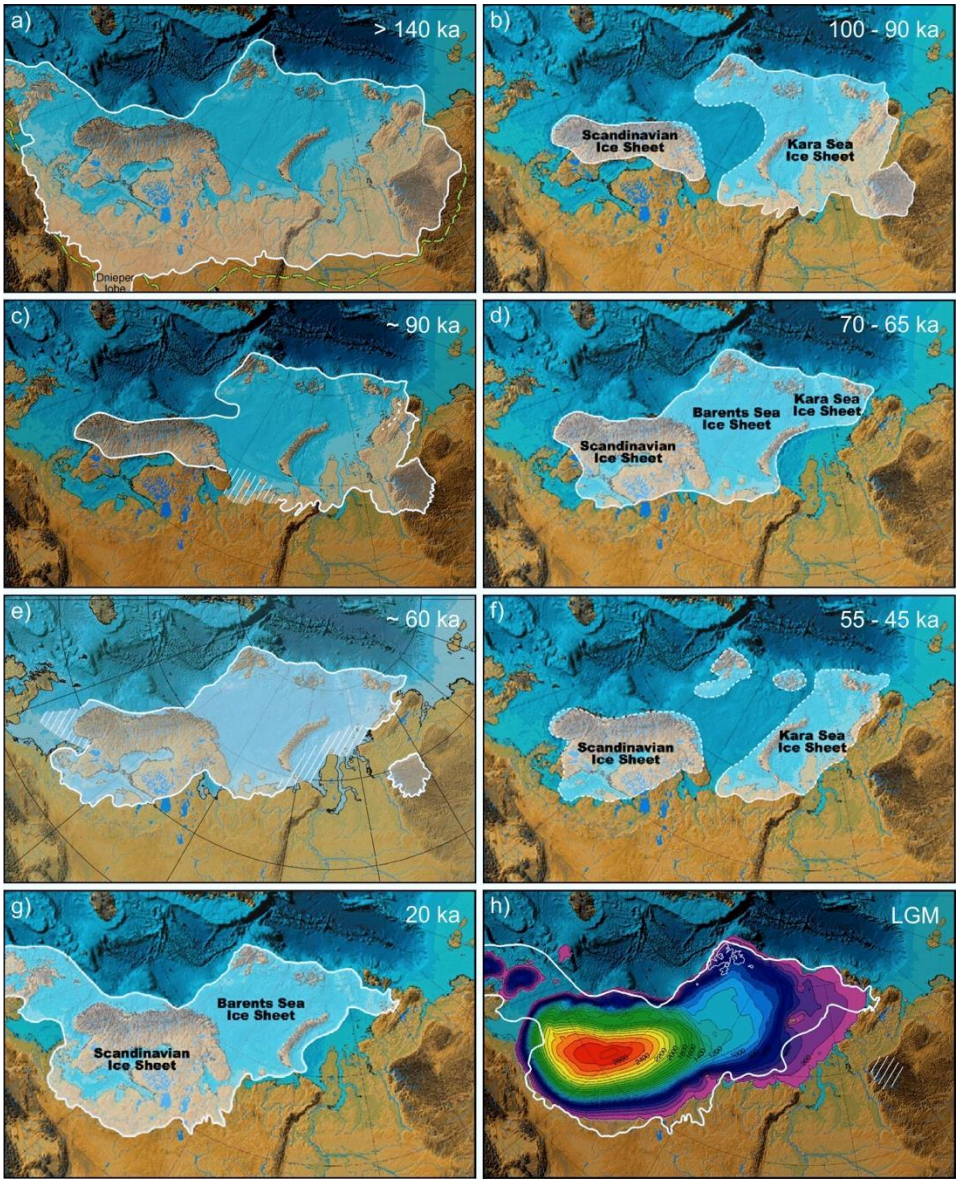

Fig. 2.4 Compilation of various reconstructions of the Eurasian Late Saalian to Weichselian ice sheet. Modified from Svendsen et al. (2004) (a, c, e, and h) and Vorren et al. (2011) (b, d, f, and g). h) shows the reconstructed LGM ice sheet limit (white line) from geological observations compared with a numerical model simulation (Siegert, 2004) of the maximum Eurasian ice sheets.

Ice advance in this area started at 180 ka and reached maximum expansion at 155 ka. Maximum expansion was followed by retreat and readvance during the

Saalian, which ended at 140-135 ka over Scandinavia (Lambeck et al., 2006; Spielhagen et al., 2004) (Fig. 2.4a). The Weichselian glaciation comprises three major ice sheet advances during stadials MIS 5b (90-80 ka), MIS 4 (60-50 ka) and the Last Glacial Maximum (LGM) (20-15 ka) (Svendsen et al., 2004a). In addition, Mangerud et al. (1998) suggested an even older glaciation around 100 ka (MIS 5d) (Fig. 2.5a). Summarizing the works from Mangerud et al. (1998), Spielhagen et al. (2004), Svendsen et al. (2004), and Vorren et al. (2011) the ice reached the shelf break around Storfjorden and Kveithola prior to 140 ka, ~90 ka, 70-60 ka, and during the LGM (Fig. 2.4g). Svendsen et al. (2004) perform a numerical model simulation of the Eurasian ice sheet thickness during the Last Glacial Maximum and previous glaciations. The maximum ice thickness is suggested to have reached around 2 km in Scandinavia while south of Svalbard was less than 300 m (Fig. 2.4h and Fig. 2.5c). Likewise, the ice thickness during the LGM was up to two times greater than in the previous Late Saalian and Early Weichselian glaciations. Studies by Hjelstuen et al. (1996) and Laberg and Vorren (1996b) in the Storfjorden and Bear Island TMFs suggest three periods in which the ice streams reached the shelf break: the Late Saalian (194-128 ka), Middle Weichselian (65-55 ka) and Late Weichselian (20-10 ka).

In the western Barents Sea, the shift from glacial to interglacial conditions and vice versa has also been influenced by interaction of ice sheets with the West Spitsbergen Current (WSC) and the East Spitsbergen Current (ESC) (Mangerud and Svendsen, 1992; Rasmussen et al., 2007; Siegert et al., 2001) (Fig. 2.6).

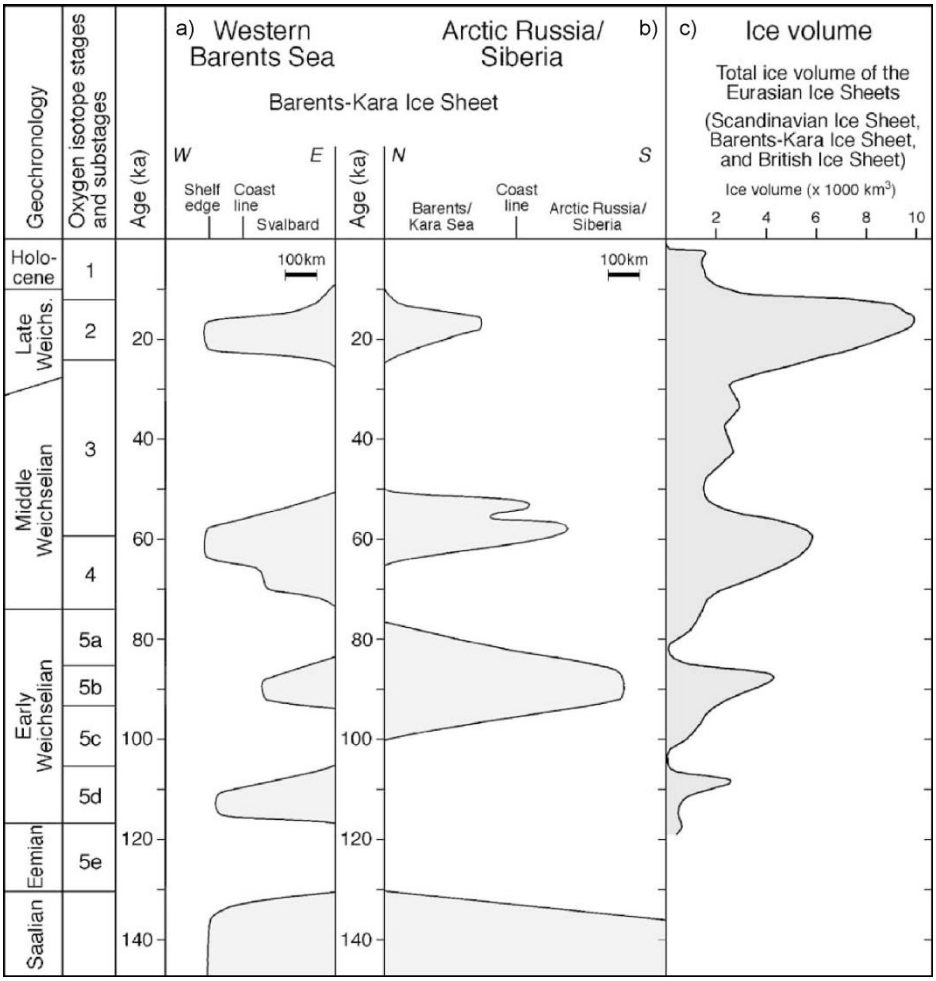

Fig. 2.5 Time-distance diagrams showing the growth and decay of the Eurasian ice sheets: (a) the Barents-Kara Ice Sheets on Svalbard in the western Barents Sea (Mangerud et al., 1998) and (b) the fluctuations of the Barents-Kara Ice Sheets in northern Russia/Siberia (Svendsen et al., 2004a). (c) Curve showing the modeled volumes of the Eurasian ice sheets (Siegert et al., 2001). Modified from Svendsen et al. (2004).

Elverhøi et al. (1998) suggest a relationship between the inflow of warm Norwegian-Atlantic Current (NAC) and increased seasonally open waters, providing moisture for ice-sheet growth on terrestrial areas. Furthermore, the

largest of these inflows of warm NAC waters ended in major glaciations (MIS, 6, MIS, 4 and MIS 2).

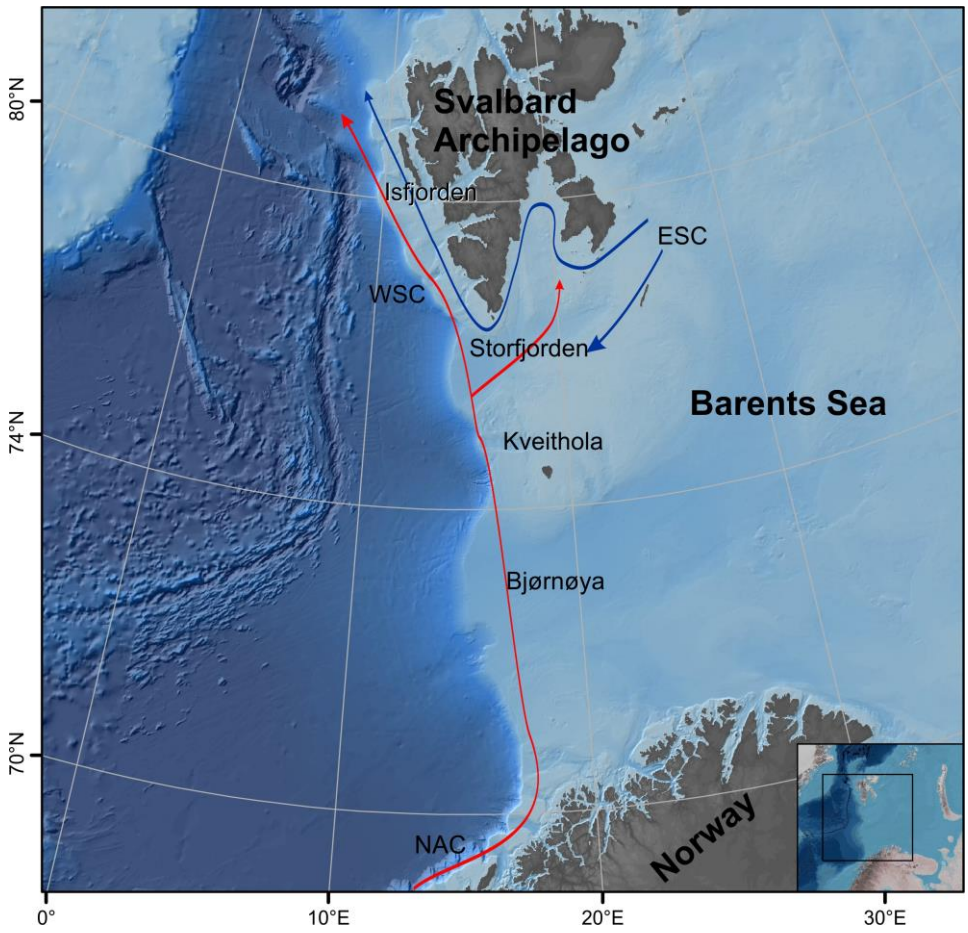

Fig. 2.6 Map of the western Barents Sea showing major surface currents. Red arrows depicts warm currents while blue arrows depict cold currents. NAC: Norwegian-Atlantic Current; WSC: West Spitsbergen Current; ESC: East Spitsbergen Current. Modified from Rasmussen and Thomsen (2015); Rasmussen et al. (2014).

Focusing in the Late Weichselian glaciation and subsequent deglaciation in the Storfjorden and Kveithola area, Hughes et al. (2016) modeled the ice sheet extent during the onset of the LGM, the glaciation and deglaciation (Fig. 2.7).

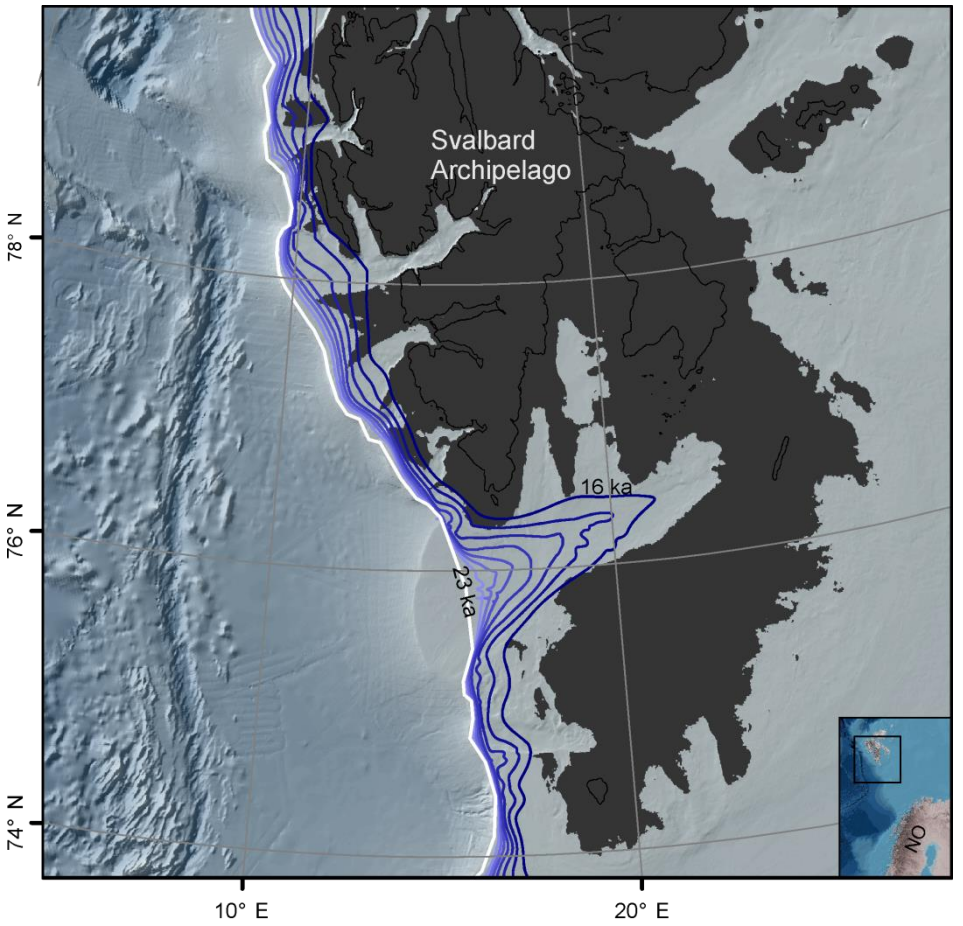

Fig. 2.7 Contours corresponding to the Last Glacial Maximum-deglacial ice extent over the Northwestern Barents Sea from 23 to 16 ka. Compilation from Hughes et al. (2016), Larsen et al. (2006) and Svendsen et al. (2004). Dark grey shows emerged land during the Last Glacial Maximum lowstand (-120 m isobath); black line depicts actual emerged land. NO: Norway.

During this time span, in the "most-credible" model, the ice front did not reach the Storfjorden shelf edge, while in Kveithola remained at the shelf edge until 20 ka. Conversely, the "maximum" modeled ice extent reached the Storfjorden shelf edge during the LGM and the retreat occurred around 19 ka. This last model is in agreement with the dates proposed by Jessen et al. (2010) and Rasmussen et al. (2007) of ~19.5 ka.

Regarding the sediment types, the Barents/Svalbard margin can be divided in three zones: a) the continental shelf mainly composed of basal deformation tills and grounding zone wedges; b) the self-edge and upper/middle slope made of till deltas that were brought to the grounding-line and interbedded with ice rafted detritus (IRD), debris flows, hemipelagic sediments and turbidites (mainly resulting from dense subglacial meltwater plumes); and c) the lower slope and abyssal plain made of distal turbidites, hemipelagic sediments, contourites and IRD (Dowdeswell et al., 1998; Ó Cofaigh et al., 2003; Rebesco et al., 2013; Stein, 2008).

Chapter 3
Methodology

Chapter 3. Methodology

The data used in this thesis were collected during three coordinated research cruises: *BIO Hespérides* cruise SVAIS (2007), R/V *OGS-Explora* cruise EGLACOM (2008), both organized within the International Polar Year (IPY) 2007-2008 Activity 367 (Neogene ice streams and sedimentary processes on high-latitude continental margins). The third cruise was the R/V Maria S. Merian cruise CORIBAR (MSM30 2013), resulting from a joint research program among the University of Bremen (Germany), the Institute of Marine Science (CSIC) of Barcelona (Spain), OGS (Italy), GEUS (Denmark), and the University of Tromsø (Norway). Data includes multibeam bathymetry, shallow sub-bottom profiles, single-channel seismic (SCS) and multi-channel seismic (MCS) reflection data, gravity cores, and piston cores (Fig. 3.6).

3.1 Geophysical data

3.1.1 Swath bathymetry data

A "swath-sounding" sonar system is one that is used to measure the depth in a line extending outwards from the sonar transducer. Systems acquire data in a swath at right angles to the direction of motion of the transducer head (Fig. 3.1). As the head moves forward, these profiles sweep out a ribbon-shaped surface of depth measurement, known as a swath. Multibeam echo sounders (MBES)

collect bathymetric soundings in a swath perpendicular to the ship track by electronically forming a series of transmit and receive beams in the transducer hardware which measure the depth to the sea floor in discrete angular increments or sectors across the swath (Hughes Clarke et al., 1996). Various transmit frequencies are utilized by different MBES systems depending on the sea floor depth. For example, low frequency (12 kHz) systems can collect swath soundings at full ocean depths, many up to 10,000 meters. In contrast, high frequency MBES systems (300+ kHz) are utilized for collecting swath bathymetry in depths of 20 meters or less.

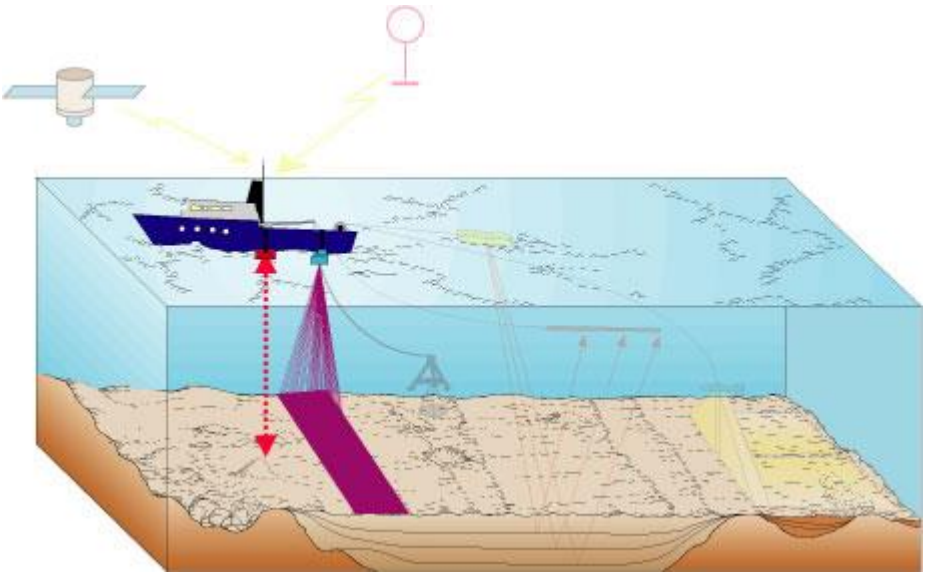

Fig. 3.1 Schematic showing the transducer as an aqua box on the sidemount. The acoustic energy pathway is shown by the fan-shaped set of purple rays fan out with increasing distance from the transducer (ship). The area of the sea floor that is ensonified is depicted by the solid-purple swath (courtesy of USGS).

Swath bathymetry acquired during the SVAIS cruise was collected using two hull mounted multibeam echo sounders: a 12 kHz Simrad EM-120 in deep waters and a 95 kHz Simrad EM-1002S in shallow waters. During the EGLACOM cruise the hull mounted 12 kHz Reson MB8150 and 100 kHz MB8111 multi-beam echo-sounders were used for deep and shallow waters respectively. The total coverage of the multibeam surveys in both cruises is around 15,340 km^2.

Table 3.1 Geophysical adquisition parameters for Multi Beam Echo Sounders used in SVAIS and EGLACOM cruises.

- Multi Beam Echo Sounders (MBES)

Deep Waters	SVAIS Cruise	EGLACOM Cruise
Model	Kongsberg Simrad EM120	Reson SeaBat8150
Installation	Hull mounted	Hull mounted
Number of beams	191	234
Beam width	1 x 2°	2 X 2°
Total beam angle	150°	-
Max swath coverage	Up to 5.5 x water depth	5 x water depth
Operating frequency	12 kHz	12kHz
Pulse length	2, 5, 15 ms	0.5-20.4 ms
Resolution in depth	10- 40 cm	0.5-20.4 ms
Depth range	20 - 11000 m	12000
Ping rate	Max. 5 Hz	15 Hz
Sea floor detection	Amp. detection & phase change	-
Sound probe	XBT	Reson SVP 25

Shallow waters		
Model	Simrad EM1002 S	Reson SeaBat8111
Installation	Hull mounted	Hull mounted
Number of beams	111	101
Beam width	2 x 2°	1.5 x 1.5º
Total beam angle	150°	150º
Max swath coverage	Up to 7.5 x water depth	Up to 7.4 x water depth
Operating frequency	95 kHz	100 kHz
Pulse length	0.2, 0.7, 2 ms	Variable
Resolution in depth	2 - 8 cm	Up to 3.7 cm
Depth range	3 - 600 m	Up to 1400 m
Ping rate	Max. 10 Hz	35 swaths per second
Sea floor detection	Amp. detection & phase change	-
Sound probe	XBT	Reson SVP 25

3.1.2 Shallow subbottom profiles

Sub-bottom profiling systems are employed to identify and characterize layers of sediment or rock under the seafloor. In sub-bottom profiling, a sound source directs a pulse toward the seafloor. Parts of this sound pulse reflect off of the seafloor, while other parts penetrate the seafloor (Fig. 3.2). The portions of the sound pulse that penetrate the seafloor are both reflected and refracted as they pass into different layers of sediment. Chirp systems sweep frequency intervals typically in the range 2-20 kHz. Since relatively low frequency/long wavelength signals have better penetration but lower resolution than relatively high frequency/short wavelength signals this allows for an optimal extraction of information from the bottom sediment.

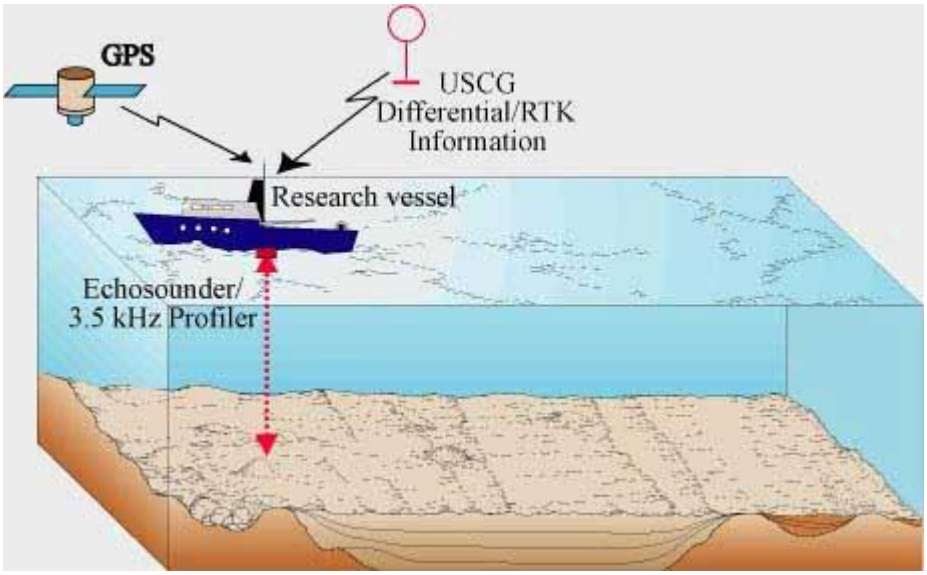

Fig. 3.2 Schematic showing the transducer as a red box, either hull-mounted or sidemounted to the ship. The acoustic energy pathway is shown by the dotted red line, with a two-way arrow, representing the direct path taken by the outgoing and returning energy (courtessy of USGS).

Table 3.2 Geophysical adquisition parameters for sub-bottom profilers used in SVAIS and EGLACOM cruises.

- Sub-bottom profilers (SBP)

	SVAIS Cruise	EGLACOM Cruise
Model	TOPAS PS 18	Benthos CAP-6600
Installation	Hull mounted	Hull mounded
Primary frequency	16 - 22 kHz	-
Secondary frequency	0.5 - 6.0 kHz	-
Depth range	30 - 10,000 m	-
Sampling frequency	16 kHz	-
Sweep range	-	2-7 kHz

Nearly 9,500 km of sub-bottom profiles were acquired using the hull mounted parametric TOPAS PS 18 (SVAIS cruise) and a BENTHOS CAP-6600 CHIRP

profiler (EGLACOM cruise) with a sweep range of 0.5-6.0 kHz and 2-7 kHz respectively.

3.1.3 Single-channel seismic (SCS) and multi-channel seismic (MSC) reflection data

The single and multi-channel seismic reflection methods are the most advanced technologies used in offshore and onshore geophysical exploration. It uses the principles of seismology to estimate the properties of the Earth's subsurface. The resulting high resolution image allows characterizing subsurface structures in a variety of scales. Although the single and multi-channel seismic reflection differs in some specific aspects of the acquisition and processing, the basic concepts are valid for both methods. Acquisition of marine single/multi-channel seismic reflection data consists of a sound source towed behind the vessel at a known depth that produces sound pulses at a controlled frequency range and at regular time intervals (Fig. 3.3).

When the elastic waves encounter a boundary between two materials with different acoustic impedances, some of the energy in the wave will be reflected at the boundary, while some of the energy will be transmitted through the boundary (Sengbush, 1983).

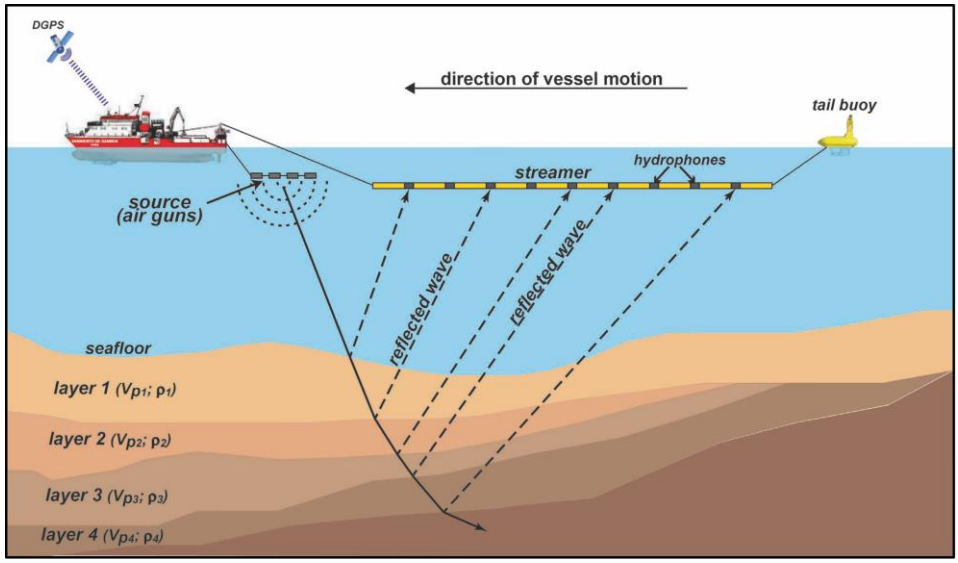

Fig. 3.3 Diagram of a standard offshore multi-channel seismic experiment. The towed seismic source (air guns) generates an acoustic pulse that is transmitted downward to the subsurface and reflected at the different interfaces (changes of acoustic impedance). The reflected waves travel upward and are recorded by hydrophones located along the streamer towed some distance away from the source to try to minimize the noise associated with the ship and the sound sources. The ray paths resulting from a single shot are displayed (courtesy of A. Lago).

The part of the reflected energy travels upward to the surface and is recorded by the hydrophones arranged in a streamer towed from the vessel (Fig. 3.3).

The SVAIS SCS data (Fig. 3.6) were collected using a 210 cubic inches GI gun and a 10 m mini-streamer towed 100 m behind the ship and recorded at a sampling rate of 0.5 ms. Data processing was limited to predictive Wiener deconvolution, bandpass filter (45-550 Hz) and AGC. The EGLACOM MCS data were acquired using a 160 cubic inches array of 4 sleeve air guns and a 1200 m digital streamer with 96 channels spaced 12.5 m, while recording was performed at a sampling rate of 1 ms. Processing at OGS using the FOCUS software from Paradigm Geophysical included a t-squared scaling for spherical

divergence correction, Multi-Channel Shot spiking deconvolution, bandpass filtering following the water bottom, and trace equalization (Rebesco et al., 2011).

Table 3.3 Geophysical adquisition parameters for single channel seismics used in SVAIS and EGLACOM cruises.

- Single channel Seismic (SSC) SVAIS Cruise

SOURCE		STREAMER	
Type	Gi-gun	Active length	10 m
Array volume	210 cu inch	Hydrophone number	10
Source depth	4.8 m	Near offset	100 m
SP interval	15.5 m (at 6kt)	Towing depth	surface

RECORDER	
Type	Delph-2 acquisition board
Sampling rate	0.5 ms
Recording length	5 s

- Multichannel Seismic (MSC) EGLACOM Cruise

SOURCE		STREAMER	
Type	Sleeve Airguns	Type	Sercel Seal
Array volume	160 cu inch	Active length	1200 m
Source depth	2.5 m ± 0.5 m	Groups No.	96
SP interval	12.5 m /25 m	Group Interval	12.5 m
SYSTEM TIMING		Towing depth	3.0 m ± 0.75 m
Controller	RTS Hot Shot	Near offset	45 m
Delay Rec-TB	100 ms	Fold coverage	48/24

RECORDER	
Type	Sercel Seal 2000
Sampling rate	1.0 ms
Recording length	5 s / 10 s
Filters	3 Hz (Low cut) and 400 Hz (High cut)
Auxiliary channels	Channel 1 near-field phone
No. Of channels	96
Coverage	48/24 fold

3.2 Core data

The core data set includes four cores from SVAIS cruise (SV-02, SV-03, SV-04 and SV-05), one core from the CORIBAR cruise (GeoB-17610-2) and physical data from ODP site 986 (Fig. 3.6).

3.2.1 Core acquisition

Gravity and piston corers are generally used in areas with soft sediment. They mainly consist in heavy tube plunged into the seafloor to extract samples of mud sediment. Inside this tube (or barrel) a plastic liner is set to accommodate the sample, also a core catcher is set at the bottom to prevent sample loss. Gravity core is equipped with a heavy weight on top and uses the pull of gravity to penetrate into the seabed.

Contrary, piston core has a piston mechanism that is triggered when the corer hits the bottom (Fig. 3.4). The piston helps to avoid disturbing the sediment. SVAIS and EGLACOM cores have been acquired by using between 3.5 to 10 m length barrels. A total of 10 core samples have been obtained.

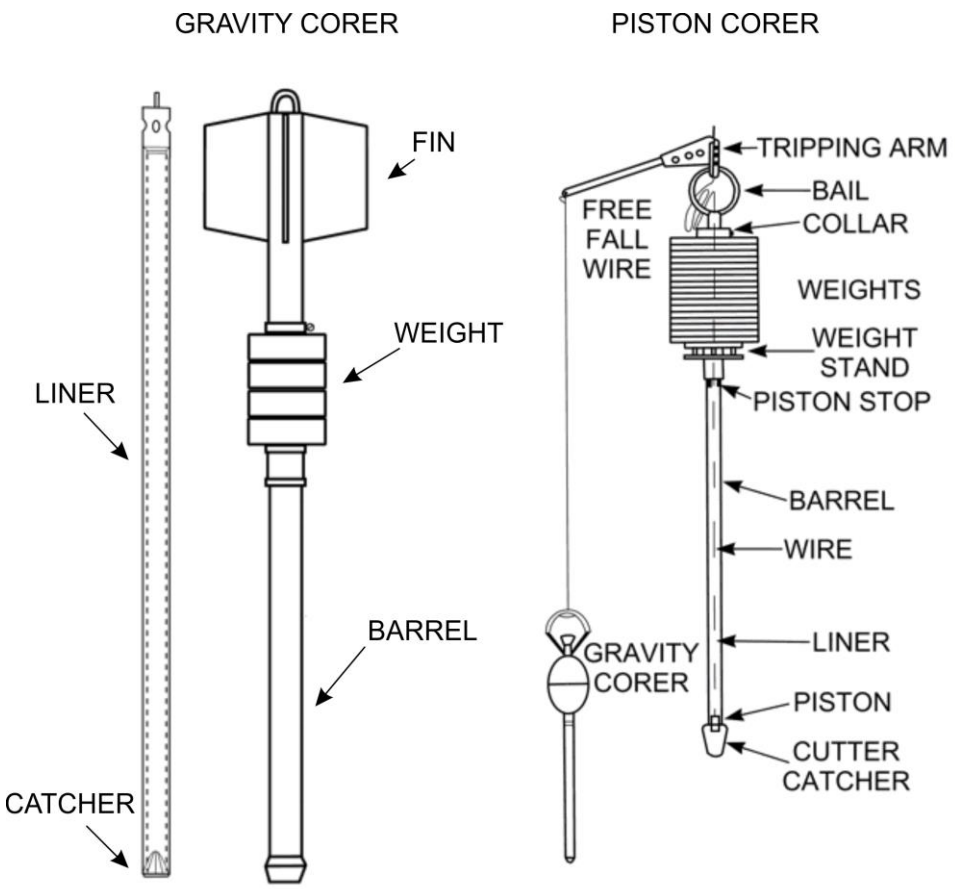

Fig. 3.4 Gravity and piston corer devices main parts.

3.2.2 Sediment properties

Core-scanning included (CAT-scan) radiographs performed prior to core opening; high-resolution digital photos, color scan and chemical composition of the sediments by means of an Avaatech Superslit X-ray fluorescence core-scan (XRF-core scan) using 10 and 50 kV instrumental settings; sediments physical properties using a multi-sensor core logger for wet bulk density and magnetic susceptibility; and paleomagnetic/rock magnetic parameters performed on u-

channels collected along the central part of the split sections. Discrete sediment samples were collected at 10–5 cm resolution and analyzed for sediment physical properties and composition. Sediment water content was determined by oven-drying the sediments at 105 °C for 24 h. Grain size analyses were performed with a coulter- counter laser Beckman LS-230 to measure the 0.04–2000 μm fraction at 0.004 μm resolution. The samples were initially treated with diluted peroxide and the disaggregated sediments were re-suspended into a 0.1% sodium-hexametaphosphate solution and left for 3 min in ultra- sonic bath prior to measurement. The results were classified according to Friedman and Sanders (1978) grain-size scale and were analyzed with the cluster statistical method. The sand fraction mineralogy was determined through optical microscope and Scanning Electron Microscope (SEM) coupled with Energy Dispersive Spectroscopy (EDAX), while the mud fraction was investigated through smear-slides (after Rothwell (1989)). For further information see Lucchi et al. (2013).

ODP site 986 is located north of the study area reaching ~964 mbsf (Raymo and Blum, 1996). Data available from this site have been used to correlate regional reflectors to the study area (Fig. 3.5). Also, sonic velocity data from ODP Site 986D have been used for the time to depth conversion of the identified units in seismic profiles.

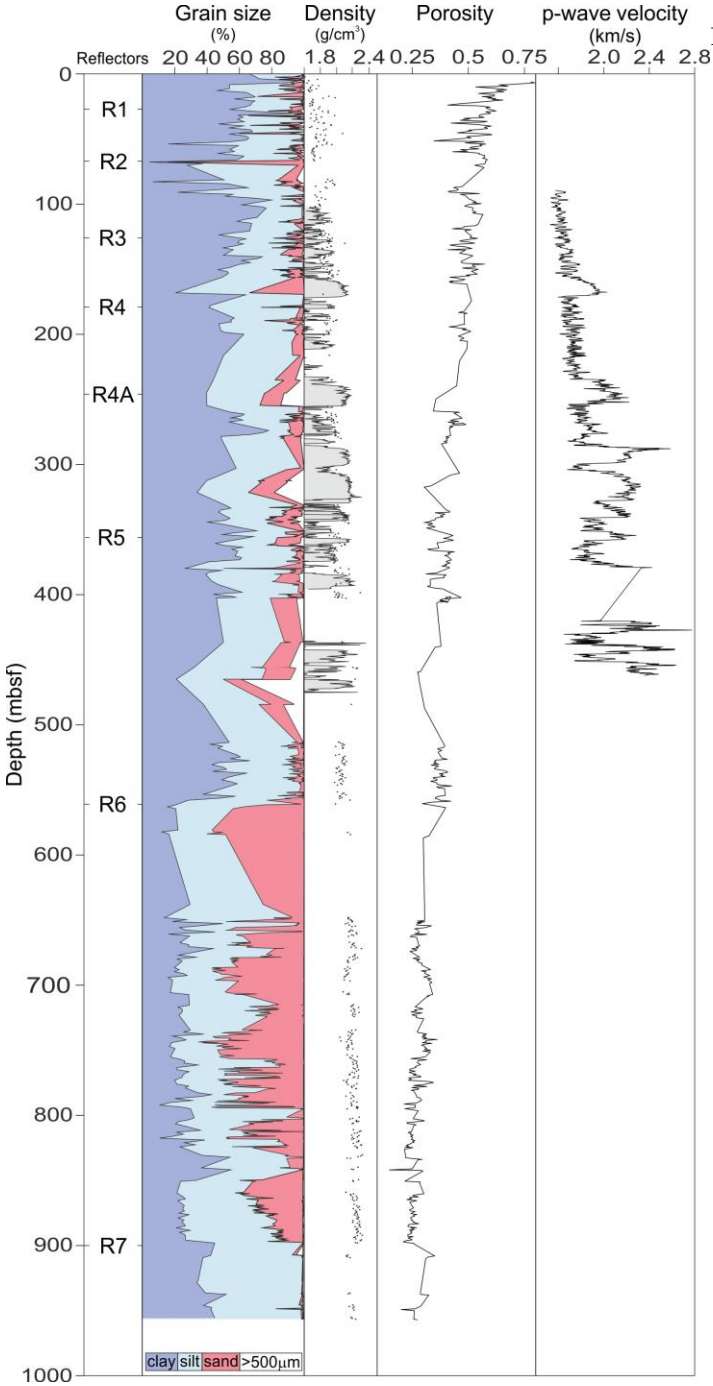

Fig. 3.5 Grain size, density, porosity and p-wave velocity from ODP site 986. Regional reflectors are also depicted. Data compilation from (Forsberg et al. (1999) and IODP data cataloge. See Fig. 3.6 for core location.

3.2.3 Age dating

Cores SV-02, SV-04 and SV-05 from the SVAIS cruise (Fig. 3.6) have been used to correlate acoustic facies with sedimentary units. AMS ^{14}C dating analyses were performed at selected stratigraphic intervals (Lucchi et al., 2012). Age calibrations were performed with the Calib 6.0 calibration software program (Stuiver and Reimer, 1993), using the marine09 calibration curve (Reimer et al., 2009), and applying an average marine regional reservoir effect $\Delta R=84\pm23$ obtained from the Marine Reservoir Correction Database in Calib 6.0 for the northwestern Barents Sea area (south of Svalbard). The mean values from the calibrated age range of $\pm1\sigma$ were then normalized to calendar years (conventionally 1950 AD) and are in the following indicated as cal. ka BP.

3.3 Integration of the geophysical and core samples dataset

Integrated data interpretation of ~9500 km of sub-bottom profiler lines, 1071 km of MCS and 518 km of SCS lines was performed using the Kingdom Suite software provided by IHS. Sub-bottom profiler data have been used to identify the shallow subsurface structure for the first 120 ms twtt penetration. The SCS and MCS were used to identify deeper sedimentary units. With the aid of swath bathymetric and seismic data, surface and shallow sub-surface features that have a sea floor expression were mapped using GIS tools.

Deeper structures were mapped using both Kingdom Suite and GIS tools. Picked reflectors were gridded using Kingdom Suite's flex algorithm with a grid spacing of 80 m. Volume and thickness calculations from the seismic data have been made using a linear p-wave seismic velocity gradient of 1.48 +1.5z km/s, where z is depth in the sedimentary section in seconds.

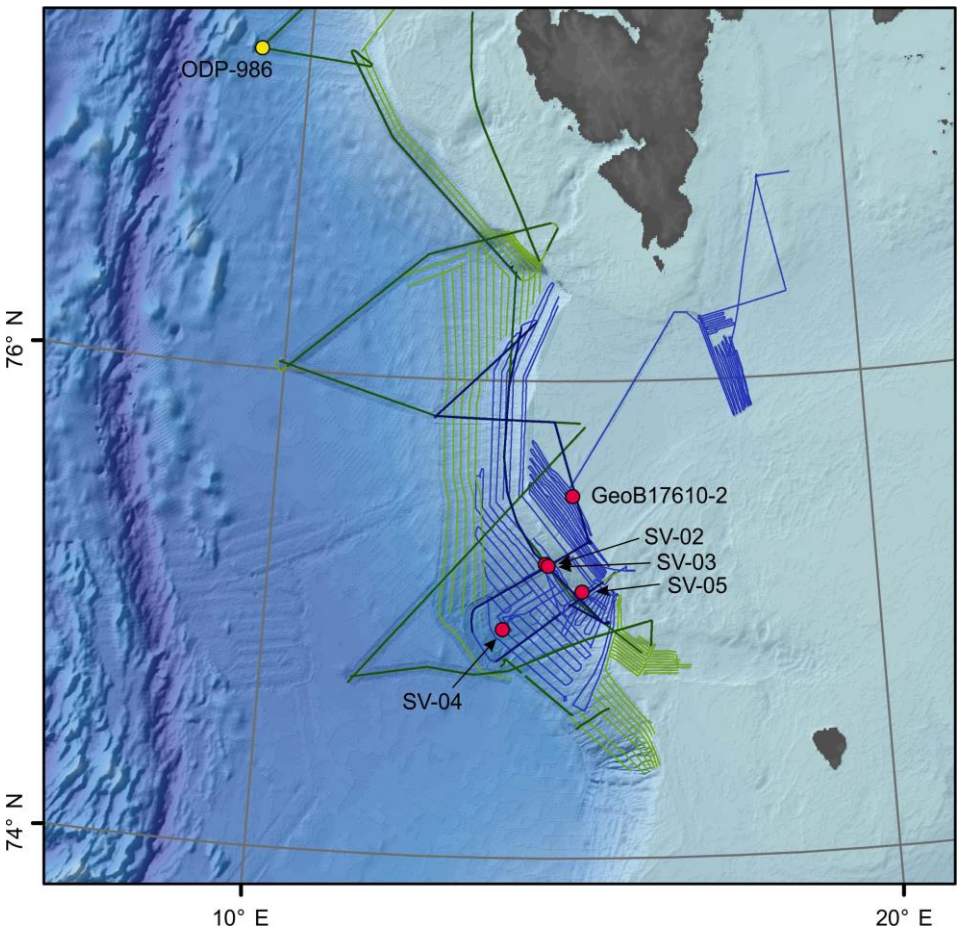

Fig. 3.6 Data set used in this Thesis. Blue lines depict SVAIS data, while green lines depict EGLACOM data. Red dots correspond to gravity cores; yellow dot corresponds to ODP Site 986. SV: SVAIS cruise, GeoB176: CORIBAR cruise.

This gradient is consistent with sonic velocity data from ODP Site 986D (Laberg et al., 1996) (Fig. 3.6) and implies that the highest velocities at the base of the studied section are ~3 km/s. Taking a constant value of 1.5 km/s and a gradient of 1.5+2.13z km/s (the velocity gradient observed in shallow sediment cores) as lower and upper values for the velocity gradient, induces an error in the calculated mean thicknesses (see below) of the deeper units of ±11%.

3.4 Geotechnical data

Five gravity cores from SVAIS and CORIBAR cruises have been used in this Thesis (Table 3.4). Consolidation and permeability tests were performed on samples from cores SV-02, SV-03 (SVAIS cruise) and GeoB17610-2 (CORIBAR cruise) (Fig. 3.6). These tests have been carried out in the Geotechnical Laboratoty of the Institut de Ciències del Mar in Barcelona (ICM) (Fig. 3.7). The consolidation tests were carried out as a stepped loading test using a GDS Rowe & Barden-type Consolidation cell equipped with three 2 MPa advanced pressure/volume controllers (Fig. 3.8).

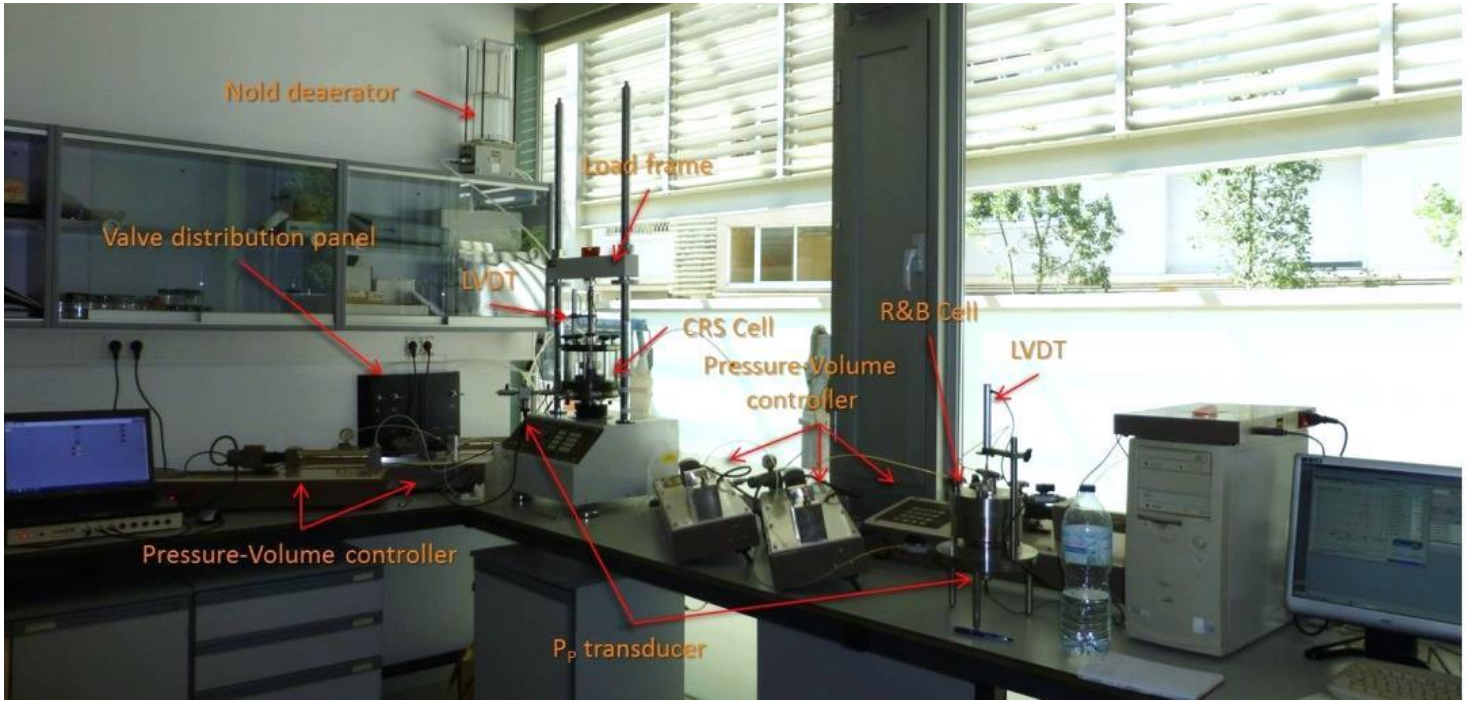

Fig. 3.7 Geotechnical Laboratory in the Institut de Ciències del Mar in Barcelona. The apparatus used to carry the geotechnical test are depicted.

Table 3.4 Core location, water depth and recovery used in this thesis.

Core	Lat N	Lon E	Water depth (m)	Recovery (cm)
SV-02	75º13.70'	14º35.96'	743	641
SV-03	75º13.35'	14º37.24'	761	642
SV-04	74º57.42'	13º53.97'	1839	303
SV-05	75º06.70'	15º13.30'	713	632
GeoB17610-2	75°30.99'	15°0.53'	387	349

This test have been performed according to the British Standard Methods for soil testing (British Standards Institution, 1990)

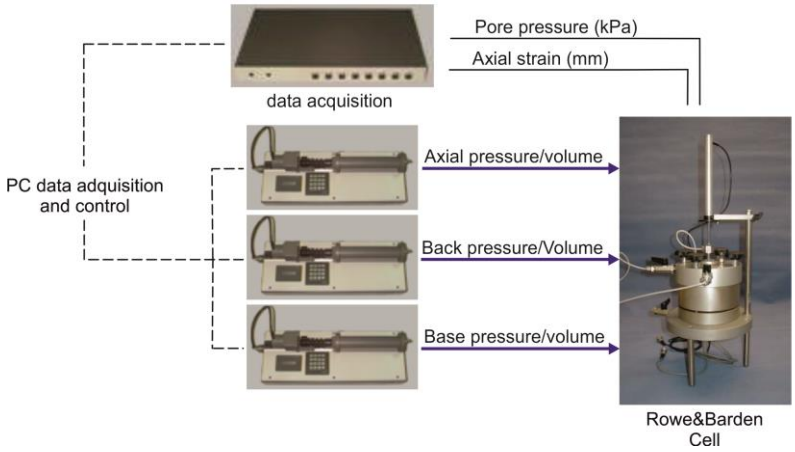

Fig. 3.8 Set-up used for consolidation and permeability test with the Rowe&Barden cell.

After each consolidation step, a permeability measurement was carried out creating a pressure gradient between both sides of the specimen and measuring the water volume that circulated through it in a given time interval. Darcy's law was then used to determine the sample permeability. A total of 11 samples were tested (Fig. 3.9).

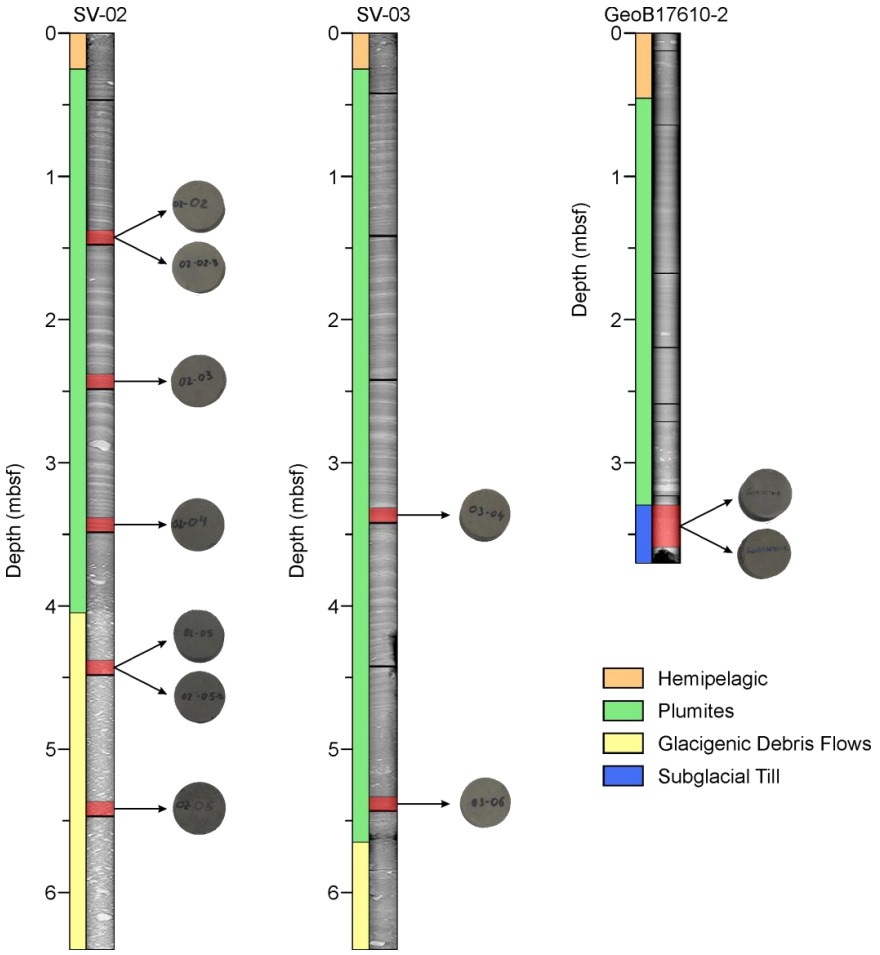

Fig. 3.9. Sediments type and x-rays of cores used in this Thesis. Whole round samples used for geotechnical testing are highlighted in red.

Due to technical issues mainly related to anomalous isolation of the sample from the upper chamber, only 8 test results have been used in this work. Each test took around one month to be completed. Consolidation data measured in plumite and GDF shallow sequences has been used to determine the compression index (C_c) and initial void ratio (e_0) from the virgin consolidation line.

3.5 Sediment self-weight decompaction

Self-weight consolidation is a fundamental post-depositional process by which pore fluid is expelled from accumulating sediment under an increasing thickness of overlying sediment (Tovey and Paul, 2001). The relationship of void ratio (porosity) to depth is highly non-linear near the seabed surface. This has major implications for determining sedimentation rates between dated levels within an already compacted sequence. Sediment layers may double their thickness when fully decompacted. In this Thesis I adopt the iterative forward modeling approach of Tovey and Paul (Tovey and Paul, 2001) to objectively compare sedimentation rates between shallow and deeper sedimentary sequences.

Using the approach of Tovey and Paul (2001) the effective stress and void ratio can be determined along each layer. A logarithmic function of the type:

$$e = e_0 + C_c \, ln \, z \qquad \text{eq. 1}$$

where e_0 and C_c are the depth (z)-related initial void ratio and compression index respectively, provides a good fit to the depth-void ratio data. The fit allows determining the mean void ratio of the layer by integrating the void ratio over the depth range of the layer at a particular point and dividing by the layer thickness at this point (eq. 2).

$$\bar{e} = \frac{\int_{z_1}^{z_2} e(z)\, dz}{z_2 - z_1} \qquad \text{eq. 2}$$

From eq. 2 it is possible to derive the reduced thickness (apparent thickness of the solid material) and the mass of solid material in each layer. In my approach, I also account for the fact that TMFs present layers of different compression characteristics (plumites and GDFs). Because of the alternating nature of these two sediment types, the depth over which the void ratio is integrated for glacial sediments (GDFs) needs to be recalculated using a second iterative process for the thickness of solids above that layer using the compressibility characteristics of glacial sediments. When it is the case, for deglacial sediments (plumites) the same process needs to be carried out using the compressibility characteristics of deglacial sediments

3.6 Finite Element Modeling (FEM)

Numerical models have been used to simulate the sedimentary evolution and pore pressure development to understand the processes that led to the Present day state of the margin (i.e. the North Sea Fan (Kvalstad et al., 2005) and the Gulf of Mexico (Stigall and Dugan, 2010; Urgeles et al., 2010)). A limited range of commercial software and research codes using different modeling techniques (i.e. Finite Element Mesh, Finite Difference Method) exist. In this Thesis four simulation software packages have been used (commercial and non-commercial) in order to validate the results obtained (BASIN, Plaxis, Basin2, and NGI-Basin). However, due to their 2D environment and versatility, the continental

margin hydrogeological model has been carried out with BASIN and Plaxis. Further details are explained in Chapter 5.8.4.

3.6.1 BASIN

Using the Finite Element Software "BASIN" (Bitzer, 1999, 1996) a continental margin hydrogeological model has been developed to simulate fluid migration and pore pressure development through the evolution of a glacially- influenced continental margin.

BASIN is based on a forward modeling approach. For a given set of initial and boundary geological conditions the sedimentary basin evolution is computed. Compaction and fluid flow are coupled through the consolidation equation and the nonlinear form of the equation of state for porosity, allowing non-equilibrium compaction and overpressure to be calculated (Bitzer, 1999). Instead of empirical porosity-effective stress equations, a physically consistent consolidation model is applied which incorporates a porosity-dependent sediment compressibility. The consolidation equation incorporating such porosity-dependent sediment compressibility and hydraulic conductivity is solved using equation (eq. 3):

$$(\partial/\partial x)\left(k_{x(\emptyset)}\partial p/\partial x\right) + (\partial/\partial x)\left(k_{z(\emptyset)}\partial p/\partial z\right) = (1-\emptyset)\rho g\alpha_{(\emptyset)}\,\partial p/\partial t \quad \text{eq. 3}$$

where $k_{x(\phi)}$ is the porosity dependent hydraulic conductivity in the x-direction, $\alpha_{(\phi)}$ is the porosity dependent sediment compressibility, p the fluid pressure and ϕ the porosity.

Sediment compressibility in BASIN is calculated from the specific storage (S_s) using eq. 4:

$$S_s = \rho_s g \alpha \qquad \text{eq. 4}$$

ρ_s: sediment density; g: gravity; α: sediment compressibility.

In BASIN (Bitzer et al., 1996, 1999) sedimentary facies are represented by a mixture of sediment types, whose composition varies according to the relative abundance of each sediment type for a given area and stratigraphic unit. Physical properties are also averaged according to the sediment mixture.

In this study pore pressure is described in terms of overpressure (λ), defined as (Flemings et al., 2008):

$$\lambda = (\mu - P_h)/(\sigma_v - P_h) \qquad \text{eq. 5}$$

μ: pore pressure; P_h:hydrostatic pressure and σ_v: lithostatic or total stress.

3.6.1.1 Model set up in BASIN

The total length of the modeled transect is around 156 km and matches with profile ITEG08-09 (Fig. 3.10 and Fig. 3.11) from which stratigraphic information is extracted. The regional reflectors R6 to R1, described in Faleide et al. (1996), were identified in the seismic reflection profiles based on ODP Site 986 data (Forsberg et al., 1999) and correlated along the entire MCS and SCS surveys based on the interpretation of Rebesco et al. (2014).

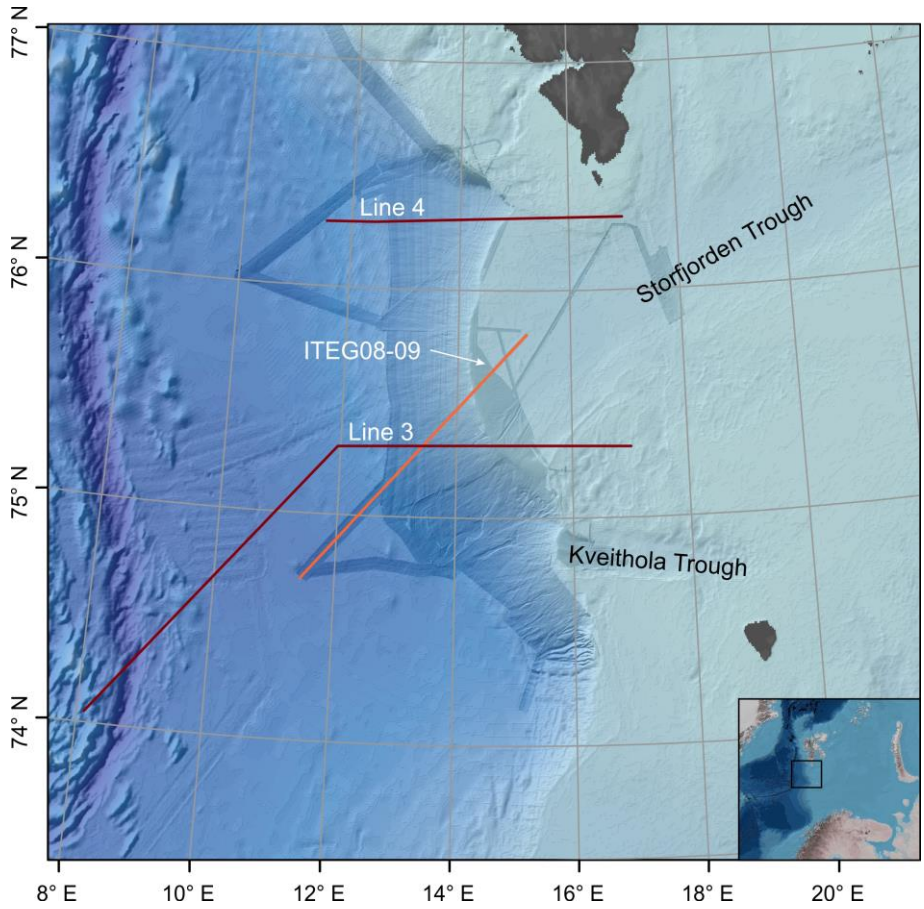

Fig. 3.10 Location of profile ITEG08-09 (orange) from EGLACOM cruise, and lines 3 and 4 from Faleide et al. (1996) (deep-red) used in the BASIN and Plaxis models.

The R7 and the OB (top of Oceanic Basement) reflectors were constrained with information from two seismic lines north (4) and south (3) of Storfjorden from Faleide et al. (1996) as the data set did not have enough penetration to image these reflectors along ITEG08-09 (Fig. 3.10, Fig. 3.11b and c).

In the model computed with BASIN, the mesh nodes are equally spaced every ~ 4 km in the x-direction and between 15-150 m in the y-direction depending on the layer thickness. Ice-induced stresses or erosion by ice have not been

considered. Time intervals between reflectors R7 and R1 were selected according to Knies et al., (2009) (Table 3.5), and above R1 a chronological framework was established in this study (see Chapter 5.3).

Table 3.5 Age of major reflectors in the western Barents Sea and base of units above reflector R1 used as input for the hydrological models.

Unit	Age (ka)
A_1	13*
A_2	19.5*
B	22.5*
C	60*
D	64*
E	135*
F	167*
G	220*
R2	500#
R3	780#
R4	990#
R4A	1200#
R5	1500#
R6	1650#
R7	2700#

*: this work, #: (Knies et al., 2009).

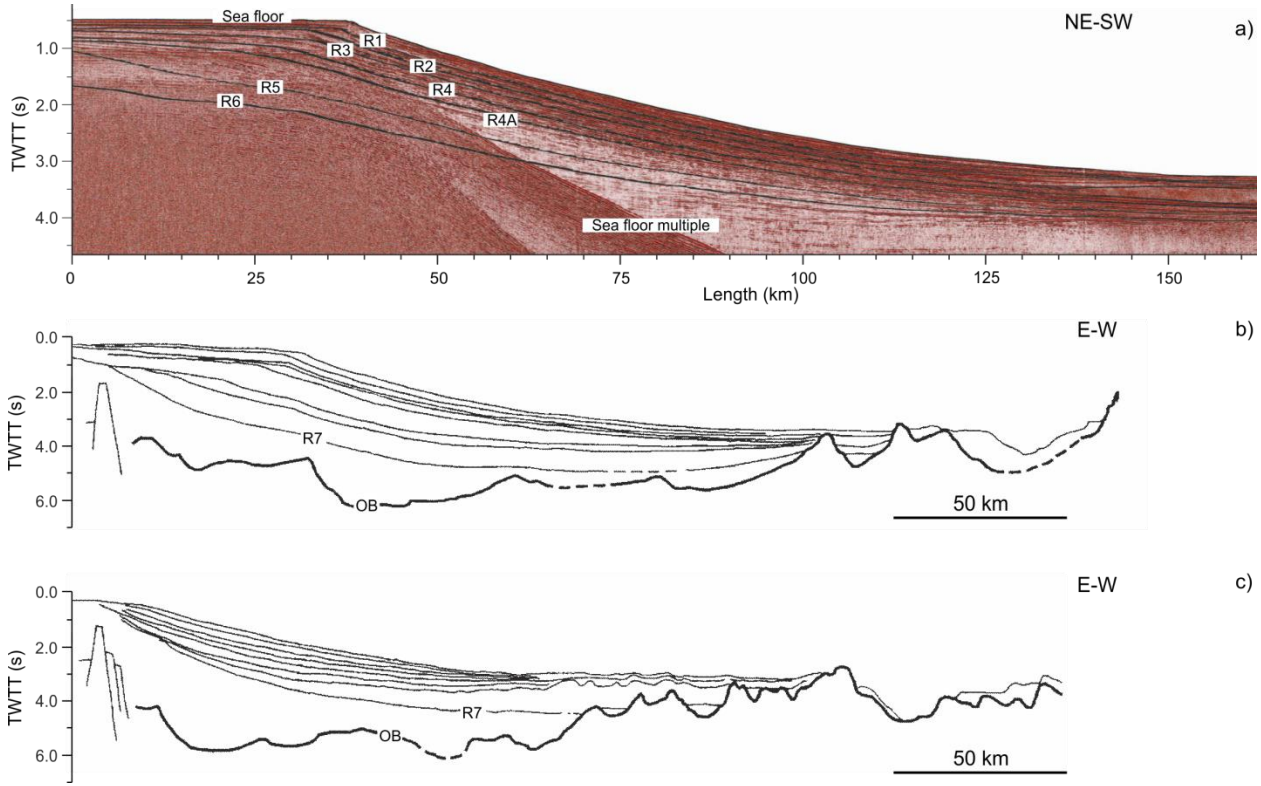

Fig. 3.11 a) Profile ITEG08-09 used for BASIN and Plaxis models. Regional reflectors R6 to R1 are highlighted. b) and c) correspond to profiles 3 and 4 from Faleide et al. (1996) used for constraining the position of R7 and the oceanic basement OB over profile ITEG08-09.

The rate of overpressure generation thus depends on sedimentation rate, sediment compressibility, and permeability. The initial thickness (H_i) of different strata used as input for the model was calculated using van Hinte's decompaction equation (Van Hinte, 1978):

$$H_i=H_f[(1-\phi_f)/(1-\phi_0)] \quad \text{eq. 6}$$

ϕ_0: initial porosity; ϕ_f:present-day porosity and H_f: present sediment thickness.

3.6.2 Plaxis

With the aim of investigating the ice loading/unloading effect over the shelf and upper slope in higher detail, the finite element software Plaxis 2015 has been used with the Soft Soil model. The Soft Soil model is a Cam-clay model especially meant for primary compression of near normally-consolidated clay-type soils. Some features of the soft-soil model are: stress dependent stiffness (eq. 7), memory for pre-consolidation stress and distinction between primary loading and unloading-reloading (Plaxis bv, 2015). In order to analyze the simultaneous development of pore pressures and deformations during sediment deposition (eq. 7 and eq. 8), a fully coupled flow-deformation analysis calculation has been performed. This computation accounts for the coupled behavior represented by both the equilibrium (eq. 7) and the continuity (eq. 8) equations of the water-soil mixture:

$$d\bar{\sigma}' = M\, d\bar{\varepsilon} \quad \text{eq. 7}$$

$$\begin{bmatrix} K & Q \\ 0 & -H \end{bmatrix}\begin{bmatrix} \bar{v} \\ \bar{p}_w \end{bmatrix} + \begin{bmatrix} 0 & 0 \\ C & -S \end{bmatrix}\begin{bmatrix} \frac{d\bar{v}}{dt} \\ \frac{d\bar{p}_w}{dt} \end{bmatrix} = \begin{bmatrix} \bar{f}_u \\ G + \bar{q}_p \end{bmatrix} \quad \text{eq. 8}$$

$\bar{\sigma}'$: effective stress vector; M: material stress-strain matrix; $\bar{\varepsilon}$: strain vector; K: stiffness matrix; Q and C: coupling matrices; H: permeability matrix; $\bar{v}$: displacement vector; $\bar{p}_w$: pore pressure vector; S: compressibility matrix; $\bar{f}_u$: load vector in an element; G: flow gravity vector in y-direction; $\bar{q}_p$: flux on the element boundaries.

The main input parameters for the Soft Soil model are: the modified compression index (λ*), modified swelling index (κ*), effective cohesion (c'), friction angle (φ) and void ratio (e). Modified indexes are related to the one-dimensional compression C_c and swelling C_s indexes from the oedometer test and void ratio following eq. 9 and eq. 10. Groundwater is computed using the Van Genuchen's (eq. 11) model with a silty-clay type sediment (g_a=0.5, g_n=1.09 and g_c=1) according to the United States Department of Agriculture (USDA) soil classification. The input parameters are the vertical and horizontal hydraulic conductivities (k), as well as the permeability change (c_k) with void ratio variation due to consolidation (eq. 12).

$$\lambda^* = \frac{C_C}{2.3(1+e)} \quad \text{eq. 9}$$

$$\kappa^* = \frac{C_s}{2.3(1+e)} \quad \text{eq. 10}$$

$$K_{rel}(S) = max\left[(S_e)^{g_a}\left(1 - \left[1 - S_e^{\left(\frac{g_n}{g_n-1}\right)}\right]^{\left(\frac{g_n-1}{g_n}\right)}\right)^2 . 10^{-4}\right] \quad \text{eq. 11}$$

$$log\left(\frac{K}{K_0}\right) = \frac{\Delta e}{c_k} \quad \text{eq. 12}$$

K_{rel}; relative permeability to the saturation; S_e: effective saturation; γ_w: unit weight of pore fluid; K: permeability; K_0: initial permeability; Δe: void ratio variation; g_a, and g_n and fitting parameters depending on USDA soil type.

3.6.2.1 Model set up in Plaxis

The length and height of the modeled transect in Plaxis are 60 km and 2.2 km, respectively. The model is ~43500 15-node elements with widths between 150 m in the deeper layers and 5 m in the shallower ones. The model is shorter than BASIN model and limited to the outermost shelf and upper slope in order to minimize calculation errors and attain convergence stability. Geologic time intervals are the same as in the BASIN model. The left and right model boundaries are constraint so that only vertical displacements are allowed (neither horizontal nor fluid flow). The bottom boundary of the model is vertically and horizontally fixed and corresponds to reflector R4A.

In order to compare the Plaxis results with those of BASIN, a basal flow has been imposed at the bottom boundary of the sedimentary succession, the reflector R4A. Such a flow accounts for the fact that the BASIN simulation spans 1.7 Myrs longer than the Plaxis model. Thus this flow boundary corresponds to the compaction-driven fluid flow contribution from the sediments below the R4A surface from 1.2 Ma to Present.

Ice loading in the shelf area has been applied as an incremental vertical load during the onset of glaciation and has been set constant during glacial maximum conditions. The ice load corresponds to the ice (h_i) thickness above sea level minus the emerged ice thickness necessary to counter the buoyancy effect.

$$h_i = \frac{\rho_w \cdot h_w}{\rho_i} + z \qquad \text{eq. 13}$$

where h_i and h_w: ice thickness and water depth; ρ_w and ρ_i: sea water and ice densities; z: height above the counter buoyancy thickness.

The ice thickness above sea level corresponds to the ice thickness necessary to counter ice buoyancy plus 120 additional meters in the inner part and 100 m in the outer shelf. The total ice thickness above sea level is around 170 m and 150 m in the inner and outer shelf respectively, which is in agreement with models by Svendsen et al. (2004) and Dowdeswell and Siegert (1999) that show ice elevation above sea level in the range of 100-200 m in the western part of the Storfjorden trough. Due to thinning of the ice sheet towards the ice edge (shelf edge during glacial maximum) the applied ice load is higher in the inner shelf than in the outer shelf. Further, during ice retreat the applied ice load has been set as decreasing trough time. Water depths are extracted from the bathymetric data and account for a ~105 m sea level lowstand during Glacial Maxima (Rohling et al., 2014). At the shelf edge, the maximum water depth is estimated to be 290 m during glacial maxima (Fig. 3.12).

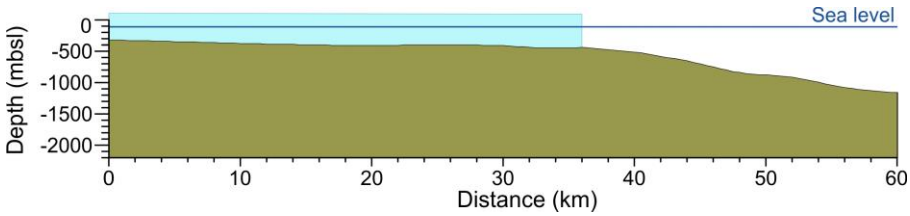

Fig. 3.12 Ice conFiguration during the Last Glacial Maximum simulation. Sea level corresponds to sea level lowstand (Rohling et al., 2014).

3.7 Model cross-validation

In order to cross-validate the results obtained with BASIN and Plaxis, a model was set up and evaluated using two additional well-established software packages: BASIN2 developed by the University of Illinois (Bethke et al., 2007) and NGI-Basin developed by Norwegian Geotechnical Institute (NGI, 2000). Because the NGI-Basin is a 1D simulation software, the problem benchmark model was designed as three horizontal layers with length to depth ratio of 100 to warrant: a) 1D compaction, b) vertical flow and c) no influence of the boundaries. The layering in the model corresponds to a glacigenic sediment layer sandwiched in between plumites (Fig. 3.13). A synthetic observation well has been located in the center of the model (Fig. 3.13). The sediment properties of plumites and glacigenic sediments were taken from the geotechnical tests performed in this study.

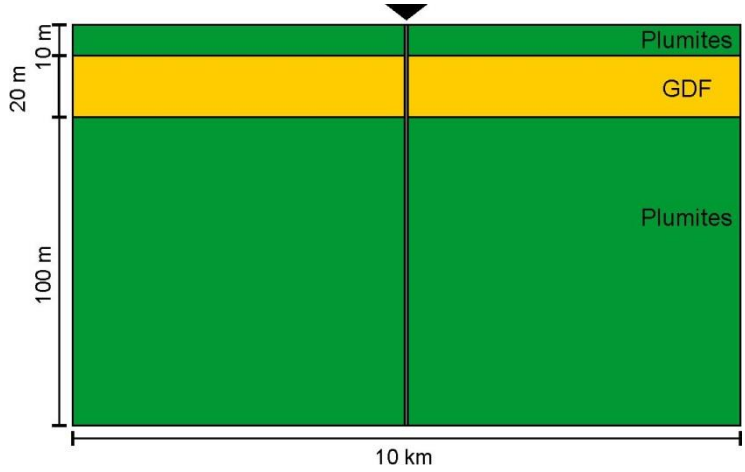

Fig. 3.13 Model conFiguration used as benchmark for cross-validation. Black arrow depicts the synthetic observation well.

3.7.1 NGI-Basin

NGI-Basin is coded in Fortran 77/90 and extends Gibson's solution to non-homogeneous sedimentation in a multi-layered soil system (NGI, 2000). This is achieved by a numerical solution of the consolidation equation using finite-element approximation in the spatial domain, and finite-difference approximation in the time domain. Other features of the model are: a) implementation of a large-strain solution algorithm using updated geometry conFiguration; and b) incorporation of user defined porosity and permeability equations.

It is assumed that the profile may already contain a layer that had consolidated under its own weight before deposition of new layers begins. Sedimentation of each layer is defined by a straight line, which defines the rate of material

deposition (e.g. kg/m^2/yr). One may also specify "quiet periods" during which no sedimentation occurs. The partial differential equation of consolidation in NGI-Basin is expressed as:

$$\frac{K}{\gamma_w}\frac{\partial^2 u}{\partial z^2} = m_v\left(\frac{\partial u}{\partial t} - \frac{\partial}{\partial t}\Delta q\right) \qquad \text{eq. 14}$$

u: excess pore-water pressure; $\Delta q = \Delta\sigma$: total stress increment (σ refers always to vertical stress); K: permeability; γ_w: unit weight of water; $m_v = a_v/(1+e)$: coefficient of volume change; $a_v = -\Delta\varepsilon/\Delta\sigma'$: coefficient of compressibility; e: void ratio.

Other related parameters are the porosity $\phi = e/(1+e)$, the coefficient of consolidation $c_v = K/(\gamma_w \cdot m_v)$, and the constrained modulus $D = 1/m_v = \Delta\sigma'/\Delta\varepsilon$, where $\varepsilon = \Delta e/(1+e_0)$ denotes the vertical strain and e_0 is the initial void ratio. Void ratio, e, is a function of effective stress (eq. 15), and permeability is a function of porosity (ϕ) (eq. 16):

$$e = e_1 - \frac{1+e_1}{(1-r)m}\left[\left(\frac{\sigma\prime}{\sigma_{ref}}\right)^{1-r} - 1\right] \qquad \text{eq. 15}$$

$$K = K_0 \cdot 10^{\frac{\emptyset - \emptyset_0}{A}} \qquad \text{eq. 16}$$

where σ_{ref} = 1 kPa reference stress; m: "module number" and r: "power order" coefficients; e_1: value of e at $\sigma' = \sigma_{ref}$; and A: coefficient depending on the material ϕ_0 and K_0 consistent pair of porosity-permeability data at deposition (σ_{ref}). Parameters m, r and A have been defined by the best fit of eq. 15 with the consolidation and permeability test results. For further details, refer to Appendix B.

3.7.2 Basin2

Basin2 is a numerical model designed in the framework of the Hydrology Program of the University of Illinois (Bethke et al., 2007) with the aim to understand the evolution of groundwater flow within sedimentary basins. Basin2 calculates groundwater flow in two dimensions. The equation of porosity evolution implemented in the model is:

$$\phi = \phi_{ir} exp(-\beta\sigma') + \phi_1 \qquad \text{eq. 17}$$

where ϕ_0: porosity at deposition; ϕ_{ir}: irreductible porosity; σ': effective stress; and β: beta porosity parameter obtained from the σ'-ϕ curve.

Also, the permeability evolution is based on the computed value of porosity according to the correlation (eq. 18), while Darcy's law gives the groundwater flows through a subsurface (eq. 19):

$$logk_i = A\phi + B \qquad \text{eq. 18}$$

$$q_i = -\frac{K_i}{\mu}\left(\frac{\partial P}{\partial x} - \rho g \frac{\partial z}{\partial x}\right) \qquad \text{eq. 19}$$

where K_i is the permeability (in the x or z direction for Darcy flow); A and B are parameters of the fitting curve in the K-ϕ graph; $q_{x,z}$: specific discharge in x or z direction; μ: fluid viscosity; P: pressure; ρ: fluid density; g:gravity.

Note that A is unitless and B is expressed in *logK*. For further information refer to Bethke et al. (2007).

3.8 Slope stability

In order to determine slope stability and the influence of fluid flow patterns on it throughout the evolution of the Storfjorden Trough Mouth Fan, safety calculations have been carried out using the *phi/c* reduction method implemented in Plaxis. This finite elements method have been selected rather than standard limit-equilibrium methods (e.g. simplified Bishop, simplified Janbu) because no assumption needs to be made in advance compared to the standard limit-equilibrium methods (e.g. shape or location of the failure surface, slice side forces and their directions) (Rabie, 2014). In addition, the results obtained by Rabie (2014) comparing finite elements method (phi/c reduction) and limit-equilibrium methods show that the last are highly conservative (the obtained SFs are the half of the finite elements method results).

In the *phi/c* reduction method, the shear strength parameters $tan\varphi$ and c (friction angle and cohesion) (Table 3.6) and the tensile strength are successively reduced until failure occurs (Plaxis bv, 2015).

Table 3.6 Values used in the safety calculation for the three sediment types used.

	Effective Cohesion (c')[(1)]	Friction angle (ϕ^o)[(2)]
Plumites	10	20
GDFs	25	29
Tills	30	29

(1): data derived from undrained shear strength mesurements on splited cores. (2) data extracted from (Kvalstad et al., 2005b).

Although the margin evolution has been modeled by using the Soft soil material type model, the phi/c reduction method is based on the Mohr-Coulomb failure criterion (eq. 20), the model behave according to Mohr-Coulomb soil type model.

$$\tau = \sigma_n tan\varphi + c \qquad \text{eq. 20}$$

where τ: shear strength of the soil material on a certain failure plane; σ_n: normal stress on failure plane; φ: internal friction angle of the soil material; and *c*: cohesion intercept of the soil material.

The SF is here calculated by means of the total multiplier *ΣMsf*. This multiplier is used to define the soil strength parameters, in a given stage, in the analysis as:

$$\Sigma Msf = \frac{tan\,\varphi_{input}}{tan\,\varphi_{reduced}} = \frac{c_{input}}{c_{reduced}} = \frac{Tensile\ strength_{input}}{Tensile\ strength_{reduced}} \qquad \text{eq. 21}$$

Where the strength parameters with the subscript '*input*' refer to input material properties and the subscript '*reduced*' refer to the reduced values used in the analysis. The incremental multiplier *Msf* is used to specify the increment of the strength reduction of the first calculation. This increment is by default set to 0.1. The strength parameters (ϕ and *c*) are successively reduced automatically until all the predefined steps have been performed (set to 100 to ensure the complete failure development). The safety factor (eq. 22) is reached when failure has completely developed and the total multiplier *ΣMsf* is constant.

$$SF = \frac{available\ strength}{strength\ at\ failure} = value\ of\ the\ \Sigma Msf\ at\ failure \qquad \text{eq. 22}$$

The safety factor has been calculated at selected time periods in the Storfjorden Trough Mouth Fan evolution. These periods correspond to the end of the glacial and interglacial periods described in 0 from 220 ka to 22.5 ka, and a detailed evolution of SF during the LGM, deglaciation and Holocene from 22.5 ka to Present. In order to understand the ice loading influence on the SF during glacial maxima, SF has been calculated in both of the models with and without ice, and the results have been compared.

Chapter 4
Results

Chapter 4. Results

4.1 Late Quaternary Development of Storfjorden and Kveithola TMFs

During the Late Saalian and Weichselian glaciations a marine ice sheet developed in the western Barents Sea (Lambeck et al., 2006; Spielhagen et al., 2004). The continental slope has been selected to study evolution of the TMF because of better imaging possibilities and higher preservation potential of the Late Quaternary glacial and interglacial deposits, which are less likely to be modified/eroded by subsequent processes (erosion by ice sheets dynamics) there. The study of the sedimentary processes that shaped the morphology of these TMFs provides a better understanding of the processes related t geohazards and of submarine landslides occurrence in high-latitude continental margins in particular. The development of the Storfjorden and Kveithola TMFs throughout the last 220 kyrs, are investigated by means of integrated data interpretation of the SVAIS and EGLACOM geophysical dataset (Fig. 4.1).

4.1.1 The sedimentary record

4.1.1.1 Seismic stratigraphy

The high-resolution seismic stratigraphy of the Storfjorden and Kveithola TMFs is dominated by a sharp alternation of acoustically "laminated" and "transparent" units, although some reflections might be present within the "transparent" units. The laminated units have relatively continuous high amplitude reflectors draping pre-existing topography, while the transparent units have a hummocky internal reflector conFiguration, a basal erosive surface and an irregular upper boundary (see also Lucchi et al., 2012). A similar set of acoustic facies has also been found in other TMFs (Laberg and Vorren, 1995; Ó Cofaigh et al., 2003). Eight seismo-stratigraphic units have been identified above reflector R1. From top to bottom, we have respectively named the stratified units A, C, E and G, while the four transparent units are α, B, D and F (Fig. 4.2 and Fig. 4.3).

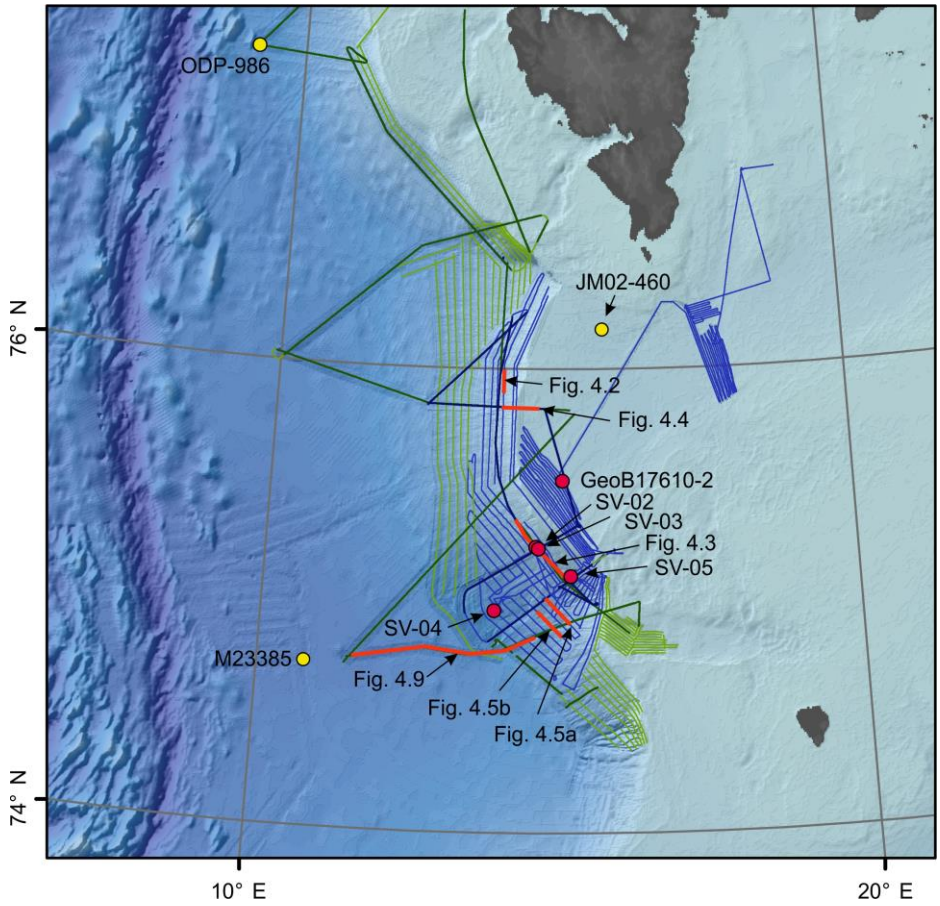

Fig. 4.1 Detailed swath bathymetry shaded relief of the study area merged with Jakobsson et al. (2012) bathymetric data showing cores from the SVAIS and CORIBAR cruises (red dots), sub-bottom profiler data from the SVAIS (blue lines) and EGLACOM (green lines) cruises, and seismic reflection profile (dark green) acquired during both the EGLACOM and SVAIS cruises. The lines highligthed in red correspond to profile sections shown in this chapter. Yellow dots correspond to ODP site 986 (Butt et al., 2000), core JM02-460 (Rasmussen et al., 2007) and core M23385 (Dokken and Hald, 1996).

On the shelf, the Storfjorden trough displays a series of stacked transparent units that are more tabular than the transparent units on the TMF. A maximum of three transparent units have been identified on the shelf (T_B, T_D, T_F).

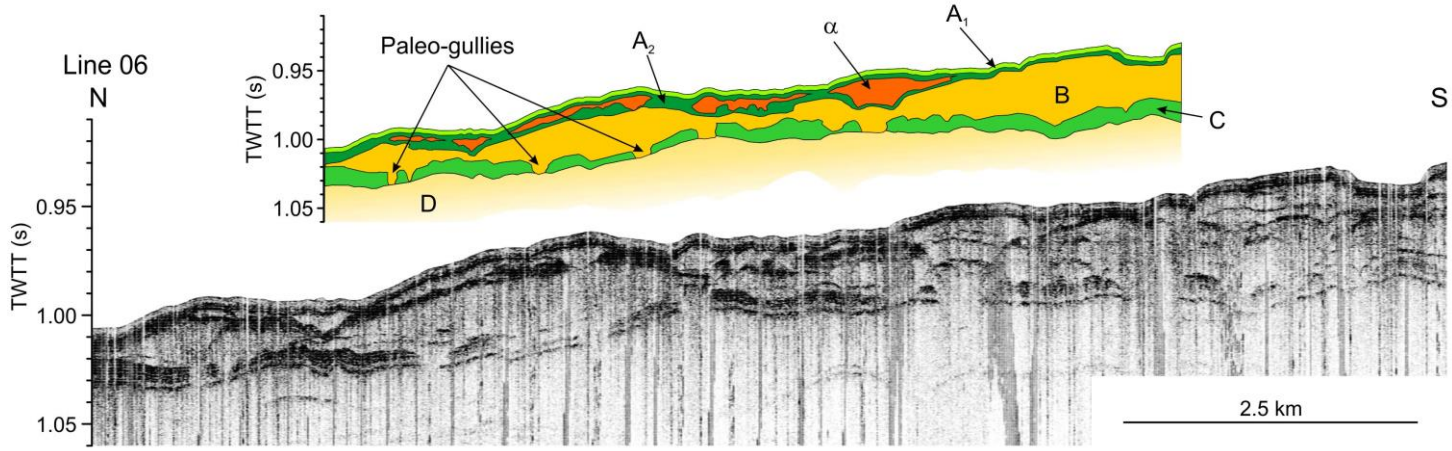

Fig. 4.2 Top interpreted cross-section. Bottom TOPAS sub-bottom profile Line 06 showing shallow subsurface TMF transparent and laminated units (for location see Fig. 4.1). Units shown in shades of yellow are interpreted to correspond to Glacial Maxima (GM) periods while units shown in shades of green are interpreted to correspond to Inter-Glacial Maxima (IGM) periods. Bottom of unit D is not completely imaged in this profile.

No laminated units occur in between these transparent shelf units. The transparent units on the shelf are separated by rather irregular to undulated surfaces (Fig. 4.4). Changes in slope and limited penetration immediately beyond the shelf edge complicate an accurate correlation of shelf and slope units along the whole dataset. Such correlation is only possible along selected SCS/MCS data (Fig. 4.4).

Scarps of multiple sizes often disrupt both laminated and transparent units, particularly near the southern limit of the Storfjorden TMF and at the confluence with the Kveithola TMF. Acoustically transparent (in sub-bottom profiles)/chaotic (in SCS and MCS data) sedimentary masses occur associated with these scarps. The chaotic character on seismic reflection data clearly stands out from that of the transparent more regionally widespread units α, B, D and F (Fig. 4.5). Furthermore, the lateral boundaries of these sedimentary masses are sharply cut into the surrounding sediments.

The acoustic character of all laminated units is quite similar. However, we can subdivide unit A into: A_1 and A_2. A_1 corresponds to the uppermost seismo-stratigraphic unit in the studied interval (Fig. 4.2). This uppermost unit is characterized by very low-amplitude reflections to almost transparent character and is the only unit which can easily be tracked across the slope and shelf. A_2 displays a more parallel laminated character, in a similar way to C, E and G. Sharply cut incisions are evident on these older laminated units which are filled

in by the overlying transparent units (e.g. unit C incisions in are filled in by unit B) (Fig. 4.3).

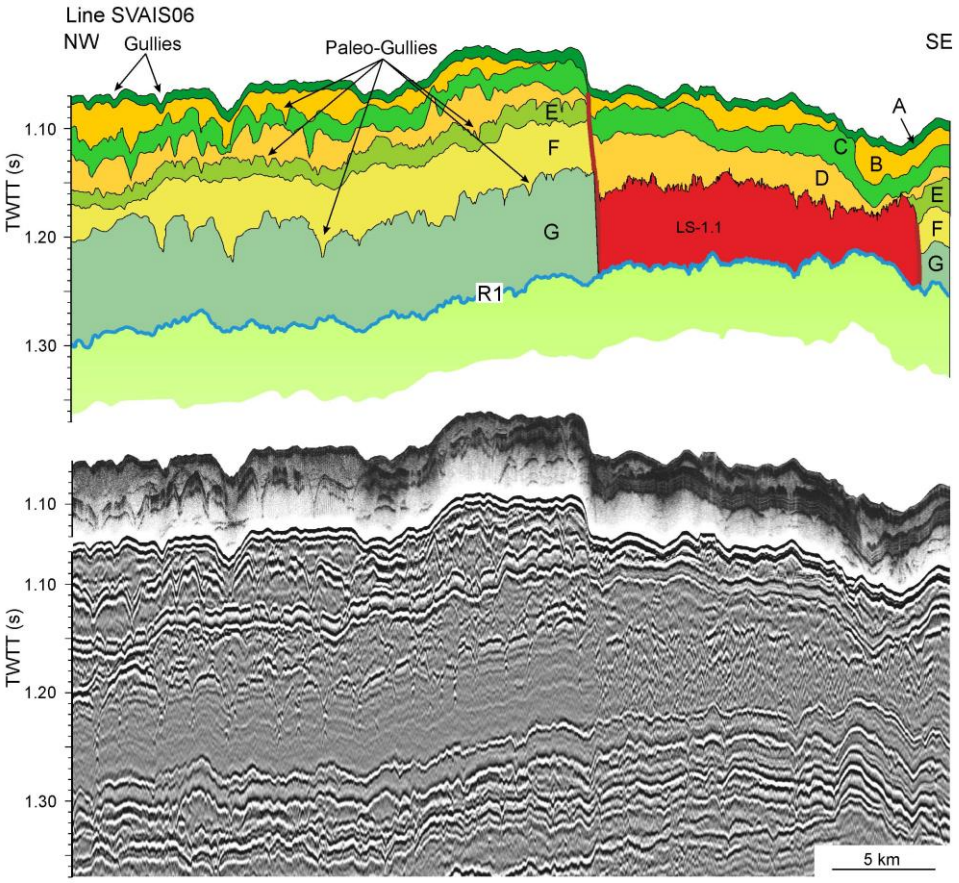

Fig. 4.3 Top. Interpreted cross-section. Bottom. Airgun seismic reflection and corresponding sub-bottom profile parallel to the shelf edge (for location see Fig. 4.1) showing gullies and paleo-gullies cutting into IGM sediments (shades of green) while they are filled by younger GM units (shades of yellow). To the south gullies and paleo-gullies disappear and the sequence is interrupted by landslide LS-1.1 (red). The base of this landslide is the regional reflector R1 (Faleide et al., 1996). The unit on top of LS-1.1 is the GM unit D. The sub-bottom profile is displayed at the same horizontal and vertical scale to show matching of acoustic facies between Airgun SCS and TOPAS parametric 3.5 kHz profiles.

Unit G, which is the thickest and deepest well-laminated unit, has a ~50 ms twtt more reflective upper part while the remainder of the unit has weaker internal reflections, except for a strong reflector located at about half its thickness.

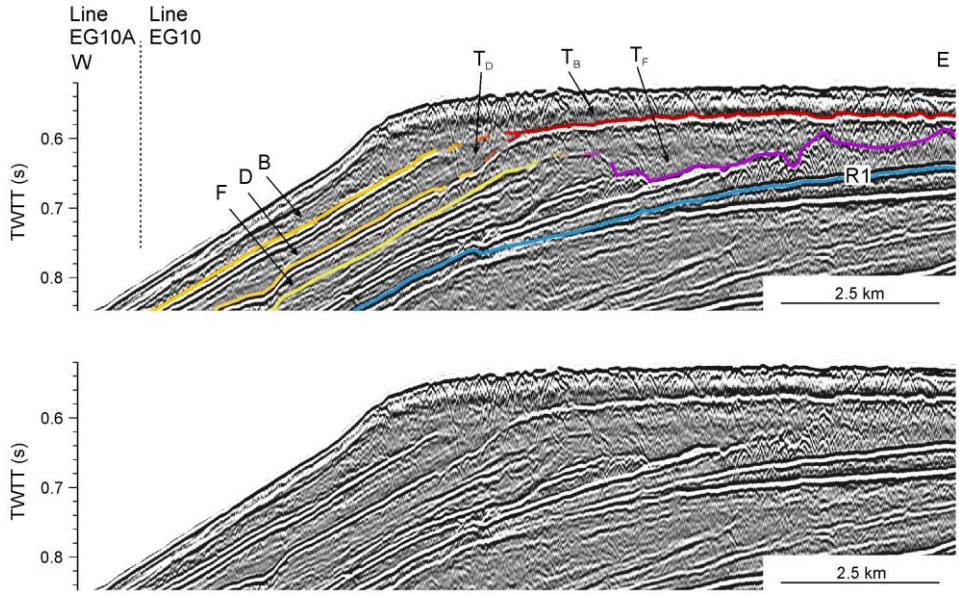

Fig. 4.4 Top. Interpreted cross-section. Bottom. MCS airgun seismic reflection profile perpendicular to the shelf edge (for location see Fig. 4.1) showing the transition between units on the shelf and slope. The red to purple lines on the shelf correspond to the base of subglacial deformation tills, which grade laterally into GM debris flows (basal reflectors marked in shades of yellow) on the slope.

Transparent units occur mainly in the upper and middle continental slope in the northern and central parts of the Storfjorden TMF and progressively pinch out 30 to 50 km west of the shelf edge. In these areas, they form a distinct package made of stacked transparent lenses. Conversely, in the southernmost part of the Storfjorden TMF, these lenses occur rather isolated within the laminated units and their continuity, particularly for unit B, might be lost (Fig. 4.5). Unit α is significantly more discontinuous than the preceding units and is present only in

the upper and mid slope in the central and northern area of the Storfjorden TMF (Fig. 4.2).

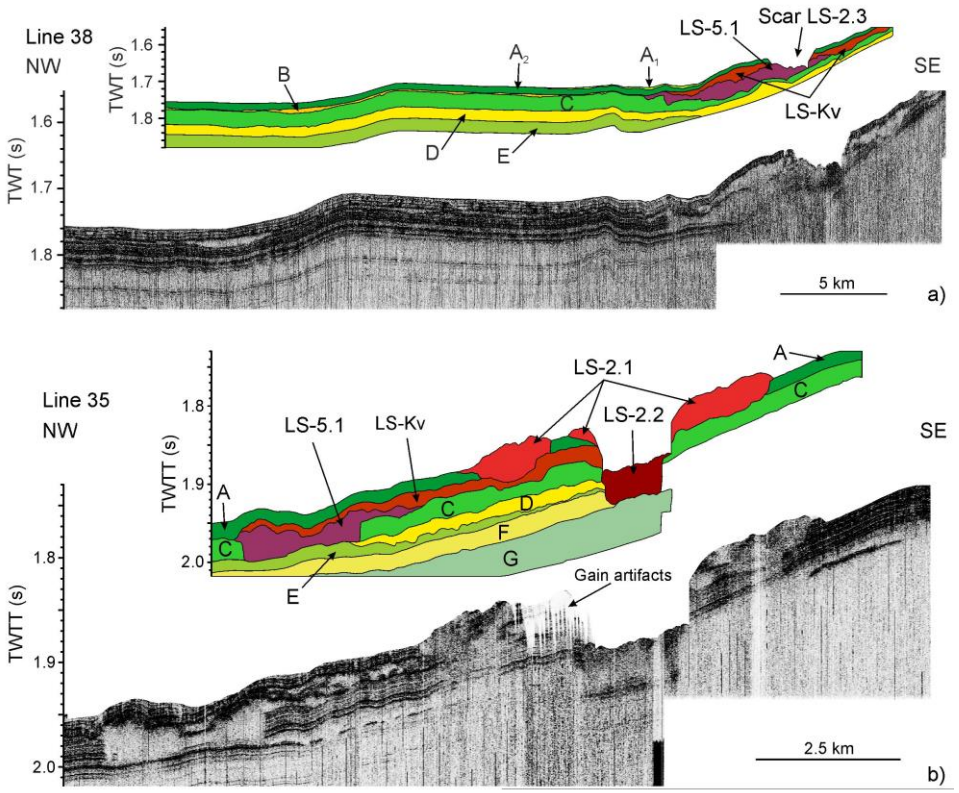

Fig. 4.5 a) Top interpreted cross-section. Bottom TOPAS sub-bottom profile Line 38 (for location see Fig. 4.1) illustrating an area with homogeneous thickness of both GDFs (shades of yellow) and IGM laminated (shades of green) units. Unit B is not present in this area. Submarine landslides (red and purple) erode laminated and transparent units. b) Top interpreted cross-section. Bottom TOPAS sub-bottom profile Line 35 (for location see Fig. 4.1) showing stacked landslides, erosive boundaries and scars associated to landslides. GDFs are shown in shades of yellow, IGM units in shades of green and submarine landslides in shades of red and purple.

4.1.1.2 Sedimentology

Cores SV-02 and SV-03 collected during the SVAIS cruise have sampled units A and B, in addition to the more chaotic units associated with scars (Fig. 4.6),

for a detailed sedimentological analysis see Lucchi et al. (2012) and Lucchi et al. (2013)). In addition, core GeB17610-2 from the CORIBAR cruise sampled unit A, as well as unit T_B. Subunit A_1 consists of heavily bioturbated and crudely layered mud, and structureless IRD-rich silt. Subunit A_2 is composed of finely laminated mud interbedded with sandy layers. At the base of unit A_2 is a thin (< 1 m) deposit of structureless medium/coarse-grained silt with sparse ice rafted debris (IRD). Red oxidized beds have also been identified near the base of unit A_2. Unit B consists of a water-poor, high shear strength diamicton. The boundary between units A_1 and A_2 has been dated in between 12 and 10 ka while the boundary between units A_2 and B has been dated at ~20 ka (Lucchi et al., 2012; Sagnotti et al., 2011). The chaotic units that are associated with slope scarps have also been sampled in core SV-03 resulting in a low-shear strength, water-rich diamicton, which physical properties resemble more those of the laminated sediments (~40% water content, shear strength up to 20 kPa) rather than those of the diamictons in unit B. Unit T_B, sampled in core GeoB17610-2, consists in a massive diamicton which shear strength increases abruptly to values around 30 kPa in the first centimeters.

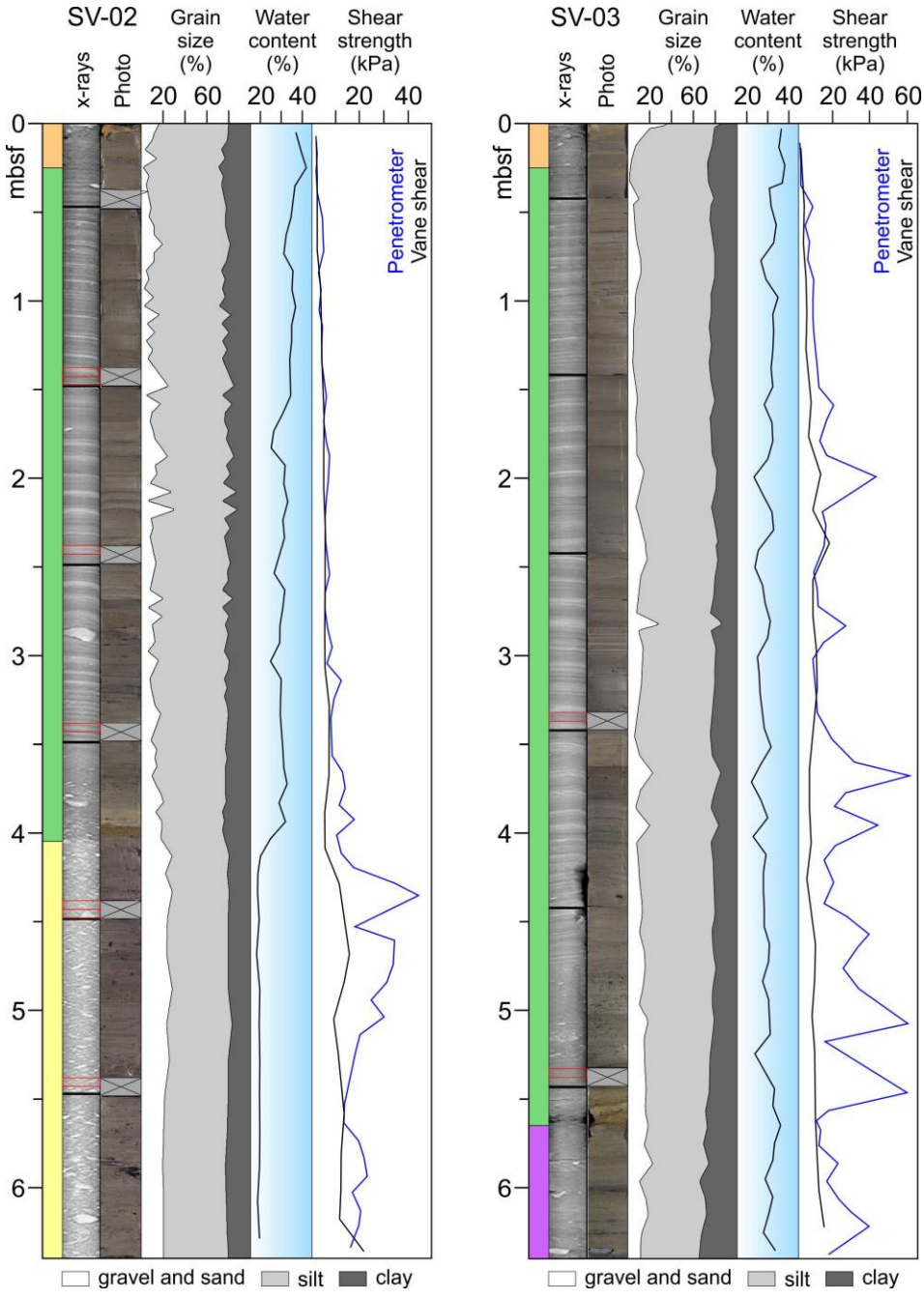
SV-02
Grain size (%)
Water content (%)
Shear strength (kPa)
x-rays
Photo
20 60
20 40
20 40
mbsf
0
1
2
3
4
5
6
Penetrometer
Vane shear
gravel and sand
silt
clay
SV-03
Grain size (%)
Water content (%)
Shear strength (kPa)
x-rays
Photo
20 60
20 40
20 40 60
mbsf
0
1
2
3
4
5
6
Penetrometer
Vane shear
gravel and sand
silt
clay

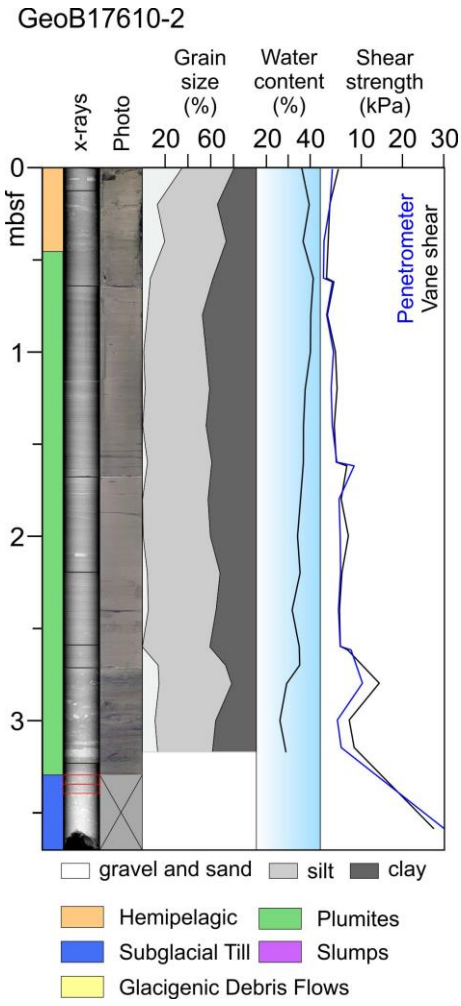

Fig. 4.6 Down core logs of physical sediment properties of the upper slope cores SV-2 and SV-3, and the outer shelf core GeoB17610-2 (see Fig. 4.1 for location). The hemipelagic and plumite units (orange and ligth green) are pressent in the upper part of the three cores. Core SV-2 sampled the glacigenic debris flows (light yellow), while core GeoB17610-2 sampled the till layer T_B. Red squares depict tested samples in the consolidation cell.

4.1.2 Surface geomorphology of sub-surface features

A number of surface morphologies on the shelf and slope are associated with sub-surface features and the sedimentary units described above, particularly the shallowest sedimentary units. On multibeam bathymetry data the most conspicuous feature on the TMF is a network of gullies on the upper slope. Individual gullies are 200-1000 m wide, 10-15 m deep and 5-50 km long and are

mainly located in the north and central part of the Storfjorden TMF. Downslope, these gullies gradually fade out (no gullies are present beyond the 1000 m isobath) and most do not cut back into the shelf. The downslope termination of these gullies often displays lobate convex-upward sedimentary bodies. Evidence for gully-like features is also observed in sub-bottom profiler, SCS and MCS data (Fig. 4.2 and Fig. 4.3). The gullies observed on bathymetric data can completely or partially cut into unit A (A_1 and A_2), be draped by unit A_1 or be filled by the entire unit A.

Paleo-gullies are wider (2-4 km) and deeper (12-40 m) than the present-day gullies observed on the bathymetric data. The paleo-gullies are also preferentially present in the northern and central part of the Storfjorden TMF and gradually disappear to the south and west. They develop at the top of well-stratified units (C, E and G), which can be completely or partially eroded, but they hardly incise into the units made of stacked transparent lenses (D and F) (Fig. 4.3). In turn, transparent units B, D and F fill the paleo-gullies. South of the Kveithola TMF, the drainage network develops from the shelf break into a dendritic canyon system rather than gullies (Fig. 4.1). The termination of these canyons is not imaged in the available data set.

The confluence between the Storfjorden and Kveithola TMFs is also the area where a series of surface scarps are located (Fig. 4.7).

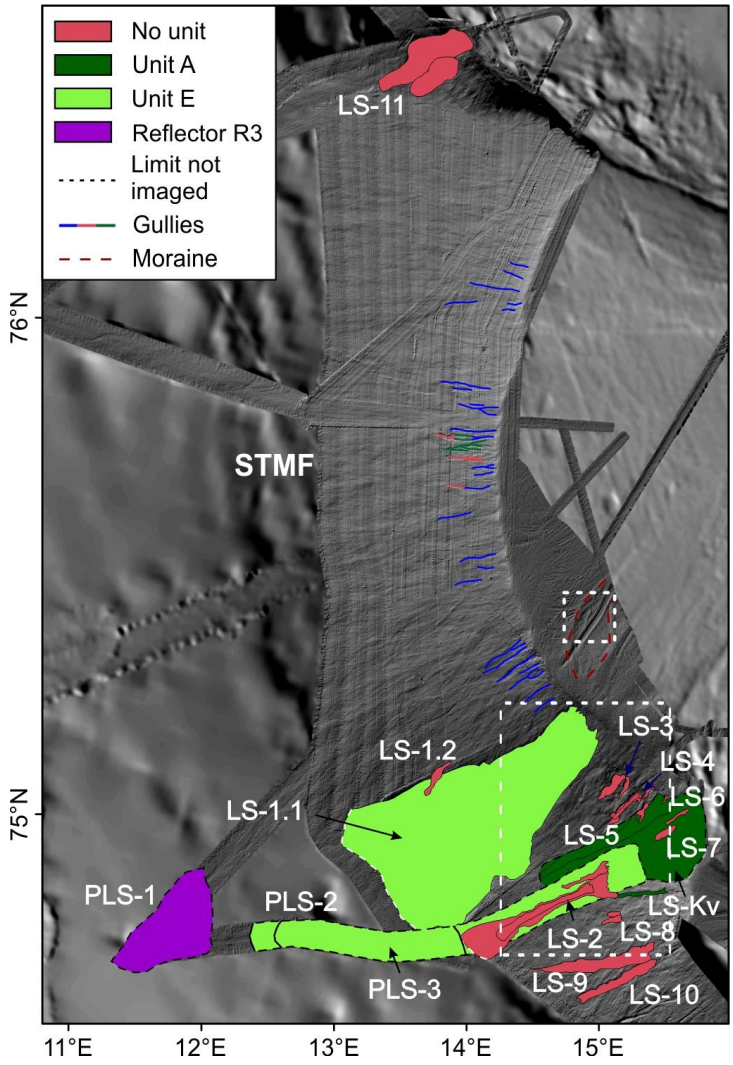

Fig. 4.7 Shaded relief image with landslides and recent gullies identified on the continental slope of the Storfjorden and Kveithola TMFs. The color-coding of landslides identifies the draping unit/reflector of the landslides. Some of the landslides are complex with multiple stages involved in the same event. For detailed characteristics of each landslide see Table 4.1. Gully color identifies the gully relationship with unit A: blue is gully fully filled with unit A; pink-red is gully with partial accumulation of unit A_2; green is gully devoid of sediments. Red dashed line marks a morainal body. White dashed squares marks the two close-up views in Fig. 4.8. STMF: Storfiorden Trough Mouth Fan; KvTMF: Kveithola Trough Mouth Fan. Note bathymetric artifacts induced by slope parallel ship tracks.

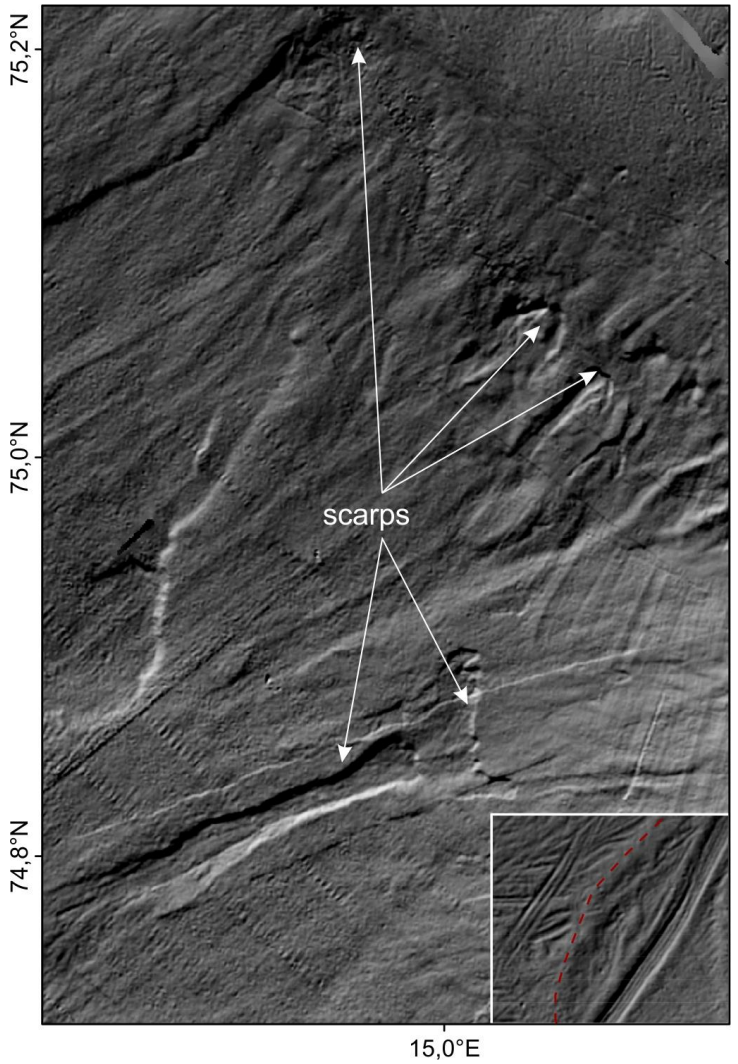

Fig. 4.8 Shaded relief bathymetry showing close-up views of slide scarps at the confluence area between the Storfjorden and Kveithola TMFs, and plough marks on the shelf (inset on lower right part of the image).

The length, width and height of these scarps are highly variable ranging from 1.7 to 40 km, 0.5 to 8 km and 10 to 50 m respectively. All scarps are located in between the shelf edge and the 1600 m isobath, but within this depth range there is no preferential depth of occurrence of the observed scarps. The scarps are associated with near-surface or sub-surface sedimentary deposits that display as

transparent (in TOPAS profiles) or chaotic (in SCS and MCS profiles) lenses (Fig. 4.5). We classify these deposits into those that have a surface expression (LS) and those that do not have such an expression (PLS). Twenty-six such bodies (LS and PLS) have been identified in the study area. In sub-bottom profiler data, most of the seismically transparent sedimentary bodies associated with slope scarps are actually composed of clustered transparent lenses. The majority of these bodies have unit C at the bottom and, in most cases, they are devoid of sediment at their top (Table 4.1, Fig. 4.5, Fig. 4.7), implying that those are amongst the most recent events in the sedimentary succession. One of the largest transparent bodies associated with scarps on the Storfjorden TMF is LS-1. The headscarp of LS-1 is made of several coalescent scarps with a total height of up to 80 m. However, typical head/side scarps are 30 to 40 m high. Several transparent/chaotic bodies are associated with the coalescent scarps of LS-1. The larger of these bodies (LS-1.1) has a minimum area of 1,340 km^2 and a mean thickness of 35 m; the total amount of sediment involved in this sedimentary body is ~47 km^3. The three deposits that have no surface expression (PLS-1, PLS-2 and PLS-3; see also Rebesco et al. (2012)) (Fig. 4.9) have a minimum volume of 45 km^3, 127 km^3 and 18 km^3 respectively (Table 4.1).

Table 4.1 Landslides characteristics. The mean thickness is calculated from the height of the scar. The volume is calculated from the area and height where the scars have been identified

	Bottom unit	Top unit	Area (km^2)	Mean thickness (m)	Volume (km^3)
LS-1.1	pre-R1	D	1338.4	35.0	46.84*
LS-1.2	B	-	11.0	15.6	0.17
LS-2.1	C	-	95.2	26.0	2.48*
LS-2.2	C	-	35.5	30.0	1.06
LS-2.3	B	-	12.7	25.0	0.32
LS-2.4	C	A	8.9	20.2	0.18
LS-3.1	C	-	12.7	21.0	0.27
LS-3.2	C	-	3.7	21.0	0.08
LS-4.1	C	-	13.0	23.0	0.30
LS-4.2	C	-	5.2	26.0	0.14
LS-4.3	A	-	2.6	12.0	0.03
LS-5.1	C	A	86.0	46.0	3.96
LS-5.2	C	A	4.8	11.2	0.05
LS-5.3	A	-	0.8	9.7	0.01
LS-6	A	-	3.8	8.2	0.03
LS-7	C	-	6.7	32.2	0.22
LS-8.1	C	-	2.9	16.4	0.05
LS-8.2	C	-	4.9	17.2	0.08
LS-9	C	-	67.3	11.2	0.75
LS-10	C	-	36.2	12.7	0.46
LS-11.1	?	-	119.9	17.2	2.06
LS-11.2	?	-	52.9	21.0	1.11
LS-Kv	C	A	459.1	8.0	3.67*
PLS-1	pre-R4	post-R3	647.7	70.0	45.34*
PLS-2	pre-R1	E	709.0	180.0	127.62*
PLS-3	pre-R2	R2	240.0	75.0	18.0

*: feature not completely imaged. ?: not visible.

On the outer shelf, the surface expression of seismic units and other sub-surface features on the seafloor is rather scarce. The only exception is a transparent sedimentary lens on the southern side of the outer Storfjorden Trough. In plan

view, this sedimentary body displays a drop-like shape (Fig. 4.8). At its top, the various units that subcrop in the near surface of the shelf display linear to curved furrows and sets of larger-scale parallel lineations. The latter typically occurs in groups of 5 to 6 lineations (Fig. 4.8).

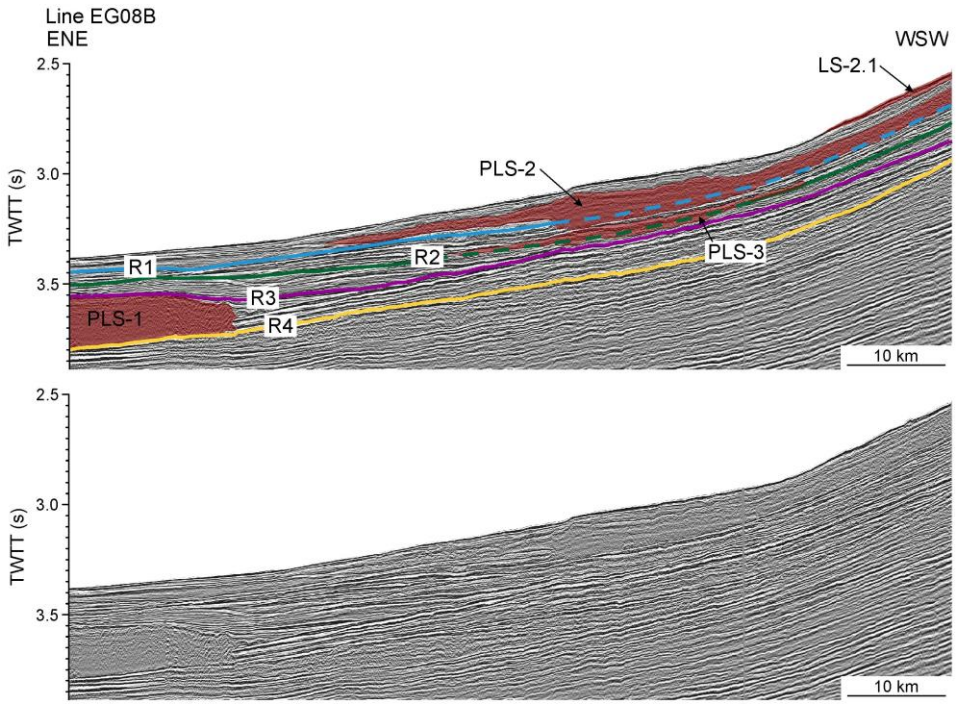

Fig. 4.9 Top. Interpreted cross-section showing landslides PLS-1, PLS-2, PLS-3 and LS-2.1. Bottom. Airgun seismic reflection profile (for location see Fig. 4.1). Regional reflectors R1 to R4 are highlighted (after Rebesco et al. (2012)). Dashed lines tentatively show the position of reflectors prior to the occurrence of landslides PLS-2 and PLS-3.

4.1.3 Seismic units distribution and related thickness

The occurrence and thickness of the "laminated" and "transparent" seismic units is not constant either laterally (along/across slope) or with depth within the

sedimentary sequence (older units). In particular, the acoustically laminated seismic units drape the entire slope of the TMF, while the transparent units develop only on the upper and middle slope, especially in the two northernmost lobes of the Storfjorden TMF (Lobes I and II).

In general, the thickness of the laminated units (A, C, E and G) increases southwards and with depth in the sedimentary column (older units). Thickness also decreases downslope showing a more constant pattern than the transparent units, which have high lateral thickness variation (Fig. 4.10). The uppermost laminated unit, unit A, drapes the entire area imaged by our data set with a mean thickness of 10 ms twtt although thickness increases both south and north to the sides of the TMF. Of these 10 ms twtt, 2-4 ms twtt correspond to subunit A_1. Subunit A_1 can be tracked on both the shelf and slope through the shelf break. Unit A's maximum thickness of 39 ms twtt is reached in the inter-TMFs area and on the Kveithola outer shelf where distinct depocenters are found both in the upper and middle slope (Fig. 4.10a). Unit C has a relatively constant thickness in the northern and central Storfjorden TMF of 20-30 ms twtt. Maximum sediment accumulations of up to 64 ms twtt occur in the southern Storfjorden and northern Kveithola TMFs close to the shelf edge (Fig. 4.10c). As is the case with unit A, a few depocenters are present in this unit. The main depocenter is located in the

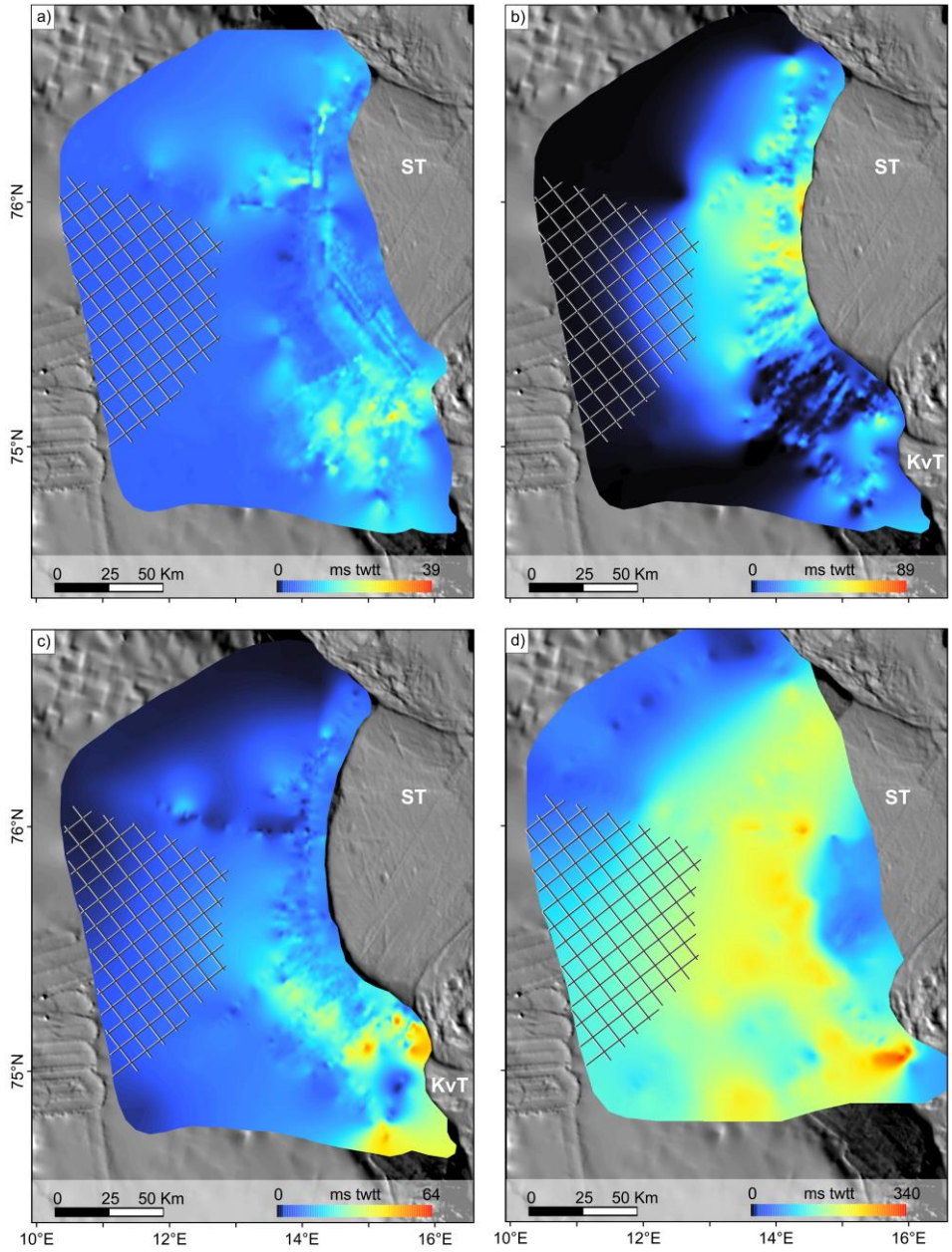

Fig. 4.10 Isochore maps showing the thickness (in ms twtt) of a) unit A, b) unit B, c) unit C and d) total thickness above the R1 regional reflector. Grey mesh depicts area with no seismic coverage and interpolated values. Grid cell size is 80 m. ST: Storfjorden Trough; KvT: Kveithola Trough. Note that color bars do not have the same scale.

upper-middle slope of the inter-TMF area, but secondary depocenters occur in the middle slope of the southern TMF. Units E and G are not sufficiently imaged, but available data suggest that unit E is similar in thickness to unit C and that unit G is the thickest laminated unit above R1 in the TMFs with a mean thickness of 90 ms twtt (Fig. 4.3). The transparent units (B, D and F) display highly variable thickness. They form relatively continuous layers in the upper and middle northern and central Storfjorden TMF. They however occur in isolated lenses or even disappear, particularly unit B, in the southern part of the Storfjorden TMF and at the confluence with the Kveithola TMF (Fig. 4.5). These units also decrease in thickness downslope and they pinch out 30-50 km away from the shelf edge. Unit B is the transparent unit which thickness is better constrained due to penetration issues. It has a spatial distribution displaying the opposite pattern to that of the above and below laminated units, A and C (Fig. 4.10b). The maximum thickness is around 89 ms twtt close to the central part of the Storfjorden TMF and almost disappears to the south of the TMF. Close to the shelf edge, a few seismic lines show evidence that the slope transparent units grade into the shelf transparent units (T_B, T_D, T_F), where their thickness varies between 3 and 120 ms twtt (Fig. 4.4).

There are few areas where unit D has been fully imaged, and therefore the isochore map does not show clear thickness trends. However, we find a more constant thickness across the study area with a mean value of ~25 ms twtt and maximum values up to 40 ms twtt in the upper central fan area (Fig. 4.4 and Fig.

4.5). Imaging of unit F in SCS and MCS data is not complete enough to produce isochore maps, however available data suggest that above R1 the three transparent units identified display an increasing thickness with depth, being the uppermost unit (unit B) thinner. The isochore map between the regional reflector R1 and the sea floor (Fig. 4.10d) computed from the interpretation of SCS and MCS data shows that the main depocenter is located in the upper/middle slope and, particularly, close to the shelf edge. The mean values in this area are 220 ms twtt, while maximum values of 340 ms twtt occur in the central part of the Storfjorden and Kveithola TMFs close to the shelf break. The thickness of the TMF above R1 quickly decreases towards the north and west displaying a pattern similar to the transparent units, which likely seem to control overall thickness above R1.

4.2 Sediment geotechnical properties and Trough Mouth Fan hydrogeological evolution

The Storfjorden and Kveithola Trough Mouth Fans (TMFs) started to develop around 2.7 Ma. Such development was enhanced by intensification of glacial conditions at 1.5 Ma (Faleide et al., 1996). The intensification led to shelf edge progradation and the rapid accumulation of tills and glacigenic debris flows due to ice streams advance during glacial conditions, while melt-water plumites were deposited during deglaciations and hemipelagic sediments draped the seafloor during interglacials (Butt et al., 2000; Laberg and Vorren, 1996b). This sequence

of events produced a stratigraphic pattern made of sediments with contrasting physical properties and sedimentation rates arranged in a non-uniform spatial pattern throughout the TMF. In absence of in-situ hydrogeological experiments, understanding TMF interstitial fluid flow patterns and development of excess pore pressures can only be achieved by modeling its sedimentary and stratigraphic evolution through time. To this end, physical/geotechnical properties of the sediments involved are of paramount importance.

Loading of shelf sediments by ice streams during glacial maxima may cause, among others, variation of fluid flow patterns and overpressures build up (i.e. Lerche et al. (1997)).

Due to limitations in BASIN to simulate the ice loading/unloading effects, the Plaxis FE modeling software has been used. The process of plumite layer deposition during the deglacial phase along the entire shelf and slope and that of erosion by ice streams and subglacial till deposition during glaciations (Laberg et al., 2009) is simulated by deposition of a plumite layer during Inter-Glacial Maxima phases and replacing it on the shelf by till layers during Glacial Maxima, when the ice load is applied. Because of the better constraints in all input parameters and versatility in terms of materials and applied loads to model the evolution from R1 to Present day, Plaxis has been selected to evaluate the ice contribution to the margin hydrogeological evolution focused in the last 220 kyrs. The model results will then be used to understand slope instability of the TMF.

4.2.1 Sediment geotechnical characterization

Consolidation and permeability testing were performed on three sediment types: a) laminated sediments interpreted as melt water plumites, b) slope chaotic sediments interpreted as glacigenic debris flows (GDFs), and c) shelf chaotic sediments interpreted as tills (see Chapter 4.1). In addition, water content and Atterberg limits were determined.

According to the core logs, shallow subsurface plumite sediments (0.5-4.5 mbsf) show a water content around 40% and an undrained shear strength between 2 to 15 kPa even though some layers show shear strength values up to 60 kPa (bright layers in the x-ray data) (Fig. 4.11). In core SV-02 the transition from plumites to GDFs is clearly shown by the water content decreasing to values close to 20% and the shear strength increasing up to 40 kPa. The lower part of core SV-03 shows a transition from well layered plumites to a rather chaotic sedimentary fabric. This transition is not depicted by the water content and shear strength that remain in the same range as in plumites. Plumites in core GeoB17610-2 are poorly layered with respect to the other two cores displaying less variability in water content and undrained shear strength. At the base of this core, till sediments have been sampled, with the lithological change reflected in an abrupt increase of the shear strength. Water content results from the samples tested in the consolidation cell (Table 4.2), show, in general terms, higher values in plumites (~40%) than in GDFs (~25%). The transition from plumites to tills in

core GeoB17610-2 is clearly depicted by an abrupt decrease in water content values (from 40% to 20%).

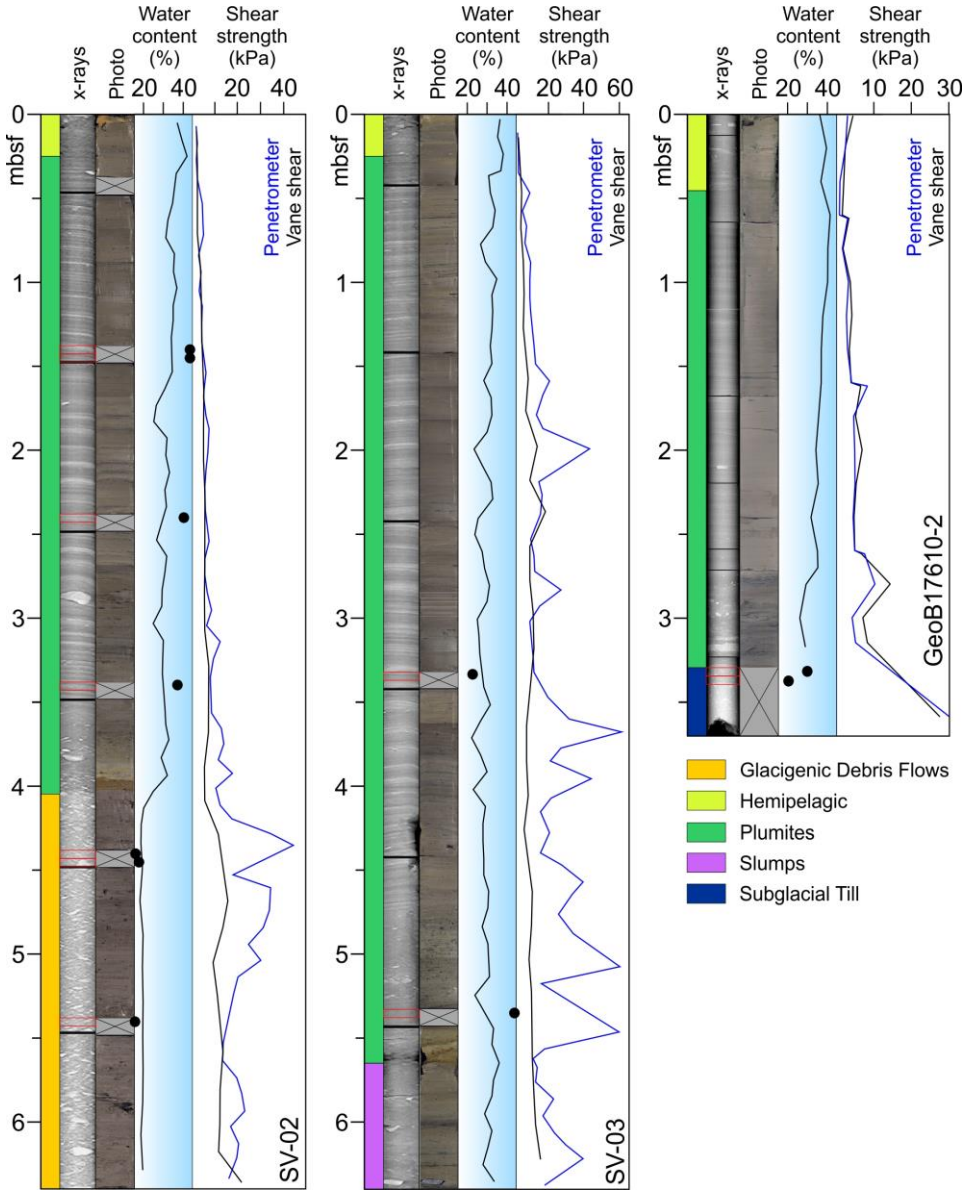

Fig. 4.11 Down core logs of physical properties. Black dots depict water content of whole round samples tested in the consolidation cell (red squares).

Table 4.2 Water content and Atterberg limits for all tested samples.

Core (Sample)	Sample depth (cm)	Sediment type	Wi (%)	W_P (%)	W_L (%)	PI (%)	IL (%)
SV02-02(A)	140	Plumites	44.2	22.0	44.3	22.4	99.5
SV02-02(B)	145	Plumites	44.2	21.5	49.8	28.3	80.2
SV02-03	240	Plumites	42.1	24.9	49.8	24.9	69.3
SV02-04	340	Plumites	39.9	19.2	47.1	27.8	74.2
SV02-05(A)	440	GDF	24.0	16.6	31.9	15.3	47.9
SV02-05(B)	445	GDF	26.6	17.2	31.4	14.2	66.4
SV02-06(B)	540	GDF	23.1	15.0	31.5	16.6	49.3
SV03-04	330	Plumites	30.0	21.2	40.3	19.1	65.4
SV03-06	530	Plumites	47.9	28.3	57.0	28.6	68.1
GeoB176010-2(319)	319	Till	35.0	18.3	42.6	24.3	61.6
GeoB176010-2(330)	330	Till	28.5	18.0	31.3	13.3	79.5

W_i: water content; W_P: plastic limit; W_L: liquid limit; IP: plasticity index; IL: liquidity index. See Fig. 4.11 for sample location within the core.

Plumite samples have a mean plasticity index (PI) of ~ 24.5 while GDFs have a mean PI of 15.3, and tills 23.8. Plotting the plasticity index versus the liquidity index of the samples, two populations can be clearly identified. Plumites can be classified as intermediate plasticity clays (CI), while GDF's and tills can be classified as low plasticity clays (CL) (Fig. 4.12). Only the till sample GeoB17610-2-319 shows an intermediate plasticity. This higher plasticity could result from higher clay content of the matrix in the upper most part of this layer. However, no grain size analyses have been carried out in till sediments. In turn, sample SV03-06 shows the highest plasticity and water content (Fig. 4.12).

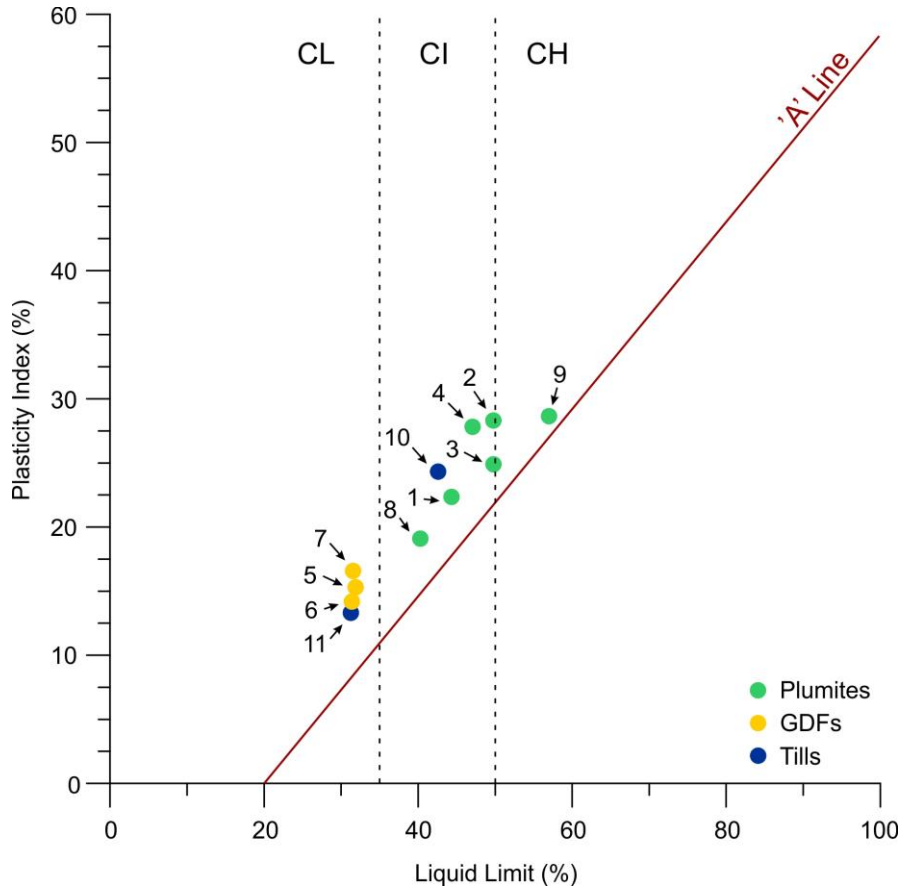

Fig. 4.12 Plasticity chart showing the relation between liquid limit and plasticity index. Plumite sediments show intermediate plasticity, while GDFs show low plasticity. Till samples depict different behaviour. The test performed on slumped material shows high plasticity. Samples 1)SV02-02(A), 2) SV02-02(B), 3) SV02-03, 4) SV02-04, 5)SV02-05(A), 6) SV02-05(B), 7) SV02-06(B), 8) SV03-04, 9) SV03-06, 10) GeoB17610-2(319), and 11) GeoB17610-2(330).

Oedometer tests carried out with the Rowe&Barden cell-type have provided the compressibility and permeability characteristics for the samples as shown in Table 4.3. The measured initial void ratio values of plumites vary between 1.1 and 1.5. In the case of GDFs the void ratios are lower (0.6-0.8). Mean void ratios at deposition e_0 (σ'=1 kPa) are 1.73 and 0.98, respectively (Table 4.3). These values have been calculated by using logarithmic regression of the virgin

consolidation line for each sediment sample. Regarding till sediments, because their deposition process occurred under the ice load, e_0 has been calculated at the pre-consolidation pressure (σ_c) with a mean value of 0.93. Hydraulic conductivities have been calculated by means of the flow-through permeability test. In general terms, the hydraulic conductivities (k) are low (10^{-10}-10^{-8} m/s). The mean initial hydraulic conductivities for plumites, GDFs and tills have been calculated at void ratio e_0: $1.1 \cdot 10^{-8}$ m/s, $7.3 \cdot 10^{-10}$ m/s and $4.0 \cdot 10^{-10}$ m/s, respectively. In turn, mean values of initial specific storage are 0.024, 0.008 and 0.005, calculated at σ'=1 kPa. The specific storage and hydraulic conductivities show also a more marked decrease with increasing stress in plumites than in GDFs or tills (Fig. 4.13). Initial values are used hereinafter as depositional values.

Table 4.3 Most important parameters derived from oedometer tests in this study.

Sample	Sediment type	e_0	k_0 (m/s)	S_0 (m^{-1})	σ_c (kPa)	OCR	C_c	C_s
SV02-02-B	Plumites	1.48	2.3E-09	0.024	18	1.0	0.33	0.062
SV02-03	Plumites	1.89	5.5E-09	0.019	32	1.1	0.41	0.066
SV02-04	Plumites	1.72	7.2E-09	0.032	44	1.0	0.38	0.043
SV03-04	Plumites	1.83	4.2E-08	0.023	42	1.0	0.37	0.058
SV03-06	Plumites	1.24	1.0E-09	0.021	59	1.0	0.24	0.029
SV02-05-B	GDF	1.04	3.6E-10	0.009	65	1.2	0.27	0.022
SV02-06	GDF	0.92	1.1E-09	0.007	73	1.1	0.20	0.026
GeoB17610-2-319	Tills	0.94 (1.38)	4.9E-10	0.006	58	1.5	0.22	0.012
GeoB17610-2-330	Tills	0.93 (1.29)	3.2E-10	0.004	57	1.5	0.20	0.027

GDF: Glacigenic Debris Flows, e_0: initial void ratio at 1kPa (void ratio of tills has been taken at σ_c, in brackets the e_0 at 1 kPa), k_0: initial hydraulic conductivity, S_0: initial

specific storage, σ_c: pre-consolidation pressure, OCR: Overconsolidation Ratio, Cc: compressibility index, Cs: swelling index.

The slope of the virgin consolidation line for plumites is steeper than that of the GDF and tills with values of C_c 0.35 for plumites 0.23 for GDFs and 0.21 for tills. C_s values are 0.052, 0.024 and 0.02, respectively. The consolidation tests performed in this study clearly show that these different sediment types have clearly distinct physical properties. In this case, samples SV02-02, SV02-03, SV02-04, SV03-04, and SV03-06, corresponding to meltwater plumites, are more porous, permeable and have higher compressibility than samples SV02-05 and SV02-06, which were taken on glacigenic debris flow sediments. These differences are partially controlled by consolidation, but trends in the virgin consolidation line and values derived at deposition (σ'=1 kPa) indicate that the differences are genuine. Plumites are finer grained and better sorted than GDF's, which is probably at the origin of the observed differences in physical properties. According to the tests performed on core SV02 and SV03 (see Lucchi et al., 2013), plumites also have higher water content and lower shear strength compared to GDFs at the same consolidation stress. As stated above, the consolidation index of plumite sediments is higher than that of GDFs, even if the percentage of pebbles in the GDFs is low. Pre-consolidation pressure indicates normally consolidated sediments for both plumites and GDFs. Conversely, the in situ effective vertical stress (assuming hydrostatic conditions) of till samples compared to the pre-consolidation effective stress shows an Over Consolidation Ratio (OCR) around 1.5.

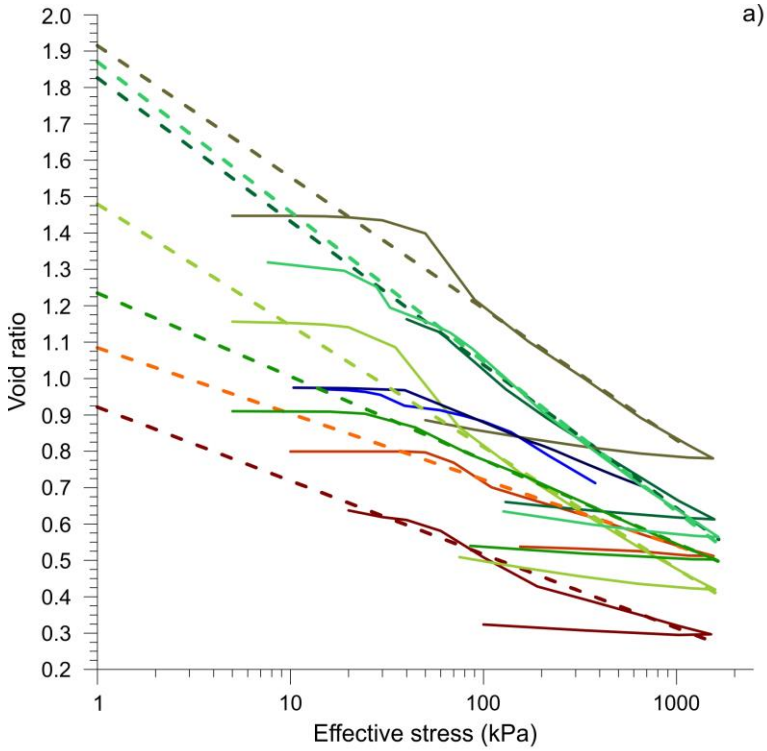
a)
Void ratio
2.0
1.9
1.8
1.7
1.6
1.5
1.4
1.3
1.2
1.1
1.0
0.9
0.8
0.7
0.6
0.5
0.4
0.3
0.2
1
10
100
1000
Effective stress (kPa)

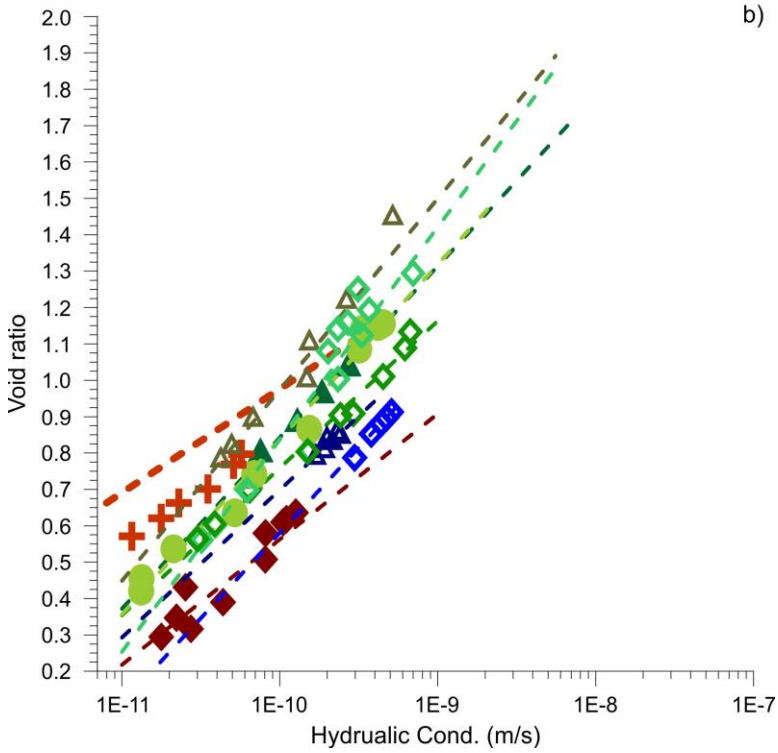
b)
Void ratio
2.0
1.9
1.8
1.7
1.6
1.5
1.4
1.3
1.2
1.1
1.0
0.9
0.8
0.7
0.6
0.5
0.4
0.3
0.2
1E-11
1E-10
1E-9
1E-8
1E-7
Hydrualic Cond. (m/s)

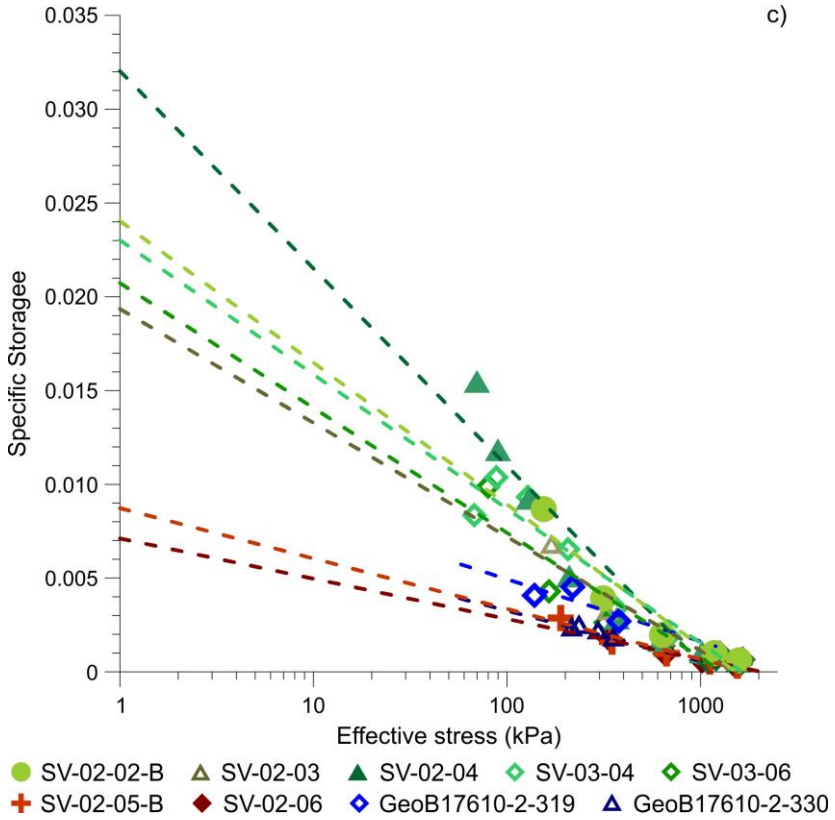

Fig. 4.13 Consolidation tests results: a) effective stress versus void ratio for the tested samples. b) flow-through hydraulic conductivity versus void ratio at the virgin consolidation part. c) effective stress versus specific storage at the virgin consolidation part. Dashed lines correspond to extrapolation to 1 kPa used to determine initial (depositional) parameters. For till samples, the initial parameters are calculated at the pre-consolidation pressure. Greenish lines correspond to plumites, reddish to GDFs and bluish to tills.

Pre-consolidation pressures from these shallow till samples, suggest that the ice load was around 60 kPa, corresponding only to ~6m of ice above the buoyancy compensation thickness. A possible explanation for the low pre-consolidation pressures is that the deposition of these tills occurred right at the beginning of the deglaciation. Alternatively, the low pre-consolidation pressures can be explained if the ice sheet was warm-based, i.e., if significant overpressure existed within

the till sediments due to loading by an impervious ice sheet. Such conditions would favor a highly mobile ice sheet and a deformable till base (Christoffersen and Tulaczyk, 2003).

4.2.2 Hydrogeological models

4.2.2.1 BASIN model

Consolidation and permeability tests provide the input parameters used for BASIN modeling. These parameters include initial porosity, initial hydraulic conductivity and initial specific storage. As mentioned in Chapter 3.3.1, BASIN allows inputting physical properties for four different sediment types. Owing to the evidences presented in Chapter 4 and the studies carried out by other authors in the study area, the sediment types were defined as plumites (including turbidites in the deeper most parts, i.e. below R7 reflector), glacigenic debris flows, tills and hemipelagic sediments. However, consolidation tests were not performed in hemipelagic sediments due to the lack of samples of this sediment type for geotechnical testing. Parameters for hydrogeological modeling for hemipelagic sediments are therefore taken from the literature (see Table 4.4).

Table 4.4 Parameters used for hydrogeological modeling with BASIN.

	Plumites	GDFs	Till	Hemipelagic sediments
ϕ_0	0.63 (1)	0.49 (1)	0.48 (1)	0.77 (2)
S_0 (m^{-1})	0.025 (1)	0.008 (1)	0.005 (1)	0.044 (2)
k_0 (m/s)	1.43E-9 (1)	7.2E-10 (1)	4.05-10 (1)	3.0E-9 (3)
ρ_g (kg/m^3)	2650	2650	2650	2650
θ	1.4	1.5	1.5	1.2

(1) this study. (2) Forsberg et al. (1999). (3) Urgeles et al. (2010). ϕ_0: initial porosity, S_0: initial specific storage, k_0: initial hydraulic conuctivity, ρ_g: grain density, θ: tortuosity ($\theta = \sqrt{1 - \ln(\phi^2)}$, Boudreau, 1996).

The other input parameters required in BASIN are the geometry (interfaces between major sedimentation packages) and the time span of deposition for each sedimentary unit. As explained in Chapter 3, the geometry assumes that the problem can be conceptualized in 2D. Such geometry is described from reflectors and sedimentary units identified from seismic line ITEG08-09 and information from two nearby legacy seismic profiles, lines 3 and 4 of Faleide et al. (1996).

The time span of deposition for each unit used in the model has been taken from Knies et al. (2009) and from the ages proposed in Chapter 3 (Table 3.5). The units between the oceanic basement and unit G have been named after their basal reflector. Therefore, the sedimentary packages between reflectors R3 and R2 correspond to unit R3. From reflector R1 to the seafloor, the units are those described in Chapter 4.1.

Below reflector R7, a transition from mixed plumites and hemipelagic sedimentary facies to purely hemipelagic sediments has been set (Fig. 4.14b). Uncertainties in sediment type distribution prevent a better characterization of this interval, but the sedimentary facies is consistent with a relatively distal position on a prograding continental margin.

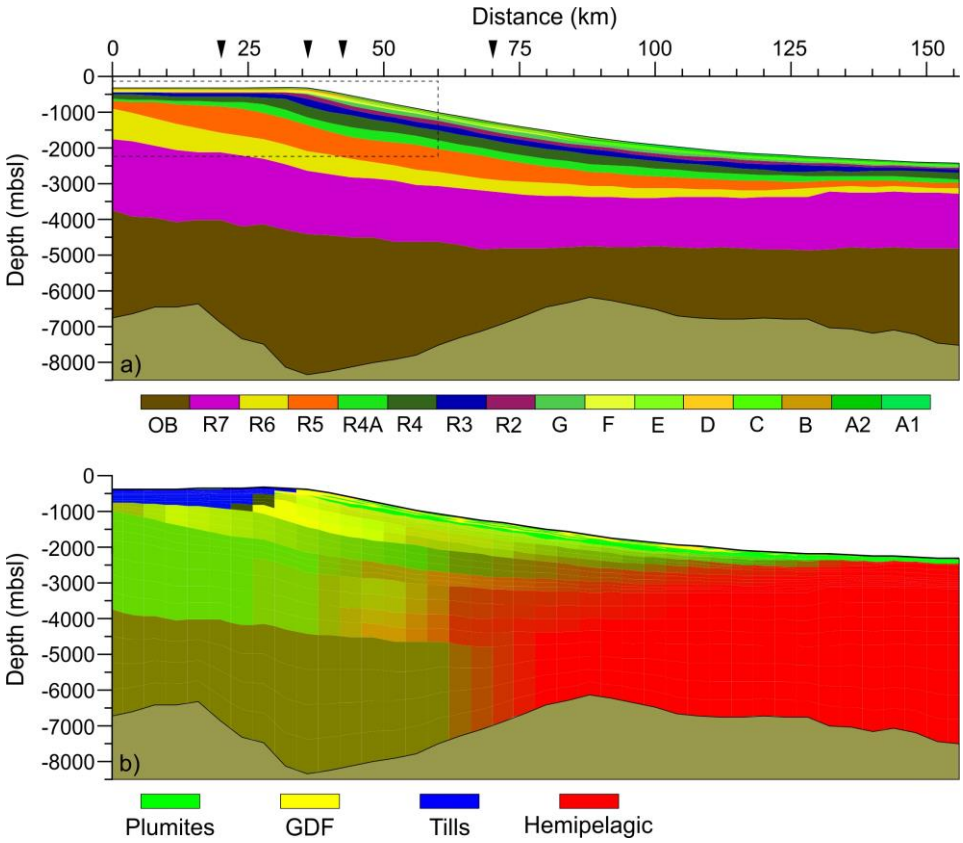

Fig. 4.14 Margin stratigraphy of the Storfjorden TMF (a) and facies distribution (b) at Present day. The units are named after their basal reflector. Vertical exaggeration 7:1. Dashed box depicts area modeled with Plaxis. Black arrows mark the location of the synthetic observation wells (

Fig. 4.16). OB: Oceanic Basement.

From onset of the Northern Hemisphere Glaciation (NHG) at 2.3 Ma to ~1.7-1.5 Ma when the ice sheets expanded to the paleo-shelf edge (Butt et al., 2000; Knies et al., 2009), a transition from plumites to glacigenic debris flows occurred in the north eastern part of the model (0-30 km) (units R7 to R6).

An increase in glacial conditions from 1.5 Ma to 0.22 Ma (corresponding to units R5 to R2) with ice streams reaching the paleo-shelf edge contributed to shelf edge progradation, deposition of tills on the shelf and build-up of the glacigenic debris flows lenses on the slope. From 220 ka (reflector R1) to Present day, glacial and interglacial cycles (see Chapter 4.1) are clearly depicted by alternation of GDFs and plumites on the slope.

Consolidation due to overburden mainly controls the porosity and permeability evolution along the modeled profile. The model outcome for the Present day state of the margin shows that porosities higher than 0.4 are present only at shallow depths where the consolidation effects due to overburden are low (Fig. 4.14a). However, at the shelf and upper slope a wedge of low porosity (below 0.15) develops, which corresponds to the area where tills and GDFs are the prevailing sediments. In this area, hydraulic conductivities are lower than in the adjacent middle and lower slope where plumite and hemipelagic sedimentation predominates. Values of hydraulic conductivities higher than 10^{-9} m/s (Fig. 4.14) are only found in the first meters below the seafloor or in the distal part of the margin, where such plumite and hemipelagic sedimentation is dominant (Fig. 4.14b). Fluid flow is mainly vertical in the entire margin, which indicates that

sediment self-weight consolidation is the main factor driving fluid flow along the margin. This flow pattern is however modified where the major depocenter occurs (between kilometers 30 and 50 in the modeled profile). In addition, near the shelf edge, the fluid is diverted to the upper slope. Such diversion is likely due to the low hydraulic conductivity of till sediments present along the shelf.

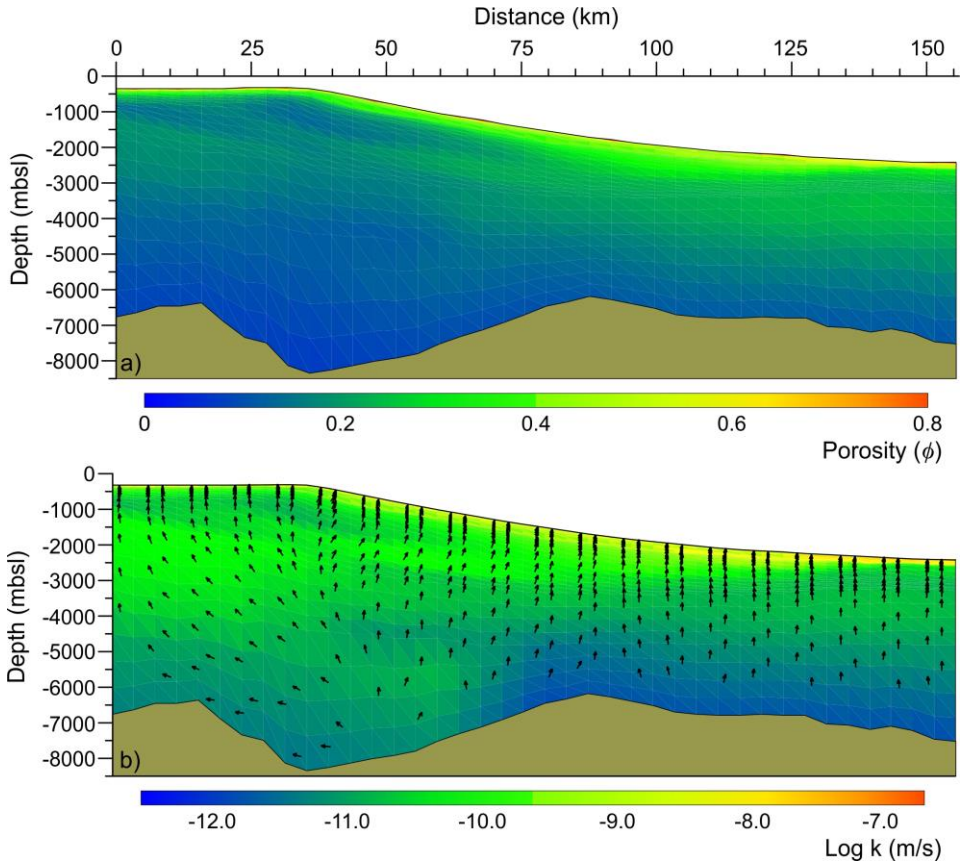

Fig. 4.15 a) Margin Fractional porosity of the Storfjorden TMF and b) log hydraulic conductivity (m/s) at Present day. Vertical exaggeration 7:1.

Sediment physical properties, stratigraphy and sedimentation rates control the pore pressure development. The deposition of sediments below reflector R7 spans 800 kyrs. At the timing of deposition of this horizon, excess pore pressures

along the margin were low (below 3 MPa). Only in the deeper part of a basement depression located between 30 to 50 km in the modeled profile, where the sedimentation rates were the highest (up to 19 $kg \cdot m^{-2} \cdot yr^{-1}$), excess pore pressures reached 7 MPa (

Fig. 4.16). From 2.7 to 1.5 Ma, excess pore pressures increased all along the margin. At ~1.5 Ma high excess pore pressures have developed in most of the deeper areas. Higher values occur again at the left part of the modeled profile, coinciding with the basement depression and favoring a depocenter formation (between 30 to 50 km) (

Fig. 4.16). In this area, excess pore pressures reach 25 MPa at 1.5 Ma. At the same time, overpressures increased up to 0.2 at the shelf and 0.3 off the shelf edge. However, the shallower thousand meters of the entire margin depict values below 0.1. The accumulation of low permeability marine sediments at relatively high sedimentation rates (particularly after onset of glacial sedimentation on the shelf and upper slope), of up to 45,7 $kg \cdot m^{-2} \cdot yr^{-1}$ has a clear impact on the development of excess pore pressure and fluid flow patterns developed on the continental margin.

Overpressures started to increase in shallower depths (above 1000-1500 mbsf) from unit R4A age (~990 ka), when onset of till sedimentation on the shelf (NE part) occurred. The coupling between excess pore pressures and overpressure,

observed in previous stages, is partially detached from 780 ka (age of R4 reflector) to Present.

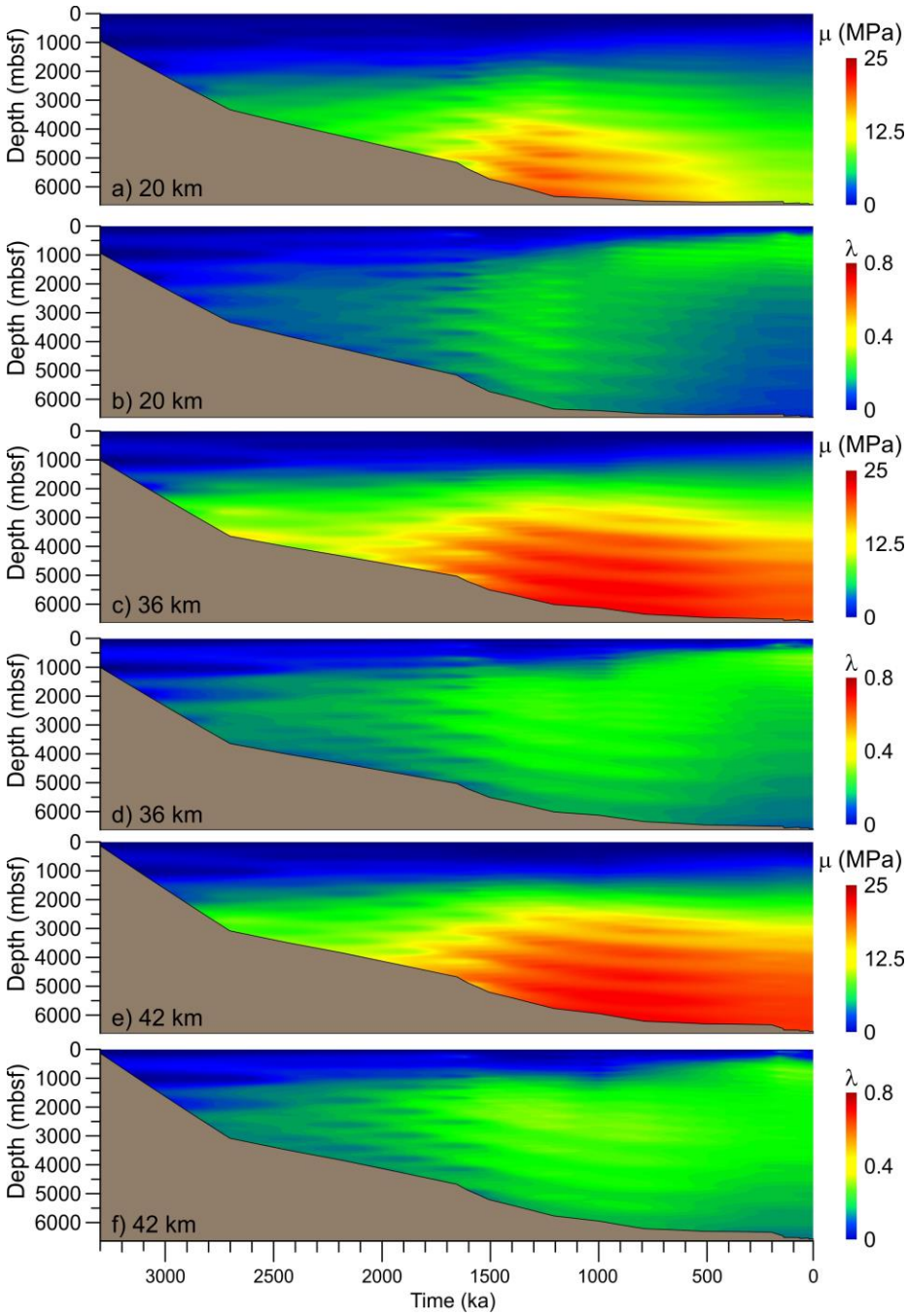

Fig. 4.16 Time vs depth evolution of excess pore pressures (a, c and e) and overpressures (b, d and f) at the synthetic observation wells located at 20 (shelf), 36 (shelf edge) and 42 km (upper slope) along the model (see Fig. 4.14 for location).

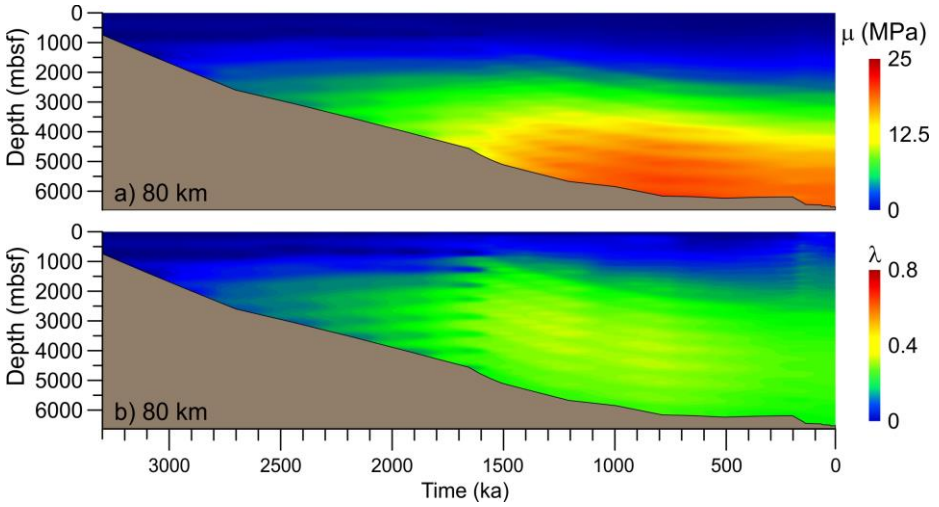

Fig. 4.17 Time vs depth evolution of excess pore pressures (a) and overpressures (b) at the synthetic observation wells loctaed at 80 km (lower slope) along the model (see Fig. 4.14 for location).

Whereas from the shelf to the middle slope overpressures sharply increased in shallower depths (above 1500 mbsf), excess pore pressures show only a gradual increase of 1-3 MPa (

Fig. 4.16). In turn, in the distal area, excess pore pressures experienced a decrease around 5-10 MPa (Fig. 4.17a). This contrasting behavior of excess pore pressure between slope and distal area is related to an increased deposition of glacigenic debris flows sediments on the slope and decreased sedimentation rates in the SW part. On the other hand, the overpressures increase is more pronounced at the shelf edge and upper slope area, than in the distal part. Due to the predominant low porosity and low permeability sediments (tills and GDFs) and the low lithostatic load at shallow depths, the resulting overpressures around

the shelf edge area and upper slope reached values of 0.4 at the end of deposition of unit R2 (220 ka), even though excess pore pressures increase with depths (

Fig. 4.16a).

From reflector R1 to Present (units G to A_1), sedimentary patterns, thickness and sedimentation rates are better constrained than in previous units (see results presented in Chapter 4). Porosity and hydraulic conductivities were in the range of 0.08-0.2 and 10^{-11}-10^{-9}, respectively, in most of the model. Only in the shallowest units (few tens of meters below sea floor) sediment physical properties were further affected by the accumulation of the new sediments. Contrasting compressibility and permeability between glacial and interglacial sediments are clearly reflected in the model results. During deposition of glacial units F and D, overpressures increased noticeably in shallower units (above 300 mbsf), whereas during deposition of deglacial and interglacial sediments overpressures decreased. Middle to high overpressures developed at the shelf edge/upper slope and middle slope areas with values up to 0.6 (

Fig. 4.16b, d and f). Also, the predominantly hemipelagic sediments of the lower slope developed overpressures during glacials, with values up to 0.4 (Fig. 4.18b). These values compared to the overpressures of 0.1-0.15 at the end of interglacial periods E and C, suggest that during the deglacial-interglacial overpressures dissipated by ~75% mainly at shallow depths (above 300 mbsf).

At the end of the Last Glacial Maximum most of the margin is dominated by overpressures ranging between 0.4 and 0.6. In the first hundred meters below the sea floor, overpressures were around 0.35-0.45. Only in the shelf edge area, overpressures reached values ~0.58 at shallow depths, while in the inner shelf overpressures were lower (~0.35).

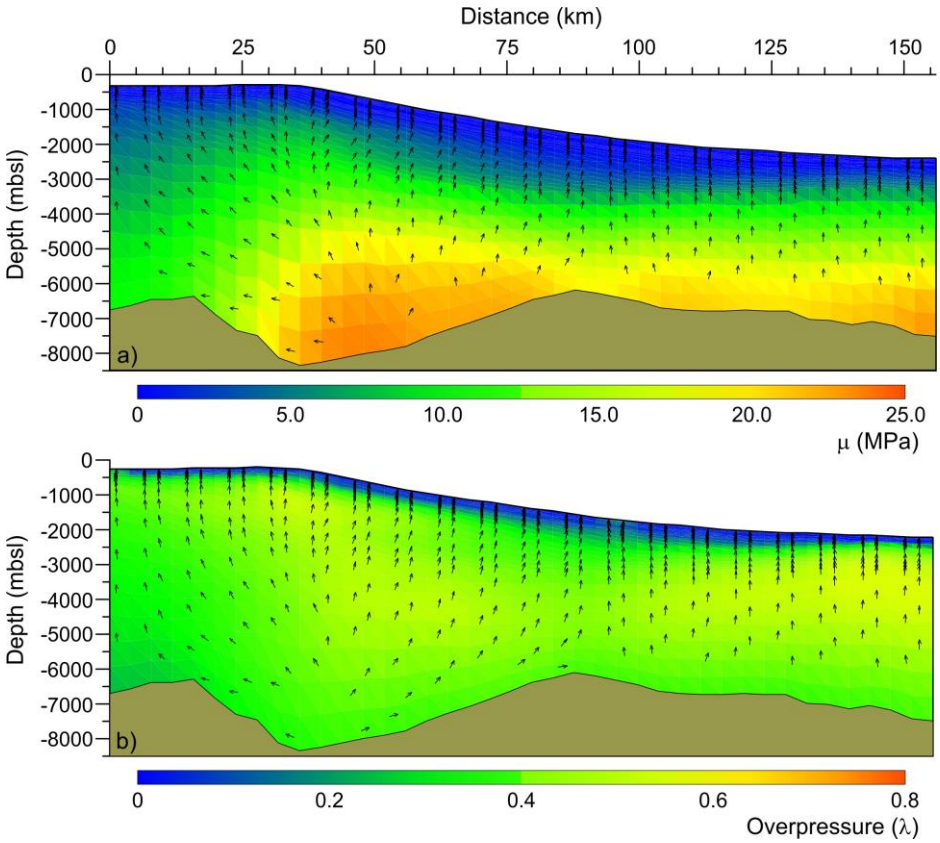

Fig. 4.18 Margin Present day conditions. a) Excess pore pressure (MPa). b) Overpressure (λ).Vertical exaggeration 7:1.

From 19.5 ka to 13 ka, i.e. during the last deglaciation, overpressures decreased about 10% in the shallower 300 m. Only a few tens of meters right below the sea floor the model shows the same overpressure values (~0.4) than at the end of the

LGM. At these shallow depths, overpressures continued to decrease during the Holocene until values below 0.1 at Present day (Fig. 4.18b). Below 300 mbsf, overpressures are maintained between 0.2-0.4 in most of the margin.

In general, Present day excess pore pressures are lower than 12 MPa in the entire margin, whereas deeper sediments of the main depocenter and the distal part of the margin show values up to 22.5 MPa (Fig. 4.18a). At shallow depths (above ~300 mbsf), excess pore pressures are lower than 5 MPa, except right below the shelf edge, where the occurrence of a depocenter has major influence.

4.2.2.2 Plaxis model

The facies distribution along the Storfjorden TMF is well constrained from the seafloor to reflector R1 (Chapter 4.1.1), but not deeper. The Plaxis software has been used to model the margin evolution from R1 to Present. As pointed above, the Plaxis model setup is based on the same margin stratigraphy and sediment geotechnical properties as the BASIN model. To guarantee the computation stability while increasing the resolution of the FEM and therefore of the output results, the model has been shortened to the northeasternmost 60 km and up to 2200 mbsl. Thus, a fluid flow time dependent boundary condition at the base of the model has been set by using the output from BASIN (Fig. 4.19). This model base or 'basement' is set to the R4A reflector. Its position in the Plaxis model setup is set to its Present day position in the margin. Therefore no compaction and/or subsidence are considered below R4A.

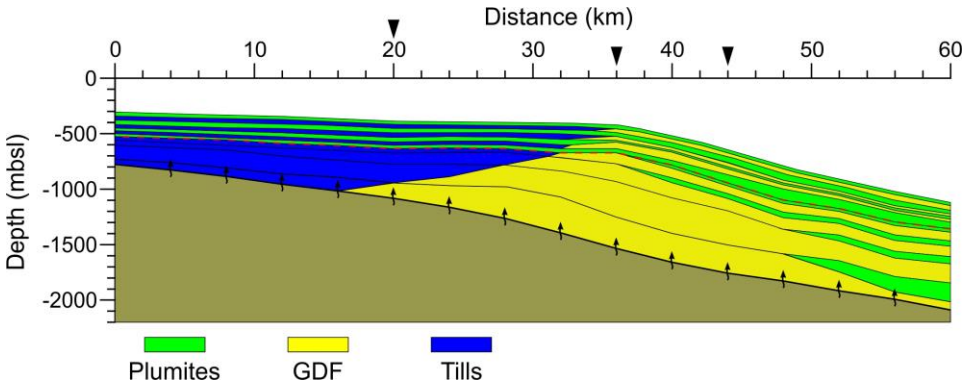

Fig. 4.19 Present day margin stratigraphy and facies distribution used in the Plaxis model setup. Such model setup is based on the seismic units described in Chapter 4. Vertical exaggeration 4:1. Red dashed line depicts reflector R1. Black line with arrows depicts flow boundary condition at reflector R4A. Top inverted black triangles mark the location of synthetic observation wells.

The model requires an initial steady-state phase for the material below reflector R4A that allows the onset of deposition in the following phases with the fully coupled flow-deformation analysis. The sedimentation of the units involved in this setup starts at 1.2 Ma (age of R4A). GDFs and tills extend over the shelf towards and upper slope up to reflector R1 (0.22 Ma). From that reflector to Present, layer composition in the simulation is in agreement with the stratigraphic setting identified in Chapter 4.1.1. During Inter-Glacial Maximum (IGM) periods, the deposits consist almost entirely of plumites, while during Glacial Maximum (GM) periods, plumites are replaced by tills along the shelf and GDFs are deposited along the slope. Replacement of plumites by tills along the shelf reproduces erosion of the underlying sediments and deposition of deformation tills during ice stream advance. In order to visualize the model evolution through time, parameters are logged at three positions: shelf (20 km), shelf break (36 km) and upper slope (42 km) (Fig. 4.19). These points have been

positioned so to coincide with the same wells than in the BASIN model in order to compare the results in both models. Because Plaxis computes pore pressures after the first initial time step (1.2 to ~1.1 Ma), the modeled pressures evolution starts at 1.1 Ma. Sediment physical properties (i.e. porosity and permeability) are clearly controlled by the consolidation due to overburden. Therefore, from 1.2 to 0.22 Ma porosity and permeability decrease with depth with the lower values located at the shelf where tills are the prevailing sediment type.

During sedimentation of unit R4A (1.2 to 0.99 Ma) pore pressures remain nearly hydrostatic. It is not until deposition of unit R4 (990 to 780 ka) that excess pore pressures and overpressures started to develop. These excess pore pressures and overpressures were mainly focused in deeper areas below the shelf with values up to 1 MPa (Fig. 4.20a). Overpressures started to increase subtly in the slope around 900 ka but values remained below 0.15 (Fig. 4.20d and f). Deep below the shelf, however, overpressures reached 0.35 (Fig. 4.20b). A progressive trend of increasing overpressure is seen until 220 ka, when deposition of unit R2 is completed. After reflector R1 (220 ka), the alternation between GM and IGM units is clearly reflected on the pore pressures evolution. Along the shelf, excess pore pressure increased in the entire sedimentary column even though values

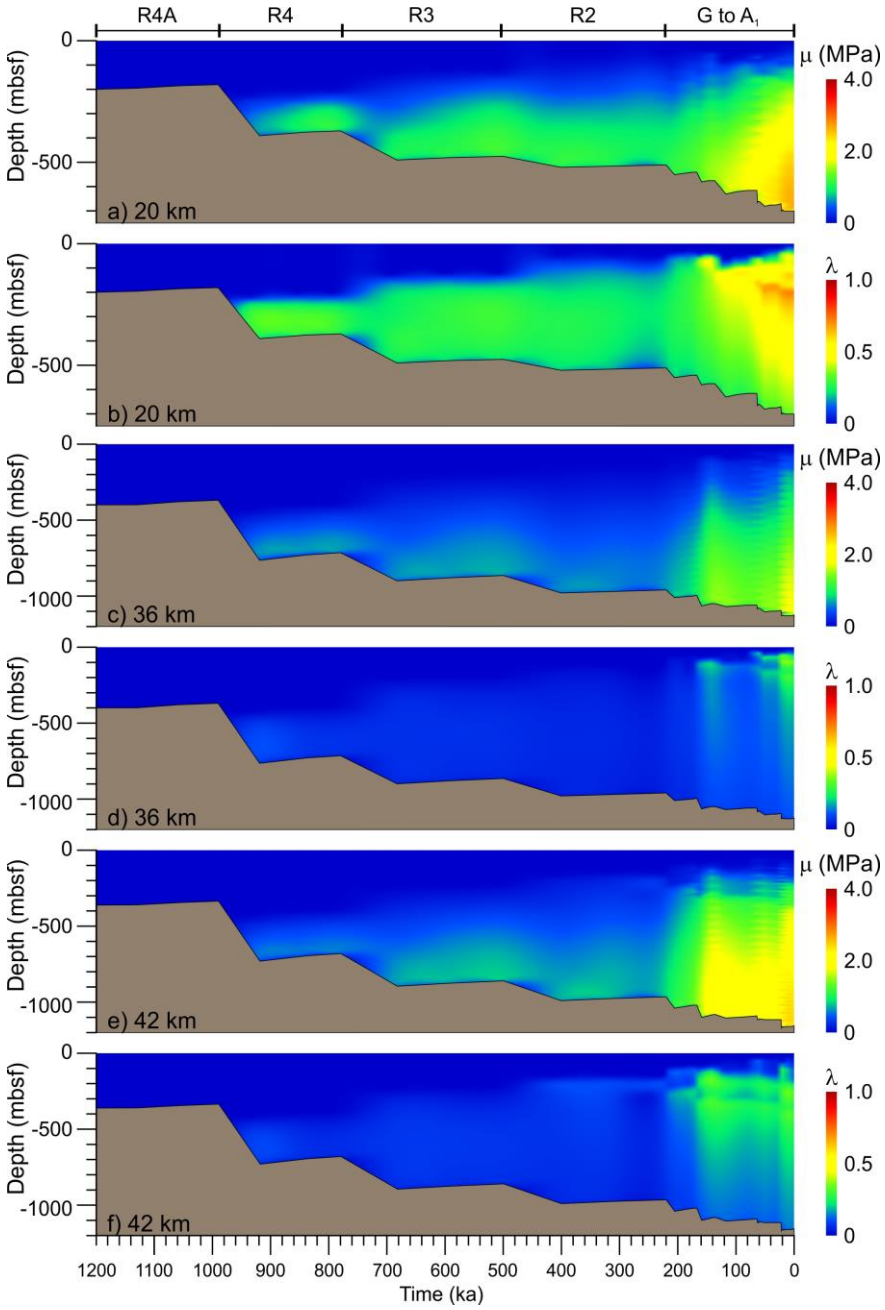

Fig. 4.20 Time vs depth evolution of excess pore pressures (a, c and e) and overpressures (b, d and f) at the synthetic observation wells located at 20 (shelf), 36 (shelf edge) and 42 km (upper slope) along the model (see Fig. 4.19 for location).

above 2.0 MPa occur only during the glacial deposition of units D and B (64-60 ka and 22.5-19.5 ka) (Fig. 4.21a, c and e). At the shelf edge, the maximum excess pore pressure throughout the simulation (~3 MPa) occurs below 450 mbsf during the LGM. Such excess pore pressure is maintained to Present (Fig. 4.21c.). Even if excess pore pressures higher than 1 MPa are located below 100-200 mbsf in the entire model, the increase in excess pore pressure at the shelf is more gradual compared to the shelf edge and upper slope, where the evolution is rather jagged. The increase in excess pore pressure during deposition of unit F (a GM unit) has almost dissipated at the time of deposition of unit D (the second GM unit). Conversely, at the beginning of deposition of unit B, the LGM, excess pore pressures higher than 1.5-2 MPa had been preserved below 350 mbsf along the shelf and middle slope.

In terms of overpressure, the highest overpressures from R1 to Present day developed along the shelf with values up to 0.7. In turn, the shelf edge area records lower overpressure than the middle slope. Along the shelf, bands of till sediments with high overpressure are depicted above 200 mbsf during the last 60 kyrs (Fig. 4.21b). The deepest of these bands started to develop high overpressures during the deposition of unit F (167 ka) and has been later maintained through time. The high sedimentation rates during the GM (up to 45 $kg \cdot m^{-2} \cdot yr^{-1}$) and the low permeability of the already deposited tills might cause this overpressure increase. In addition, the deposition of unit D, between 64 and 60 ka, produced significant overpressure from the previous GM to Present.

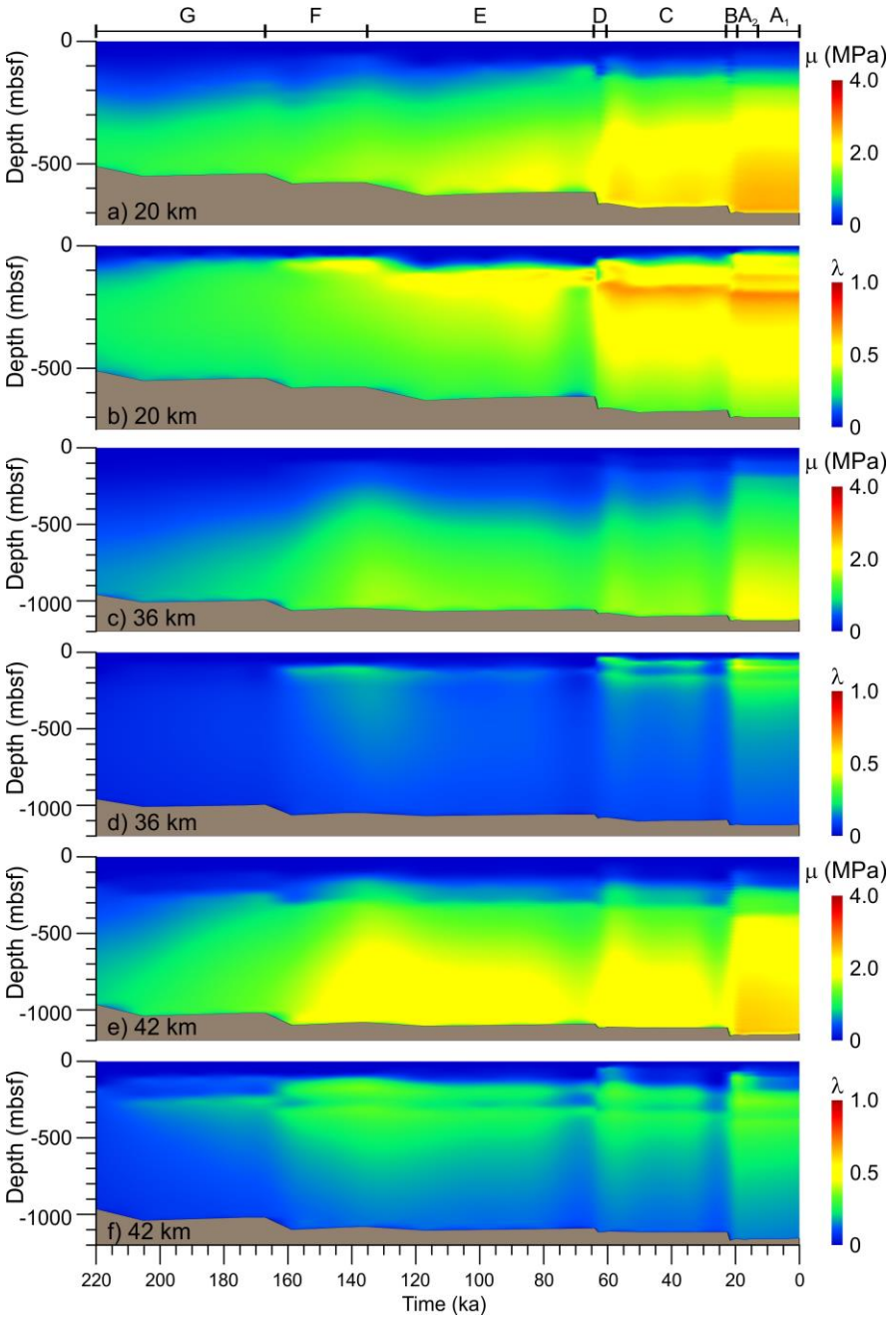

Fig. 4.21 Close-up view of time vs depth evolution of excess pore pressures (a, c and e) and overpressures (b, d and f) at the synthetic observation wells located at 20 (shelf), 36 (shelf edge) and 42 km (upper slope) along the model (see Fig. 4.19).

While overpressures almost dissipated at the shelf edge and middle slope during the deglacial and interglacial periods with a rate around 0.02 $kyrs^{-1}$, did not at the shelf (Fig. 4.21b, d and f). From the LGM onwards, overpressures higher than 0.35 (up to 0.5 at the shelf) developed at depths above 40 mbsf at the shelf and shelf edge, as well as around 70 mbsf in the middle slope area. The layering of higher and lower overpressures is more pronounced in the porosity and permeability fields (Fig. 4.22). Although a porosity and permeability decrease with depth is shown, as it would be expected in a margin where porosity reduction is driven by normal consolidation, at shallow depths it is clear that areas of alternating high and low porosity and permeability are depicted. The low porosity/permeability bands have two orders of magnitude lower hydraulic conductivity than the sediments immediately above and below them (Fig. 4.22b, d and f). However, porosity variations are less evident (Fig. 4.22c and e). They correspond to the tills on the shelf and GDF on the slope that started to deposit at 167 ka.

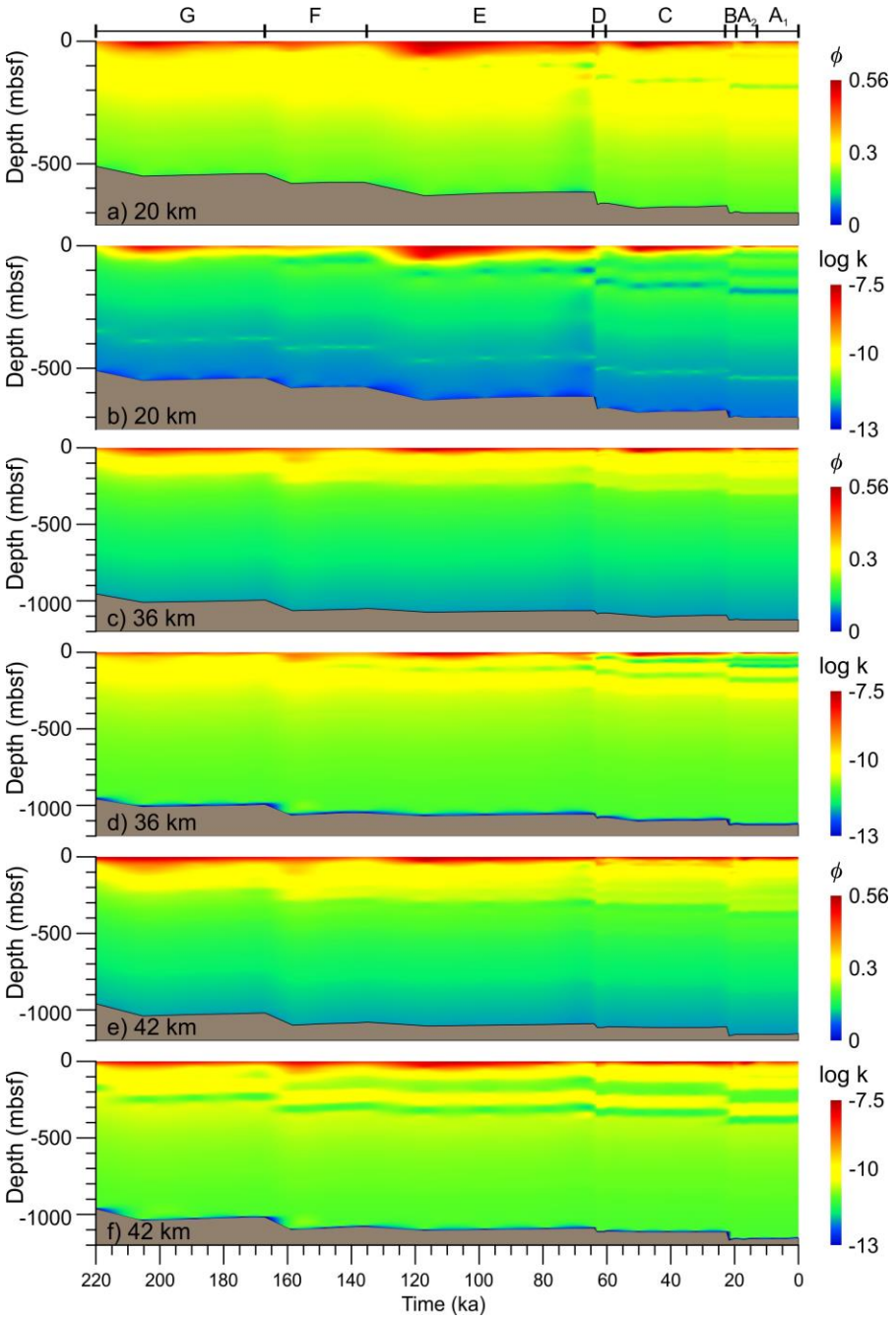

Fig. 4.22 Close-up of time vs depth evolution of porosity (a, c and e) and hydraulic conductivity (m/s) (b, d and f) at the synthetic observation wells located at 20 (shelf), 36 (shelf edge) and 42 km (upper slope) along the model (see Fig. 4.19).

Although excess pore pressures partially dissipated all along the margin during the last deglacial and Holocene, values above 1 MPa are still expected nowadays around 100-150 mbsf (Fig. 4.23c). Also, mid to high overpressures are expected along the shelf and the shelf edge below 40-50 mbsf. This wedge-shaped area with overpressures up to 0.75 is clearly related to the units where tills are the predominant lithology (Fig. 4.23d). The tills develop low hydraulic conductivity, with values around 10^{-12} m/s in the shelf sediments. Expected Present overpressures are lower in the upper slope, where they may attain values of 0.15 in the first 40-80 mbsf, than below the shelf. On the other hand, overpressures are pretty homogenous in the middle slope area below ~200 mbsf, although some not very defined layering is also observed. The porosity and hydraulic conductivity fields there, shows that the units made of plumites display lower porosity and hydraulic conductivity at depth. Such low porosity and hydraulic conductivity at depth is due to the higher compressibility of these sediments compared to the surrounding GDFs (Fig. 4.23c and d). This higher compaction due to the GDFs deposition causes a rapid discharge of the pore water and a final slightly lower overpressure, and lower porosity and permeability of the plumites layers.

The fluid flow driven by the pore pressure field is mostly vertical, as it is normally expected for a continental margin where self-weight consolidation predominates. However, at some specific locations along the model the pattern

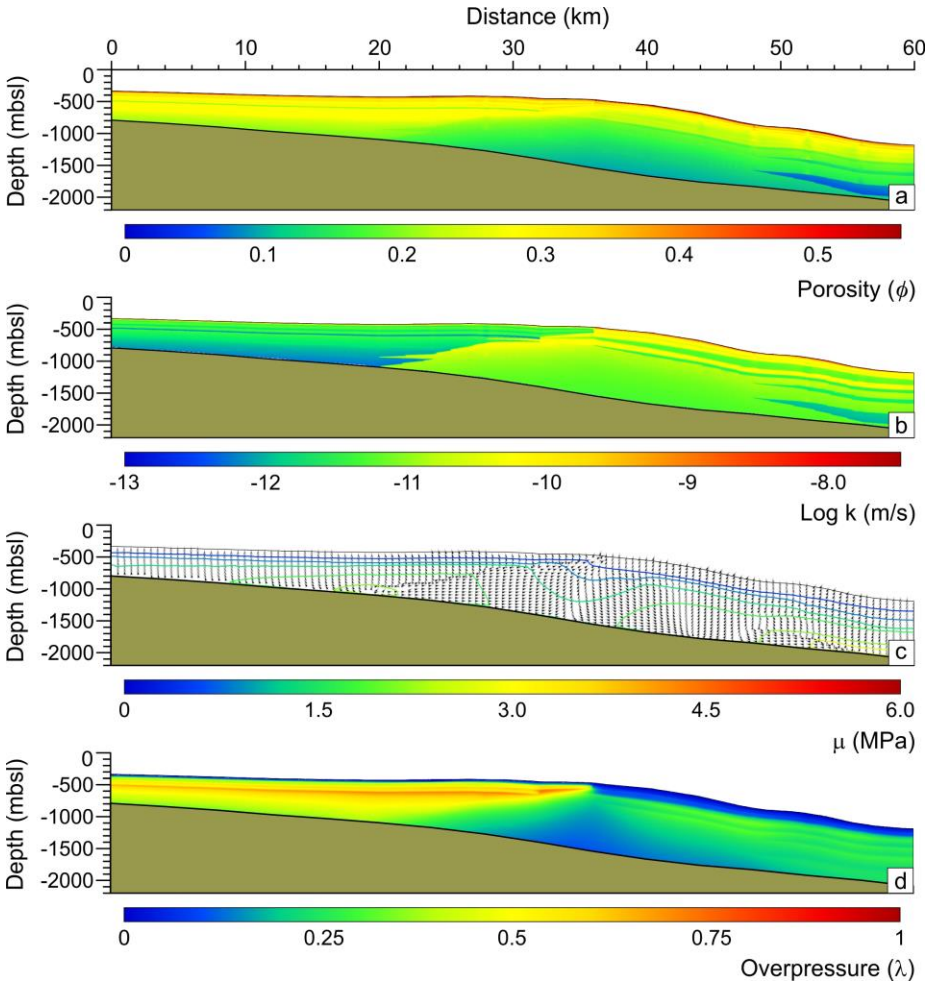

Fig. 4.23 Margin stratigraphic and hydrodynamic modeling with Plaxis at final simulated Present day. a) Fractional porosity. b) Log hydraulic conductivity (m/s). c) Excess pore pressure (MPa) and fluid flow (max $1.81e^{-11}$ m/s). d) Overpressure (λ).

differs from the usual upward flow. The clearest example is the low permeability till sediments on the shelf, which divert fluid flow towards the shelf edge. In this area, the fluid discharge is up to three orders of magnitude higher than in the shelf and two orders of magnitude higher than in the middle slope. This causes high shallow overpressures up to 0.7 at the upper slope in the few tens of meters below the sea floor. This fact is depicted by a thin layer with overpressures 0.15

higher than the surrounding sediments (Fig. 4.21d). In addition, the low porosity and permeability plumite units, when buried at depth in the middle slope, divert fluid towards the upper slope.

4.2.3 Models comparison

Two software have been used to model the evolution of Storfjorden Trough Mouth Fan. The combined use of the two models provides complementary information on the Storfjorden TMF hydrogeological evolution from the initial growth (2.7 Ma) to Present. BASIN is mainly focused on the understanding of the long-term evolution of the margin since 2.7 Ma, while Plaxis in the most recent 220 kyrs. BASIN is limited in the number of sediment types, up to four, and in the maximum number of elements in the horizontal direction (40). Such a number of elements for a model of 160 km results in a cell size of 4 km. Therefore, the results for models containing relatively thin layers might be questionable. In contrast, Plaxis allows a higher computational load, although there are restrictions to the size of the model that can be implemented. Therefore, in Plaxis the model has been shortened in space and time. Nevertheless, the resolution obtained in Plaxis shows local effects that are not depicted by BASIN as bands of low and high porosity/permeability or abrupt increase of overpressures right at the beginning of a GM.

Both software establish coincident fluid flow patterns along the margin and areas affected by moderate to high overpressures. However, there are slight differences

between the two models. These differences are mainly located in the continental shelf area. There, Plaxis model shows overpressures 0.35 higher than BASIN in the last ~150 kyrs. These differences are likely associated to the BASIN elongated finite cell elements of units F to A_1 that led to inaccurate results even though they satisfy a low error tolerance (0.00000001 in Fehlberg4, see Bitzer, 1996). The porosity and permeability evolution show the same pattern in both models, although the Plaxis model clearly depicts the differential evolution of the units G to A_1, deposited during the last 220 kyrs, made of alternating tills and plumites. The difference in the definition of the layer composition could be at the origin of these discrepancies. In the BASIN model the layers below unit G have a smooth transition from one sediment type to another while in Plaxis this transition is sharp. This may play an important role in pore pressures dissipation mainly at the shelf edge area. Thus, fluid expulsion potential in the BASIN layers (below unit G) is higher due to the transition from lower to higher porosity/permeability sediments (i.e. tills to GDFs/plumites).

The higher resolution of the Plaxis model, therefore allows us to understand in detail the role of each sediment type in the margin hydrogeological evolution. This fact combined with the higher confidence in the results of the last 220 kyrs, confers more reliability to Plaxis model.

The results obtained indicate that BASIN is reliable to investigate thick sedimentary sequences deposited during long time spans, while Plaxis is more reliable for rather detailed short-term studies. Nevertheless, both are

complementary. BASIN software computational time is in the range of a few minutes while Plaxis is in the range of hours. Therefore, BASIN is useful to provide the long-term evolution results (i.e. fluid flow) as boundary conditions for Plaxis model.

Chapter 5
Discussion

Chapter 5. Discussion

5.1 Interpretation of acoustic facies and seismic units

Using the cores collected in the Storfjorden trough and TMF, the uppermost seismo-stratigraphic units can be correlated to sedimentary lithofacies. The uppermost subunit A_1 is characterized by a poorly laminated and bioturbated mud in sedimentary cores and it is interpreted as Holocene interglacial sediments (Lucchi et al., 2013, 2012). The high-amplitude well laminated A_2 subunit is characterized by finely laminated mud interbedded with sandy layers and it is interpreted to result from meltwater sediment-laden plumes induced by lift-off and rapid retreat of the ice sheet during deglaciation of the margin. Because the acoustic character of unit A_2 is very similar to that of units C, E and G, we interpret those to be formed under similar environmental conditions and to correspond also to meltwater plumites. The top of the transparent unit B has been sampled in core SV-02 and is characterized by highly consolidated diamicton. Unit B has been interpreted as a series of amalgamated glacigenic debris flows (GDFs), which were deposited during glacial maxima (Pedrosa et al., 2011). The GDFs originated from glacigenic sediments dumped over the shelf edge as this sediment was being pushed by the ice streams (see also Laberg and Vorren, 1995). GDFs of unit B have low water content (~23%) and high shear strength (~40 kPa) compared with the sediments of unit A that have water contents ~45% and shear strengths ranging between 2 and 12 kPa. The hemipelagic sediments of

unit A_1 and plumites of unit A_2 are found both on the slope and continental shelf, while GDFs on the slope grade into transparent units on the continental shelf. These transparent units on the shelf have a more tabular character and a distinct morphological expression with respect to the transparent units of the slope. Amongst the features associated with these shelf transparent units are linear to curved furrows and sets of larger-scale parallel lineations (Fig. 4.8). From these characteristics and sedimentary facies on core GeoB17610-2, we interpret the transparent units on the continental shelf as a series of ice front and basal deformation tills. On the shelf, we identified three till units (T_B, T_D, T_F). These tills grade laterally, across the shelf edge, into units B, D and F respectively (Fig. 4.4). Erosion during ice stream readvance over the shelf may partially or completely erode older till units. An additional T_α unit, much thinner, located just below unit A_1, has been mapped along a few lines on the Storfjorden shelf but could not be confidently correlated through the shelf edge with unit α.

Cores SV-03, SV-04 and SV-05 (Fig. 4.1) sampled the transparent bodies on the slope associated with scarps and frequent lateral erosive boundaries cutting into units A and B. These sediments are diamictons characterized by high water content and relatively low bulk density when compared to the GDF of unit B. These diamictons have been identified as debris flows associated with submarine landslides. They respond to the dynamics of the slope rather than to processes originating in the continental shelf, as in the case of GDFs. Most of the landslides are located at the confluence of the Storfjorden and Kveithola TMFs

and have an acoustically laminated unit at their base and either are devoid of sediments or have another laminated unit at their top.

5.2 Glacial dynamics of the Storfjorden paleo-ice stream

The relative high-density of high-resolution seismic reflection profiles available in the area provides a unique opportunity to understand the detailed history of sediment delivery from the Storfjorden and Kveithola paleo-ice streams to the respective TMFs. Such sediment delivery was highly variable in space and time (Fig. 4.10). Subunit A_2, a deglacial unit largely corresponding to meltwater plumites, displays a thicker sediment package to the south of the Storfjorden TMF (lobe III; Fig. 4.5) and on the Kveithola TMF. On the other hand, unit B corresponding to GDFs deposited during the Last Glacial Maximum shows thicker sediment accumulations in the north and central part of the Storfjorden TMF. The isochore map of unit B displays a radial pattern spreading from the shelf edge, which results from the presence of GDF downslope elongated lenses. These GDF lenses are comparatively thicker than the other lenses within the unit in the northern and central TMF or they occur as isolated lenses within the bounding laminated units in the southern TMF. Such distribution indicates that individual sedimentary bodies within the transparent unit originate from the shelf break and are transported downslope to the mid-slope (Fig. 4.10b). Seismic records where previous units can be imaged, suggest that deglacial and glacial maximum related units display a similar distribution pattern to units A_2 and B

respectively. The thicker GDF units in the northern fan area significantly contributed to shelf edge progradation from R1 time to present. In lobe I this progradation is around 6 km while in the southernmost lobe III it is just 2.2 km. The difference in progradation and better developed GDF units supports the idea suggested by Pedrosa et al. (2011) that, to the north, the Storfjorden ice stream had thicker and perhaps faster ice. Alternatively, the northern sub-ice stream I could have transported a higher sediment load from drainage of a distal and larger ice source. Two shallow banks on the outer shelf of lobe I (60-70 m above the surrounding shelf) (Fig. 5.1) could have provided an anchoring area for the ice stream in the northern sector. In turn, lobe III and the Kveithola Trough could have slower and thinner ice within the ice stream that was fed from a smaller catchment area in Spitsbergenbanken, therefore preventing more significant erosion and supply of sediment to the shelf edge in the form of GDFs.

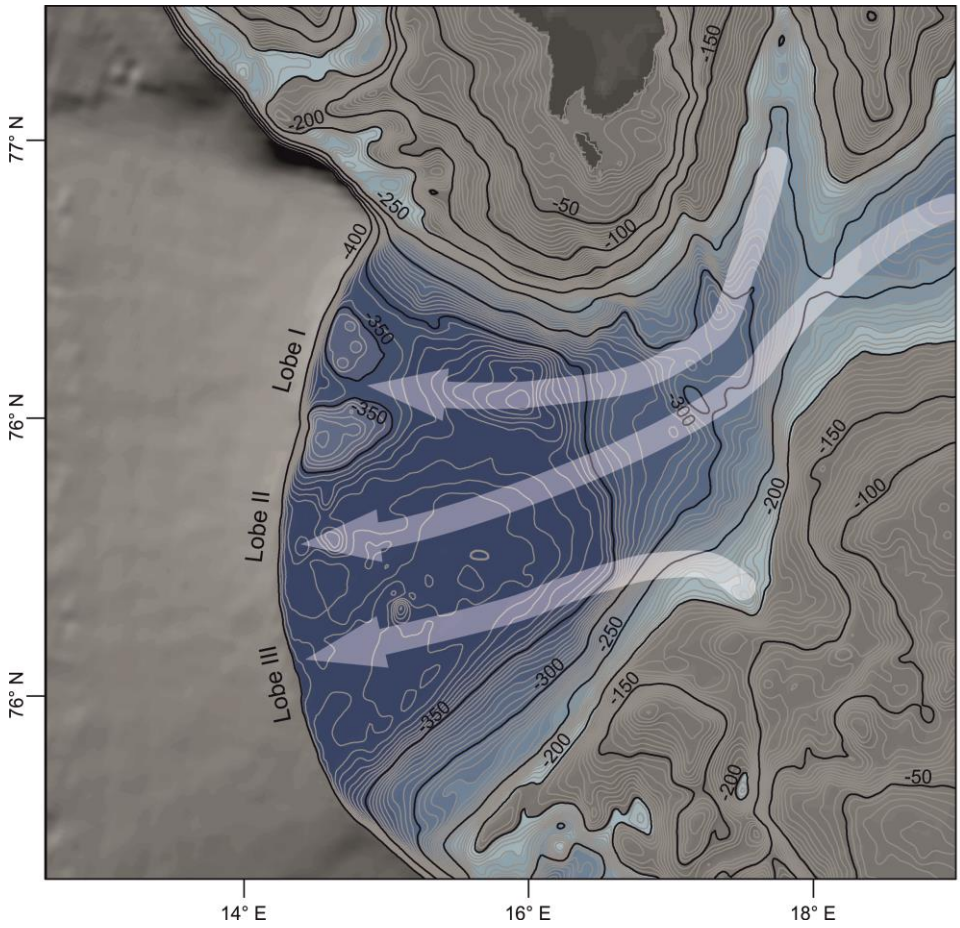

Fig. 5.1 IBCAO bathymetric data showing of the Storfjorden trough (Jakobsson et al., 2012). The two shallow banks in the lobe I area are shown. White arrows tentatively depict the ice streams pathways.

The thinner "laminated units" in the northern and central lobes suggest also that the last deglaciation of Storfjorden was relatively rapid. The outer Storfjorden Trough is devoid of laminated units such as those found in the TMF, however the Kveithola Trough hosts a 15 m thick glacimarine sequence inferred to have

been deposited during the last deglaciation (Bjarnadóttir et al., 2013; Rebesco et al., 2011). This suggests that there was significantly higher sediment availability in the Kveithola system during the deglaciation, likely because a marine-based ice cap remained closer to or sitting on the shallow banks surrounding the Kveithola Trough. Plumites were possibly funneled through the narrow Kveithola Trough and redistributed along the Kveithola TMF and may possibly have been drifted to the southern Storfjorden TMF by the WSC.

Meltwater discharge from underneath an ice sheet grounded at the shelf edge may have also contributed to gully formation (Gales et al., 2013; Lucchi et al., 2013; Noormets et al., 2009; Pedrosa et al., 2011). The fact that some gullies are often draped by unit A_1 (Holocene sediments) and in some instances they even have some A_2 infill (Fig. 4.3), suggest that they were formed synchronous with plumite deposition. Preferential occurrence of the gullies in the northern and central part of the Storfjorden TMF suggests that the meltwater discharge was more intense and again points to a faster ice-stream retreat in the northern part of the trough.

5.3 Storfjorden TMF chronostratigraphic framework

Eight units have been mapped above regional reflector R1. These units involve the same time interval as units B to G of Sættem et al. (1994, 1992), units III to VIII of Laberg and Vorren (1996a) in the Bear Island TMF, and units C to G of Laberg and Vorren (1996b) in Storfjorden (Fig. 5.2). They all belong to the

megasequence GIII of Hjelstuen et al. (1996) (Table 5.1). Nevertheless, there is significant variability in the ages proposed for the different units largely owing to the various dating methodologies. Laberg and Vorren (1996b) used the land record (Mangerud and Svendsen, 1992) as well as correlation to the oxygen isotope curve of Williams et al. (1988) to constrain the age of their units E, F and G (Fig. 5.2). These units respectively match the Marine Isotopic Stages (MIS) 2, 4 and 6 (Hao et al., 2012; Lisiecki and Raymo, 2005). Mangerud et al. (1998) also suggested that 4 major ice advances occurred over the Western Svalbard shelf (Fig. 5.2). Their glaciations G, E and A respectively correspond to our glacial units B, D and F.

In this study, we propose an age model for the observed units in the Storfjorden and Kveithola TMFs that takes into account ages reported in the area (Laberg and Vorren, 1996b; Mangerud et al., 1998) as well as dating of the SVAIS and EGLACOM sediment cores (Lucchi et al., 2013; Sagnotti et al., 2011) . The basis for our age model are the AMS ^{14}C dating of the boundary between units A and B on cores SV-02 and SV-05, representing the transition from the LGM to deglaciation, at 18-20 ka cal BP.

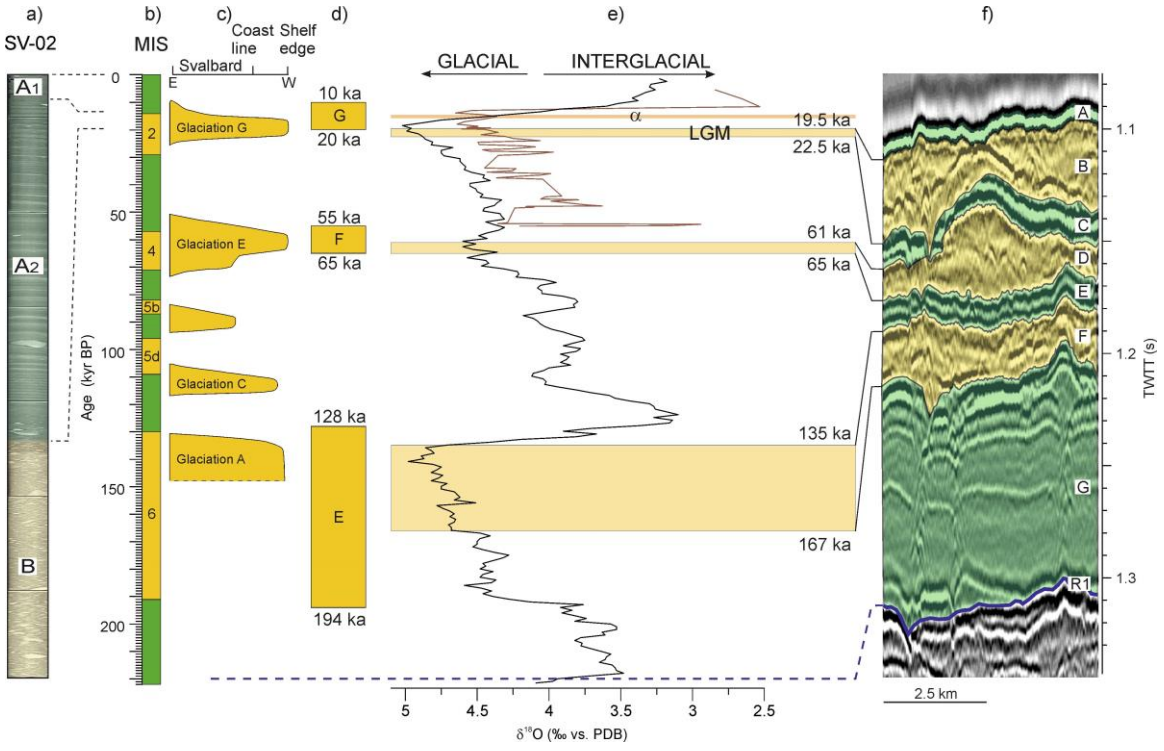

Fig. 5.2 Proposed age model of the different GM (shades of yellow) and IGM (shades of green) units. a) Core SV-02, b) Marine Isotopic Stages (Lisiecki and Raymo, 2005), c) advance over the shelf of the western Svalbard ice sheets (Mangerud et al., 1998), d) age estimates of glacigenic units based on correlation to the Svalbard land record (Laberg and Vorren, 1996b), e) proposed ages in this study, black line: δ^{18} oxygen isotope curve for a world composite of 57 cores (Hao et al., 2012; Lisiecki and Raymo, 2005), red line: δ^{18} oxygen isotope curve of core M23385 (see Fig. 4.1), f) seismic stripe from line SVAIS06 of full studied period.

These dates are in agreement with those of Andersen et al. (1996) and Mangerud et al. (1998) indicating that, the ice sheet in the Svalbard-Barents Sea retreated from the outer shelf earlier than 17.7 ka BP. Jessen et al. (2010) and Rasmussen et al. (2007) also point that the Storfjorden ice stream had retreated at least 35 km from the shelf edge at 19.2 ka BP. These dates are also in agreement with the scenario outlined by Bjarnadóttir et al. (2013) in the Kveithola Trough, documenting the onset of deglaciation between 21.5 and 19 cal ka. The Kveithola Trough is much smaller and slightly shallower than Storfjorden and the ice source, in Spitsbergenbanken, is also closer to the trough, which resulted in slightly lower retreat rates than in Storfjorden (Bjarnadóttir et al. (2013); Fig. 4.1). Because the passage from the acoustically transparent unit B to the laminated unit A in SVAIS cores involves the transition from the LGM to the deglaciation phase, we infer that all passages from acoustically transparent to laminated units represent the transition from previous glacial maxima to the deglaciation phases. In this study we combine the 57 $\delta^{18}O$ worldwide composite record of Lisiecki and Raymo (2005) and Hao et al. (2012) with the $\delta^{18}O$ record from core M23385 (Dokken and Hald, 1996), located around 135 km off the Storfjorden shelf edge at 2498 m water depth (Fig. 4.1 and Fig. 5.2), to constrain the ages of units B, C, D, E, F and G. Since the deglacial and interglacial sediments inside previous laminated units cannot be properly separated in the seismic record, we choose to divide the sequence into Glacial Maximum (GM) and Inter-Glacial Maximum (IGM) periods, the latter corresponding to the

deglaciation/interglacial/onset-of-glaciation interval, rather than the classical glacial/interglacial periods. Onset of the last deglacial sedimentation in the Storfjorden TMF, according to the SVAIS cores, starts 5 kyrs earlier than the transition from MIS 2 to 1 (Fig. 5.2). For preceding glacial maxima, we therefore tentatively estimate the onset of deglacial sedimentation 5 kyrs earlier than transition from a "cold" to a "warm" MIS (Fig. 5.2, Table 5.1).

The seismic record indicates the existence of a minor GDFs event (unit α) within unit A_2. Unit α possibly correlates with a deformation till Tα on the northern shelf record (Fig. 4.2). The existence of a massive IRD layer within already IRD-rich bioturbated sediments has been associated with Heinrich layer H1 (16.8 cal. ka BP) (Lucchi et al., 2013). From its stratigraphic position unit α most likely correlates also to Heinrich layer H1, indicating a short-lived re-advance of ice sheets on the shelf south of Svalbard similar to the one that occurred in Kveithola between 16-15.5 cal. ka (Bjarnadóttir et al., 2013).

With regard to the onset of glacial maximum sedimentation (GDFs), we have no absolute ages for the time when ice streams reached the shelf edge in the Storfjorden and Kveithola Troughs at the beginning of the Late Weichselian glacial maximum. Recent studies indicate that the ice sheet reached the shelf break west of Svalbard at 24 ka BP (Jessen et al., 2010). South of Storfjorden, in Bjørnøyrenna, ice streams reached the shelf break around 22 ka BP (Landvik et al., 1998; Svendsen et al., 2004a). Available data therefore suggest that unit B,

Table 5.1 Correlation of seismic stratigraphic units in this work with those of previous studies in the western Barents Sea continental margin. See text for further discussion.

Western Barents Sea	Bear Island TMF				Storfjorden TMF						
**Faleide et al. (1996) #Butt et al (2000)	Sættem et al. (1992, 1994)		Laberg and Vorren (1996)		Hjelstuen et al. (1996b)	Laberg and Vorren (1996b)		This work			
	Unit	Age (ka)	Unit	Age (ka)		Unit	Age (ka)	Unit	Age (ka)	Mean compacted sed. rates (m/kyr) †	Mean decompacted sed. rates (m/kyr) †
								A_1	13-0	**0.1**	
	G	<30						α	~16.8*	**~5***	**0.6**
			VIII	24-12				A_2	19.5-13	**0.4**	
	F					G	20-10	B	22.5-19.5	6.9-**6.9**-7.0	17.6-**17.7**-18.1 (46.9)^
	E	130-?						C	61-22.5	**0.3**	**0.8**
	D_2	<200-130	VI	194-128		F	65-55	D	65-61	5.2-**5.4**-5.6	15.1-**15.7**-16.3 (35.1)^
								E	135-65	**0.1**	**0.3**
	D_1	<330	V	313-258		E	194-128	F	167-135	0.7-**0.7**-0.8	3.0-**2.1**-2.2(7.4)^
	C		IV	386-359							
R1<440 ka**, 200 ka#	B	<440	III	486-430	GIII (440 ka)			G	220-167	1.3-**1.4**-1.5	3.1-**3.5**-3.7

* Unit α is embedded within A_2.

† Minimum - **most probable** - maximum sedimentation rates respectively computed with a constant 1.5 km/s velocity, a p-wave velocity increasing with a 1.48 + 1.5z function (consistent with the overall velocity gradient for the upper 250 m in ODP Site 986) and a velocity increasing with a 1.5 + 2.13z function (consistent with the velocity gradient in the SVAIS piston cores). Minimum and maximum values are only plotted if they differed by one significant decimal with respect to the mean value.

^ Highest decompacted sediment rates during Glacial Maxima. computed with a p-wave velocity increasing with a 1.48 + 1.5z function.

corresponding to the Weichselian glacial maximum, was deposited from 22.5 ka BP. Therefore, the ice stream grounded at the shelf edge ~6 kyrs later than the start date of MIS 2. Based on this criterion, we estimate the onset of previous GM sedimentation (GDF) 6 kyrs later than the transition from a "warm" to a "cold" MIS (Fig. 5.2). In the case of unit F, onset of GDF sedimentation is made proportionally to the length of the glacial period (24 kyrs).

According to the aforementioned criteria, we propose that the GM units D and F are 61-65 ka BP and 135-167 ka BP, respectively (Table 5.1). The base of unit G corresponds to reflector R1. The ages proposed for reflector R1 are 700 ka BP (Vorren et al., 2011), 440 ka BP (Sættem t al., 1992, 1994; Faleide et al., 1996; Hjelstuen et al., 1996) and 220 ka BP (Butt et al., 2000; Knies et al., 2009; Rebesco et al., 2014). Because we find only three GM units above reflector R1 in the Storfjorden TMF area, we favor the 220 ka BP age, in agreement with Butt et al. (2000), Knies et al. (2009) and Rebesco et al. (2014).

Based on the proposed age model for GM units, the mean decompacted sedimentation rates are 2 to 18 kg m^{-2} yr^{-1} during glacial maxima (Table 5.1). Where the thickest sediment accumulations occur, the sedimentation rates during GM may reach values of 47 kg m^{-2} yr^{-1} (24 m/kyr for non-decompacted sedimentation rates). The mean sedimentation rates in between GM are very similar and one to two orders of magnitude lower than those of glacial maxima (Table 5.1). It is possible, as shown by Lucchi et al. (2013), that most sediment in IGM units accumulated in the short deglaciation phases. In this regard, the

sedimentation pattern during GM periods is much more punctuated and considering individual GDF lenses may lead to sporadic but much higher instantaneous sedimentation rates. It is clear from these data that the buildup of the Storfjorden TMF, and possibly of all major TMFs, occurs in short pulses during GM and, to a lesser extent during deglaciation. The somewhat lower sedimentation rates in the GM unit F, despite the potentially longer duration of glaciation may be explained from the dynamic behavior of the ice sheet, which could possibly be cold-based with less sediment transported subglacially (Cuffey et al., 2000; Winsborrow et al., 2010). In the case of the IGM unit G, the high sedimentation rates (3.5 kg m^{-2} yr^{-1}) compared to units A, C and E (0.3-0.8 kg m^{-2} yr^{-1}) may point to an older age of reflector R1. An age of 440 ka as suggested by Faleide et al. (1996), Hjelstuen et al. (1996); and Sættem et al., (1994, 1992), would yield mean sedimentation rates of 0.6 kg m^{-2} yr^{-1}, similar to the other IGM units. This would imply however, that 2 GM phases (units D and C of Laberg and Vorren 1996b) would have left no record in the TMF.

5.4 Control of TMF architecture on submarine slope failure and timing

It is known that high sedimentation rates, particularly in low permeability sediments, may induce excess pore pressure and subsequent slope instability (Dimakis et al., 2000; Lee, 2009; Micallef et al., 2009). This is often recorded as submarine landslides on continental margins. Given the high sedimentation rates

that the Storfjorden TMF experienced during glacial maximum periods, it is highly likely that excess pore pressure could cause the observed landslides (Fig. 4.7). However, we find that whenever the landslides have a younger unit on top, this unit is either an IGM unit (Fig. 4.5) or a fully preserved GM unit, suggesting that the landslides occurred during the deglaciation or subsequent interglacial period (Fig. 5.3a). Here we consider that landslides without cover (identifiable on TOPAS profiles) occurred after deposition of the deglaciation unit A_2, and sometime during the sedimentation of the present interglacial unit A_1.

Comparing the sedimentation rates of the different units with the volume and number of submarine landslides (Fig. 5.3b) shows that the number of landslides was highest after deposition of unit B, which also shows the highest sedimentation rates. However, there is very likely a bias in the number of landslides that can be observed in the most recent units, as those can be mapped from higher resolution data. Most (~75%) of the landslides have an IGM unit as the detachment layer suggesting that loading by GDFs built-up pore pressure in these water-rich sediments (see also Laberg et al. (2002) and Bryn et al. (2005b) for similar slope failure scenarios in formerly glaciated margins). Nevertheless, the largest landslides occurred after sedimentation of the GM units that showed lower sedimentation rates. PLS-2, the largest landslide in the study area (Table 4.1, Fig. 4.7) is located below unit E and affected units F (GM) and G (IGM), the latter being the thickest IGM unit above reflector R1. Most landslides are located in the inter-TMF area between Storfjorden and Kveithola where the IGM units

are also thicker. From this, we infer that the volume of the landslides (and perhaps the number) is not controlled by the sedimentation rates of the GM units, but rather by the sedimentation rates and overall accumulation of sediments deposited during the previous IGM period (Fig. 5.3). This leads to several pre-conditioning (pore-pressure build-up) scenarios depending on multiple combinations: deposited thickness of IGM sediments and subsequent accumulation rates of GDF units during GM. The timing of the landslides indicates that sedimentation of this "unfavorable" stratigraphy was, however, not enough to trigger the landslides, as we observe that failure occurred post-deposition of the GDF units.

Numerous faults are present in and nearby the Storfjorden Trough (Fig. 2.1). The Hornsund fault zone is a major NW-SE structural lineament with clear bathymetric expression located 70 km from the shelf edge around bathymetric contour -350m (Fig. 5.1) (Faleide et al., 2008). Other tectonic structures in southern Svalbard continue offshore with a clear bathymetric expression. Hampel et al. (2009) modeled fault response during growth and decay of an ice sheet. Their results indicate that ice unloading increases the number and magnitude of earthquakes compared to the loading phase. These periods of increased seismic activity last a few thousand years until activity returns to the normal situation. During the maximum seismogenic phase earthquakes with a moment magnitude M_w~8 were possible in the NW Barents Sea.

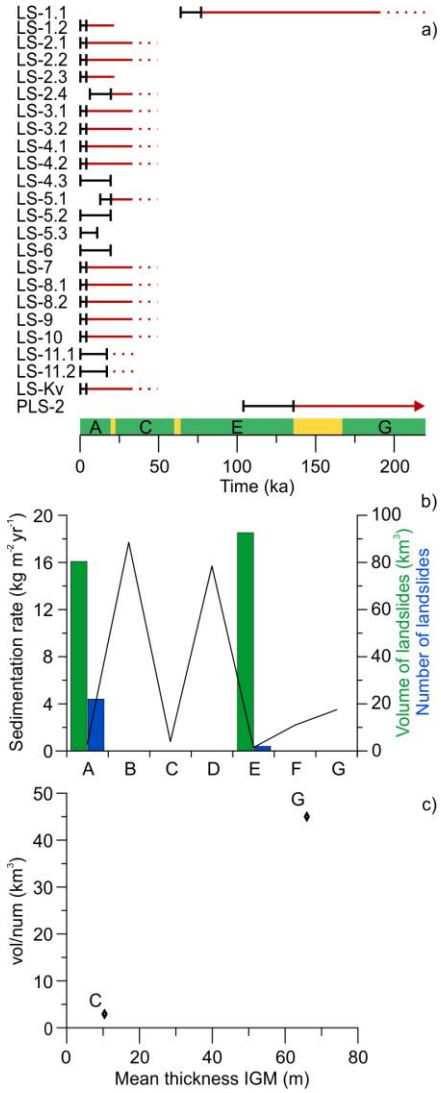

Fig. 5.3 a) Inferred landslide ages (black line) and age of sedimentary section removed by each landslide (red). b) Mean decompacted sedimentation rates of the different units versus volume and number of landslides for each period. c) Mean thickness of Inter-Glacial Maximum units deposited in the previous interglacial versus landslide unit volume (i.e., landslides that occurred during deposition of unit A are plotted with respect to the thickness of the previous IGM unit, which is unit C). Thicknesses have been calculated using a depth variable sound speed according to the relationship $v_p = 1.48+1.5z$ km/s. Note that only landslides above reflector R1 are included.

The sequence of events leading to the observed instabilities would therefore involve: 1) overpressure build-up in the high water content IGM laminated units during rapid deposition of thick GDF units, preconditioning the margin to failure and 2) triggering by earthquakes induced by isostatic rebound during, or shortly after, the ice retreat. Recurrent, large-scale, climatically controlled slope failures

also exists in the Bjørnøya and Isfjorden TMFs, south and north of the study area (Hjelstuen et al., 2007; Marr et al., 2002).

Modeling the continental margin hydrogeology requires of a good knowledge of a) the stratigraphic evolution, b) the sediment physical properties and c) the timing of external factors that could play an important role during the margin evolution. In Chapter 4 the surface and subsurface geomorphology, glacial dynamics and chronostratigraphic framework have been established. In turn, Chapter 5 presents the physical sediment properties, the hydrogeological models results and the influence of overpressure generation over the slope stability. The present chapter accomplishes the complete integration and discussion of the previously presented results, as well as their validation.

5.5 Pore pressure development in a glacially loaded/unloaded continental margin

Sediment self-weight consolidation is the main process controlling the porosity and permeability reduction with depth in passive margins if no external factors intervene. In this case, ice loading on the shelf clearly modifies the shallow (upper 100 mbsf) porosity and permeability evolution. The ice loading decrease the shallower porosities by about 0.18 in the shelf sediments and 0.1 in the shelf edge (Fig. 5.4a and c). In turn, hydraulic conductivities of these sediments (tills) is reduced two orders of magnitude (from 10^{-10} to 10^{-12} m/s) (Fig. 5.4b and d).

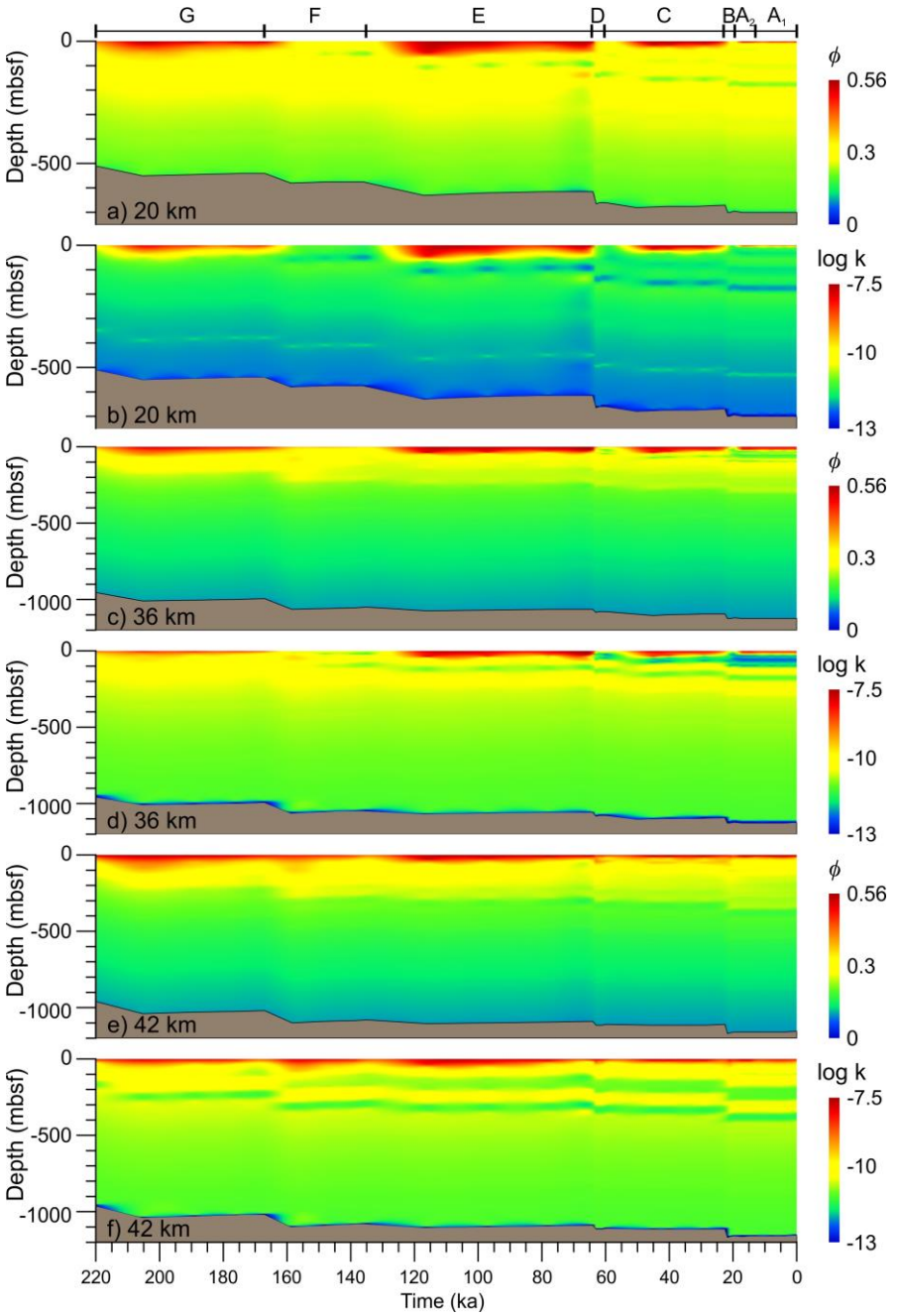

Fig. 5.4 Porosity (a, c and e) and hydraulic conductivity (m/s) (b, d and f) evolution induced by the ice loading during glacial maximum. Results correspond to the three synthetic observation wells located at 20 (shelf), 36 (shelf edge) and 42 km (upper slope) along the model (see Fig. 4.14 for location).

This effect is reduced seawards (Fig. 5.4e and f). In addition, bands of low to high porosity/permeability are depicted in the entire margin. Below the shelf and shelf edge, these low porosity/permeability bands correspond to layers deposited before the GM, which could expel the interstitial fluids before the onset of glacial conditions, and consolidate during the ice loading. The results show that this effect is restricted to the uppermost sediment layers (~100 mbsf). In turn, below the middle slope the bands correspond to the alternating plumite and GDFs layers.

Below the shelf, excess pore pressures increase in the entire sedimentary column to about 1 MPa during glaciation F. At the same time, overpressures increases up to 0.7 in shallower depths (Fig. 5.5a and b). During phase E both excess pore pressures and overpressures decrease slightly, but it is not until the last millennia of phase E that they reach the same values as before phase F. In the next two glacial cycles (D and B), excess pore pressures reaches values up to 4 MPa and high overpressures (up to 0.75) develop between 40 and 400 mbsf. Also, overpressures higher than 0.5 are preserved from deglacial phase C to LGM, and are still preserved nowadays. At the shelf edge, excess pore pressures and overpressures show a more punctuated evolution; increasing during the glacial maximum and decreasing a few thousand years afterwards (Fig. 5.5c and d). Maximum values of overpressure reached at the shelf edge of 0.6 are located in the first hundred meters below the seafloor. Towards the upper slope the pore

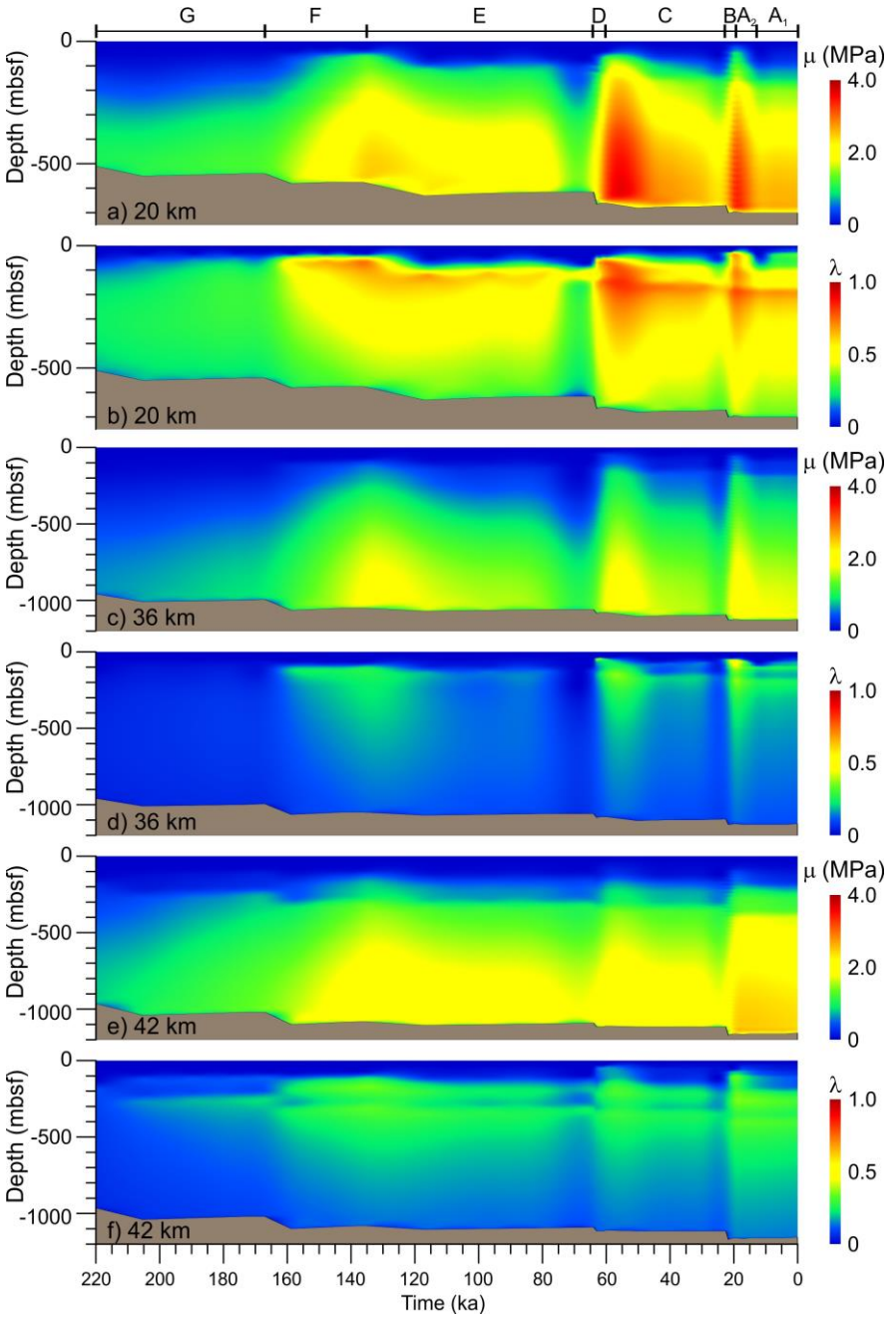

Fig. 5.5 Excess pore pressures (MPa) (a, c and e) and overpressures (b, d and f) evolution induced by the ice loading during glacial maximum. Results correspond to the three synthetic observation wells located at 20 (shelf), 36 (shelf edge) and 42 km (upper slope) along the model (see Fig. 4.14 for location).

pressures evolution is more constant rather than punctuated (Fig. 5.5e and f). In this area, overpressures around 0.2-0.35 are present from glacial maximum F, but during glaciations D and B mid overpressures (up to 0.55) reached shallower sediments.

5.6 Impact of ice in pore pressure development: comparing models with and without ice

The models presented in Chapters 4.2.2 and 5.5 (without and with ice load respectively) have been compared by subtracting the model results (ice model minus no ice model) (Fig. 5.6, Fig. 5.7 and Fig. 5.8). The same three synthetic observation wells as in the previous models are used for such purpose. The increase in total stress induced by the ice load obviously led to further consolidation of the sediments below. The porosity and permeability therefore respond to such changes in total stress. Regarding the porosity and permeability field (Fig. 5.6), it is clear that sediments on the shelf that were loaded by the ice acquired lower porosity and permeability than the sediments in the model where no ice-loading is considered. Despite throughout the deglaciation surface sediments continued showing lower porosities and permeabilities in the ice loading model, during the interglacial these surface sediments evolve to lower porosities and permeabilities without the ice load. These differences between glacial and deglacial/interglacial phases may be explained by contrasts in the rate of interstitial fluid discharge (Fig. 5.7).

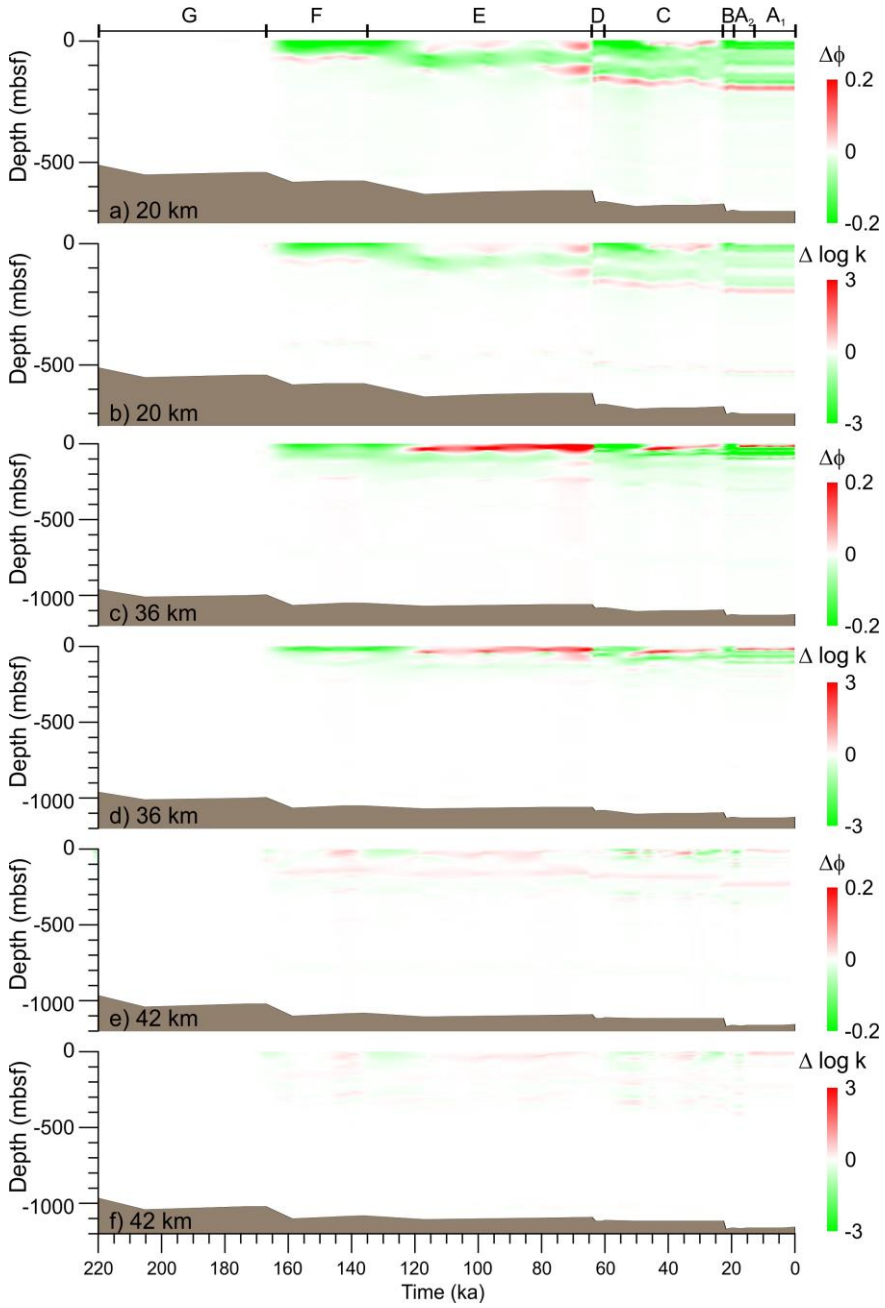

Fig. 5.6 Comparison of the evolution between the models accounting/not accounting for ice load. Porosity (a, c and e) and log of hydraulic conductivity (m/s) (b, d and f) are shown at the synthetic observation wells located at 20 (shelf), 36 (shelf edge) and 42 km (upper slope) along the model (see Fig. 4.14 for location). Redish colors of porosity/hydraulic conductivity imply higher values in the model accounting for ice load.

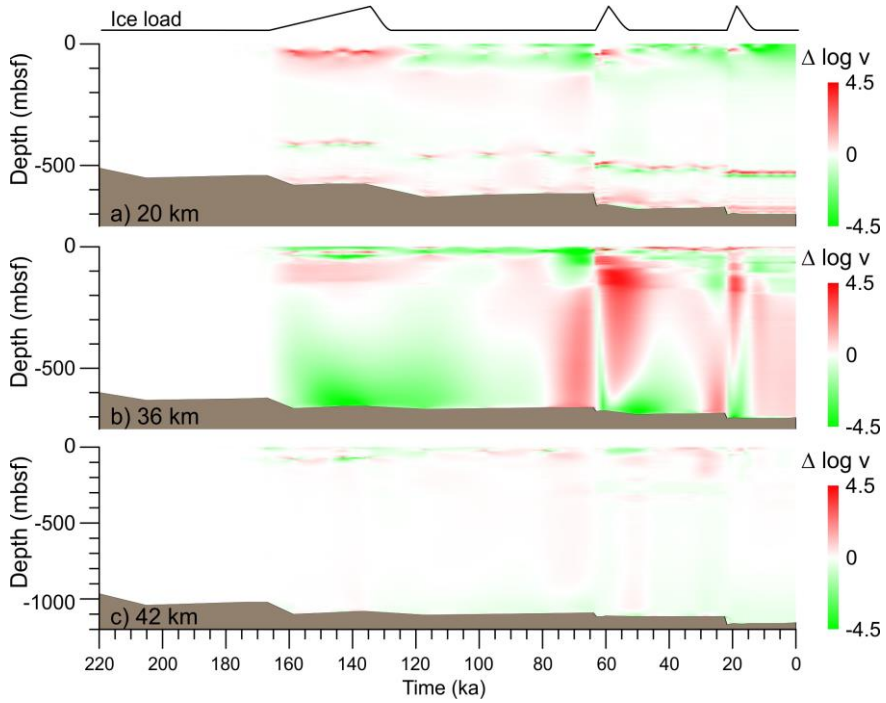

Fig. 5.7 Comparison of the evolution in fluid flow rate (m/s) between the models accounting/not accounting for ice load at the synthetic observation wells located at 20 (shelf), 36 (shelf edge) and 42 km (upper slope) along the model (see Fig. 4.14 for location). Velocities values coded in red mean higher fluid flow discharge in the model accounting for ice load. Simulated ice loading phases are shown with a black line.

When the sediments are loaded by ice along the shelf, the rate of interstitial fluid flow discharge to the seafloor and shelf edge is higher (Fig. 5.7a) allowing further sediment consolidation, hence decreasing their porosity and permeability (Fig. 5.7).

In the model that does not account for ice load, there is therefore additional pore water in previous sediments that is loaded by the newly deposited deglacial and interglacial sediments and therefore higher potential for the development of excess pore pressure during interglacials. In addition, the lower consolidation

rate without ice load, compared to the ice loading model, leads to lower porosity and permeability values ~18 kyrs after the end of the GM. During the interglacials, and mainly the few thousand years before the next GM, the model without ice load shows a higher rate of fluid flow. This difference is more evident at the shelf edge at the end of interglacial E (76 to 64 ka). The high rate of fluid expulsion and rapid decrease of porosity and permeability shown by the model with ice load seem to reach a threshold where porosity and permeability evolution switch to a rather smooth decrease and the fluid flow is considerably reduced. At this time is when the model without the ice load shows lower porosities/permeabilities and higher fluid flow discharge.

These differences with burial history are more evident on the shelf, where ice loads have been applied. However, the influence of ice load in terms of porosity and permeability is also present on the upper slope and gradually decreases towards the middle slope. Also, the differences in porosity and permeability between the two models vanish with depth.

In general terms, comparison at the three wells shows that excess pore pressures and overpressure are higher in the model where ice loading is considered. During glaciation F (167-135 ka), the maximum excess pore pressures difference between the two models is reached at the end of the glaciation. However, the maximum difference in excess pore pressure between the two models is not reached at the end of the shorter glaciations D and B, but during the following deglaciation. The same trend is shown in the overpressure field. The ice load

induces an increase in overpressures of up to 0.45 in the shallower areas of the shelf, while at the shelf edge the difference between the two models is below 0.25 (Fig. 5.8). This increase in overpressures is related to the higher fluid flow expulsion rates in the model accounting the ice load. The influence of such ice loading decreases towards the middle slope, were the difference between the two models is limited. This however shows that the effect of ice on the continental shelf extends far beyond the shelf edge. The increase in overpressure difference between the two models was maximum at the end of the glaciations and persisted during the following deglaciation: ~50 kyrs during phase E, ~10 kyrs in C and ~3 krys at last deglaciation. The differential model evolution shows that if the ice load is not taken into account during the glaciation, the fluid discharge is only controlled by the overburden induced by new sediment deposition; consolidation continues, during the deglacial/interglacial phase, albeit at a slower pace due to the higher fluid discharge from the less consolidated sediments below. This effect is clearly shown on the shelf, but not at the shelf edge (Fig. 5.7b), because beyond this point no ice load is applied. The rate of ice loading exerts a stronger control on the difference in porosity/permeability (and resulting overpressure) at the end of the interglacial than the amount of ice load itself; the shorter is the glaciation, the higher is the fluid discharge and the shorter is the time in which fluids are discharged at this high rate.

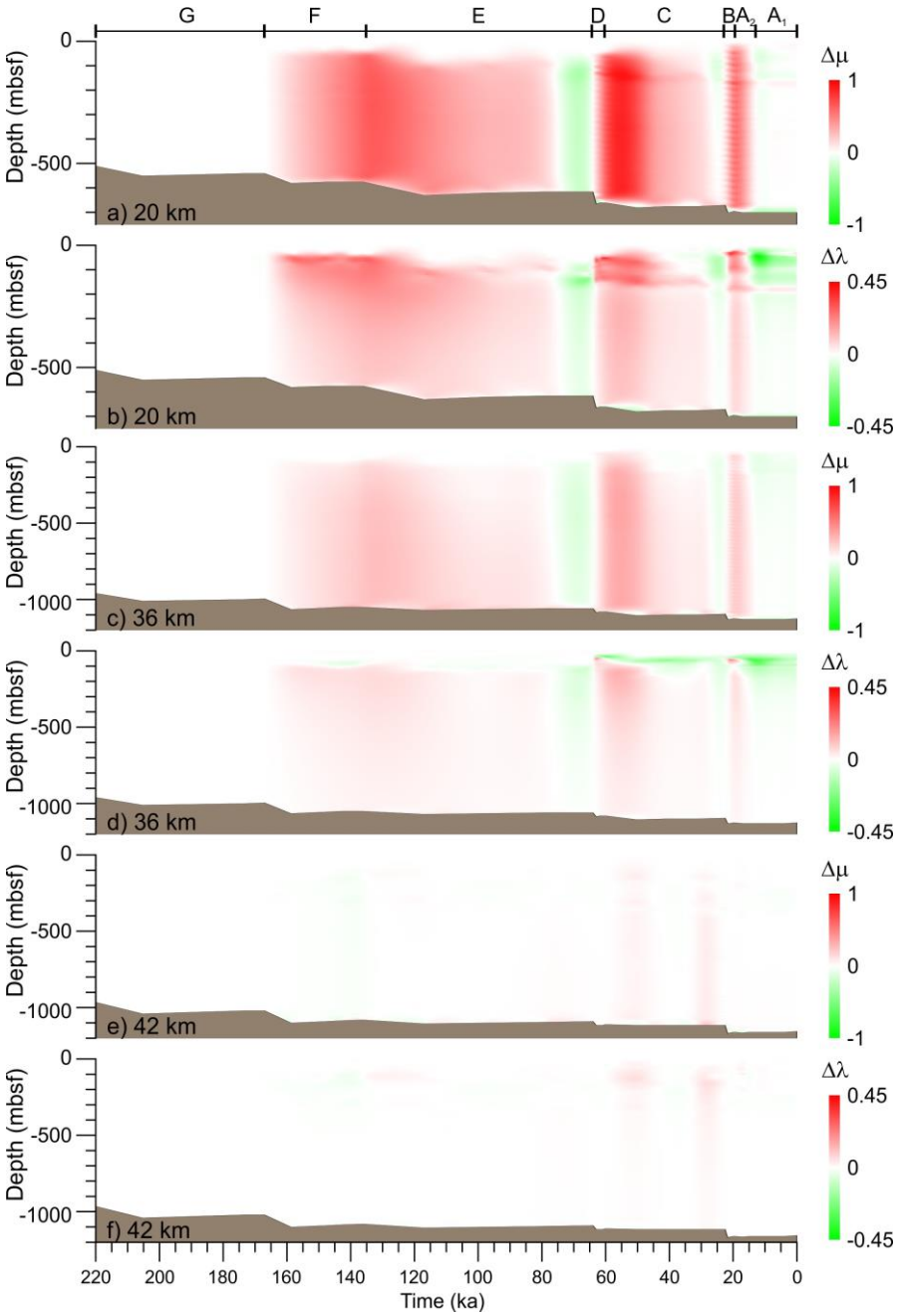

Fig. 5.8 Comparison of the evolution between the models accounting/not accounting for ice load. Excess pore pressures (MPa) (a, c and e) and overpressures (b, d and f) difference at the synthetic observation wells located at 20 (shelf), 36 (shelf edge) and 42 km (upper slope) (see Fig. 4.14 for location).

In the middle slope, fluid discharge differences are lower than in the shelf, but the units primarily made of plumite sediments show higher fluid flow velocities in the model with the ice load. The higher permeability of plumites combined with overpressures that remain higher during the deglaciation provide an efficient mechanism for fluid evacuation towards the upper slope and excess pore pressure dissipation along the shelf. In turn, such increase in fluid flow towards the slope plumites drives excess pore pressure (and overpressure) within these units because fluids cannot drain easily into the overlying lower permeability GDFs, thus hindering expulsion to the sea floor.

5.7 Influence of glaciation in Trough Mouth Fan slope instability.

Along the Norwegian and Western Barents Sea continental margin, a number of landslides have been identified (Haflidason et al., 2005; Laberg and Vorren, 2000; Sejrup et al., 2005). Most of these landslides are located in to the side of its related TMF. The larger landslides in this area are Storegga Slide (Bugge et al., 1987; Haflidason et al., 2005), Bjørnøyrenna Slide (Laberg and Vorren, 1995, 1993), Trænadjupet Slide (Laberg and Vorren, 2000), Andøya Slide (Laberg et al., 2000). Pre-conditioning factors such as high sedimentation rates, excess pore pressure development, gas hydrates dissociation and dissolution, or presence of weak layers may have led to failure of these slopes (Sultan et al., 2004a; Urlaub et al., 2013; Vanneste et al., 2012). High sedimentation rates

coupled with static ice loading on the shelf during glacial maxima produce excess pore pressures that cannot be dissipated with the sediment and ice drainage capabilities. Such increase in excess pore pressures may lead to undrained failures in the upper slope and bearing capacity failures in the middle and lower slope (Mulder and Moran, 1995). In this work, the relation between overpressure development associated to high accumulation rates, ice loading during glacial cycles and slope instabilities has been investigated. As shown in the previous sections, the highest overpressures occurred during the loading of the continental margin by the ice streams during glacial maxima. Alternating glacial and glaci-marine sedimentary conditions also caused the sedimentation of materials with contrasting physical properties. With burial and ice loading such difference in physical properties between sediments deposited during glacial maxima and those deposited during the subsequent deglaciation and interglacial are further accentuated. However, most of the landslides identified in the Storfjorden and Kveithola TMFs seem to have occurred during a deglaciation phase (Chapter 4.7).

It must be first recognized that glaciation and the sedimentary architecture developed throughout TMF progradation involved the development of focused fluid flow towards the slope and allowed mid to high overpressures to be maintained during the first thousands years in the following deglaciation. However, the question still remains as to whether these overpressures were high enough to trigger these failures and what other mechanisms could have played a

role in the onset of slope failure. Here we investigate how TMF slope stability evolved through time. Thus, the evolution of the safety factor (SF) during the last 220 kyrs is analyzed in Plaxis using the phi-c reduction method. We also carry out a more detailed analysis for the period spanning from the Last Glacial Maximum to the base of the Holocene (Fig. 5.9). In this regard, the safety factor has been calculated in detail from 22.5 to 13 ka. The safety factor evolution not accounting for ice loading has been investigated as well to determine the influence of such ice in the slope stability.

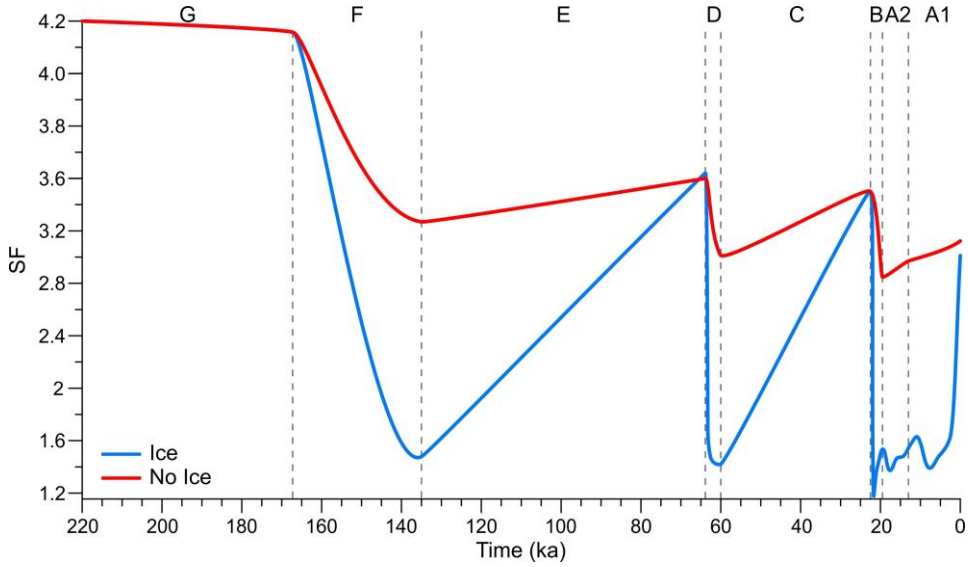

Fig. 5.9 Evolution of the safety factor (SF) throughout the last 220 kyrs. The minimum SF occurred in the first thousand years of the Last Glacial Maximum.

As expected, safety factor values around 4-4.2 at the beginning and end of deposition of unit G are found in both models (ice and no ice loading). The differences become evident at the start of deposition of unit F. While the model that does not accounts for ice loading shows a safety factor that only decreases to

~3.2, the model that accounts for such ice loading decreases to 1.5. During inter-glacial maximum E both models converge again to values around 3.7. During the next glacial maximum (unit D, 64 to 60 ka), the safety factor reaches a value around 1.4, while in the model without ice the safety factor decreases to 3.0. After this minimum, the overpressures remain high but gradually dissipate. Thereafter, the SF increases during the IGM C reaching a maximum of 3.5 right at the beginning of the LGM in both models. Again, the high sedimentation rates, but mainly, ice loading by the ice streams on the shelf during the LGM drive an increase of fluid flow towards the plumite layers in the upper slope leading to an increase in overpressure. As a result, a sudden decrease of the SF to 1.18 at 21.7 ka occurs. At this time, overpressures reach a maximum value of 0.7 between 30 and 50 mbsf. After this minimum, SF values increase to around 1.5 at the end of the LGM. In the model where the shelf is not loaded by ice, which records lower overpressures at the end of the LGM, depicts a minimum SF value of 2.8. During the last deglaciation and deposition of unit A_2 the SF of the model accounting for ice load is kept below 1.5 as the overpressures from the previous glaciation are preserved. It is in this period when most of the landslides identified in the area occurred (see Chapter 4.1.2). On the other hand, the model without ice depicts a fairly constant increase of SF until values of 3.1 at Present.

In the model that accounts for ice load, the SF at the beginning of the Holocene (around 7.9 ka) decreases slightly to 1.4. This minimum is fairly coincident with the dating for the Storegga slide (i.e. Bondevik et al., 2012). Bryn et al. (2005b)

pointed that the pore pressure transferred from the shelf edge to the middle slope can be higher than the increase in overburden stress during the deglacial. As a result, a swelling and unloading occurs in the middle slope inducing a delay in peak pore pressure response during the next interglacial.

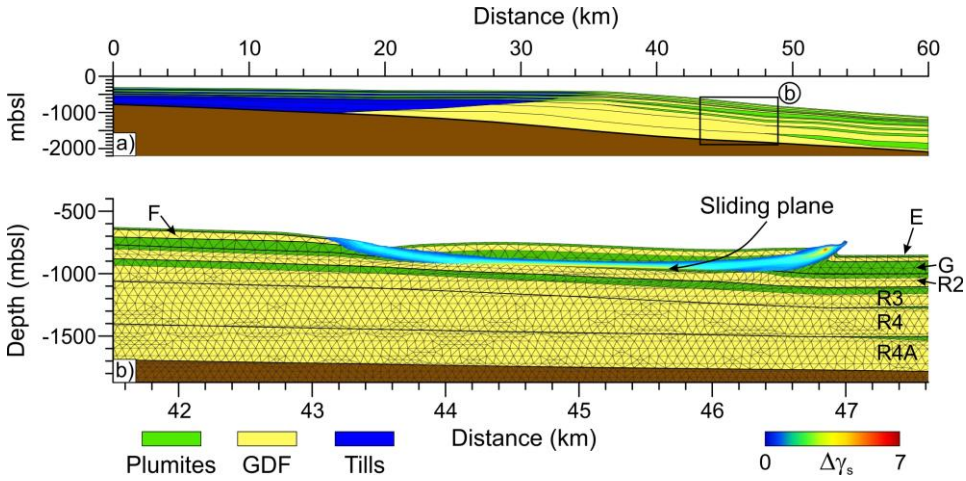

Fig. 5.10 a) Present day margin stratigraphy and facies distribution used in the Plaxis model setup (vertical exhageration 1:2). Black square depicts bottom close-up. b) Deformed mesh resulting from the safety factor analysis in Plaxis during deposition of IGM E (scaled down 0.05 times, no vertical exhageration). Bluish to reddish shading depicts the incremetal deviatoric strain around most critical failure.

Although the SF during the IGM E is rather high, the safety analysis shows a critical failure surface whose characteristics resemble landslide LS-1.1 (Chapter 4.1.2). The modeled most critical failure surface located close the base of unit G (reflector R1), and occurs on the middle slope (Fig. 5.10). The rooting depth and the spatial position match those of landslide LS-1, the largest observable on the surface of the Storfjorden TMF. Like most of the landslides identified in the study area, landslide LS-1.1 is rooted in a plumite layer. Even though the stratigraphy for the last 220 kyrs is fairly detailed, local sediment variations are

not excluded. The existence of thin more permeable water rich contourite layers within the IGM units that contain the plumites could allocate higher water content and develop further overpressures than the overall unit (Baeten et al., 2014). Contourites are more sensitive and have a more brittle nature that could favor the formation of a glide plane (Bryn et al., 2005a).

As explained earlier, the SF at the end of deposition of unit E, an IGM unit, when the landslide LS-1.1 occurred is ~3.7, which indicated a slope stable per se. For this reason additional mechanisms need to be invoked to explain the onset of slope failure in the TMF. In this sense it has already been pointed that the loading applied by earthquakes during the deglaciation form isostatic rebound could lead to slope rupture (L'Heureux et al., 2013). The Hordsund Fault Zone crosses the outer shelf of the Storfjorden and Kveithola troughs and could lead to significant earthquakes. Hampel et al. (2009) modeled the seismicity associated to fault reactivation during the ice advance and retreat obtaining a possible earthquake of magnitude $M_w \approx 8$. As explained in Chapter 4.1.2, no evidences of IGM unit E are found on the top of the landslides LS-1.1 deposit, while the thickness of GM unit D is equal on top of the landslide than in the surrounding areas. This suggests that the earthquake which triggered the landslide LS-1.1 occurred during the transition from IGM E to GM D. The ground motions generated by those earthquakes on the Storfjorden TMF could reduce the SF below 1 triggering landslide LS-1.1. In addition, Bungum et al. (2005) suggested that earthquakes of magnitude $M_w \approx 6.5$-7 could occur up to 5-6

kyrs after the last deglaciation, which could trigger the identified landslides during the Holocene.

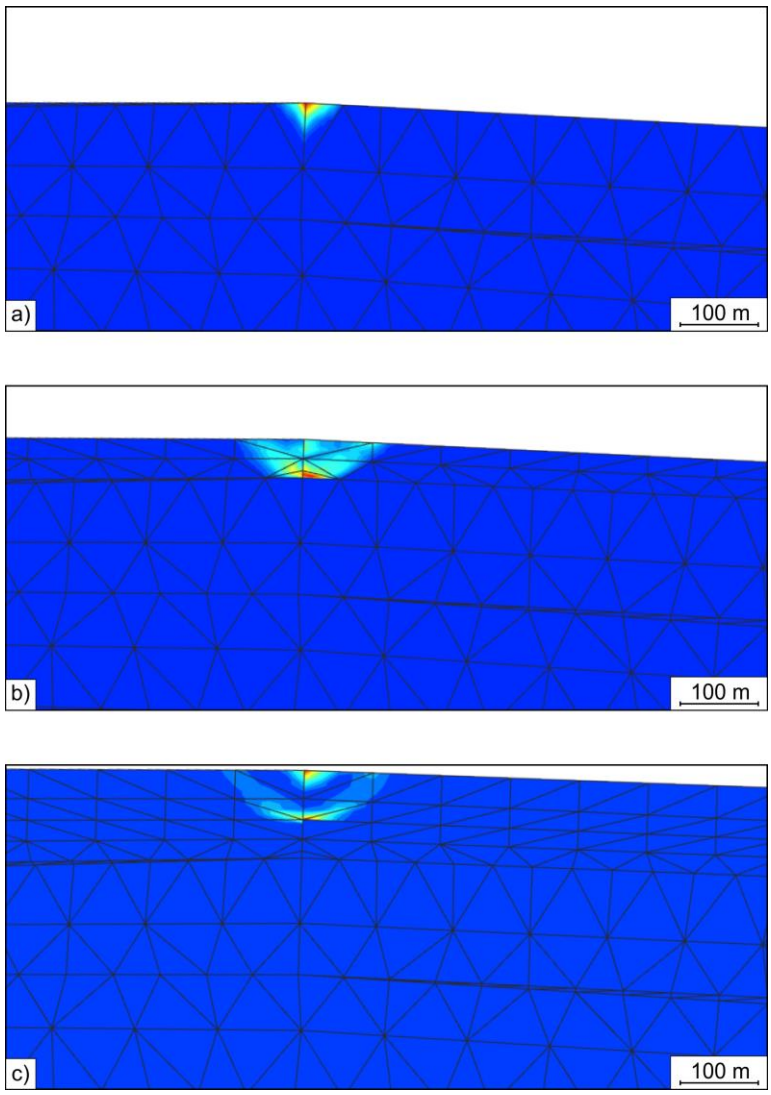

Fig. 5.11 Plaxis safety analysis results of most probable slides located at the shelf edge for a) GM F, b) GM D, and c) GM B with safety factor values 1.37, 1.51 and 1.18, respectively. Shading corresponds to the incremental deviatoric strain. The GM B safety model shows two possible sliding planes.

Plaxis model shows the minimum values of SF occur during the LGM (1.18). The most critical failure surfaces associated to this low SF are located right at the shelf edge (Fig. 5.11) and have rather limited extent; few hundred meters long and few tens of meters deep.

The same behavior is also observed for GM F and D (Fig. 5.11). This could explain how local slope and load variations associated to till deposition in front of the ice streams could result in small landslides and GDFs. During a GM period, numerous such events are expected to occur as portrayed on the geophysical data (Fig. 4.2 and Fig. 4.5). The SF values during the last deglaciation are also low (<1.6). The combined loading by the small landslides during the LGM and the dynamic earthquake loading could easily trigger the landslides identified in the study area.

5.8 Validation of input parameters, model limitations and uncertainty estimation

Modeling real-world processes must often be performed in a stochastic system (Arregui-Mena et al., 2014). The model input parameters demand a sensitivity analysis in order to validate the results and determine the associated uncertainty (Pellissetti and Schuëller, 2009). In this work, the models require three different inputs: geometry of the layers, sedimentation rates and physical properties of each material used. Physical properties have a major influence on the final

models result than the other two inputs: a variation in the physical properties can lead to a variation in the compacted thickness of the layers, and therefore in their sedimentation rates. Thus, in order to validate the results presented in the previous chapters, four different methods have been used to validate input parameters and estimate model output uncertainty: a geotechnical test simulation, modeling limitations consideration, a Monte Carlo analysis, and a multi-model evaluation.

5.8.1 Oedometer simulation

Oedometer tests in the laboratory have been carried out in three sediment types and used as input for the models presented in Chapter 5.1. Despite results from tests carried out in similar sediment types should also follow similar patterns, minor changes in mineralogy, grain size, sorting and consolidation state, amongst others, could lead to substantial differences in the shape of the consolidation curve. In this regard, the compression characteristics of the various laboratory tests for each sediment type have been averaged to be used as input in the basin analyses. To validate these input parameters a simulated oedometer test is carried out in Plaxis and the simulated results are compared to the actual laboratory consolidation tests results (Fig. 5.12). The swelling index for till sediments could not been obtained from laboratory tests due to technical issues with the consolidation cell. Since GDFs derive from till sediments and their geotechnical behavior is relatively similar, the swelling index from GDFs has

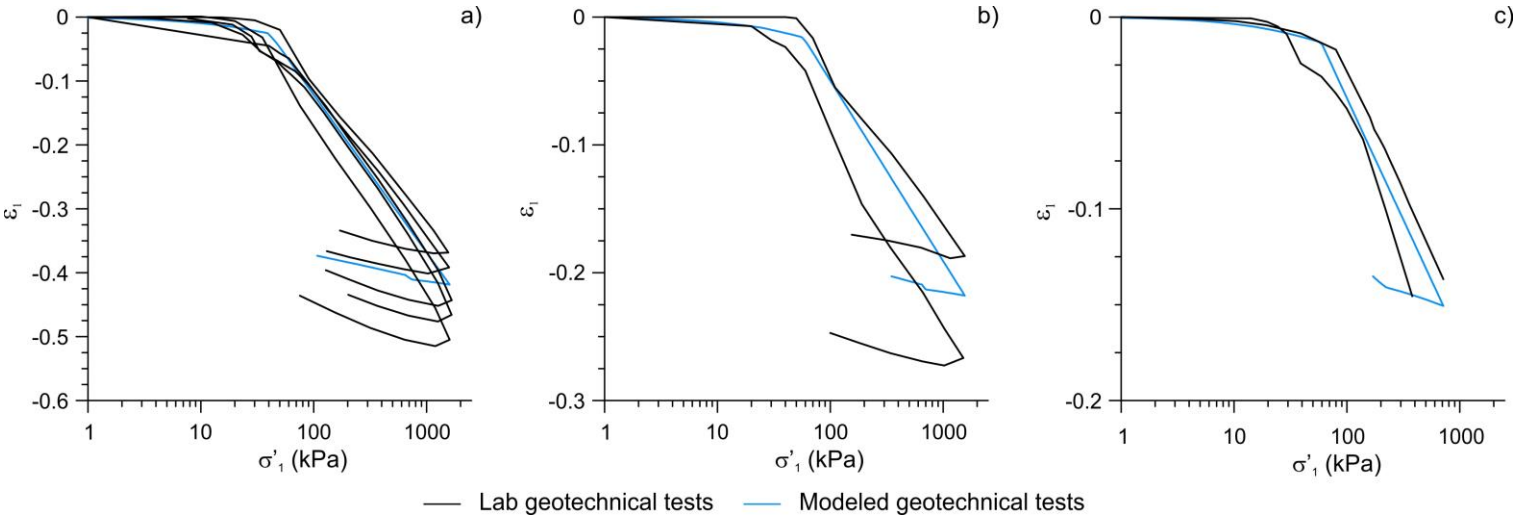

Fig. 5.12 Oedometer tests for a) plumites, b) GDFs and c) tills. Laboratory results (black lines) and synthetic results with Plaxis (blue line) of the mean values used as input for the hydrogeological models.

also been used for tills. The virgin consolidation slopes of the laboratory and synthetic tests are clearly similar in the three cases. The best fit between synthetic and laboratory test data occurs in the case of plumites, only the sample SV02-02 appears to have relatively higher compressibility (C_c=0.39) compared to the other four tests performed in this sediment type. This higher compressibility could be attributed to the fact that this sample comes from a relatively shallow position (~1.5 mbsf) and may correspond to a more transitional plumites to hemipelagic sediments rather than purely plumites. Higher variability in compression characteristics occurs in GDFs and to a lesser extent in tills. The changes in the slope of the virgin consolidation are not reflected by the modeled curve. These changes could be attributed to the presence of pebbles in these samples due to its own diamictic composition. In the three cases the synthetic mean consolidation curves are fit to the range of stresses applied in the laboratory. Thus, the mean values for each sediment type are suitable to be used in the hydrogeological models.

5.8.2 Model limitations: the ice-sediment interface

As it has been pointed in Chapter 5.5, fluid flow along the shelf is diverted to the shelf edge, particularly when the ice seats on top of glacigenic sediments. However, a portion of this fluid can be discharged and incorporated to the subglacial meltwater. Factors such as sediment permeability, hydrostatic pressure, thermal conditions beneath an ice stream, presence of subglacial melt-

water channels and ice flow velocity control the pore water evacuation or excess pore pressures development (i.e. Christoffersen and Tulaczyk, 2003; O'Regan et al., 2010; Sættem et al., 1996). The overpressure dissipation of the shallower most sediments on the shelf is controlled by the pressure of the water in the ice sediment interface (Boulton and Hindmarsh, 1987). Piotrowski and Kraus (1997) find that pore water pressure beneath of the ice could reach the flotation pressure in areas of low hydraulic conductivity substratum preventing overpressure dissipation. In turn, high basal water pressures and ice melting favor a lower basal friction and faster ice advance (Tulaczyk et al., 2000). Thus, high overpressures within the shelf sediments (tills) could increase the ice velocity and ice thinning (Luo et al., 2015). The model is not able to simulate all of these processes in detail largely owing to the 2D nature of the model. Furthermore, there are uncertainties in the amount of ice load transmitted to the sediment; a range from 0 to 1 MPa with a longitudinal loading gradient has been already tested. The load induced by ice is initially linearly transmitted to the excess pore pressure as the sediment is fully saturated with pore water. Thus, the larger is the ice load the greater is the compression on the shelf sediments and the more focused is the pore fluid discharge towards the upper slope. This effect is also reflected in the comparison between the models accounting/not accounting for ice load.

Depending on the climatic conditions and ice supply, an ice stream could behave as fast- or slow-flowing. The pressure of melted water below the ice, among

others, plays an important role in the frictional resistance of the subglacial sediments and therefore in the ice velocity (Christoffersen and Tulaczyk, 2003). Thus, the pore fluid evacuation through the sea floor depends on this water pressure beneath the ice. Due to the limitations imposed by 2D simulation these processes occurring at the ice-sediment interface have been evaluated by considering an impervious overlying ice layer vs. an overlying ice layer of limited permeability (the same as that of the till materials below) (Fig. 5.13). Because the ice is modeled in PLAXIS as a series of loads the permeability condition is imposed to the seafloor.

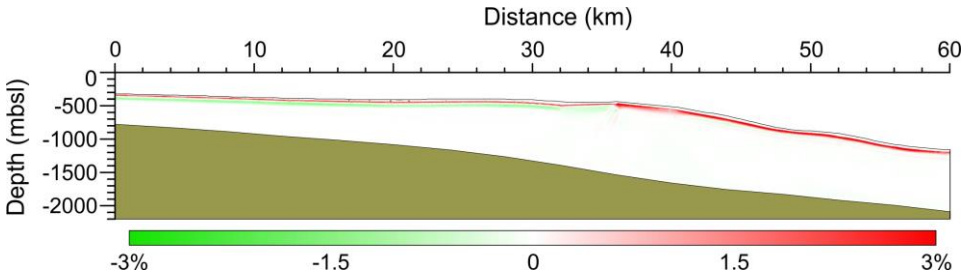

Fig. 5.13 Overpressure variation between the model with an overlying impervious ice and the model with a permeable ice–sediment interface along the shelf (difference between impervious-permeable ice-sediment interface). Vertical exaggeration 4:1.

Comparison between the two models shows that overpressures increase around 20 mbsf in the shelf up to 1.2% and decrease below that depth around 0.75% in the model with an impervious ice-sediment boundary. The impervious barrier blocks the vertical fluid discharge increasing the overpressure right below the ice. This barrier induces a lateral fluid towards the shelf edge which decreases the overpressure below 20 mbsf. To the contrary, in the slope overpressures are

higher in the model with impervious ice-sediment interface (up to 1.5%) only between 20-40 mbsf. The influence of the fluid discharged from the shelf to the upper slope is transmitted downslope increasing the overpressures in the shallowermost sediments. Several authors suggest that cross-shelf troughs and trough mouth fans in the Barents Sea and Svalbard are the result of fast-flowing ice streams over the shelf during glacials (Dowdeswell and Siegert, 1999; Solheim et al., 1998; Vorren et al., 2011). In this case, because the models presented in section 5.2 to 5.4 do not assume an impervious ice-sediment interface, the calculated overpressures could be up to 1.5% higher than the ones that have been obtained.

5.8.3 Uncertainty in hydrogeological models: Monte Carlo analysis

In order to understand uncertainty in the hydrogeological models, a Monte Carlo analysis has been carried out. To do so, the BASIN software (Bitzer, 1999) has been used. The lower computational time and the possibility to test the four sediment types make it the best option. In the case where models are made of independent variables, the ideal approach would be to test the influence of the different geotechnical parameters used in the simulation one at a time. In this case, this procedure is however not adequate because porosity, permeability and compressibility/specific storage are interdependent parameters. A decrease in the porosity has to be associated also to a decrease in the other two parameters, and vice versa. Thus, when porosity is increased, permeability and specific storage

Table 5.2 Parameters derived from geotechnical tests in this study, mean values, standard deviation and coefficient of variation for each physical property and sediment type. Coefficient of variation has been used in the Montecarlo analisys.

	SV02-02	SV02-03	SV02-04	SV03-04	SV02-05	SV02-06	GeoB17610-2-319	GeoB17610-2-330
Sediment type	Plumites	Plumites	Plumites	Plumites	GDF	GDF	Tills	Tills
e_0	1.48	1.89	1.72	1.83	1.04	0.92		0.93
m	1.73				0.98		0.94	
σ	0.164				0.0084		0.007	
C_{vn}	0.1				0.09		0.01	
k_0 (m/s)	2.30E-09	5.50E-09	7.20E-09	4.20E-08	3.60E-10	1.08E-09	4.90E-10	3.20E-10
m	1.43E-08				7.20E-10		4.05E-10	
σ	1.7E-8				5.1E-10		.2E-10	
C_{vn}	1.48				0.71		0.30	
S_0 (m^{-1})	0.024	0.019	0.032	0.026	0.009	0.007	0.0057	0.0039
m	0.025				0.008		0.005	
σ	0.0049				0.0014		0.0012	
C_{vn}	0.21				0.18		0.27	

GDF: Glacigenic Debris Flows. e_0: initial void ratio at 1 kPa, k_0: initial hydraulic conductivity at e_0, S_0: initial specific storage at e_0, m: mean, σ: standard deviation, C_{vn}: coefficient of variation.

are increased as well following the regression curves obtained from the geotechnical tests. Depending on the sediment type and the geotechnical property, the variability on the laboratory results changes (Table 5.2). Due to lack of tests on hemipelagic sediments, the coefficients of variation from plumites have been used for this sediment type.

The set of parameters created for Monte Carlo analysis have been obtained by using a Simple Random Sampling in between the range of the coefficient of variation obey (Hurtado and Barbat, 1998). Hence, four sets of parameters for each sediment type and a total of 256 models have been created by combining the parameters randomly. The results of overpressure from all the models have been averaged and the standard deviation to the reference model (Chapter 5.5) has been calculated (Fig. 5.14).

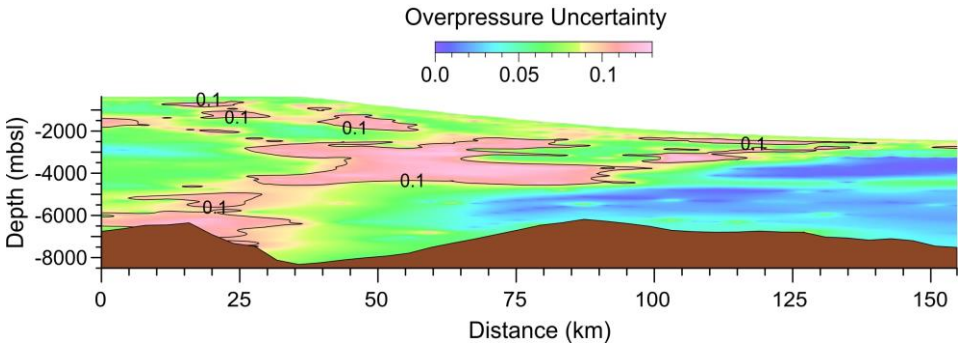

Fig. 5.14 Overpressure uncertainity from Monte Carlo analysis carried out with BASIN (Bitzer, 1999) software.

The mean value of uncertainty in the whole model is around 7%. The maximum uncertainty around 13% occurs chiefly in the area enclosed between 50-75 km

and 2500-4500 m depth. In this area, where transition from plumites to GDFs or hemipelagic sediments occurs (Fig. 4.14), values above 10% are found. It can therefore be seen that the plumites maximum permeability variation of 148% exerts a significant influence on the uncertainty when it is combined with other sediments. The lowest uncertainty values occur in the area where only hemipelagic sediments are present.

5.8.4 Multi-model evaluation

In order to analyze the goodness of the BASIN (Bitzer, 1999) and PLAXIS models, a comparative evaluation with other well established software packages has been carried out. As explained in Chapter 3.7, the stratigraphic model for the comparative evaluation has been designed ad-hoc. The physical properties of the two sediments used (plumites and GDFs) have been taken from: a) geotechnical test performed in the laboratory, and b) equations presented in Chapter 3.7 (Table 5.3). Here, the pore pressures and overpressures evolution have been analyzed for the four models: BASIN, PLAXIS, Basin2 and NGI-Basin

The results show that pore pressures obtained with BASIN are the ones closer to hydrostatic (Fig. 5.15). In general terms, the overpressures are not high in all models, but the distribution obtained with the NGI-Basin software is higher than that obtained with the other models.

In the first five meters Basin2 and Plaxis pore pressures are slightly above hydrostatic, while NGI-Basin shows lower pore pressures than the hydrostatic in these first meters. However, these pore pressures result from the way in which NGI- Basin builds the points where calculations are done; the first point below the sea floor corresponds to the top of the GDF's layer, 10 mbsf. The pore pressure is around 15-18% above the hydrostatic and remains at similar values or decreases only slightly to the base of the model.

The trends in pore pressure and overpressure in BASIN are smooth with reaching maximum values of overpressure ~0.01 around 20 mbsf decreasing to ~0.005 at the base of the model. Plaxis shows an abrupt increase in the first couple of meters with overpressure values up to ~0.018 owing to the higher resolution FE mesh. In the next 20 m the overpressure increases slightly until the base of the GDFs layer at ~30 mbsf. Then the trend is a parabola with decreasing values until hydrostatic conditions are reached at 120 mbsf. In the case of Basin2, the overpressure behavior is relatively erratic and displays a maximum value of 0.114 at the base of the upper plumite layer. The overpressures are between 0.03 and 0.1 above 30 mbsf. Below 30 mbsf the overpressure values are similar to those of BASIN. The overpressure in NGI-Basin shows an initial sharp increase with a maximum overpressure of 0.15 occurring at the base of the upper plumite layer. The overpressure tends to decrease below the base of the GDFs and then there is a second peak in overpressure within the first plumite layer at 0.165. Below that peak values gradually decrease to the base of the model.

Table 5.3 Parameters used in the multi-model evaluatio.

	BASIN		NGI-Basin		Basin2		Plaxis	
	Plumites	GDF	Plumites	GDF	Plumites	GDF	Plumites	GDF
ϕ_0	0.63	0.49	0.63	0.49	0.63	0.49	-	-
e_1	-	-	1.73	0.98	-	-	1.73	0.98
S_0 (m^{-1})	0.025	0.008	-	-	-	-	-	-
k_0 (m/s)	1.43E-08	7.20E-10	1.43E-08	7.20E-10	-	-	1.43E-08	7.20E-10
C_c	-	-	-	-	-	-	0.34	0.23
C_s	-	-	-	-	-	-	0.043	0.024
m	-	-	12.00	22.50	-	-	-	-
r	-	-	1.12	1.05	-	-	-	-
A	-	-	0.15	0.14	-	-	-	-
ϕ_1	-	-	-	-	0.02	0.02	-	-
β_{por}	-	-	-	-	0.07	0.15	-	-
$A_{(darcy)}$	-	-	-	-	6.62	6.99	-	-
$B_{(log\ darcy)}$	-	-	-	-	-4.3	-4.01	-	-
p_KxKz	1.5	1.5	-	-	1.5	1.5	1.5	1.5

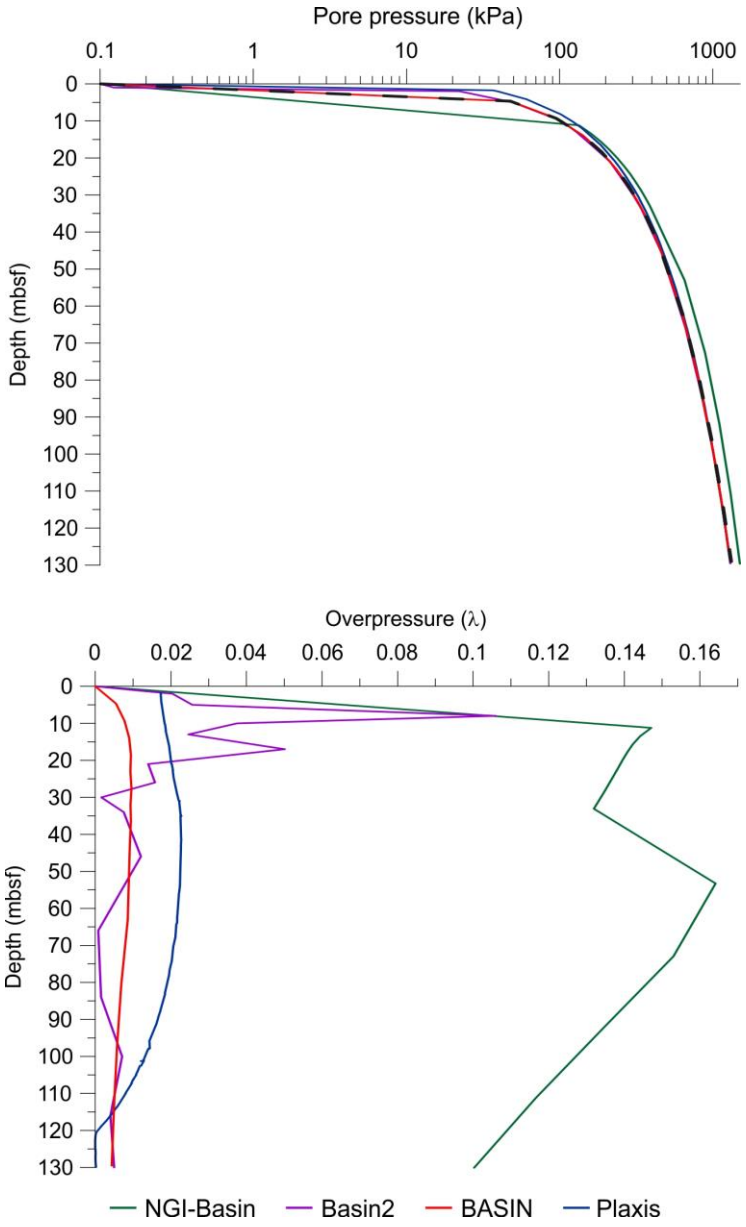

Fig. 5.15 Results from the four models. Top: Pore pressure versus depth. Bottom: Overpressure versus depth. Black dashed line depicts hydrostatic pressure. Notice the data points depend on model mesh resolution.

The comparison between the different models shows that, despite minor differences, Basin2, BASIN and Plaxis show similar results. The maximum

differences in between the three models (below 10%) are concentrated in the first 10-20 m where the GDFs layer is located. However, despite pore pressure trends are similar, when results are shown in terms of overpressure NGI-Basin shows significantly higher overpressures. Basin2 also shows a sharp increase in overpressure in the first 20 mbsf, despite values then become closer to those obtained with BASIN and Plaxis. Both Basin2 and NGI-Basin, use input parameters that are partially derived from regression curves and not directly from geotechnical tests (see Chapter 3.7). In fact, Basin2 has only the porosity and NGI-Basin porosity and permeability as direct input parameters. Compressibility (or specific storage) is key to calculate the variation of porosity and permeability with burial. The estimation of sediment compressibility from porosity values, and in turn, recalculation of porosity and permeability may produce inconsistencies, especially when sediments changes in between two consecutive nodes. These differences in the way the parameters are input to the different software packages could be at the origin of the observed differences. It is our opinion that, the way in which parameters are input to BASIN and Plaxis offers reliable solutions and are more suitable to perform the hydrogeological modeling.

5.9 Integrated evolution of Storfjorden TMF

5.9.1 Stratigraphy and hydrogeology coupling

Reflector R7 (2.7 Ma) has been interpreted as an initial growth phase when glaciers terminated in the coast line and prevailed glacimarine meltwater overflows (Eldholm et al., 1984; Fiedler and Faleide, 1996; Knies et al., 2009; Laberg et al., 2010). This phase changed around 1.5 Ma to glacial conditions with glaciers reaching the paleo shelf edge during the early Pleistocene. The large-scale intensification of glaciation occurred at 1.0 Ma dominated by sedimentation of tills in the shelf and glacigenic debris flows in the slope, with a meltwater input during interglacials (Butt et al., 2000; Faleide et al., 1996; Forsberg et al., 1999; Knies et al., 2009). Under these conditions, in the proximal area till sediments deflects most of the vertical fluid flow towards the shelf edge where sediments with higher hydraulic conductivities are located (plumites). At the shelf edge and few thousands meters seaward, overpressures show values up to 0.35 in the shallower most sediments due to this lateral fluid flow. Previous to R1 reflector time (220 ka) Basin model shows that overpressures around 0.3 are common in the slope. This is caused by fluid flow expulsion from plumites and hemipelagic sediments. Their high water content and high compressibility release a large amount of water due to overburden. The increase of content GDFs in the upper slope (with lower permeability) due to shelf edge progradation and glacial intensification from 1.0 Ma to 220 ka, decreased the permeability of the

shallower sediments and, in turn, reduced the fluid scape towards the sea floor. The increase of overpressures up to 0.3 in the shelf/shelf edge shallower most sediments is the result of this glacial intensification conditions.

As has been pointed previously, a good knowledge of processes and sediments involved in the TMF development trough time are key for a reliable hydrogeological model results. Although a lot of works have been carried in the western Barents Sea continental margin, and especially in the Storfjorden area, deeper units (R7-R2) are not sufficient characterized. A general agreement exist in the global processes that result in the tree main sequences: interglacial to glacial conditions transition (GI), glacial intensification with glaciers reaching the shelf edge (GII), and full glacial conditions (GIII) (Butt et al., 2002, 2000; Faleide et al., 1996; Hjelstuen et al., 1996; Laberg and Vorren, 1996b). Result from Plaxis model from the last 220 kyrs, show a crucial effect of glacial and interglacial changing conditions on TMF hydrogeology, and in turn, in the slope stability. In this regard, results from Basin model from 2.7 to 0.22 Ma have to be considered as the base of a more detailed study based on an appropriate knowledge of stratigraphy and deposition periods.

From 220 ka four Inter-Glacial Maximum periods (IGM) (G, E, C, and A) and three Glacial Maximum periods (GM) (F, D and B) have been identified. Plumite deposition occurred during IGM while tills/glacigenic debris flows during GM. Plaxis software has been used to understand, in higher detail, the margin evolution from 220 ka to Present and the climatically induced shifting conditions

(glacial and interglacial) over the margin, and ice influence during glaciations as well.

The alternation of low and high sedimentation rates during interglacials and glacial maxima, and glacier-fed submarine fan progradation, clearly switch the fluid flow patterns and pressures distribution (Dowdeswell et al., 1998; Laberg and Vorren, 2004). The ice loading on the shelf increased the overpressures during the GM and, the longer was the glacial phase the longer took the excess pore pressures to dissipate during the following IGM. However, the higher thickness of the plumite layer G and the low sedimentation rate during glacial F contributed to a quick discharge of the water coming from the shelf sediments towards the upper slope. Thus, the overpressures at the shelf edge shallower sediments were mainly dissipated during the first thousands years after unit F deposition. Contrary, this decrease was lower in the middle slope due to the continued fluid escape from the plumites. Even so, values higher than 0.5 were only preserved in the shelf area at the end of inter-glacial maximum E. This behavior is not observed in the following glaciations D and B: mid to high overpressures reached shallower sediments and remained during the following inter-glacial maximum in the shelf and middle slope, not at the shelf edge. Contrary, higher overpressures (up to 0.65) were reached in depths around 30-50 mbsf at the shelf edge during the GM D and B but were dissipated faster. The higher fluid flow discharge coming from the shelf contributed to this faster dissipation while increased the overpressures.

The Late Weichselian glacial maximum has been largely studied in the Barents Sea area (e.g. Landvik et al., 1998). While there is a general agreement than Barents and Kara seas were occupied by ice during the LGM, the thickness of this ice and the time span that the glaciers were grounded at the shelf edge is not clear (Mangerud et al., 1998; Spielhagen et al., 2004; Svendsen et al., 2004a; Vorren et al., 2011). The model is well constrained from LGM to Present day by using the data presented in this thesis and previous works available. The ice streams were grounded at the shelf break at first time during the LGM at 22.5 ka. Some works pointed an ice thickness around 150-200 masl (e.g. Dowdeswell and Siegert, 1999) during the LGM. At this time, the ice stream bulldozing and sediment oversteepening at the shelf edge during glacial maxima, induces intense glacially-derived mass wasting downslope as glacigenic debris flows (Ó Cofaigh et al., 2013; Taylor et al., 2002; Vorren and Laberg, 1997). The occurrence of these debris flows was more punctuated rather than continuous and their sedimentation rates were high. Also, these glacigenic debris flows lobes modified locally the slope angle and the stress field.

During the Last Glacial Maximum GDFs sedimentation rates might have reach 47 kg m^{-2} yr^{-1}. In this time Plaxis model shows overpressures around 0.65-0.75 at very shallow depths in the shelf and shelf edge, while in the middle slope the overpressures were slightly lower and located deeper. The LGM glacigenic debris flows isopach map shows a mean thickness of ~50 m in the upper slope and around 20 m in the middle slope. This high accumulation of GDFs in the

upper slope plus the fluid flow discharge towards the plumite layers from the shelf could be the reason of these high overpressures.

The role of the ice loading over a glacial margin during glacial periods has been evidenced. The coupling of rapid loading on the shelf, the high fluid discharge towards the upper slope, the existence of higher permeability plumite layers, and the rapid loading of these layers by the GDFs let to a noticeably overpressure increase.

Overpressures, weak layers or gas hydrates dissociation, among others, have been considered as a pre-conditioning factors for the slope failure (e.g. Bryn et al., 2005; Dimakis et al., 2000; Dugan, 2014; Stigall and Dugan, 2010). Gas hydrate dissociation could affect the slope during the sea level fall in the onset of glaciations or during the deglacial due to water temperature increase (Grozic, 2010; Mienert and Posewang, 1999). However, no evidences of present or past gas/fluid venting have been found in the study area, notwithstanding evidences of gas/fluid venting (i.e. pockmarks like features) have been found north and south of the Storfjorden and Kveithola TMFs (e.g. Canals et al., 2004; Roy et al., 2014; Vogt et al., 1999). Weak layers have been considered as a pre-conditioning factor in this area. Although the initial shear resistance of plumites (~10 kPa) is lower than GDF (~25 kPa), the strength contrast is not than high to be considered as a weak layer (Locat et al., 2014).Thus, overpressures have to be considered as the main pre-conditioning factor in Storfjorden and Kveithola TMFs.

5.9.2 Overpressure, source of slope instability

The coupled analysis of the safety factor and the pore pressures evolution depicts that overpressure generation clearly decreased the safety factor of the slope during glacial maximum and a few thousand years after pre-conditioning the slope to fail. A total of 23 recent landslides (last ~220 kyrs) have been identified in the Storfjorden and Kveithola TMFs. They can be split in three periods: prior to GM D (64 ka), last deglaciation and Holocene. The finite elements stability model shows that the lowest safety factor (~1.2) occurred at 21.7 ka, despite none of the landslide identified in the study area occurred at this time. Even so, seven of this landslides may occurred during the last deglacial and were rooted at depths around 15-40 mbsf. These landslides match the time and depths were the model shows mid to high overpressures at the middle slope. Even a better time window for the occurrence of the landslides during the last deglaciation can be achieved by using the Plaxis results. Hence, overpressures higher than 0.5 were preserved only until ~15 ka. So according with these results, the time window for the most probable occurrence of the landslides during the last deglaciation was only of ~4.5 kyrs (19.5 to 15 ka). This is also support for the SF evaluation results. The minimum SF during the last deglacial (1.4) was around 17 ka. Moreover, ten of the landslides identified in the area do not appear to have any deglacial sediments on top according to the geophysical data. Thus, they may be occurred during the Holocene. Despite the overpressures in the slope decreased during the Holocene, the analysis of the SF show another minimum of around

~1.4 at 7.9 ka. Kvalstad et al. (2005a) modeled the overpressure and slope stability in the Storegga landslide area. The results also agree that high sedimentation rates of low permeability sediments caused high overpressures, and in turn, a decrease in the slope stability. In both cases (Storfjorden/Kveithola and Storegga), although the low safety factor, a triggering mechanism was needed to initiate the landslides (Leynaud et al., 2007; Micallef et al., 2007).

Some works pointed at the isostatic rebound during the deglacial phase as a major factor for fault reactivation and earthquake generation (e.g. Leynaud et al., 2009; Sultan et al., 2004). Dugan (2014) also investigated the coupling between overpressure and fluid flow focusing and their relation with slope failures in Gulf of Mexico, Storegga and Cascadia concluding that although high overpressures occurred, earthquake shaking was the ultimate trigger. L'Heureux et al. (2013) pointed that in the Norwegian margin an earthquake with a return period of 10 kyrs or even lower could increase the overpressures up to 20% and decrease the safety factor below 1 in shallow sediments. In turn, Hampel et al. (2009) modeled fault response during growth and decay of an ice sheet. Their results indicate that ice unloading increases the number and magnitude of earthquakes compared to the loading phase. These periods of increased seismic activity last a few thousand years until activity returns to the normal situation. During the maximum seismogenic phase earthquakes with a moment magnitude Mw ~8 were possible in the NW Barents Sea (Hampel et al., 2009). All of these works supports the model presented in Chapter 4.8 where the landslides occurred

during the deglaciation phase. Thus, the sequence of events leading to the observed instabilities would therefore involve: 1) fluid flow focusing towards the upper slope due to till sediments aquitard effect over the shelf; 2) overpressure build-up in the high water content IGM laminated units during rapid deposition of thick GDF units, preconditioning the margin to failure; and 3) triggering by earthquakes induced by isostatic rebound during, or shortly after, the ice retreat.

However, the occurrence of landslides triggered by earthquakes during the Holocene, or even landslide LS-1.1 (occurred right before 64 ka), may not be associated to the isostatic rebound. The earthquake historical record south off Svalbard Archipelago shows that earthquakes up Mw≈5 occurred in the last decades. The closest structure to the study area, the Horndsund Fracture Zone, could be reactivated at any time without any ice influence (i.e. during IGM E). During IGM counturitic deposition were common along the Norwegian and western Barents Sea margins (Bryn et al., 2005; Rebesco et al., 2013). In fact, Rebesco et al. (2013) described counturitic deposits in the lower slope of Isfjorden and Bellsund fans (nth of the study area). Their high porosity, water content and under-consolidation favor liquefaction due to eartquake shaking (Laberg and Camerlenghi, 2008; Sultan et al., 2004a). In this frame, counturites could deposit during IGM G at the base of the Storfjorden slope, being rapidly loaded by sedimentation of GDF during GM F and afterwards by unit E, and liquefacted by an earthquake produced by the HFZ could be at the origin of landslide LS-1.1. In addition, the area affected by mass wasting can be large

because the contourites may have a very large areal distribution due to the intrabasinal extent of thermohaline current systems (Laberg and Camerlenghi, 2008). This could explain why landslide LS-1.1 involved up to 10 times more sediments than other recent landslides identified in the study area.

5.9.3 A cyclic model for TMF evolution

Alternation of GDF units and meltwater plumite units provides the more manifest evidence for a cyclic pattern in sedimentary processes during development of TMFs. However, there is a complex series of sedimentary and erosive processes that act at different periods within a glacial/interglacial cycle to deliver a series of deposits and to produce several landforms (see also Laberg and Vorren, 1996a, 1996b, Taylor et al., 2002, Ó Cofaigh et al., 2003, Lucchi et al. 2013). In this study we suggest a four-stage model for the evolution of Arctic TMFs (Fig. 5.16), and particularly for the Storfjorden TMF. The model considers the shape and location of the surface and subsurface erosive and depositional features in a spatial frame in combination with the sedimentary record. The location of canyons, gullies, submarine landslides and the GDFs lenses, or even the location within the TMF of all these features contributes to this understanding. These stages are:

a) Interglacial stage: During the present (and previous interglacials) hemipelagic and contour-current influenced sedimentation predominate (Fig. 5.16a). Based on their stratigraphic position in our seismic records,

gully formation in the Storfjorden and Kveithola TMFs cannot be ascribed to only one process or one particular stage. They form by interplay of various processes that act at different stages of TMF evolution. The process and timing of gully formation both in the Arctic and Antarctic have been long discussed (Gales et al., 2013; Laberg and Vorren, 1996b, 1995; Lucchi et al., 2013; Noormets et al., 2009; Pedrosa et al., 2011; Vorren et al., 1989). Because these gullies are most often draped by unit A_1 (Fig. 4.3), we mainly ascribe them to stage c). However, some gullies are completely devoid of sediment (Fig. 4.3) implying recent erosion. We hypothesize that some gullies are maintained by dense shelf water cascading (Martin and Cavalieri, 1989; Quadfasel et al., 1988; Schauer and Fahrbach, 1999). During this period overpressures decrease in the whole slope reaching values at the end of the interglacial around 0.2-0.3.

b) Glaciation and Glacial maximum stage: Onset of glaciation is marked by the advance of the ice streams from inland or from the inner shelf seawards and IRD distribution due to iceberg calving (Dowdeswell and Elverhøi, 2002). During glacial maxima, ice sheets reach the shelf edge, and the grounding zone sediments together with deforming subglacial till from beneath the ice stream is remobilized as GDFs, due to ice pushing and slope instability (Dowdeswell et al., 1998; Hillenbrand et al., 2005; King et al., 1998; Laberg and Vorren, 2000, 1995; Ó Cofaigh

et al., 2002) (Fig. 5.16b). From the onset of full GM, overpressures increase. At the shelf and upper slope overpressure values reach 0.7 while in the middle slope maximum values located at the first 100 mbsf reach 0.45. The fluid flow focusing towards the shelf edge and upper slope is maximum in this stage.

c) Deglaciation stage: Rapid deglaciation induces the deposition of plumites along the ice-free shelf and slope. These plumites are the result of subglacial meltwater discharge during rapid ice sheet retreat (Hesse et al., 1997), although meltwater plumes may also occur during the entire life-span of the ice sheet (i.e. Ó Cofaigh et al., 2013). According to dates obtained from the cores in the Storfjorden TMF it is likely, however, that intense plumite deposition took place during the early phase of ice sheet retreat (Lucchi et al., 2013). The rapid decay of the ice sheet was also responsible for the release of large volumes of ice rafted debris throughout the shelf and slope (Fig. 5.16c and Fig. 5.2d). Plumite deposition during the deglaciation was accompanied by extensive gully development. Most of the gullies identified developed in between two adjacent GDFs lobes and eroded little into these latter deposits. Erosion or deposition of plumite deposits by subsequent meltwater high-density underflows was determined by the density and velocity of these flows. Overpressures during this stage start to decrease although slightly.

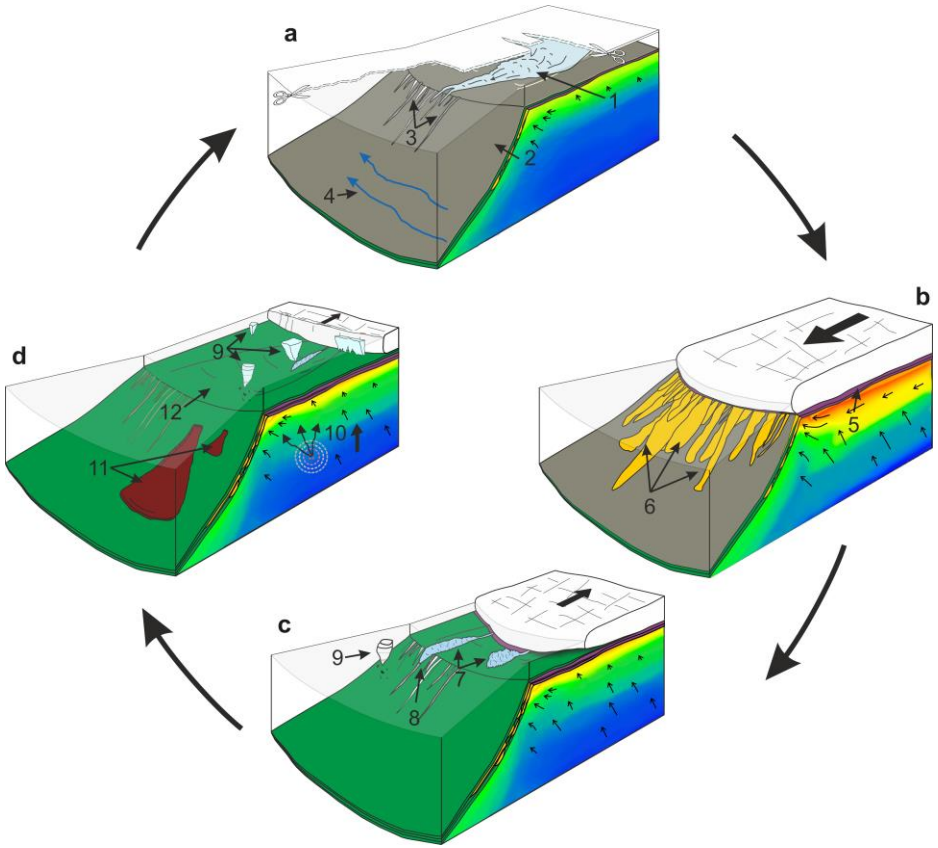

Fig. 5.16 Conceptual model of TMF evolution during a full glacial/interglacial cycle. a: Interglacial stage with hemipelagic sedimentation. During winter, dense shelf water flows due to sea ice formation and brine release maintain free of sediment some of the upper and middle slope gullies excavated during the deglaciation. b: GM, the material transported by ice streams is dumped over the shelf edge as debris flows which can erode the underlying sediments. c: Deglaciation: the turbid meltwater plumes leave a bed of plumites/turbidite sediments covering the shelf and TMF area, while the most energetic flows excavate gullies on the upper slope. The thickness of this unit increases towards the south. d: Submarine landslides triggered by earthquakes from isostatic rebound induced by ice sheet retreat. (1) hyperpycnical flow; (2) hemipelagic (interglacial) sediments; (3) gullies; (4) contour currents, (5) subglacial (diamicton) till; (6) debris flows; (7) meltwater plumes; (8) gully erosion and plumites/turbidite sedimentation; (9) iceberg rafting; (10) earthquake; (11) landslides; (12) glacial trough. In b) to d) sea-ice is not shown for a better visualization of the slope processes. Overpressure shading and fluid flow vectors are depicted.

Overpressures at the shelf remains with values around 0.6 while at the slope, maximum values are around 0.4.

d) Slope failure stage: Shortly after deglaciation, unloading of the shelf from the ice mass causes isostatic rebound and associated earthquakes. Ground shaking in already overpressured plumites triggers abundant submarine landslides (Fig. 5.16d). The location and extent of landslides is related to the thickness of plumite sediments of the previous IGM unit. The debris flows deposits that these landslides produce are completely different in terms of genetic mechanisms, physical properties and timing, than GDFs.

Chapter 6
Conclusions and Outlook

Chapter 6. Conclusions and Outlook

The combined analysis of an extensive high resolution geophysical dataset, core sedimentological data, geotechnical tests, and 2D hydrogeological and slope performance modeling of the Storfjorden TMF provides a better picture of the geological processes controlling the occurrence of submarine landslides during evolution of the margin. In this chapter, the most relevant findings of this thesis are summarized and some of the frontiers that could be addressed by future research are proposed.

6.1 Conclusions

Late Quaternary sedimentary history of the Storfjorden and Kveithola trough mouth fans

(1) Trough mouth fan architecture: The Late Quaternary (<220 ka) Storfjorden and Kveithola TMFs are made of eight units that alternate glacigenic debris flows (GDF) sedimentation delivered by ice streams grounded at the shelf edge during glacial maxima, and laminated plumite sequences deposited during the early deglaciation phase. The units made of stacked GDFs are mainly present in the northern and central part of the Storfjorden TMF where they are thicker and pinch out towards the lower slope. They also grade into what are probably

subglacial deformation tills on the shelf. Deglacial plumite sedimentation is spatially widespread over the TMF, but thicker sequences occur at the confluence of the Storfjorden and Kveithola TMFs. Plumite and interglacial hemipelagic sediments may partially fill gullies on the upper slope, but some gullies are devoid of sediment fill. We interpret that those gullies form by dense melt-water plumes and, in some instances, may remain active and maintained by cascading of dense shelf-waters.

(2) Cyclic evolution: We suggest a sedimentary model for Arctic TMFs with four major stages involving distinct deposits and sedimentary features. These include a) an interglacial stage dominated by hemipelagic sedimentation and maintenance of gullies carved during the previous deglaciation; b) a Glaciation and Glacial Maximum stage dominated by GDF deposition; c) a deglaciation stage characterized by the rapid accumulation of meltwater plumites and gully erosion, and d) a submarine landslide stage. Within the climate cycle, TMFs mainly record stages b and c, which are likely the shortest periods within a climate cycle. This indicates that sedimentation in TMFs is mainly punctuated rather than continuous through time.

(3) Age of the Late Quaternary units: Based on dates from sediment cores and correlation to adjacent areas and previous records, an age model for the identified units is proposed. The age of the GDFs corresponding to the last shelf edge glaciation periods is tentatively estimated at 19.5-22.5 ka (unit B), 61-65 ka (unit D) and 135-167 ka (unit F). The number of GDF units above regional

reflector R1 (three) is in agreement with a 220 ka age for this reflector. Ensuing mean decompacted sedimentation rates for glacigenic units are 17.7 kg m^{-2} yr^{-1} for unit B, 15.7 kg m^{-2} yr^{-1} for unit D and 2.2 kg m^{-2} yr^{-1} for unit F, one to two orders of magnitude larger than those of combined deglacial-interglacial sedimentation.

(4) Sedimentary control on submarine landslide occurrence: Several submarine landslides have been identified on the surface and sub-subsurface of the TMFs. We find that the majority of landslides occurred during deglaciation or early in the interglacial cycles and they are most often rooted in the previous deglacial/interglacial. From this, we infer that the mechanisms inducing slope failure involve a combination of factors: overpressure and earthquakes due to post-glacial isostatic rebound. An "unfavorable" stratigraphy arises from rapid loading by GDF of the previously deposited water-rich meltwater plumites, thus resulting in increased pore pressure development. A total of 24 landslides bodies occurred during the Late Quaternary and mainly in the past ~20 kyrs. Most of these landslides are located at the confluence of the Storfjorden and Kveithola trough mouth fans where the plumite thickness is maximum. Thus, thickness of meltwater plumites deposits likely exerts a major control on the number and volume of submarine landslides.

(5) Sediment geotechnical properties: Consolidation tests of glacial and glacially influenced sediments of the Storfjorden outer shelf and upper slope show that plumites (glacial melt-water plume derived sediments) have high void ratios and permeabilities with respect to glacigenic debris flows and tills at initial deposition conditions. Also, the compressibility index of plumite sediments is higher than glacigenic debris flows and tills. The tested till sediments, that supposedly carried the load of the tip of the ice-sheet, show low overconsolidation ratio (OCR~1.5). The latter is suggested to result from warm-based ice-sheet conditions and/or limited ice thickness close to the ice-sheet terminus.

(6) Plio-Quaternary hydrogeological evolution: "BASIN" modeling has been used to model the evolution of the Storfjorden TMF from 2.7 to 0.2 Ma. The model results show that onset of glacial sedimentation (~1.5 Ma) has a significant role in developing permeability barriers (tills) on the shelf decreasing upward fluid flow and diverting it towards the slope. These tills, coupled with the occurrence of intercalated plumite layers, two orders of magnitude higher permeability at initial deposition conditions, on the continental slope controls the margin fluid migration pathways. From 2.7 Ma to 220 ka the model shows relatively uniform overpressure distribution (0.35-0.60) along the margin with a

mean value around 0.5. At this stage the values below 0.1 are located at few hundred of meters below the sea floor and the higher values (up to 0.6) are located below the shelf edge and in the most distal part of the model.

(7) Influence of glaciation on margin hydrogeology: A detailed high resolution hydrogeological model of the last four glacial/inter-glacial cycles has been carried out by using the Finite Element PLAXIS software. Ice loading during Glacial Maxima caused high initial overpressures and promoted consolidation of the shelf sediments. These processes induced by rapid ice loading caused, in turn, high fluid expulsion rates. The low permeability tills on the shelf focused fluid flow towards the upper slope, while the shallower plumite sediments on the slope took in this outflow, preventing further consolidation while building up pore pressure that attained values up to 0.6 inside these layers. The higher overpressures (0.75) occurred during the Last Glacial Maximum and a few thousand years after. Despite overpressures underwent a decrease around of 2% per kyr during the deglacial, mid to high overpressures (0.5-0.7) remained at the end of the following inter-glacial stage mainly on the shelf but also in areas of the middle slope. However, the shallower sediments of the upper slope (above 50 mbsf) show values around 0.4 and 0.3-0.4 in the middle slope.

(8) Decreased stability of the Storfjorden and Kveithola TMFs during the last glacial cycle: Detailed slope stability analysis through the Last Glacial Maximum, last deglaciation and Holocene shows that overpressure development due to glacial and related sedimentary processes reduced the

Present-day safety factor of the margin by up to one half. Minimum values of ~1.2 occurred during the last glacial maximum, but low values around 1.3 were preserved throughout the last deglaciation. These low values of the SF during the last deglaciation could be responsible for the many the landslides rooted in the previous IGM plumite layer in the middle slope area. The mean thickness of the modeled landslide this landslide (most critical failure surface) is 30-40 m and mobilizes around 2.5 km of along-slope sediments. The occurrence of these lower values during the last deglaciation, matches the timing of the most recent landslides identified in the study area. In addition, despite the SF analysis during IGM E increases up to 3.6, the most critical failure surface matches with the area, location and rooting depth of the largest landslide identified in the area (LS1). The headscarps of these landslides are present in the middle slope and likely promoted a retrogressive slide process. Because the values of the SF remain above 1 despite the simulated landslides characteristics (most critical failure surfaces) match with those identified in the study area, an external trigger mechanisms such as earthquakes induced by glacio-eustatic rebound needs to be considered.

6.2 Outlook

This Thesis provides a comprehensive overview of the glacial, sedimentary, hydrogeological and mechanical processes involved in slope stability of formerly glaciated continental margins with an example of the western Barents Sea: The

Storfjorden TMF. The work has allowed clarifying some largely debated issues, such as the coupling between sedimentary depositional patterns and hydrogeological evolution and their relationship with the slope stability. From these new constraints, a Late Quaternary evolutionary model of high-latitude continental margins has been proposed. However, further geological, geotechnical and geophysical investigations are needed to deepen our understanding, ground truth the models and address some new questions arising from the findings in this thesis.

The detailed high resolution sub-bottom profiler dataset has been useful to properly identify the seismostratigraphy of the Storfjorden and Kveithola TMFs. However, this dataset only imaged the shallower ~120 ms twtt below seafloor. Single and multi-channel seismic lines have been used to identify the deeper units, but the coverage of these data is rather scarce. In addition, the deeper areas of the fans are not completely imaged, which makes impossible to properly define the characteristics of some of the identified landslides. To solve these issues a geophysical experiment including multibeam mapping, sub-bottom profiler and multi-channel seismic data that complement the existing data is proposed (Fig. 6.1). Across and along slope multichannel seismic profiles are needed to image and delimit the extent and volume of landslide LS-1, as well as sub-bottom profiler data at the toe of the slide. Also, these lines need to expand further to the SW in order to image the paleo-landslide PLS-1 and try to define its source area and volume. A few of these proposed experiments have been

initially planned in the frame of the EDIPO-DEGLABAR cruise performed on September-October, 2015. In addition, samples from hemipelagic sediments from the distal part of the slope, as well as deeper till samples from the shelf are needed to improve the geotechnical dataset available and better constrain the results from the hydrogeological models.

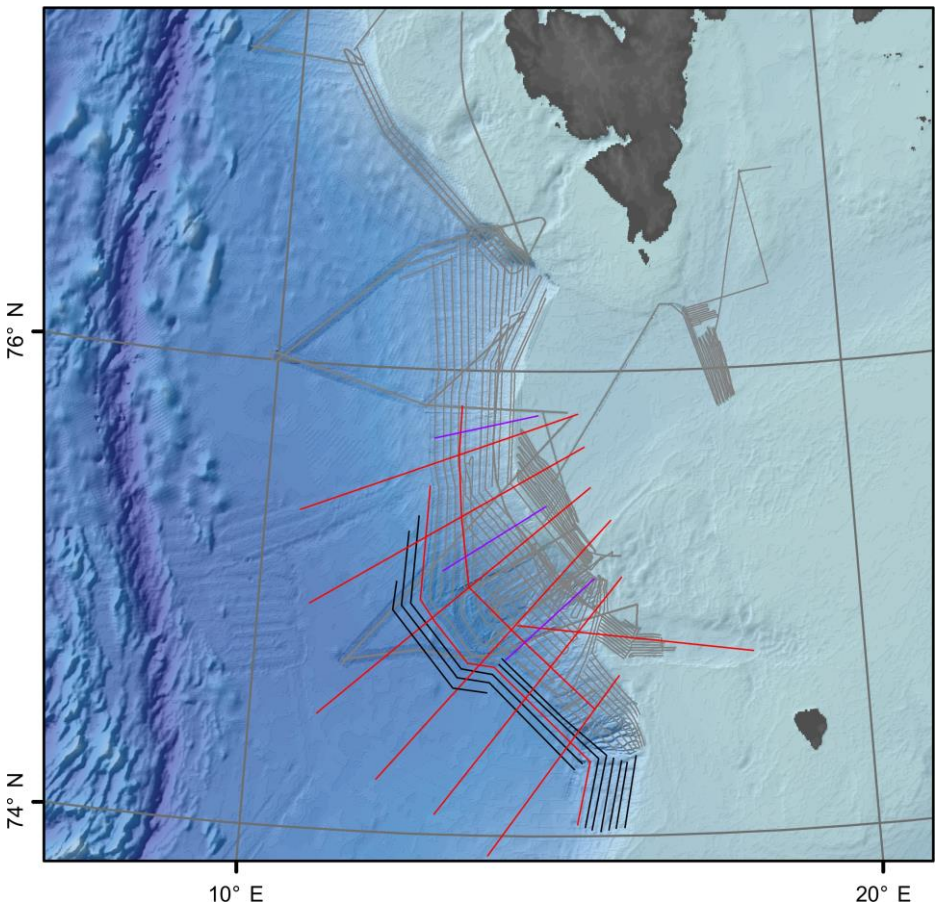

Fig. 6.1 Proposed sub-bottom (black), multi-channel seismic (red) and pore pressure penetrometer profiles (violet) to constrain different landslides identified in the area and verify the Present day sediment pore pressures field. In grey geophysical data acquired in the frame of SVAIS and EGLACOM cruises.

No chronostratigraphic data is available for units older than the Last Glacial Maximum. An age dating of the units below unit B (LGM) is needed to properly constraint the temporal evolution and sedimentation rates. These age constraints may also improve the hydrogeological models. Despite ODP site 986 and DSDP site 344 were drilled west off Svalbard, the sediments mainly correspond to distal environments rather than TMF sediments. An IODP proposal drilling the Storfjorden and Bear Island TMF would: elucidate the sediment characteristics and depositional environments throughout of the entire history of the TMF; provide a detailed chronostratigraphic framework for further numerical models; and contribute to the understanding of the climatically controlled evolution of a TMF, to that of the NW Barents Sea and, by extension, of the whole Earth climatic system.

Two software packages have been used in this thesis to model the hydrogeological evolution of the margin due to different limitations in both codes. Ideally, one modeling software package should account for sedimentation during the whole Plio-Quaternary, multiple materials, and model the ice loading effects while providing good mesh resolution. BASIN software is an open source program 2D finite element code written in Fortran 77/90, and could be updated to include these characteristics. An in situ pore pressure measurement experiment could be useful to validate the results obtained in the models and verify the Present day stress-state of the fan. In this regards a three multi-station along slope profiles are proposed (Fig. 6.1).

The models results show that despite the low values of the SF an external loading is needed to trigger the landslides. The earthquakes associated to the glacio-eustatic rebound induced by the ice retreat during the deglaciation have to be considered. The instrumental record that show earthquakes up to Mw~6 occurred in the last 55 years in the area, however larger earthquakes could have occurred during the last deglaciation. Turpeinen et al. (2008) modeled the ice growth and decay effect on fault reactivation and earthquake generation. Results from this modeling exercise suggest that the Hornsund Fracture Zone was likely reactivated due to these glacio-eustatic adjustments and may have caused larger earthquakes than at Present. In this regard, the study of the earthquake effects on the Storfjorden TMF sediments and the ground motions needed to trigger landslides of different sizes could help explain the origin of the identified landslides. It should be noticed that, despite significant overpressures are generated during the sedimentary evolution of the TMMF, slope SF values remain above 1, with values up to 3.6 when landslide LS-1 occurred. In addition, it is necessary to understand the actual stress conditions and characteristics of the nearby HFZ and its actual rupture probability combined with a study of its tsunamigenic potential and that of the past landslides for a complete thorough geohazard assessment.

An additional line of study in this area involves accurate dating of the landslides occurred since the last deglacial. Due to the limited sub-bottom profiles (and their resolution) it is presently difficult to assess the thickness of hemipelagic

sediments on the top of the landslides (which is in the order of centimeters). A proper dating using core samples could help to elucidate their timing throughout the last deglaciation and the Holocene, determine the frequency vs magnitude relationships for these late Quaternary landslides and assess clustering at particular times in the evolution of the TMF.

References

References

Alley, R.B., Blankenship, D.D., Rooney, S.T., Bentley, C.R., 1989. Sedimentation beneath ice shelves - The view from ice stream B. Marine Geology 85, 101–120.

Andersen, E.S., Dokken, T.M., Elverhøi, A., Solheim, A., Fossen, I., 1996. Late quaternary sedimentation and glacial history of the western Svalbard continental margin. Marine Geology 133, 123–156. doi:10.1016/0025-3227(96)00022-9

Arregui-Mena, J.D., Margetts, L., Mummery, P.M., 2014. Practical Application of the Stochastic Finite Element Method. Archives of Computational Methods in Engineering 171–190. doi:10.1007/s11831-014-9139-3

Atakan, K., Ojeda, A., 2005. Stress transfer in the Storegga area, offshore mid-Norway. Marine and Petroleum Geology 22, 161–170. doi:10.1016/j.marpetgeo.2004.10.005

Baeten, N.J., Laberg, J.S., Vanneste, M., Forsberg, C.F., Kvalstad, T.J., Forwick, M., Vorren, T.O., Haflidason, H., 2014. Origin of shallow submarine mass movements and their glide planes-Sedimentological and geotechnical analyses from the continental slope off northern Norway. Journal of Geophysical Research: Earth Surface 119, 2335–2360. doi:10.1002/2013JF003068

Behnia, P., Harris, J.R., Harrison, C., St-Onge, M., Okulitch, A., Irwin, D., Gordey, S.P., 2013. Geo-mapping Frontiers: compilation and interpretation of geologic structures north of 60°, Canada. doi:10.4095/292917

Behrmann, J.H., Flemings, P.B., John, C.M., Behrmann, J.H., Flemings, P.B., John, C.M., Iturrino, G.J., Aizawa, Y., Binh, N.T.T., De Silva, N., Dugan, B., Edeskär, T.M., Franke, C., Gay, A., Gilhooly, W.P., Gutierrez-Pastor, J., Jiang, S.Y., Long, H., Moore, J.C., Nonoura, T., Pirmez, C., Reichow, M., Sawyer, D.E., Schneider, J., Shumnyk, A. V., Suzuki, T., Takano, Y., Urgeles, R., Yamamoto, Y., Zampetti, V., 2006. Rapid sedimentation, overpressure, and focused fluid flow, gulf of mexico continental margin. Scientific Drilling 1, 12–17. doi:10.2204/iodp.sd.3.03.2006

Bergh, S.G., Grogan, P., 2003. Tertiary structure of the Sørkapp-Hornsund Region, South Spitsbergen, and implications for the offshore southern extension of the fold-thrust Belt. Norsk Geologisk Tidsskrift 83, 43–60.

Bethke, C.M., Lee, M., Park, J., 2007. Basin Modeling with Basin2. University of Illinois, Illiniois.

Bitzer, K., 1996. Modeling consolidation sedimentary and fluid basins flow. Computers & Geosciences 22, 467–478.

Bitzer, K., 1999. Two-dimensional simulation of clastic and carbonate sedimentation,

consolidation, subsidence, fluid flow, heat flow and solute transport during the formation of sedimentary basins. Computers & Geosciences 25, 431–447. doi:10.1016/S0098-3004(98)00147-2

Bjarnadóttir, L.R., Rüther, D.C., Winsborrow, M.C.M., Andreassen, K., 2013. Grounding-line dynamics during the last deglaciation of Kveithola, W Barents Sea, as revealed by seabed geomorphology and shallow seismic stratigraphy. Boreas 42, 84–107. doi:10.1111/j.1502-3885.2012.00273.x

Bondevik, S., Løvholt, F., Harbitz, C., Mangerud, J., Dawson, A., Svendsen, J.I., 2005. The Storegga Slide tsunami - Comparing field observations with numerical simulations. Marine and Petroleum Geology 22, 195–208. doi:10.1016/j.marpetgeo.2004.10.003

Bondevik, S., Stormo, S.K., Skjerdal, G., 2012. Green mosses date the Storegga tsunami to the chilliest decades of the 8.2 ka cold event. Quaternary Science Reviews 45, 1–6. doi:10.1016/j.quascirev.2012.04.020

Boudreau, B.P., 1996. The diffusive tortuosity of fine-grained unlithified sediments. Geochimica et Cosmochimica Acta 60, 3139–3142. doi:10.1016/0016-7037(96)00158-5

Boulton, G.S., Hindmarsh, R.C.A., 1987. Sediment deformation beneath glaciers: Rheology and geological consequences. Journal of Geophysical Research 92, 9059. doi:10.1029/JB092iB09p09059

British Standards Institution, 1990. Part 6. Consolidation and permeability test in hydraulic cells and with pore pressure measurement, in: Soils for Civil Engineering Purposes. Road Enineering Satndards Committee, p. 61.

Brothers, D.S., Luttrell, K.M., Chaytor, J.D., 2013. Sea-level-induced seismicity and submarine landslide occurrence. Geology 41, 979–982. doi:10.1130/G34410.1

Bryn, P., Berg, K., Forsberg, C.F., Solheim, A., Kvalstad, T.J., 2005. Explaining the Storegga Slide. Marine and Petroleum Geology 22, 11–19. doi:10.1016/j.marpetgeo.2004.12.003

Bryn, P., Berg, K., Stoker, M., Haflidason, H., Solheim, A., 2005. Contourites and their relevance for mass wasting along the Mid-Norwegian Margin. Marine and Petroleum Geology 22, 85–96. doi:10.1016/j.marpetgeo.2004.10.012

Bugge, T., Befring, S., Belderson, R.H., Eidvin, T., Jansen, E., Kenyon, N.H., Hoitedahi, H., Petter, H., 1987. A Giant Three-Stage Submarine Slide Off Norway. Geo-Marine Letters 7, 191–198.

Bungum, H., Lindholm, C., Faleide, J.I., 2005. Postglacial seismicity offshore mid-Norway with emphasis on spatio-temporal-magnitudal variations. Marine and Petroleum Geology 22, 137–148. doi:10.1016/j.marpetgeo.2004.10.007

Bunz, S., Mienert, J., Bryn, P., Berg, K., 2005. Fluid flow impact on slope failure from

3D seismic data: a case study in the Storegga Slide. Basin Research 17, 109–122. doi:10.1111/j.1365-2117.2005.00256.x

Butt, F.A., Drange, H., Elverhøi, A., Otterå, O.H., Solheim, A., 2002. Modelling Late Cenozoic isostatic elevation changes in the Barents Sea and their implications for oceanic and climatic regimes: preliminary results. Quaternary Science Reviews 21, 1643–1660. doi:10.1016/S0277-3791(02)00018-5

Butt, F.A., Elverhøi, A., Solheim, A., Forsberg, C.F., 2000. Deciphering late cenozoic development of the western Svalbard Margin from ODP Site 986 results. Marine Geology 169, 373–390. doi:10.1016/S0025-3227(00)00088-8

Canals, M., Lastras, G., Urgeles, R., Casamor, J.L., Mienert, J., Cattaneo, A., De Batist, M., Haflidason, H., Imbo, Y., Laberg, J.S., Locat, J., Long, D., Longva, O., Masson, D.G., Sultan, N., Trincardi, F., Bryn, P., 2004. Slope failure dynamics and impacts from seafloor and shallow sub-seafloor geophysical data: Case studies from the COSTA project. Marine Geology 213, 9–72. doi:10.1016/j.margeo.2004.10.001

Christoffersen, P., Tulaczyk, S., 2003. Signature of palaeo-ice-stream stagnation: till consolidation induced by basal freeze-on. Boreas 32, 114–129. doi:10.1111/j.1502-3885.2003.tb01433.x

Cuffey, K.M., Conway, H., Gades, A.M., Hallet, B., Lorrain, R., Severinghaus, J.P., Steig, E.J., Vaughn, B., White, J.W.C., 2000. Entrainment at cold glacier beds. Geology 28, 351. doi:10.1130/0091-7613(2000)28<351:EACGB>2.0.CO;2

Dahlgren, K.I., Vorren, T.O., Stoker, M.S., Nielsen, T., Nygård, A., Petter Sejrup, H., 2005. Late Cenozoic prograding wedges on the NW European continental margin: their formation and relationship to tectonics and climate. Marine and Petroleum Geology 22, 1089–1110. doi:10.1016/j.marpetgeo.2004.12.008

DeConto, R.M., Pollard, D., 2003. Rapid Cenozoic glaciation of Antarctica induced by declining atmospheric CO2. Nature 421, 245–249. doi:10.1038/nature01290

Dimakis, P., Elverhøi, A., Høeg, K., Solheim, A., Harbitz, C., Laberg, J.S., O. Vorren, T., Marr, J., 2000. Submarine slope stability on high-latitude glaciated Svalbard-Barents Sea margin. Marine Geology. doi:10.1016/S0025-3227(99)00076-6

Dokken, T.M., Hald, M., 1996. Rapid climatic shifts during isotope stages 2 – 4 in the Polar North Atlantic. Geology 24, 599–602. doi:10.1130/0091-7613(1996)024<0599

Dowdeswell, J.A., Cofaigh, C.Ó., Noormets, R., Larter, R.D., Hillenbrand, C., Benetti, S., Evans, J., Pudsey, C.J., 2008. A major trough-mouth fan on the continental margin of the Bellingshausen Sea , West Antarctica : The Belgica Fan 252, 129–140. doi:10.1016/j.margeo.2008.03.017

Dowdeswell, J.A., Elverhøi, A., 2002. The timing of initiation of fast-flowing ice streams during a glacial cycle inferred from glacimarine sedimentation. Marine

Geology 188, 3–14.

Dowdeswell, J.A., Elverhøi, A., Spielhagen, R., 1998. Glacimarine sedimentary processes and facies on the Polar North Atlantic margins. Quaternary Science Reviews 17, 243–272. doi:10.1016/S0277-3791(97)00071-1

Dowdeswell, J.A., Kenyon, N.H., Elverhøi, A., Laberg, J.S., Hollender, F.-J., Mienert, J., Siegert, M.J., 1996. Large-scale sedimentation on the glacier-influenced polar North Atlantic Margins: Long-range side-scan sonar evidence. Geophysical Research Letters 23, 3535–3538. doi:10.1029/96GL03484

Dowdeswell, J.A., Siegert, M.J., 1999. Ice-sheet numerical modeling and marine geophysical measurements of glacier-derived sedimentation on the Eurasian Arctic continental margins. Geological Society of America Bulletin 111, 1080–1097. doi:10.1130/0016-7606(1999)111<1080:ISNMAM>2.3.CO;2

Dugan, B., 2014. A Review of Overpressure, Flow Focusing, and Slope Failure, in: Krastel, S., Behrmann, J.-H., Völker, D., Stipp, M., Berndt, C., Urgeles, R., Chaytor, J., Huhn, K., Strasser, M., Harbitz, C.B. (Eds.), Submarine Mass Movements and Their Consequences, Advances in Natural and Technological Hazards Research. Springer International Publishing, Cham, pp. 85–94. doi:10.1007/978-3-319-00972-8

Dugan, B., Flemings, P.., 2000. The New Jersey margin: compaction and fluid flow. Journal of Geochemical Exploration 69–70, 477–481. doi:10.1016/S0375-6742(00)00058-3

Dugan, B., Sheahan, T.C., 2012. Offshore sediment overpressures of passive margins: Mechanisms, measurement, and models. Reviews of Geophysics 50, 1–20. doi:10.1029/2011RG000379

Eldholm, O., Sundvor, E., Myhre, A.M., Faleide, J.I., 1984. Cenozoic evolution of the continental margin off Norway and western Svalbard, in: Spencer, A.M. (Ed.), Petroleum Geology of the North European Margin. Springer Netherlands, Dordrecht, pp. 3–18. doi:10.1007/978-94-009-5626-1

Elverhøi, A., Dowdeswell, J.A., Funder, S., Mangerud, J., Stein, R., 1998. Glacial and oceanic history of the polar north atlantic margins: An overview. Quaternary Science Reviews 17, 1–10. doi:10.1016/S0277-3791(97)00073-5

Elverhøi, A., Svendsen, J.I., Solheims, A., Andersen, E.S., Milliman, J., Mangerud, J., Hooke, R.L., 1995. Late Quaternary sediment yield from the high Arctic Svalbard area. Journal of Geology 103, 1–17. doi:10.1086/629718

Evans, D., Harrison, Z., Shannon, P.M., Laberg, J.S., Nielsen, T., Ayers, S., Holmes, R., Hoult, R.J., Lindberg, B., Haflidason, H., Long, D., Kuijpers, a., Andersen, E.S., Bryn, P., 2005. Palaeoslides and other mass failures of Pliocene to Pleistocene age along the Atlantic continental margin of NW Europe. Marine and Petroleum Geology 22, 1131–1148. doi:10.1016/j.marpetgeo.2005.01.010

Faleide, J.I., Gudlaugsson, S.T., Eldholm, O., Myhre, A.M., Jackson, H.R., 1991. Deep seismic transects across the sheared western Barents Sea-Svalbard continental margin. Tectonophysics 189, 73–89. doi:10.1016/0040-1951(91)90488-E

Faleide, J.I., Solheim, A., Fiedler, A., Hjelstuen, B.O., Andersen, E.S., Vanneste, K., 1996. Late Cenozoic evolution of the western Barents Sea-Svalbard continental margin. Global and Planetary Change 12, 53–74. doi:10.1016/0921-8181(95)00012-7

Faleide, J.I., Tsikalas, F., Breivik, A.J., Mjelde, R., Ritzmann, O., Wilson, J., Eldholm, O., 2008. Structure and evolution of the continental margin off Norway and the Barents Sea. Episodes 31, 82–91.

Faleide, J.I., Vdgnes, E., Gudlaugsson, S.T., 1993. Late Mesozoic-Cenozoic evolution of the south-western Barents Sea in a regional rift-shear tectonic setting. Marine and Petroleum Geology 10, 186–214.

Fiedler, A., Faleide, J.I., 1996. Cenozoic sedimentation along the southwestern Barents Sea margin in relation to uplift and erosion of the shelf. Global and Planetary Change 12, 75–93. doi:10.1016/0921-8181(95)00013-5

Flemings, P., Long, H., Dugan, B., Germaine, J., John, C., Behrmann, J., Sawyer, D., 2008. Pore pressure penetrometers document high overpressure near the seafloor where multiple submarine landslides have occurred on the continental slope, offshore Louisiana, Gulf of Mexico. Earth and Planetary Science Letters 269, 309–325. doi:10.1016/j.epsl.2007.12.005

Forsberg, C.F., Solheim, A., Jansen, E., Andersen, E.S., 1999. The Depositional Enviroment of the Western Svalbard Margin During the Late Pliocene and the Pleistocene: Sedimentary Facies Changes at Site 986. Proceedings of the Ocean Drilling Program, Scientific Results 162, 233–246. doi:10.2973/odp.proc.sr.162.1999

Friedman, G.M., Sanders, F.E., 1978. Principles of sedimentology. John Wiley & Sons, New York.

Gales, J.A., Larter, R.D., Mitchell, N.C., Dowdeswell, J.A., 2013. Geomorphic signature of Antarctic submarine gullies: Implications for continental slope processes. Marine Geology 337, 112–124. doi:10.1016/j.margeo.2013.02.003

Grozic, J.L.H., 2010. Interplay Between Gas Hydrates and Submarine Slope Failure. Submarine Mass Movements and Their Consequences. Advances in Natural and Technological Hazards Research 28, 11–30.

Gutierrez, M., Wangen, M., 2005. Modeling of compaction and overpressuring in sedimentary basins. Marine and Petroleum Geology 22, 351–363. doi:10.1016/j.marpetgeo.2005.01.003

Haflidason, H., Lien, R., Sejrup, H.P., Forsberg, C.F., Bryn, P., 2005. The dating and morphometry of the Storegga Slide. Marine and Petroleum Geology 22, 123–136.

doi:10.1016/j.marpetgeo.2004.10.008

Hampel, A., Hetzel, R., Maniatis, G., Karow, T., 2009. Three-dimensional numerical modeling of slip rate variations on normal and thrust fault arrays during ice cap growth and melting. Journal of Geophysical Research 114, B08406. doi:10.1029/2008JB006113

Hao, Q., Wang, L., Oldfield, F., Peng, S., Qin, L., Song, Y., Xu, B., Qiao, Y., Bloemendal, J., Guo, Z., 2012. Delayed build-up of Arctic ice sheets during 400,000-year minima in insolation variability. Nature 490, 393–6. doi:10.1038/nature11493

Hesse, R., Khodabakhsh, S., Klaucke, I., Ryan, W.B.F., 1997. Asymmetrical turbid surface-plume deposition near ice-outlets of the Pleistocene Laurentide ice sheet in the Labrador Sea. Geo-Marine Letters 17, 179–187. doi:10.1007/s003670050024

Hillenbrand, C.-D., Baesler, a., Grobe, H., 2005. The sedimentary record of the last glaciation in the western Bellingshausen Sea (West Antarctica): Implications for the interpretation of diamictons in a polar-marine setting. Marine Geology 216, 191–204. doi:10.1016/j.margeo.2005.01.007

Hjelstuen, B., Eldholm, O., Faleide, J., 2007. Recurrent Pleistocene mega-failures on the SW Barents Sea margin. Earth and Planetary Science Letters 258, 605–618. doi:10.1016/j.epsl.2007.04.025

Hjelstuen, B.O., Elverhøi, A., Faleide, J.I., 1996. Cenozoic erosion and sediment yield in the drainage area of the Storfjorden Fan. Global and Planetary Change 12, 95–117. doi:10.1016/0921-8181(95)00014-3

Hughes, A.L.C., Gyllencreutz, R., Lohne, Ø.S., Mangerud, J., Svendsen, J.I., 2016. The last Eurasian ice sheets - a chronological database and time-slice reconstruction, DATED-1. Boreas 45, 1–45. doi:10.1111/bor.12142

Hughes Clarke, J.E., Mayer, L.A., Wells, D.E., 1996. Shallow-water imaging multibeam sonars: A new tool for investigating seafloor processes in the coastal zone and on the continental shelf. Marine Geophysical Researches 18, 607–629. doi:10.1007/BF00313877

Hühnerbach, V., Masson, D.G., 2004. Landslides in the North Atlantic and its adjacent seas: An analysis of their morphology, setting and behaviour. Marine Geology 213, 343–362. doi:10.1016/j.margeo.2004.10.013

Hurtado, J.E., Barbat, A.H., 1998. Monte Carlo Techniques In Computational Stochastic Mechanics. Archives of Computational Methods in Engineering 5, 3–29. doi:10.1007/BF02736747

Jakobsson, M., Mayer, L., Coakley, B., Dowdeswell, J.A., Forbes, S., Fridman, B., Hodnesdal, H., Noormets, R., Pedersen, R., Rebesco, M., Schenke, H.W., Zarayskaya, Y., Accettella, D., Armstrong, A., Anderson, R.M., Bienhoff, P., Camerlenghi, A., Church, I., Edwards, M., Gardner, J. V., Hall, J.K., Hell, B.,

Hestvik, O., Kristoffersen, Y., Marcussen, C., Mohammad, R., Mosher, D., Nghiem, S. V., Pedrosa, M.T., Travaglini, P.G., Weatherall, P., 2012. The International Bathymetric Chart of the Arctic Ocean (IBCAO) Version 3.0. Geophysical Research Letters 39, n/a-n/a. doi:10.1029/2012GL052219

Jessen, S.P., Rasmussen, T.L., Nielsen, T., Solheim, A., 2010. A new Late Weichselian and Holocene marine chronology for the western Svalbard slope 30,000–0 cal years BP. Quaternary Science Reviews 29, 1301–1312. doi:10.1016/j.quascirev.2010.02.020

King, E.L., Haflidason, H., Sejrup, H.P., Løvlie, R., 1998. Glacigenic debris flows on the North Sea Trough Mouth Fan during ice stream maxima. Marine Geology 152, 217–246.

Kleiber, H.., Knies, J., Niessen, F., 2000. The Late Weichselian glaciation of the Franz Victoria Trough, northern Barents Sea: ice sheet extent and timing. Marine Geology 168, 25–44. doi:10.1016/S0025-3227(00)00047-5

Knies, J., Kleiber, H., Matthiessen, J., Muller, C., Nowaczyk, N., 2001. Marine ice-rafted debris records constrain maximum extent of Saalian and Weichselian ice-sheets along the northern Eurasian margin. Global and Planetary Change 31, 45–64. doi:10.1016/S0921-8181(01)00112-6

Knies, J., Matthiessen, J., Vogt, C., Laberg, J.S., Hjelstuen, B.O., Smelror, M., Larsen, E., Andreassen, K., Eidvin, T., Vorren, T.O., 2009. The Plio-Pleistocene glaciation of the Barents Sea–Svalbard region: a new model based on revised chronostratigraphy. Quaternary Science Reviews 28, 812–829. doi:10.1016/j.quascirev.2008.12.002

Kvalstad, T.J., Andresen, L., Forsberg, C.F., Berg, K., Bryn, P., Wangen, M., 2005a. The Storegga slide: evaluation of triggering sources and slide mechanics. Marine and Petroleum Geology 22, 245–256. doi:10.1016/j.marpetgeo.2004.10.019

Kvalstad, T.J., Nadim, F., Kaynia, A.M., Mokkelbost, K.H., Bryn, P., 2005b. Soil conditions and slope stability in the Ormen Lange area. Marine and Petroleum Geology 22, 299–310. doi:10.1016/j.marpetgeo.2004.10.021

L'Heureux, J.S., Vanneste, M., Rise, L., Brendryen, J., Forsberg, C.F., Nadim, F., Longva, O., Chand, S., Kvalstad, T.J., Haflidason, H., 2013. Stability, mobility and failure mechanism for landslides at the upper continental slope off Vesterålen, Norway. Marine Geology 346, 192–207. doi:10.1016/j.margeo.2013.09.009

Laberg, J.., Vorren, T.., Dowdeswell, J.., Kenyon, N.., Taylor, J., 2000. The Andøya Slide and the Andøya Canyon, north-eastern Norwegian–Greenland Sea. Marine Geology 162, 259–275. doi:10.1016/S0025-3227(99)00087-0

Laberg, J.S., Andreassen, K., Knies, J., Vorren, T.O., Winsborrow, M., 2010. Late Pliocene-Pleistocene development of the Barents Sea Ice Sheet. Geology 38, 107–110. doi:10.1130/G30193.1

Laberg, J.S., Camerlenghi, A., 2008. THE SIGNIFICANCE OF CONTOURITES FOR SUBMARINE SLOPE STABILITY, First Edit. ed, CONTOURITES. Elsevier. doi:10.1016/S0070-4571(08)10025-5

Laberg, J.S., Eilertsen, R.S., Vorren, T.O., 2009. The paleo-ice stream in Vestfjorden, north Norway, over the last 35 k.y.: Glacial erosion and sediment yield. Geological Society of America Bulletin 121, 434–447. doi:10.1130/B26277.1

Laberg, J.S., Forwick, M., Husum, K., 1996. Proceedings of the Ocean Drilling Program, 162 Initial Reports. Proceedings of the Ocean Drilling Program 162, 2973. doi:10.2973/odp.proc.ir.162.1996

Laberg, J.S., Stoker, M.S., Dahlgren, K.I.T., Haas, H. De, Haflidason, H., Hjelstuen, B.O., Nielsen, T., Shannon, P.M., Vorren, T.O., van Weering, T.C.E., Ceramicola, S., 2005. Cenozoic alongslope processes and sedimentation on the NW European Atlantic margin. Marine and Petroleum Geology 22, 1069–1088. doi:10.1016/j.marpetgeo.2005.01.008

Laberg, J.S., Vorren, T.O., 1993. A Late Pleistocene submarine slide on the Bear Island Trough Mouth Fan. Geo-Marine Letters 13, 227–234. doi:10.1007/BF01207752

Laberg, J.S., Vorren, T.O., 1995. Late Weichselian submarine debris flow deposits on the Bear Island Trough Mouth Fan. Marine Geology 127, 45–72. doi:10.1016/0025-3227(95)00055-4

Laberg, J.S., Vorren, T.O., 1996a. The Middle and Late Pleistocene evolution of the Bear Island Trough Mouth Fan. Global and Planetary Change 12, 309–330.

Laberg, J.S., Vorren, T.O., 1996b. The glacier-fed fan at the mouth of Storfjorden trough, western Barents Sea: a comparative study. Geologische Rundschau. doi:10.1007/BF02422239

Laberg, J.S., Vorren, T.O., 2000. The Trænadjupet Slide, offshore Norway - Morphology, evacuation and triggering mechanisms. Marine Geology 171, 95–114. doi:10.1016/S0025-3227(00)00112-2

Laberg, J.S., Vorren, T.O., 2004. Weichselian and Holocene growth of the northern high-latitude Lofoten Contourite Drift on the continental slope of Norway. Sedimentary Geology 164, 1–17. doi:10.1016/j.sedgeo.2003.07.004

Laberg, J.S., Vorren, T.O., Mienert, J., Evans, D., Lindberg, B., Ottesen, D., Kenyon, N.H., Henriksen, S., 2002. Late Quaternary palaeoenvironment and chronology in the Trænadjupet Slide area offshore Norway. Marine Geology 188, 35–60. doi:10.1016/S0025-3227(02)00274-8

Lambeck, K., Purcell, A., Funder, S., Kjær, K., Larsen, E., Möller, P., 2006. Constraints on the Late Saalian to early Middle Weichselian ice sheet of Eurasia from field data and rebound modelling. Boreas 35, 539–575. doi:10.1080/03009480600781875

Landvik, J.Y., Bondevik, S., Elverhøi, A., Fjeldskaar, W., Mangerud, J., Salvigsen, O., Siegert, M.J., Svendsen, J.-I., Vorren, T.O., 1998. Last Glacial Maximum of Svalbard and the Barents Sea Area: Ice Sheet Extent and Configuration. Quaternary Science Reviews 17, 43–75. doi:10.1016/S0277-3791(97)00066-8

Larsen, E., Kjær, K., Demidov, I., Funder, S., Grøsfjeld, K., Houmark-Nielsen, M., Jensen, M., Linge, H., Lysså, A., 2006. Late Pleistocene glacial and lake history of northwestern Russia. Boreas 35, 394–424. doi:10.1080/03009480600781958

Lee, H.J., 2009. Timing of occurrence of large submarine landslides on the Atlantic Ocean margin. Marine Geology 264, 53–64. doi:10.1016/j.margeo.2008.09.009

Lee, S., Shaw, J., Ho, R., Burger, J., Singh, S., Troyer, B., 1999. Illuminating the shadows: Tomography, attenuation and pore pressure processing in the South Caspian Sea. Journal of Petroleum Science and Engineering 24, 1–12. doi:10.1016/S0920-4105(99)00019-4

Lerche, I., Yu, Z., Tørudbakken, B., Thomsen, R.O., 1997. Ice loading effects in sedimentary basins with reference to the Barents sea. Marine and Petroleum Geology 14, 277–338. doi:10.1016/S0264-8172(96)00059-1

Leynaud, D., Mienert, J., Nadim, F., 2004. Slope stability assessment of the Helland Hansen area offshore the mid-Norwegian margin. Marine Geology 213, 457–480. doi:10.1016/j.margeo.2004.10.019

Leynaud, D., Mienert, J., Vanneste, M., 2009. Submarine mass movements on glaciated and non-glaciated European continental margins : A review of triggering mechanisms and preconditions to failure. Marine and Petroleum Geology 26, 618–632. doi:10.1016/j.marpetgeo.2008.02.008

Leynaud, D., Sultan, N., Mienert, J., 2007. The role of sedimentation rate and permeability in the slope stability of the formerly glaciated Norwegian continental margin: The Storegga slide model. Landslides 4, 297–309. doi:10.1007/s10346-007-0086-z

Lindberg, B., Laberg, J.S., Vorren, T.O., 2004. The Nyk Slide-morphology, progression, and age of a partly buried submarine slide offshore northern Norway. Marine Geology 213, 277–289. doi:10.1016/j.margeo.2004.10.010

Lisiecki, L.E., Raymo, M.E., 2005. A Pliocene-Pleistocene stack of 57 globally distributed benthic δ 18 O records. Paleoceanography 20, 1–17. doi:10.1029/2004PA001071

Liu, Y., Qiu, N., Yao, Q., Chang, J., Xie, Z., 2016. Distribution, origin and evolution of the Upper Triassic overpressures in the central portion of the Sichuan Basin, SW China. Journal of Petroleum Science and Engineering 146, 1116–1129. doi:10.1016/j.petrol.2016.08.016

Llopart, J., Urgeles, R., Camerlenghi, A., Lucchi, R.G., De Mol, B., Rebesco, M., Pedrosa, M.T., 2014. Slope Instability of Glaciated Continental Margins:

Constraints from Permeability-Compressibility Tests and Hydrogeological Modeling Off Storfjorden, NW Barents Sea, in: Krastel, S., Behrmann, J.-H., Völker, D., Stipp, M., Berndt, C., Urgeles, R., Chaytor, J., Huhn, K., Strasser, M., Harbitz, C.B. (Eds.), Submarine Mass Movements and Their Consequences, Advances in Natural and Technological Hazards Research 37. Springer International Publishing, pp. 95–104. doi:10.1007/978-3-319-00972-8_9

Locat, J., Lee, H.J., 2000. Submarine Landslides : Advances and Challenges, in: Bromhead, E., Dixon, N., Ibsen, M.-L. (Eds.), Proceedings of the 8th International Symposium on Landslides, Volume 2. Thomas Telford, London, pp. 1–30.

Locat, J., Leroueil, S., Locat, A., Lee, H., 2014. Weak layers: their definition and classification from a geotechnical perspective, in: Krastel, S., Behrmann, J.-H., Völker, D., Stipp, M., Berndt, C., Urgeles, R., Chaytor, J., Huhn, K., Strasser, M., Harbitz, B.C. (Eds.), Submarine Mass Movements and Their Consequences: 6th International Symposium. Springer International Publishing, Cham, pp. 3–12. doi:10.1007/978-3-319-00972-8_1

Lucchi, R.G., Camerlenghi, A., Rebesco, M., Colmenero-Hidalgo, E., Sierro, F.J., Sagnotti, L., Urgeles, R., Melis, R., Morigi, C., Barcena, M.A., Giorgetti, G., Villa, G., Persico, D., Flores, J.A., Rigual, A., Pedrosa, M.T., Macri, P., Caburlotto, A., 2013. Postglacial sedimentary processes on the Storfjorden and Kveithola trough mouth fans: Significance of extreme glacimarine sedimentation. Global and Planetary Change 111, 309–326. doi:10.1016/j.gloplacha.2013.10.008

Lucchi, R.G., Pedrosa, M.T., Camerlenghi, A., Urgeles, R., De Mol, B., Rebesco, M., 2012. Recent Submarine Landslides on the Continental Slope of Storfjorden and Kveithola Trough-Mouth Fans (North West Barents Sea), in: Yamada, Y., Kawamura, K., Ikehara, K., Ogawa, Y., Urgeles, R., Mosher, D., Chaytor, J., Strasser, M. (Eds.), Submarine Mass Movements and Their Consequences, Advances in Natural and Technological Hazards Research 31. Springer Netherlands, Dordrecht, pp. 735–745. doi:10.1007/978-94-007-2162-3

Luo, G., Flemings, P.B., Hudec, M.R., Nikolinakou, M. a, 2015. The role of pore fluid overpressure in the substrates of advancing salt sheets, ice glaciers, and critical-state wedges. Journal of Geophysical Research: Solid Earth 120, 87–105. doi:10.1002/2014JB011326

Mangerud, J., Dokken, T., Hebbeln, D., Heggen, B., Ingólfsson, Ó., Landvik, J.Y., Mejdahl, V., Svendsen, J.I., Vorren, T.O., 1998. Fluctuations of the Svalbard-Barents sea ice sheet during the last 150000 years. Quaternary Science Reviews 17, 11–42. doi:10.1016/S0277-3791(97)00069-3

Mangerud, J., Svendsen, J.I., 1992. The last interglacial-glacial period on Spitsbergen, Svalbard. Quaternary Science Reviews 11, 633–664.

Marín-Moreno, H., Minshull, T.A., Edwards, R.A., 2013. A disequilibrium compaction model constrained by seismic data and application to overpressure generation in The Eastern Black Sea Basin. Basin Research 25, 331–347. doi:10.1111/bre.12001

Marr, J.G., Elverhøi, A., Harbitz, C., Imran, J., Harff, P., 2002. Numerical simulation of mud-rich subaqueous debris flows on the glacially active margins of the Svalbard-Barents Sea. Marine Geology 188, 351–364. doi:10.1016/S0025-3227(02)00310-9

Martin, S., Cavalieri, D.J., 1989. Contributions of the Siberian Shelf Polynyas to the Arctic Ocean Intermediate and Deep Water. Journal of Geophysical Research 94, 12725–12738.

Masson, D.G., Wynn, R.B., Talling, P.J., 2014. Large Landslides on Passive Continental Margins: Processes, Hypotheses and Outstanding Questions, in: Submarine Mass Movements and Their Consequences. Springer Netherlands, Dordrecht, pp. 85–94. doi:10.1007/978-3-319-00972-8

Maubeuge, F., Lerche, I., 1994. Geopressure evolution and hydrocarbon generation in a north Indonesian basin: two-dimensional quatitative modelling. Marine and Petroleum Geology 11, 104–115. doi:10.1016/0264-8172(94)90013-2

Micallef, A., Masson, D.G., Berndt, C., Stow, D. a. V., 2009. Development and mass movement processes of the north-eastern Storegga Slide. Quaternary Science Reviews 28, 433–448. doi:10.1016/j.quascirev.2008.09.026

Micallef, A., Masson, D.G., Berndt, C., Stow, D.A. V, 2007. Morphology and mechanics of submarine spreading: A case study from the Storegga Slide. Journal of Geophysical Research: Earth Surface 112, 1–21. doi:10.1029/2006JF000739

Mienert, J., Posewang, J., 1999. Evidence of shallow- and deep-water gas hydrate destabilizations in North Atlantic polar continental margin sediments. Geo-Marine Letters 19, 143–149. doi:10.1007/s003670050101

Mienert, J., Vanneste, M., Bünz, S., Andreassen, K., Haflidason, H., Sejrup, H.P., 2005. Ocean warming and gas hydrate stability on the mid-Norwegian margin at the Storegga Slide. Marine and Petroleum Geology 22, 233–244. doi:10.1016/j.marpetgeo.2004.10.018

Mulder, T., Moran, K., 1995. Relationship among submarine instabilities, sea level variations, and the presence of an ice sheet on the continental shelf: An example from the Verrill Canyon Area, Scotia Shelf. Paleoceanography 10, 137–154.

Nadim, F., Kvalstad, T.J., Guttormsen, T., 2005. Quantification of risks associated with seabed instability at Ormen Lange. Marine and Petroleum Geology 22, 311–318. doi:10.1016/j.marpetgeo.2004.10.022

NGI, 2000. Ormen Lange - Slope stability assessment, soil parameters and material models. NGI report no. 993016. Oslo.

Noormets, R., Dowdeswell, J.A., Larter, R.D., Ó Cofaigh, C., Evans, J., 2009. Morphology of the upper continental slope in the Bellingshausen and Amundsen Seas – Implications for sedimentary processes at the shelf edge of West Antarctica. Marine Geology 258, 100–114. doi:10.1016/j.margeo.2008.11.011

O'Regan, M., Jakobsson, M., Kirchner, N., 2010. Glacial geological implications of overconsolidated sediments on the Lomonosov Ridge and Yermak Plateau. Quaternary Science Reviews 29, 3532–3544. doi:10.1016/j.quascirev.2010.09.009

Ó Cofaigh, C., Andrews, J.T., Jennings, A.E., Dowdeswell, J.A., Hogan, K.A., Kilfeather, A.A., Sheldon, C., 2013. Glacimarine lithofacies, provenance and depositional processes on a West Greenland trough-mouth fan. Journal of Quaternary Science 28, 13–26. doi:10.1002/jqs.2569

Ó Cofaigh, C., Taylor, J., Dowdeswell, J.A., Pudsey, C.J., 2003. Palaeo-ice streams , trough mouth fans and high-latitude continental slope sedimentation. Boreas 32, 37–55. doi:10.1080/03009480310001858.

Ó Cofaigh, C., Taylor, J., Dowdeswell, J.A., Rosell-Melé, A., Kenyon, N.H., Evans, J., Mienert, J., 2002. Sediment reworking on high-latitude continental margins and its implications for palaeoceanographic studies: insights from the Norwegian-Greenland Sea. Geological Society, London, Special Publications 203, 325–348. doi:10.1144/GSL.SP.2002.203.01.17

Osborne, M.J., Swarbrick, R.E., 1997. Mechanisms for generating overpressure in sedimentary basins; a reevaluation. AAPG Bulletin 81, 1023 LP-1041.

Owen, M., Day, S., Maslin, M., 2007. Late Pleistocene submarine mass movements: occurrence and causes. Quaternary Science Reviews 26, 958–978. doi:10.1016/j.quascirev.2006.12.011

Pedrosa, M.T., Camerlenghi, A., De Mol, B., Urgeles, R., Rebesco, M., Lucchi, R.G., 2011. Seabed morphology and shallow sedimentary structure of the Storfjorden and Kveithola trough-mouth fans (North West Barents Sea). Marine Geology 286, 65–81. doi:10.1016/j.margeo.2011.05.009

Pellissetti, M.F., Schuëller, G.I., 2009. Scalable uncertainty and reliability analysis by integration of advanced Monte Carlo simulation and generic finite element solvers. Computers and Structures 87, 930–947. doi:10.1016/j.compstruc.2009.04.003

Piotrowski, J. a., Kraus, A.M., 1997. Response of sediment to ice-sheet loading in northwestern Germany: Effective stresses and glacier-bed stability. Journal of Glaciology 43, 495–502.

Pirli, M., Schweitzer, J., Paulsen, B., 2013. The Storfjorden, Svalbard, 2008–2012 aftershock sequence: Seismotectonics in a polar environment. Tectonophysics 601, 192–205. doi:10.1016/j.tecto.2013.05.010

PLAXIS bv, 2015. Plaxis 2015 User's Manual. Delf, The Netherlands.

Quadfasel, D., Rudels, B., Kurz, K., 1988. Outflow of dense water from a Svalbard fjord into the Fram Strait. Deep Sea Research Part A. Oceanographic Research Papers 35, 1143–1150. doi:10.1016/0198-0149(88)90006-4

Rabie, M., 2014. Comparison study between traditional and finite element methods for

slopes under heavy rainfall. HBRC Journal 10, 160–168. doi:10.1016/j.hbrcj.2013.10.002

Rasmussen, T.L., Thomsen, E., 2015. Palaeoceanographic development in Storfjorden, Svalbard, during the deglaciation and Holocene: Evidence from benthic foraminiferal records. Boreas 44, 24–44. doi:10.1111/bor.12098

Rasmussen, T.L., Thomsen, E., Skirbekk, K., Ślubowska-Woldengen, M., Klitgaard Kristensen, D., Koç, N., 2014. Spatial and temporal distribution of Holocene temperature maxima in the northern Nordic seas: interplay of Atlantic-, Arctic- and polar water masses. Quaternary Science Reviews 92, 280–291. doi:10.1016/j.quascirev.2013.10.034

Rasmussen, T.L., Thomsen, E., Ślubowska, M. a., Jessen, S., Solheim, A., Koç, N., 2007. Paleoceanographic evolution of the SW Svalbard margin (76°N) since 20,000 14C yr BP. Quaternary Research 67, 100–114. doi:10.1016/j.yqres.2006.07.002

Raymo, J.E., Blum, M.E., 1996. Site 986, in: Proceedings of the Ocean Drilling Program, 162 Initial Reports. Ocean Drilling Program, pp. 287–343. doi:10.2973/odp.proc.ir.162.109.1996

Rebesco, M., Laberg, J.S., Pedrosa, M.T., Camerlenghi, A., Lucchi, R.G., Zgur, F., Wardell, N., 2014. Onset and growth of Trough-Mouth Fans on the North-Western Barents Sea margin – implications for the evolution of the Barents Sea/Svalbard Ice Sheet. Quaternary Science Reviews 92, 227–234. doi:10.1016/j.quascirev.2013.08.015

Rebesco, M., Liu, Y., Camerlenghi, A., Winsborrow, M., Laberg, J.S., Caburlotto, A., Diviacco, P., Accettella, D., Sauli, C., Wardell, N., Tomini, I., 2011. Deglaciation of the western margin of the Barents Sea Ice Sheet — A swath bathymetric and sub-bottom seismic study from the Kveithola Trough. Marine Geology 279, 141–147. doi:10.1016/j.margeo.2010.10.018

Rebesco, M., Pedrosa, M.T., Camerlenghi, A., G, R., Sauli, C., Mol, B. De, Madrussani, G., Urgeles, R., Rossi, G., Böhm, G., 2012. One million years of climatic generated landslide events on the northwestern Barents Sea continental margin, in: Yamada, Y., Kawamura, K., Ikehara, K., Ogawa, Y., Urgeles, R., Mosher, D., Chaytor, J., Strasser, M. (Eds.), Submarine Mass Movements and Their Consequences, Advances in Natural and Technological Hazards Research 31. Springer Netherlands, Dordrecht, pp. 747–756. doi:10.1007/978-94-007-2162-3_66

Rebesco, M., Wåhlin, A., Laberg, J.S., Schauer, U., Beszczynska-Möller, A., Lucchi, R.G., Noormets, R., Accettella, D., Zarayskaya, Y., Diviacco, P., 2013. Quaternary contourite drifts of the Western Spitsbergen margin. Deep Sea Research Part I: Oceanographic Research Papers 79, 156–168. doi:10.1016/j.dsr.2013.05.013

Reimer, P.J., Baillie, M.G.L., Bard, E., Bayliss, A., Beck, J.W., Blackwell, P.G., Ramsey, C.B., Buck, C.E., Burr, G.S., Edwards, R.L., Friedrich, M., Grootes,

P.M., Guilderson, T.P., Hajdas, I., Heaton, T.J., Hogg, A.G., Hughen, K.A., Kaiser, K.F., Kromer, B., McCormac, F.G., Manning, S.W., Reimer, R.W., Richards, D.A., Southon, J.R., Talamo, S., Turney, C.S.M., van der Plicht, J., Weyhenmeyer, C.E., 2009. IntCal09 and Marine09 radiocarbon age calibration curves, 0-50,000 years CAL BP. Radiocarbon 51, 1111–1150.

Rodrigues Duran, E., di Primio, R., Anka, Z., Stoddart, D., Horsfield, B., 2013. 3D-basin modelling of the Hammerfest Basin (southwestern Barents Sea): A quantitative assessment of petroleum generation, migration and leakage. Marine and Petroleum Geology 45, 281–303. doi:10.1016/j.marpetgeo.2013.04.023

Rohling, E.J., Foster, G.L., Grant, K.M., Marino, G., Roberts, a P., Tamisiea, M.E., Williams, F., 2014. Sea-level and deep-sea-temperature variability over the past 5.3 million years. Nature 508, 477–82. doi:10.1038/nature13230

Rothwell, R.G., 1989. Minerals and Mineraloids in Marine Sediments, Elsevier Applied Science Publishers Publishers. Springer Netherlands, Dordrecht. doi:10.1007/978-94-009-1133-8

Roy, S., Senger, K., Braathen, A., Noormets, R., Hovland, M., Olaussen, S., 2014. Fluid migration pathways to seafloor seepage in inner Isfjorden and Adventfjorden, Svalbard. Norwegian Journal of Geology 94, 99–119.

Sættem, J., Bugge, T., Fanavoll, S., Goll, R.M., Mork, A., Mork, M.B.E., Smelror, M., Verdenius, J.G., 1994. Marine Cenozoic margin development and erosion of the Barents Sea : Core evidence from southwest of Bjornoya. Marine Geology 118, 257–281.

Sættem, J., Poole, D.A.R., Ellingsen, L., Sejrup, H.P., 1992. Glacial geology of outer Bjornoyrenna , southwestern Barents Sea. Marine Geology 103, 15–51.

Sættem, J., Rise, L., Rokoengen, K., By, T., 1996. Soil investigations, offshore mid Norway: A case study of glacial influence on geotechnical properties. Global and Planetary Change 12, 271–285. doi:10.1016/0921-8181(95)00024-0

Sagnotti, L., Macrì, P., Lucchi, R., Rebesco, M., Camerlenghi, A., 2011. A Holocene paleosecular variation record from the northwestern Barents Sea continental margin. Geochemistry, Geophysics, Geosystems 12, Q11Z33. doi:10.1029/2011GC003810

Schauer, U., Fahrbach, E., 1999. A dense bottom water plume in the western Barents Sea : downstream modification and interannual variability. Deep-Sea Research I 46, 2095–2108. doi:10.1016/S0967-0637(99)00046-1

Sejrup, H.P., Hjelstuen, B.O., Dahlgren, K.I.T., Haflidason, H., Kuijpers, A., Nygård, A., Praeg, D., Stoker, M.S., Vorren, T.O., 2005. Pleistocene glacial history of the NW European continental margin. Marine and Petroleum Geology 22, 1111–1129. doi:10.1016/j.marpetgeo.2004.09.007

Sengbush, R.L., 1983. Seismic Exploration Methods, International Human Res. Dev.

Corp. Springer Netherlands, Dordrecht. doi:10.1007/978-94-011-6397-2

Siegert, M., 2004. Numerical reconstructions of the Eurasian Ice Sheet and climate during the Late Weichselian. Quaternary Science Reviews 23, 1273–1283. doi:10.1016/j.quascirev.2003.12.010

Siegert, M.J., Dowdeswell, J.A., Hald, M., Svendsen, J., 2001. Modelling the Eurasian Ice Sheet through a full (Weichselian) glacial cycle. Global and Planetary Change 31, 367–385.

Ślubowska-Woldengen, M., Koç, N., Rasmussen, T.L., Klitgaard-Kristensen, D., Hald, M., Jennings, A.E., 2008. Time-slice reconstructions of ocean circulation changes on the continental shelf in the Nordic and Barents Seas during the last 16,000 cal yr B.P. Quaternary Science Reviews 27, 1476–1492. doi:10.1016/j.quascirev.2008.04.015

Solheim, A., Andersen, E.S., Elverhøi, A., Fiedler, A., 1996. Late Cenozoic depositional history of the western Svalbard continental shelf, controlled by subsidence and climate. Global and Planetary Change 12, 135–148. doi:10.1016/0921-8181(95)00016-X

Solheim, A., Faleide, J.I., Andersen, E.S., Elverhøi, A., Forsberg, C.F., Vanneste, K., Uenzelmann-Neben, G., Channell, J.E.T., 1998. Late Cenozoic Seismic Stratigraphy and Glacial Geological Development of the East Greenland and Svalbard–Barents Sea Continental Margins. Quaternary Science Reviews 17, 155–184. doi:10.1016/S0277-3791(97)00068-1

Spielhagen, R., Baumann, K.-H., Erlenkeuser, H., Nowaczyk, N.R., Nørgaard-Pedersen, N., Vogt, C., Weiel, D., 2004. Arctic Ocean deep-sea record of northern Eurasian ice sheet history. Quaternary Science Reviews 23, 1455–1483. doi:10.1016/j.quascirev.2003.12.015

Stein, R., 2008. Glacio-Marine Sedimentary Processes. Marine Geology 2, 87–132.

Stigall, J., Dugan, B., 2010. Overpressure and earthquake initiated slope failure in the Ursa region, northern Gulf of Mexico. Journal of Geophysical Research 115, 1–11. doi:10.1029/2009JB006848

Stricker, S., Jones, S.J., Grant, N.T., 2016. Importance of vertical effective stress for reservoir quality in the Skagerrak Formation, Central Graben, North Sea. Marine and Petroleum Geology 59, 593–610. doi:10.1016/j.marpetgeo.2016.03.001

Stuiver, M., Reimer, P.J., 1993. Extended 14C data base and revised CALIB 3.0 14C age calibration program. Radiocarbon 35, 215–230.

Sultan, N., Cochonat, P., Canals, M., Cattaneo, A., Dennielou, B., Haflidason, H., Laberg, J.S., Long, D., Mienert, J., Trincardi, F., Urgeles, R., Vorren, T.O., Wilson, C., 2004a. Triggering mechanisms of slope instability processes and sediment failures on continental margins: a geotechnical approach. Marine Geology 213, 291–321. doi:10.1016/j.margeo.2004.10.011

Sultan, N., Cochonat, P., Foucher, J.P., Mienert, J., 2004b. Effect of gas hydrates melting on seafloor slope instability. Marine Geology 213, 379–401. doi:10.1016/j.margeo.2004.10.015

Svendsen, J.I., Alexanderson, H., Astakhov, V.I., Demidov, I., Dowdeswell, J.A., Funder, S., Gataullin, V., Henriksen, M., Hjort, C., Houmark-Nielsen, M., Hubberten, H.W., Ingólfsson, Ó., Jakobsson, M., Kjær, K.H., Larsen, E., Lokrantz, H., Lunkka, J.P., Lyså, A., Mangerud, J., Matiouchkov, A., Murray, A., Möller, P., Niessen, F., Nikolskaya, O., Polyak, L., Saarnisto, M., Siegert, C., Siegert, M.J., Spielhagen, R., Stein, R., 2004a. Late Quaternary ice sheet history of northern Eurasia. Quaternary Science Reviews 23, 1229–1271. doi:10.1016/j.quascirev.2003.12.008

Svendsen, J.I., Gataullin, V., Mangerud, J., Polyak, L., 2004b. The glacial History of the Barents and Kara Sea Region, in: Ehlers, J., Gibbard, P.L. (Eds.), Quaternary Glaciations Extent and ChronologyPart I: Europe. Elsevier, pp. 369–378. doi:10.1016/S1571-0866(04)80086-1

Talling, P., Clare, M., Urlaub, M., Pope, E., Hunt, J., Watt, S., 2014. Large Submarine Landslides on Continental Slopes: Geohazards, Methane Release, and Climate Change. Oceanography 27, 32–45. doi:10.5670/oceanog.2014.38

Talwani, M., Eldholm, O., 1977. Evolution of the Norwegian-Greenland Sea. Geological Society of America Bulletin 88, 969–999. doi:10.1130/0016-7606(1977)88<969

Tappin, D.R., 2010. Submarine mass failures as tsunami sources: their climate control. Philosophical Transactions of the Royal Society A: Mathematical, Physical and Engineering Sciences 368, 2417–2434. doi:10.1098/rsta.2010.0079

Taylor, J., Dowdeswell, J.A., Kenyon, N.H., O Cofaigh, C., 2002. Late Quaternary architecture of trough-mouth fans: debris flows and suspended sediments on the Norwegian margin, in: Dowdeswell, J.A., Ó Cofaigh, C. (Eds.), Geological Society, London, Special Publications. Geological Society, London, Special Publications, London, pp. 55–71. doi:10.1144/GSL.SP.2002.203.01.04

Tovey, K.N., Paul, M.A., 2001. Modelling self-weight consolidation in Holocene sediments. Bulletin of Engineering Geology and the Environment 61, 21–33. doi:10.1007/s100640100126

Tulaczyk, S., Kamb, W.B., Engelhardt, H.F., 2000. Basal mechanics of Ice Stream B, west Antarctica: 2. Undrained plastic bed model. Journal of Geophysical Research. doi:10.1029/1999JB900328

Turpeinen, H., Hampel, A., Karow, T., Maniatis, G., 2008. Effect of ice sheet growth and melting on the slip evolution of thrust faults. Earth and Planetary Science Letters 269, 230–241. doi:10.1016/j.epsl.2008.02.017

Urgeles, R., Locat, J., Sawyer, D.E., Flemings, P.B., Dugan, B., Binh, N.T.T., 2010. History of Pore Pressure Build Up and Slope Instability in Mud-Dominated Sediments of Ursa Basin , Gulf of Mexico Continental Slope, in: Submarine Mass

Movements and Their Consequences, Advances in Natural and Technological Hazards Research, 28, Spinger, Dordrecht (The Netherlands). pp. 179–190.

Urlaub, M., Talling, P.J., Masson, D.G., 2013. Timing and frequency of large submarine landslides: implications for understanding triggers and future geohazard. Quaternary Science Reviews 72, 63–82. doi:10.1016/j.quascirev.2013.04.020

Van Hinte, J.E., 1978. Geohistory analysis; application of micropaleontology in exploration geology. AAPG Bulletin 62, 201–222.

Vanneste, M., Heureux, J.L., Baeten, N., Brendryen, J., Vardy, M.E., Steiner, A., Forsberg, C.F., Kvalstad, T.J., Laberg, J.S., Chand, S., Longva, O., Rise, L., Haflidason, H., Hjelstuen, B.O., Forwick, M., Morgan, E., Lecomte, I., Kopf, A., Vorren, T.O., Reichel, T., 2012. Shallow landslides and their dynamics in coastal and deepwater environments, Norway, in: Yamada, Y., Kawamura, K., Ikehara, K., Ogawa, Y., Urgeles, R., Mosher, D., Chaytor, J., Strasser, M. (Eds.), Submarine Mass Movements and Their Consequences, Advances in Natural and Technological Hazards Research 31. Springer Netherlands, Dordrecht, pp. 29–41. doi:10.1007/978-94-007-2162-3

Vogt, P.R., Gardner, J., Crane, K., 1999. The Norwegian-Barents-Svalbard (NBS) continental margin: Introducing a natural laboratory of mass wasting, hydrates, and ascent of sediment, pore water, and methane. Geo-Marine Letters 19, 2–21.

Vorren, T.O., Laberg, J.S., 1997. Trough Mouth Fans - Paleoclimate and ice-sheet monitors. Quaternary Science Reviews 16, 865–881.

Vorren, T.O., Laberg, J.S., Blaume, F., Dowdeswell, J.A., Kenyon, N.H., Mienert, J., Rumohr, J., Werner, F., 1998. The Norwegian – Greenland Sea continental margins: Morphology and Late Quaternary sedimentary processes and environment. Quaternary Science Reviews 17, 273–302. doi:10.1016/S0277-3791(97)00072-3

Vorren, T.O., Landvik, J.Y., Andreassen, K., Laberg, J.S., 2011. Glacial History of the Barents Sea Region, in: Ehlers, J., Gibbard, P.L., Hughes, D. (Eds.), Developments in Quaternary Sciences. Elsevier, pp. 361–372. doi:10.1016/B978-0-444-53447-7.00027-1

Vorren, T.O., Lebesbye, E., Andreassen, K., Larsen, K.-B., 1989. Glacigenic sediments on a passive continental margin as exemplified by the Barents Sea. Marine Geology 85, 251–272. doi:10.1016/0025-3227(89)90156-4

Williams, D.F., Thunell, R.C., Tappa, E., Rio, D., Raffi, I., 1988. Chronology of the pleistocene oxygen isotope record: 0–1.88 m.y. B.P. Palaeogeography, Palaeoclimatology, Palaeoecology 64, 221–240. doi:10.1016/0031-0182(88)90008-9

Winsborrow, M.C.M., Andreassen, K., Corner, G.D., Laberg, J.S., 2010. Deglaciation of a marine-based ice sheet: Late Weichselian palaeo-ice dynamics and retreat in the southern Barents Sea reconstructed from onshore and offshore glacial

geomorphology. Quaternary Science Reviews 29, 424–442. doi:10.1016/j.quascirev.2009.10.001

Yardley, G.S., Swarbrick, R.E., 2000. Lateral transfer: a source of additional overpressure? Marine and Petroleum Geology 17, 523–537. doi:10.1016/S0264-8172(00)00007-6

Appendices

Appendix A. Symbology

a_v	:	Coefficient of compressibility (kPa)
C_{vn}	:	Coefficient of variation
m_v	:	Coefficient of volume change (kPa^{-1})
c_c	:	Compressibility index
S	:	Compressibility matrix
D	:	Constrained modulus
Q *and* C	:	Coupling matrices
$\bar{v}$	:	Displacement vector
c', c	:	Effective cohesion, cohesion (kPa)
σ'_v	:	Effective stress (kPa)
μ	:	Excess pore-water pressure (kPa)
H_f	:	Final compacted sediment thickness
g_w	:	Flow gravity vector in y-direction
$\overline{\overline{q_p}}$	:	Flux on the element boundaries
φ	:	Friction angle
k, k_0	:	Hydraulic conductivity (m/s), initial (at 1 kPa)
P_h	:	Hydrostatic pressure (kPa)
ρ_i	:	Ice density (kg/m^3)
hi	:	Ice thickness (m)
H_i	:	Initial decompacted sediment thickness
σ_v	:	Lithostatic or total stress (kPa)
$\overline{f_u}$	:	Load vector in an element
M	:	Material stress-strain matrix
λ^*	:	Modified compression index
κ^*	:	Modified swelling index
σ_n	:	Normal stress
λ	:	Overpressure
c_k	:	Permeability change with void ratio
H	:	Permeability matrix
K, K_0	:	Permeability, initial (at 1 kPa) (m^2)

$\bar{p}_w$	:	Pore pressure vector
S_{sat}	:	Pore saturation
ϕ, ϕ_0, ϕ_{ir}	:	Porosity, initial, irreductible (at 1 kPa)
S_{res}	:	Residual saturation
ϕ_p	:	Saturation to the pressure head
ρ_w	:	Sea water density (kg/m^3)
α, $\alpha_{(\phi)}$	:	Sediment compressibility, porosity dependent (m^2/N)
ρ_s	:	Sediment density (kg/m^3)
τ	:	Shear strength (kPa)
S_s, S_{s0}	:	Specific storage, initial (m^{-1})
σ	:	Standard deviation
K	:	Stiffness matrix
$\bar{\varepsilon}$	:	Strain vector
c_s	:	Swelling index
θ	:	Tortuosity
γ_w	:	Unit weight of pore fluid (kN/m^3)
ε	:	Vertical strain (m)
e, e_0	:	Void ratio, initial (at 1 kPa)
h_w	:	Water depth (m)

Appendix B. NGI-Basin model description

NGI-Basin is coded in Fortran 77/90 and extends Gibson's solution to non-homogeneous sedimentation in a multi-layered soil system (NGI, 2000). This is achieved by a numerical solution of the consolidation equation using finite-element approximation in the spatial domain, and finite-difference approximation in the time domain. Other features of the model are: i) implementation of a large-strain solution algorithm using updated geometry conFiguration, and ii) incorporation of user defined porosity and permeability equations.

It is assumed that the profile may already contain a layer that had consolidated under its own weight before deposition of new layers begins. Sedimentation of each layer is defined by a straight line, which defines the rate of material deposition (e.g. kg/m^2/yr). One may also specify "quiet periods" during which no sedimentation occurs. The partial differential equation of consolidation in NGI-Basin is expressed as:

$$\frac{k}{\gamma_w}\frac{\partial^2 u}{\partial z^2} = m_v\left(\frac{\partial u}{\partial t} - \frac{\partial}{\partial t}\Delta q\right) \qquad \text{eq. 23}$$

u: excess pore-water pressure; $\Delta q = \Delta\sigma$: total stress increment (σ refers always to vertical stress); k: permeability; γ_w: unit weight of water; $m_v = a_v/(1+e)$: coefficient of volume change; $a_v = -\Delta\varepsilon/\Delta\sigma'$: coefficient of compressibility; e: void ratio.

Other related parameters are the porosity $n=e/(1+e)$, the coefficient of consolidation $c_v = k/(\gamma_w \cdot m_v)$, and the constrained modulus $D = 1/m_v = \Delta\sigma'/\Delta\varepsilon$, where $\varepsilon = \Delta e/(1+e_0)$ denotes the vertical strain and e_0 is the initial void ratio. Void ratio, e, is a function of effective stress, and permeability is a function of void ratio using eq. 2and eq. 3:

$$e = e_1 - \frac{1+e_1}{(1-r)m}\left[\left(\frac{\sigma'}{\sigma_{ref}}\right)^{1-r} - 1\right] \qquad \text{eq. 24}$$

$$k = k_0 \cdot 10^{\frac{n-n_0}{A}} \qquad \text{eq. 25}$$

σ_{ref} = 1 kPa reference stress; *m:* "module number" and *r:* "power order" coefficients; e_1: value of e at $\sigma' = \sigma_{ref}$; and A: coefficient depending on the material with n_0 and k_0 consistent pair of porosity-permeability data at deposition (σ_{ref}). Parameters m, r and A have been defined by the best fit of eq. 14 with the consolidation and permeability test results.

Using the eq. 2 and the definition of m_v, eq. 4 can be derived:

$$m_v = \frac{1}{\sigma_{ref}} \frac{(1+e_1)}{(1+e)\cdot m}\left(\frac{\sigma'}{\sigma_{ref}}\right)^{-r} \qquad \text{eq. 26}$$

Using a 1st order 2-noded finite-element (FE) for representation of space variable, the eq. 1 can be expressed for a generic element j with length l as

$$K^j U^j + C^j U_j = Q^j \qquad \text{eq. 27}$$

where U^j is the vector of the pore-pressure at the two nodes, and

$$K^j = \frac{k^j}{\gamma_w}\begin{bmatrix} 1/l & -1/l \\ -1/l & 1/l \end{bmatrix} \qquad \text{eq. 28}$$

$$C^j = m_v \begin{bmatrix} l/3 & l/6 \\ l/6 & l/3 \end{bmatrix} \qquad \text{eq. 29}$$

$$Q^j = m_v \frac{\partial q}{\partial t}\begin{pmatrix} l/2 \\ l/2 \end{pmatrix} \qquad \text{eq. 30}$$

Assembling the above individual matrices for all finite elements in the model and introducing the implicit finite difference scheme of Crank-Nicholson to approximate the time derivation over time interval τ and substituting into eq. 5, expressed at times *t* and *t+ τ*, one can derive the following expression:

$$\left(K + \frac{2}{\tau}C\right) U_{t+\tau} = \left(\frac{2}{\tau}C - K\right) U_t + 2Q_t \qquad \text{eq. 31}$$

U: global vector of excess pore-pressure at the FE nodes and Q: corresponding vector of total stresses.

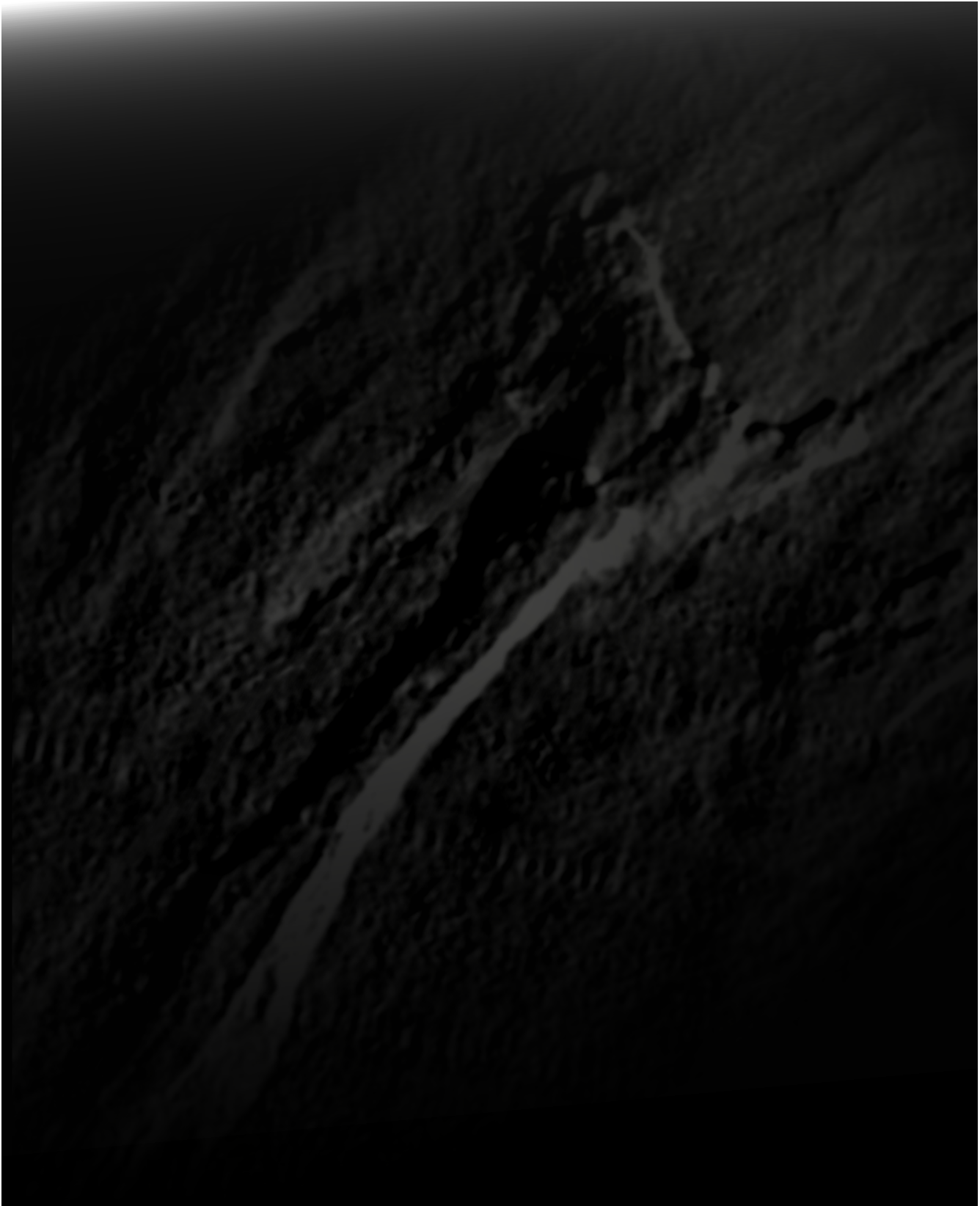

Acknowledgements to:

UNIVERSITAT DE BARCELONA

CSIC
CONSEJO SUPERIOR DE INVESTIGACIONES CIENTÍFICAS

ICM Institute of Marine Sciences